19950811 062

DTIC
SELECTED
AUG 1 5 1995
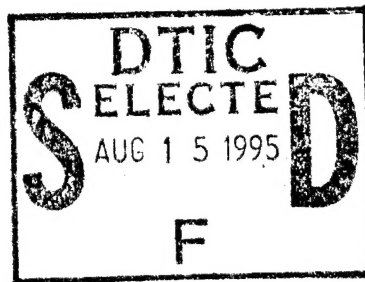F

DESIGN, FABRICATION, MODELING, AND TESTING OF
SURFACE-MICROMACHINED MICROMIRROR DEVICES

THESIS

M. Adrian Michalicek, BS Phys
2nd Lieutenant, USAF
AFIT/GE/ENG/95J-01

# DESIGN, FABRICATION, MODELING AND TESTING OF SURFACE MICROMACHINED MICROMIRROR DEVICES

THESIS

Presented to the Faculty of the Graduate School of Engineering

of the Air Force Institute of Technology

Air University

In Partial Fulfillment of the

Requirements for the Degree of

Master of Science in Electrical Engineering

M. Adrian Michalicek, BS Phys.

Second Lieutenant, USAF

June 1995

# ACKNOWLEDGMENTS

I would like to acknowledge the efforts of my research advisor, Dr. Victor Bright, for his guidance during my studies at AFIT. He saw the opportunity to expand the scope of my thesis research at a time when I was not satisfied with its content. As a result, I was able to conduct much more significant research and I am pleased with its outcome.

I would also like to thank Captain John Comtois for his incessant helpfulness and willingness to provide information and advice. He seemed to answer all my questions with "Here, I've already done that. This is what happens . . . " and was always available to supply vintage study music that made the long hours much more bearable. Also, after witnessing the "Michalicek" wire-bonding process, John was very willing to bond all my test chips for me. I think he just wanted to practice my method.

Likewise, the entire group of "VLSI Guys" and everyone else in the MEMS group made the long hours and occasional setbacks seem somewhat comical. It was nice to have others in the same pressure situations who could maintain a sense of humor. To all of you, I am grateful for your ability to laugh and never accept defeat.

The research conducted in this thesis would not have been possible without the technical support and generosity of Captain Gary Mauersberger of System Support, Robert Conkle and Richard Wager of the Digital Lab, and Chris O'Brien and Bill Trop of the Devices Lab. Each provided time and/or lab equipment and supplies to help me accomplish various tasks throughout the research process.

Finally, I would like to thank my wife, Kimberly, for her unending tolerance of my absence that seemed to become a weekly or even daily ritual. She understood that long hours were by no means desirable, but were sometimes quite necessary. I could always count on her support and she routinely volunteered to go out of her way to provide assistance at any time or in any form. She always seemed to know exactly what I needed and when I needed it. I owe all my accomplishments, AFIT and elsewhere, to her.

# TABLE OF CONTENTS

# LIST OF FIGURES

# LIST OF TABLES

# ABSTRACT

## DESIGN, FABRICATION, MODELING AND TESTING OF SURFACE MICROMACHINED MICROMIRROR DEVICES

The Flexure-Beam Micromirror Device (FBMD) is a phase-only piston style spatial light modulator demonstrating properties which can be used for phase adaptive-corrective optics. This thesis presents a complete study of new designs of FBMDs and other micromirror devices, from original design considerations through final device testing and verification of ideal and advanced models. The models relate the electrical and mechanical properties of the device by equating the electrostatic force of a parallel-plate capacitor with the counteracting spring force of the device's support flexures. For the advanced model of the Flexure-Beam micromirror device, the capacitor solution is derived via the Schwartz-Christoffel transformation such that the final solution accounts for non-ideal electric fields. This model describes the behavior of any Flexure-Beam device, given its geometry and material properties. It includes operational parameters such as drive frequency and temperature, as well as fringing effects, mirror surface deformations, and cross-talk from neighboring devices. Comparisons are made between the ideal and advanced Flexure-Beam micromirror models.

Several forms of micromirror devices studied in this thesis were commercially fabricated in a standard surface micromachining process. Design considerations for these and other devices are presented. These micromirror devices were tested using a microscope-based laser interferometer in which a laser beam reflected from the device under test modulates a fixed reference beam. The mirror's displacement is then determined from the phase difference. This procedure generates a continuous stream of data for each selected position on the mirror surface. Plots of this data describe the localized surface deflection as a function of drive voltage.

# DESIGN, FABRICATION, MODELING, AND TESTING OF SURFACE-MICROMACHINED MICROMIRROR DEVICES

## *(I) INTRODUCTION*

In recent years, deformable mirror devices (DMDs) have emerged as a new microelectromechanical (MEM) technology with tremendous potential for future applications. As shown in Fig. 1-1, the concept of deformable mirrors was developed and utilized as early as 211 BC by Greek soldiers to destroy enemy ships [1].
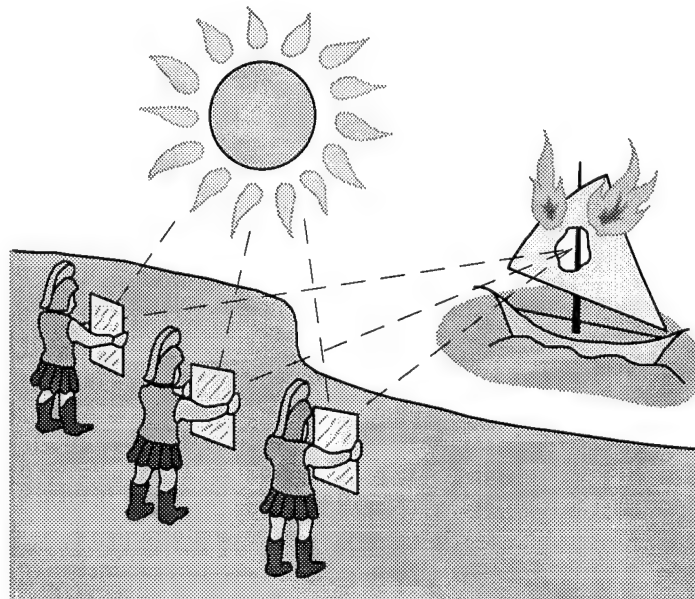


**Figure 1-1.** Greek soldiers using deformable mirrors [1].

However, it was not until 1973 that serious development of micromirror devices began to emerge. Currently, several designs of deformable mirrors have been fabricated, some before a practical use had been identified. It is these devices that are now receiving serious attention as optical communication and related fields are expanding.

## *(1.1)* BACKGROUND

Deformable mirror devices are a specific type of spatial light modulator (SLM). Spatial light modulators are devices that can alter the phase, amplitude, and/or the direction of propagation of an incident beam of light. Deformable mirror devices do this by moving a reflective surface to achieve the desired effect. Currently, two distinct types of micromirrors are used. Continuous surface devices use one large reflective membrane that is locally controlled by individual actuators to form a continuous reflective surface. Circus "fun house" mirrors are an example of such a device. Segmented devices, on the other hand, use a mirror surface that is divided into numerous individually controllable smaller mirrors. Greek soldiers used segmented mirrors to form a parabolic reflective surface which was used to focus sunlight onto enemy ships.
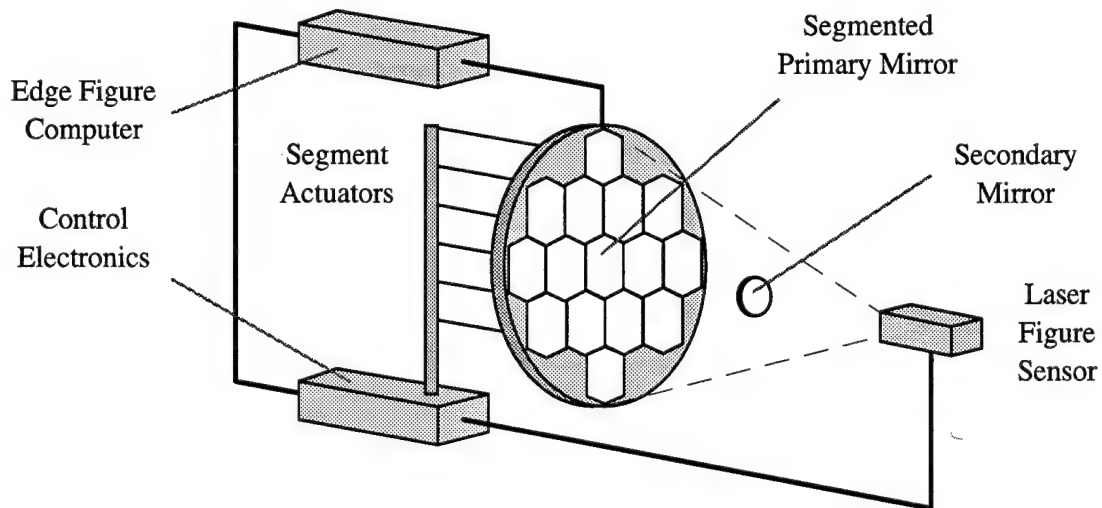


**Figure 1-2.** Telescopic system with segmented primary mirror [1].

Segmented devices are used today in the formation of large parabolic mirrors. As shown in Figure 1-2, the primary mirror of many modern optical telescope systems is comprised of segmented deformable mirrors. In the past, the size-limiting factor in such systems has been the size of the primary mirror which had to be mechanically stable yet

1-2

light enough to move to various positions throughout a full field of view. Larger mirrors were frequently damaged or caused damage to other components of the telescope when movement was attempted. With the application of segmented deformable mirror technology, the practical limit in telescopic primary mirror size can be extended since much lighter and smaller mirrors can be individually anchored, controlled, and placed adjacent to each other to form the necessary parabolic mirror.

The segmented mirrors are not only placed at a slight angle to each other, but are shaped by the segmented actuators and are free to bend to form smaller parabolically curved surfaces. The segmented actuators are manipulated by the control electronics which receive information from the laser figure sensor and the edge computer which is then translated into a necessary change in the position or shape of the mirrors. These monitoring devices continually check the status of the segmented mirrors to maintain the parabolic form of the entire device and to ensure that no gaps or severe discontinuities are present in the surface of the primary mirror which would result in a distorted image or a loss in image resolution.

The basic principles of this macroscopic technology can also be used in microscopic applications which involve fabricating deformable mirrors on integrated circuits. Several forms of micromirrors have emerged that combine on-chip addressing electronics with the micro-mechanical mirrors [2,3]. The geometric and material variations of these devices demonstrate that deformable mirrors can be designed and implemented for a variety of specific uses. The research presented in this thesis involves the design, fabrication, modeling, and testing of various forms of micromirror devices.

The micromirror devices studied are segmented surface devices in which the actuation of a small reflective mirror is controlled by a single address electrode. The metallized mirror and the address electrode of the device form a parallel plate capacitor. The voltage between the mirror and the electrode creates an electrostatic force acting on the mirror in the downward direction. The flexures holding the mirror are designed to

deform, allowing the mirror to move vertically with applied voltage. The resulting spring force of the flexures acts on the mirror in the upward direction, countering the electrostatic force of the capacitor.

Various types of devices were designed and fabricated in order to characterize the general behavior of electrostatically actuated micromirrors. Of particular interest, however, is the piston device known as the Flexure-Beam Micromirror Device (FBMD). Figure 1-3 shows a square Flexure-Beam device as seen from directly overhead and from the side, illustrating the vertical motion of the mirror.
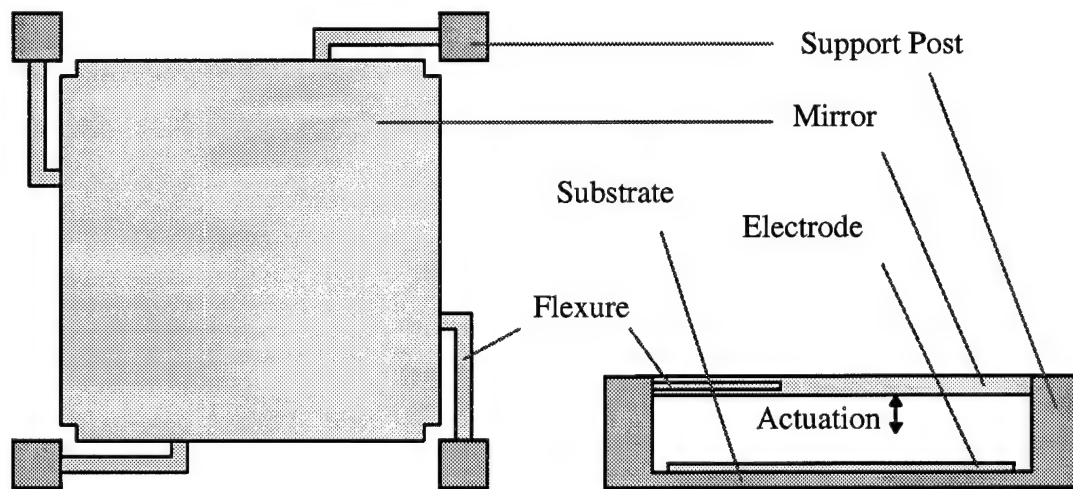


**Figure 1-3.** Overhead and side views of a square Flexure-Beam micromirror device.

The Flexure-Beam device is a "phase-only" device since the direction of motion of the mirror is orthogonal to the reflective surface. Therefore, the optical path length can be altered while the direction of propagation remains unchanged. This makes the piston device very appealing for phase modulated filters or for adaptive phase correcting optics.

Since the forces due to electrostatic actuation and the flexure support are functions of deflection distance, equating them will produce a characteristic equation relating the applied actuation potential between the mirror and electrode to the downward deflection distance of the mirror. Using ideal models of both the capacitor and spring, this

characteristic equation is quite simple. However, it becomes obvious that the actual behavior of the device is not ideal and involves realistic effects of these models such as fringing effects of the electric fields within the capacitor or surface deformations of the mirror itself. Therefore, the ideal model can be developed as a starting point for describing the device behavior. The non-ideal effects are then incorporated so that the characteristic model more closely resembles the actual behavior of the device.

## (1.2) PROBLEM STATEMENT AND OBJECTIVES

One application of the FBMD is in laser communications between objects in rapid relative motion. It is in the interest of the Air Force to design a system that will allow for laser communications between aircraft in flight. The primary design consideration for such a system is the correction of phase aberrations in the laser beam that are created as the beam passes through the atmosphere and windows in the aircraft fuselage.
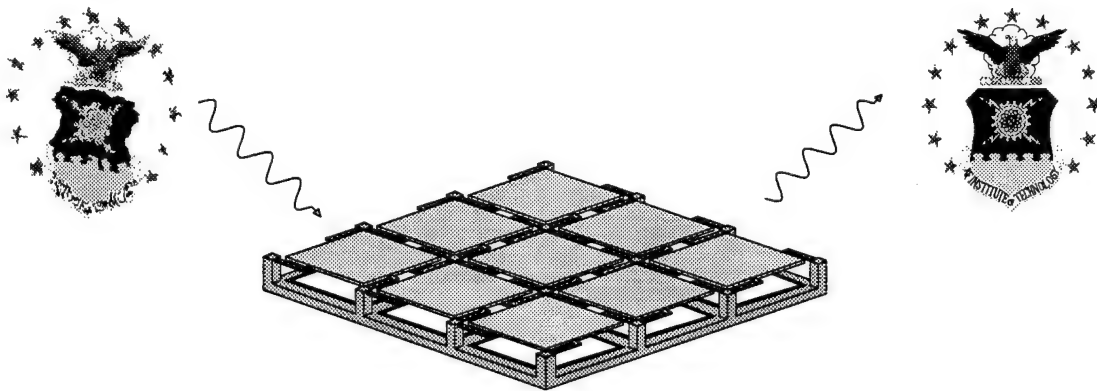


**Figure 1-4.** Illustration of phase aberration compensation using FBMD arrays.

The system must be able to employ an array of Flexure-Beam devices to discretely alter the path length of the beam across the phase-front to remove these induced aberrations. Figure 1-4 illustrates the use of such an array of devices. Outside each window, strong currents of turbulent air form random pockets of various air pressures and densities. The

laser beam containing the communications signal passes through these pockets and is distorted from an ideal plane wave due to the varying atmospheric densities which slightly alter the propagation velocity and direction of the beam. Therefore, the phase-front of the laser beam becomes aberrated throughout its cross section and requires phase aberration compensation to retrieve the information encoded within the beam.
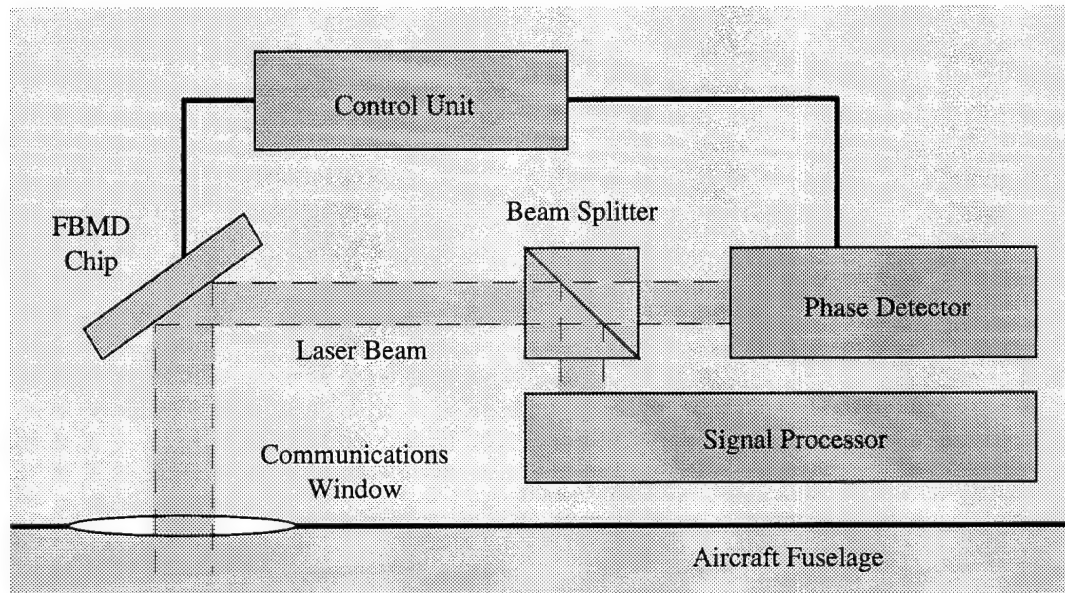


**Figure 1-5.** Proposed laser communication system using FBMD beam correction.

The proposed laser communication system is shown in Fig. 1-5 which illustrates the use of the FBMD chip containing an array of micromirrors. For this system to function as desired an extremely accurate device model must be developed and implemented by a control unit which dictates the behavior of the mirrors on the FBMD chip. This control unit must receive information from a phase sensory unit that informs it as to how much phase correction is needed in order to fully rectify the beam phase aberrations created as the beam passes through air pockets located outside the communication windows. The control unit, in turn, uses the device model to translate the needed phase correction into distances that individual mirrors must be displaced and their corresponding electrode potentials which must be applied to achieve the rectified beam.

The critical point in this system is the FBMD control unit which utilizes the model of how the individual mirrors of the device will respond to applied potentials. Therefore, the model must further account for any and all non-ideal physical behavior observed in the operation of the device. This must incorporate various parameters such as operating temperature, drive frequency, and the geometry and material properties of the flexures and mirrors as well as other elements related to specific fabrication processes.

The FBMD chip which must be used in this system has two dimensional arrays of individually actuated piston devices. It is desirable to design the micromirrors such that the devices can be closely packed together to maximize the active area of the chip.
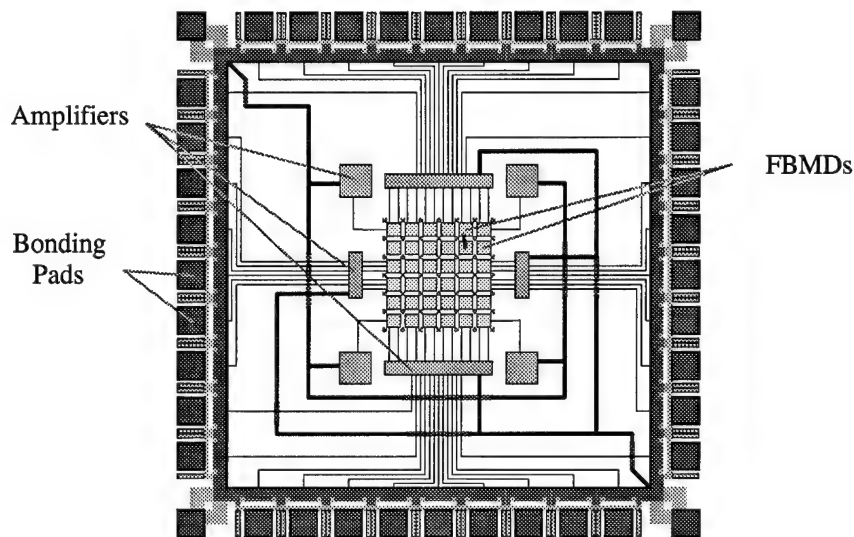


**Figure 1-6.** Drawing of a basic layout of an individually addressable FBMD chip.

Portions of the laser beam that reflect from other surfaces on the chip can not be modulated and will therefore maintain the noise characteristic of the aberrated beam. A basic FBMD chip is shown in Fig. 1-6 which illustrates the relative proximity of the devices and demonstrates how the devices are set inside a standard integrated circuit pad frame. Shown with the devices are various amplifiers which may be included to operate the array. It is easy to see that the mirrors can be significantly smaller than each bonding pad. Therefore, a larger array of devices would require a much larger pad frame due to

the number of bonding pads required. It is for this reason that some other technology is being sought for routing purposes, one that could possibly bond and route incoming signals below the substrate surface. As shown in Fig. 1-7(a), the array of mirrors is closely packed together to maximize the active area inside the optical target zone. This presents routing problems when trying to connect bonding pads to the address electrodes of devices at the center of the array. Most test devices have been fabricated using row and column addressing to avoid these problems. Such an array is shown in Fig. 1-7(b).
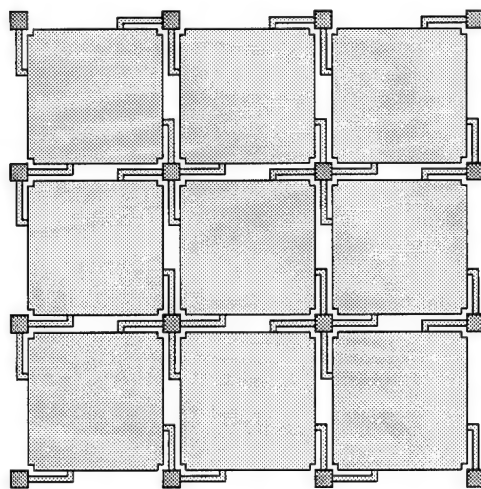


(a) Drawing of the Array          (b) Photograph of the Array [4]
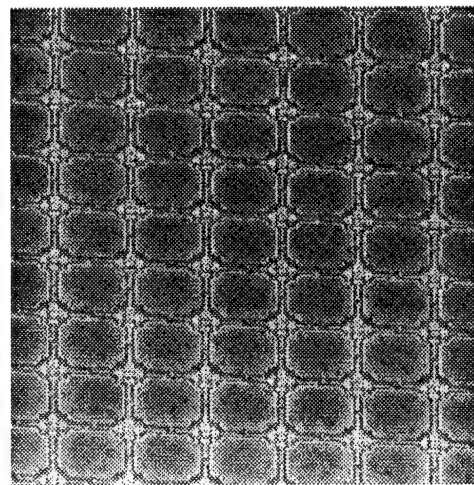
**Figure 1-7.** Array of square Flexure-Beam devices used in phase adaptive optics.

It is obvious that the signal reflected by the mirrors will dominate the output of the device, but the sharp edges and gaps in the surface as well as the etch holes created for the chemical release process tend to reduce its optical efficiency.

To use this device in the suggested communication system, its behavior must first be modeled. To do this, the device must be experimentally characterized so that its behavior can be related to applied voltages. However, given slight variations in the flexures and posts, mostly due to the fabrication process, one mirror may not behave exactly as another. For this reason, the device is characterized using a statistical

assumption such that an average behavior can be described for any mirror [5]. First, the phase errors are assumed to be random so that a full range of phase is made available to the distribution with all phases equally weighted. Also, the individual mirrors are assumed to be statistically independent of each other and identically distributed. Although some cross-talk may exist between mirrors where the voltage applied to one electrode may affect the deflection of the neighboring mirror, this interdependence is relatively predictable and shall be included in the model rather than in this statistical assumption. Fortunately, the device behavior follows a Gaussian distribution in which the average behavior, which is predicted by the characteristic model, is related to the mean of the curve. As depicted in Fig. 1-8, for a given voltage, the probability is greatest that the predicted vertical deflection will occur.
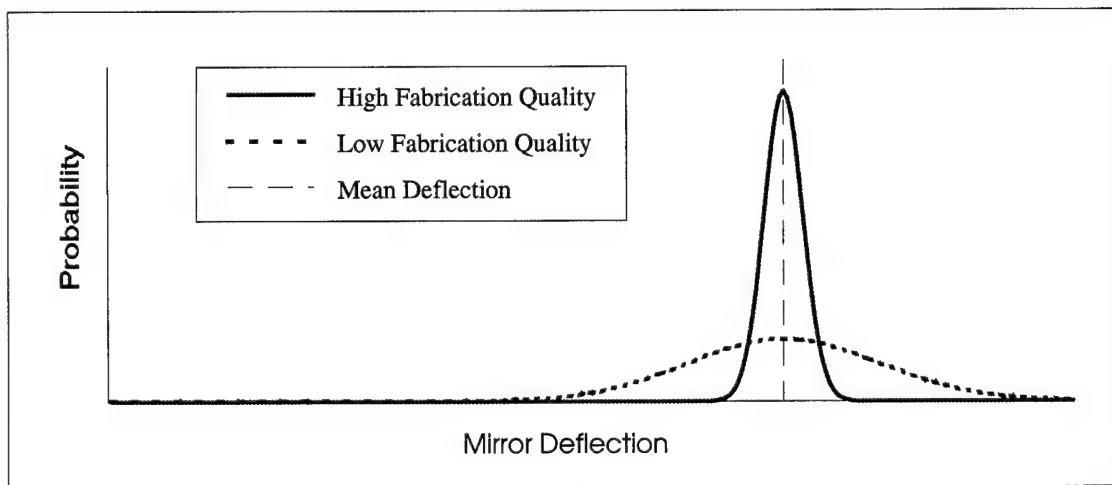


**Figure 1-8.** Gaussian distributions of deflection distance for any applied voltage.

Any variation in an individual device may cause it to deflect some distance other than predicted. For example, the fabrication process may leave some residue on the flexures that alters device behavior. If it resists the downward motion of the mirror more than expected, the deflection distance of the mirror will be reduced. Fortunately, the probability of any significant variation in the deflection distance is small compared to that

of the mean deflection distance. Starting from such a statistical approach, it is now required to develop the characteristic equation which will serve as a very precise and well-developed model of the device.

## (1.3) APPROACH

In order to develop the characteristic model of the Flexure-Beam micromirror device, it must first be characterized by equating the electrostatic actuation force of the parallel plate capacitor with the mechanical restoring force of the spring. Figure 1-9 shows a Flexure-Beam device in the resting ( $V = 0$ ) and active ( $V > 0$ ) modes where $z_m$ represents the vertical height of the mirror above the address electrode. It is initially assumed that when no electrode potential is applied, the mirror rests firmly in the resting position, $z_0$, where the deflection distance, $d$, at all points on the mirror is zero.
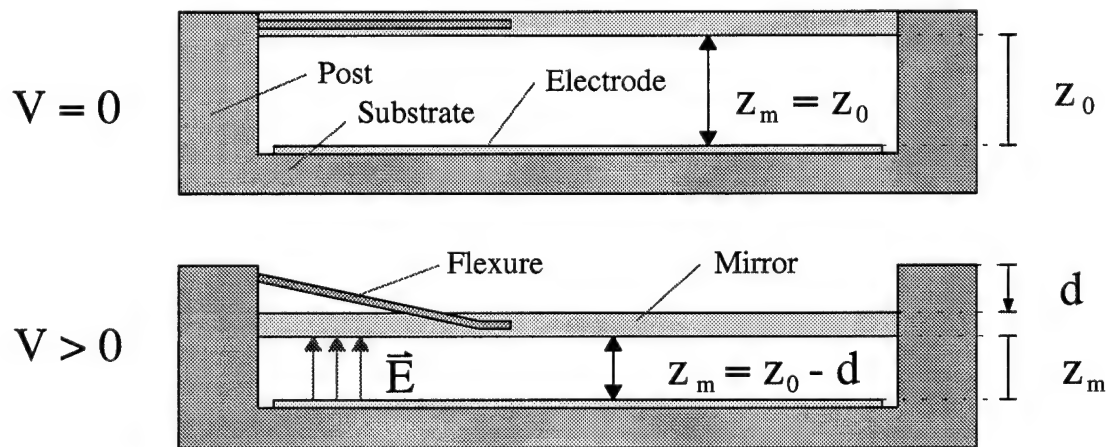


**Figure 1-9.** Flexure-Beam Micromirror Device in resting and active mode.

The geometry of the Flexure-Beam device is such that an electric field is induced between the mirror held at a negative voltage ( or ground ) and the electrode that is allowed to vary between zero and some maximum positive voltage. This maximum electrode voltage

must be maintained below a point where the device is permanently damaged by irreversibly deforming the flexures or the mirror itself.

The flexures of the FBMD are designed to provide a restoring force on the mirror counteracting the electrostatic force supplied by the address electrode. These flexures are modeled as portions of a standard spring providing a direct relationship between the force supplied by the flexures and the mirror deflection distance. Figure 1-10(a) shows a device flexure modeled as a portion of a rectangular spring. Using this representation, the complete operational model of the device reduces to that shown in Fig. 1-10(b).



(a) Device Flexure                    (b) Operational Representation
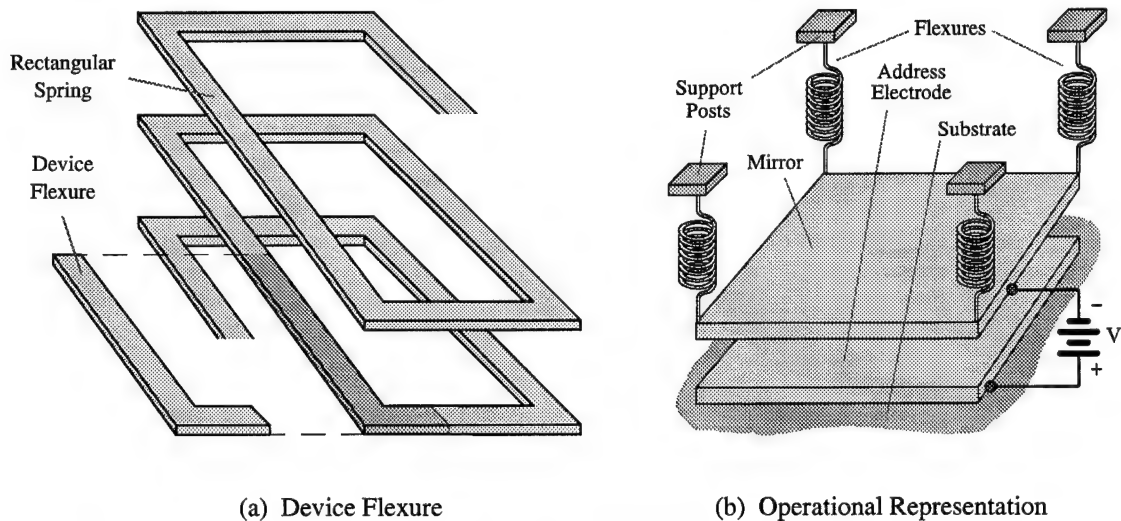
**Figure 1-10.** Device flexure and complete operational representation of the FBMD.

The spring constant is a function of several parameters such as temperature and driving frequency which tend to alter its value and therefore the restoring force. Furthermore, this spring constant can be closely predicted using basic mechanical engineering techniques in which the dimensions and material properties of the flexures determine a known behavior. Knowing this constant, and the electrostatic force, the behavior of the device can be predicted before it is actually fabricated allowing for modifications and refinements of the device during the design stage.

The induced electric field is shown in Fig. 1-11 in which the field lines are uniform and orthogonal to the mirror and electrode surface in the center of the cell.

1-11

Moving outward to the edges of the mirror, the field lines slowly become less uniform until they are rounded outward at the edges of the mirror and electrode. It is easy to see that this figure represents the electric field lines as viewed from any rotated angle within the cell. It is these fringing effects that will prevent the use of the ideal force equation for a parallel plate capacitor because the force is no longer uniform across the mirror surface. As devices become smaller, the effects of fringing fields become increasingly significant making more detailed models necessary.
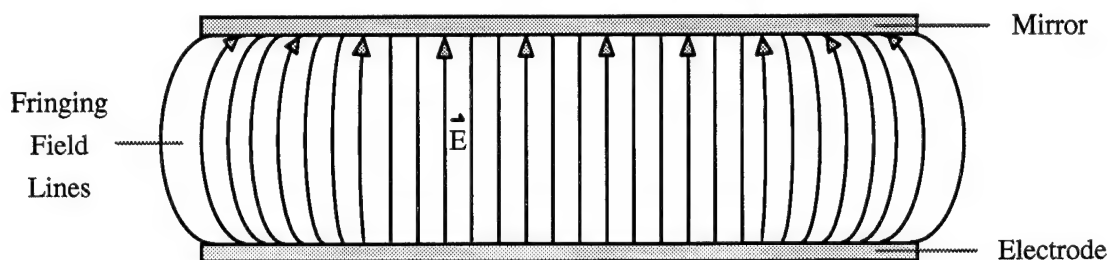


**Figure 1-11.** Electric field induced within the FBMD.

Likewise, the mirror surface is ideally assumed to be perfectly rigid such that no surface deformations exist throughout the range of motion of the device. Such an assumption is incorrect since any membrane or suspended structure will deform according to the force applied across its surface.
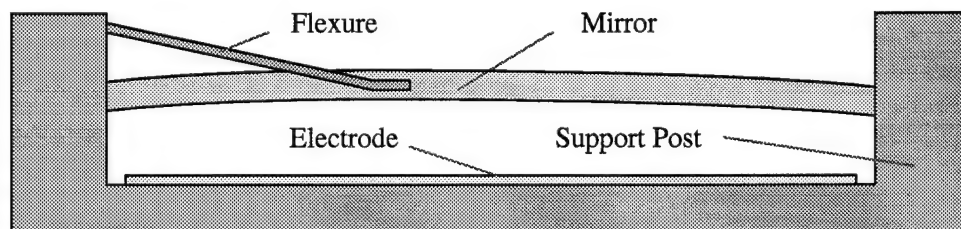


**Figure 1-12.** Possible deformation of mirror surface due to electrostatic actuation.

Figure 1-12 shows a cross section of how the mirror may deform as voltage is applied to the address electrode. As this voltage creates a force along the surface of the mirror in the

downward direction, the portions of the mirror attached to the flexures will be rigidly suspended while the remainder of the mirror is free to deform or deflect downward. The degree of deformation is related to the applied voltage as well as the mirror geometry and the material properties from which it is constructed. A more detailed model of this device must account for non-ideal behavior such as surface deformations.

The deflection of a micromirror device is measured using a microscope-based laser interferometer in which a collimated laser beam is split into an object and reference beam. The object beam is reflected from the mirror surface and is recombined with the constant reference beam to form a modulated output beam. The interference between the two beams creates an optical intensity pattern which is measured by a photodetector. An output voltage is generated relative to this optical intensity. The input and output voltages are captured from an oscilloscope and the resulting analysis yields a curve in which the mirror deflection is plotted against the driving address potential.
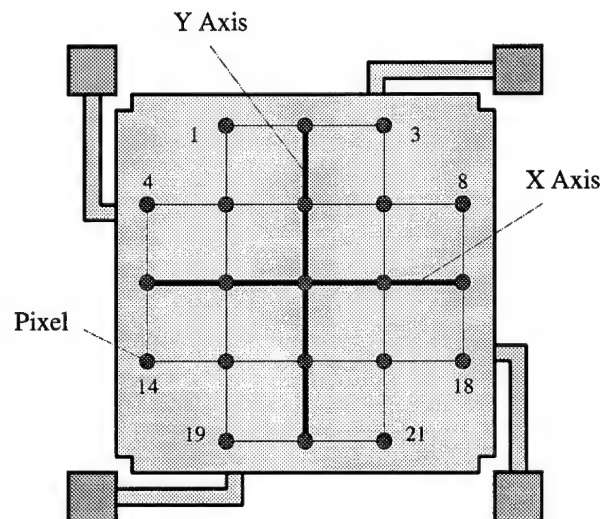


**Figure 1-13.** Division of mirror surface into pixel points [6].

The mirrors of the FBMD are generally much larger than the 4 μm diameter of the laser spot focused on the mirror surface. This allows for a division of the mirror surface into several pixels that can be individually studied. Therefore, the mirror displacement

can be measured over the entire surface in the pattern shown in Fig. 1-13. These pixels will be used to quantify the corresponding region of the mirror surface to allow for observations concerning the rigidness of the mirror itself. Any deformation in the surface of the mirror as larger and larger potentials are applied to the address electrode can be detected by monitoring the displacement at each pixel.

The course of action for the research presented in this thesis is to develop a theoretical model for the behavior of FBMDs and collect experimental data from these devices. Then, the experimental data collected from each pixel on various devices will be used to verify the overall deflection model for the mirror surface as a function of applied potential. This model includes various operating parameters such as temperature and driving frequency and also incorporates non-ideal behavior of the devices such as surface deformations, fringing field losses, and drive interference from neighboring devices known as cross-talk.

## (1.4) SEQUENCE OF PRESENTATION

The concepts and related information mentioned in Chapter (I) are expounded in the following chapters. Chapter (II) contains a review of current micromirror technology involving a wide variety of device designs and possible applications. In addition, related research involving the FBMD is reviewed for the purpose of establishing a reasonable foundation upon which new research should build.

Chapter (III) presents the theoretical approach to modeling the FBMD by developing mathematical relationships between the forces governing the behavior of the device. The theory is developed from basic physical principals concerning the electrostatic force of the parallel plate capacitor, the spring force of the device flexures, and various effects of operating parameters. The final product of this chapter is a complete theoretical model of the behavior of the FBMD for any geometry or materials.

Chapter (IV) presents the experimental setup and procedure which are used to verify the model developed in Chapter (III). The purpose of this chapter is to carefully outline the steps involved in gathering data as well as to identify the equipment used and lessons learned in the process. A complete description of the devices under test is presented so that the goal and desired outcome of the data collection are made clear.

Chapter (V) consists of the discussion and analysis of the data collected from the various devices under test. The empirical data is compared to the theoretical model so as to verify its precision and reliability throughout various test devices. When applicable, explanations are presented as to why a predicted outcome was not observed.

Chapter (VI) concludes the information presented in the thesis. The key points of the research are highlighted and the suggested course of future research is described in detail to aid in the further development of FBMD technology.

# (II) LITERATURE REVIEW

To become familiar with the current level of technology concerning micromirrors, a complete background review was conducted using published journal articles and related reference materials. It was determined that micromirror devices have been widely accepted as a highly adaptable and efficient means of manipulating optical systems. It was also determined that these devices have only recently been implemented for these purposes, primarily due to lengthy research and development periods. Regardless of current limitations, however, the development of micromirror devices is considered to be essential to future optical applications in communications and signal processing.

## (2.1) DEFORMABLE MICROMIRROR DEVICES

Among the micromirrors already developed are two forms of continuous surface devices and a large variety of segmented devices. Their fundamental operation is common in micro-mechanical devices such that an electrostatic force created between electrodes directs the motion of the mirrors. Each of the micromirror designs has distinct operating characteristics that distinguish them for use in specific applications. Some devices tilt the mirror, some lower it, and others do both to varying degrees. This means that each specific device is limited in its application either by a lack in range of motion or other effects such as losses in amplitude or redirection of the incident beam of light. The designs presented in this chapter are primarily first-generation devices with basic characteristics that are used to describe most similar designs. Many geometric and material variations have recently been designed to overcome some of these limitations.

The most important characteristic is optical efficiency. Optical efficiency is the maximum modulated energy deflected into the ( M, N ) diffraction order divided by the total energy illuminating the device [3]. This efficiency is largely dominated by the

geometric design and operation of the various deformable micromirror devices [7]. For the continuous surface devices, the optical efficiency is reduced due to the bending of the mirror which reflects the incident light away from the optical path. The segmented devices share this characteristic to some degree, but have a more distinguishable trait. The sharp edges and gaps in the surface of the segmented devices tend to scatter the light away from the desired optical path, reducing the optical efficiency of the design.

The two types of continuous surface devices, shown in Fig. 2-1, are characterized by how the reflective surface is supported on the substrate. All other characteristics such as the electrostatic actuation of the reflective surfaces remain the same.



(a) Elastomer Device                    (b) Membrane Device
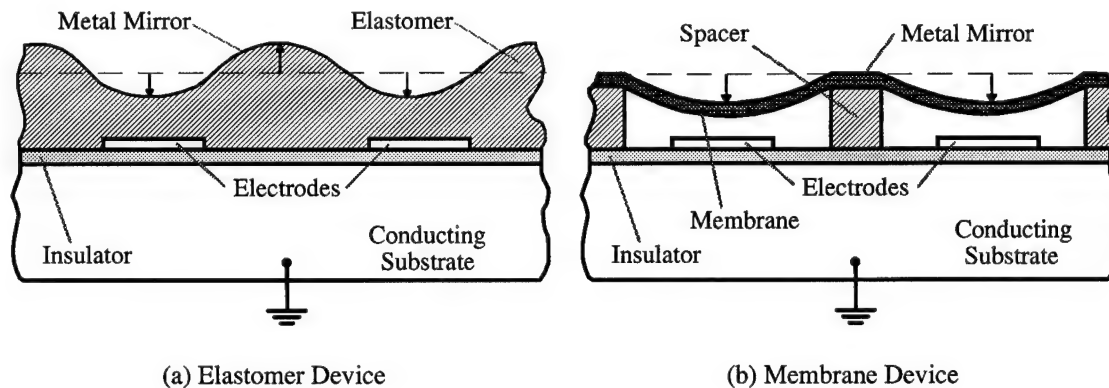
**Figure 2-1.** View of Elastomer and Membrane continuous surface devices [2].

The Elastomer device supports the mirror with a displaceable elastic spacer between the reflective surface and the addressing electrodes. This allows for a smooth continuity in the surface of the mirror. Unfortunately, this creates other problems that may disable the design for a specific application. For instance, the metallized reflective surface shared by adjacent cells is more likely to move than to stretch. Therefore, an individually addressed electrode that is activated would tend to pull the surface away from a neighboring electrode that is not activated. This creates severe "cross-talk" problems between cells.

The Membrane device supports the mirror with rigid spacers that hold portions of the mirror fixed in one position while the remainder of the surface is allowed to flex

downward toward the electrodes. One disadvantage of this device is that a large portion of the mirror, as much as 75% of the surface, is required for stability and can not be used as a modulating element. As shown in Fig. 2-2, the reflective surface above the spacers will reflect light directly back along the optical path, reducing desired effects.



Electrode
Channel Stop
Polysilicon Gate
Drain
Floating Source
Channel Stop
Mirror
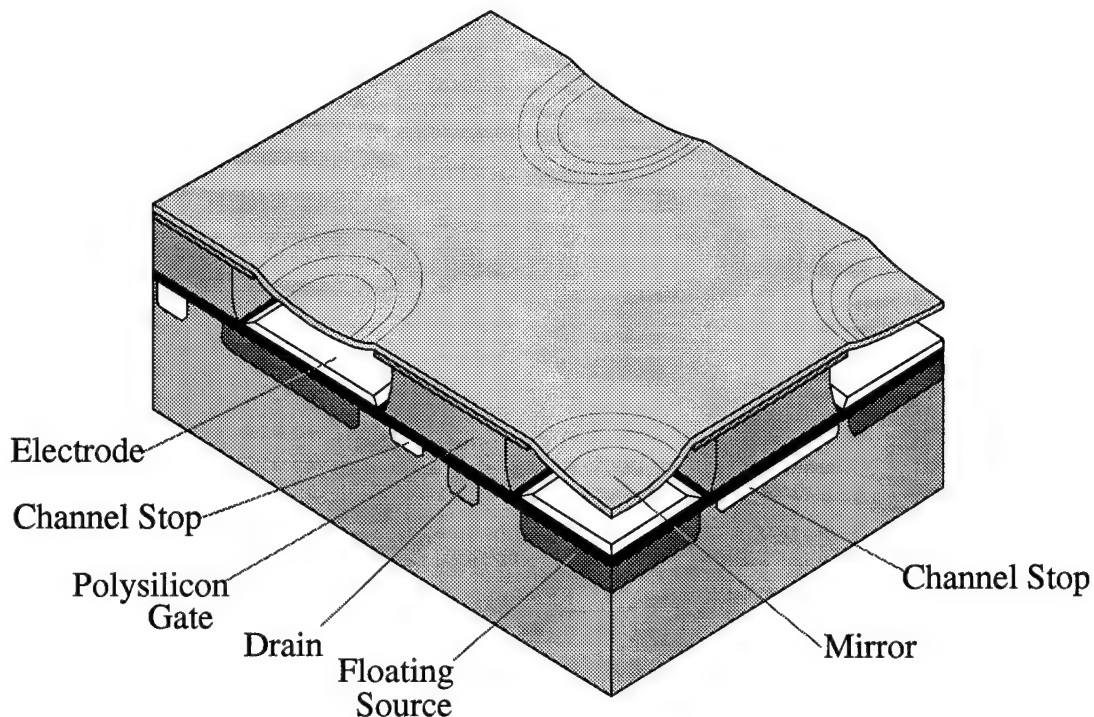
**Figure 2-2.** The Membrane continuous surface deformable mirror device [8].

Both designs of continuous surface devices share a common limitation in possible applications. As the surface is deflected downward, the deflection distance is not uniform across the mirror cell. Therefore, any use as a phase-modulating element would result in a loss of signal intensity as the beam is reflected circularly away from the optical path.

The segmented devices include the Inverted Cloverleaf, Cloverleaf, Quad-Cantilever, Torsion-Beam, and the Piston type FBMD. The FBMD is of specific interest to the Air Force for the laser communication system due to its phase-only characteristics.

The first segmented deformable micromirror device to be designed and fabricated was the Inverted Cloverleaf design shown in Fig. 2-3. This device has four reflective

surfaces per pixel, each fixed by the outside corner to the surface of the device. The reflective surfaces are free to move along the vertical axis. As the electrode potential increases, the cantilever surfaces bend downward at the center of the pixel. This creates a phase modulation by lengthening the optical path of the incident beam and an amplitude reduction by redirecting some of the light away from the pixel [3]. It is obvious that the four cantilever surfaces within each pixel will not redirect the light in the same direction. Also, the phase modulation in the beam is not uniform as the center of the pixel will generate a greater modulation than the outer edges. As shown in Fig. 2-3, much of the surface of the device is stationary.
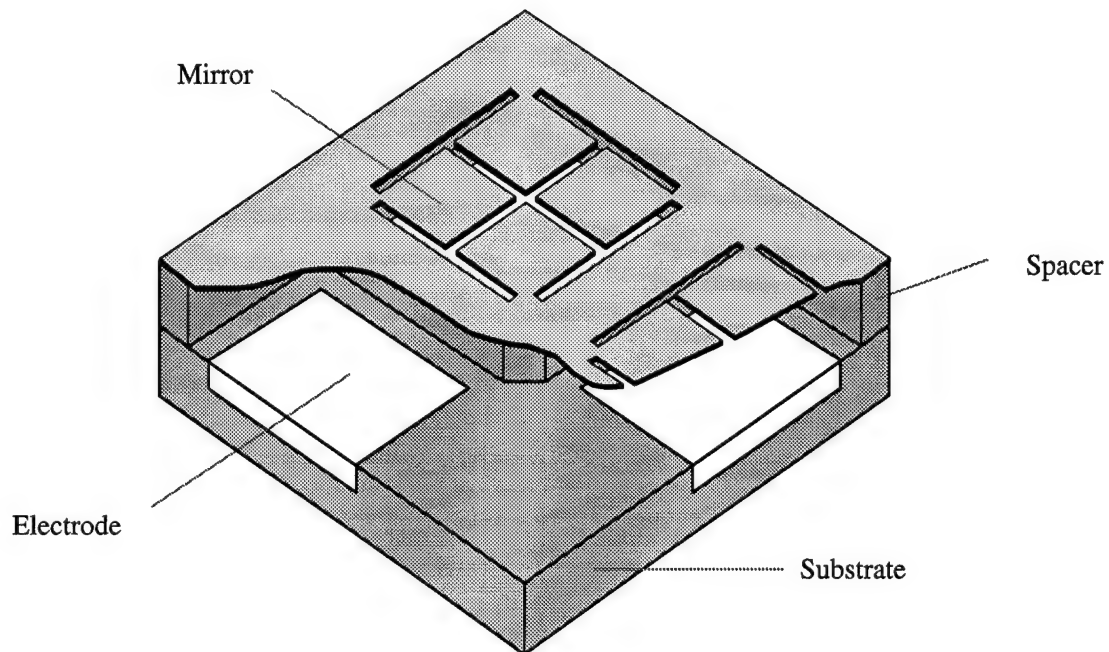


**Figure 2-3.** The Inverted Cloverleaf deformable mirror device [2].

The active micro-mechanical surface of the device comprises only a small percentage, as little as 26%, of the total surface area and thus the entire device is limited in operation since a beam reflected by the device will be dominated by the background reflection of the incident beam [2]. These drawbacks have made other designs more desirable.

One design improvement is another cantilever device known as the Cloverleaf. As shown in Fig. 2-4, the flexures holding the reflective surfaces are placed in the center of the pixel [9]. This takes the basic design of the Inverted Cloverleaf and reduces some of the negative effects observed. Also, the electrodes are located directly beneath each mirror which allows the cantilever surfaces to be individually addressable.
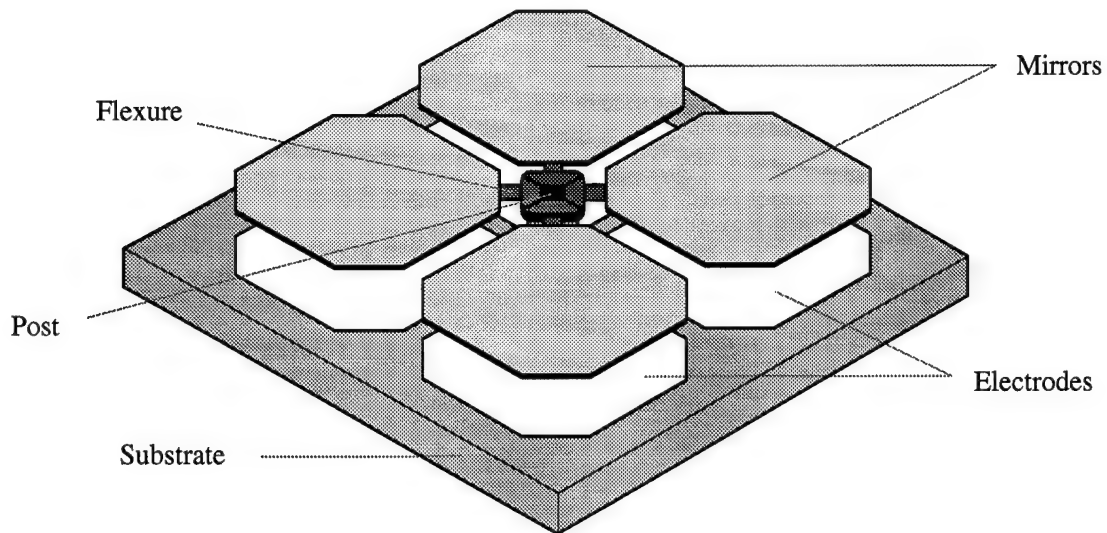


**Figure 2-4.** The Cloverleaf deformable micromirror device [9].

Moving the support for the mirrors to the center of the pixel cell allows for better use of overall space. Now, the pixels can be placed so that adjacent cells nearly touch each other with only a small gap required between the mirrors of one cell and the mirrors of another. Most of the total surface area of the device is reserved for the active elements with the exception of the posts which hold the mirrors in place. This increases the active area of the device to as much as 86% which is similar to the remaining devices described in this chapter. This device, however, maintains the side effect of redirecting an incident beam of light in four distinct directions.

In this thesis, several cloverleaf devices were designed and fabricated for testing so that the characteristic behavior of the cantilever micromirror device could be studied. The devices were designed with various mirror sizes and shapes and various lengths of

flexures to provide a wide variety of samples. Each mirror was tested individually on a point-by-point basis using the microscope-based laser interferometer. Descriptions of these devices are presented in greater detail in Chapter (IV).

The third design is the Quad-Cantilever device shown in Figure 2-5. The primary advantage over the Inverted-Cloverleaf design is that this device geometry allows for obvious improvements in the active area and the motion of the cantilever surfaces.
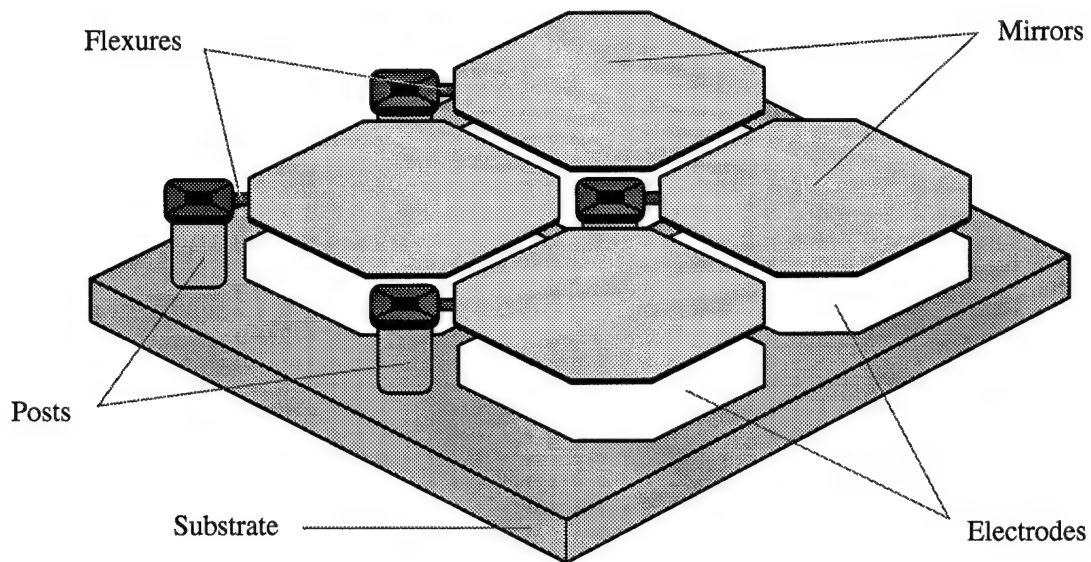


**Figure 2-5.** The Quad-Cantilever deformable micromirror device [3].

The significant advantage over the Cloverleaf devices is that the mirrors are aligned so that the redirection of the incident beam of light is in a common direction. This allows the device to be capable of switching or redirecting the incident light with little loss in amplitude. One characteristic similar to the Inverted Cloverleaf and Cloverleaf devices is the slanted behavior of the deflected mirror. This behavior is typical with cantilever devices and creates a non-uniform phase response across the surface of each mirror.

Another common deformable micromirror design is the Torsion-Beam device. This design has a wider range of motion than the above designs since its tilted surface is directed by a rotation about the center axis. Instead of bending in only one direction, this

design allows for a bending in the opposite direction as well. This increases the switching ability of the device and allows for a greater diversity of possible applications.

The Torsion-Beam device, shown in Fig. 2-6, has several electrodes located beneath each reflective mirror. This allows for a uniform force distribution along the mirror surface in order to reduce any deformations of the mirror during operation.
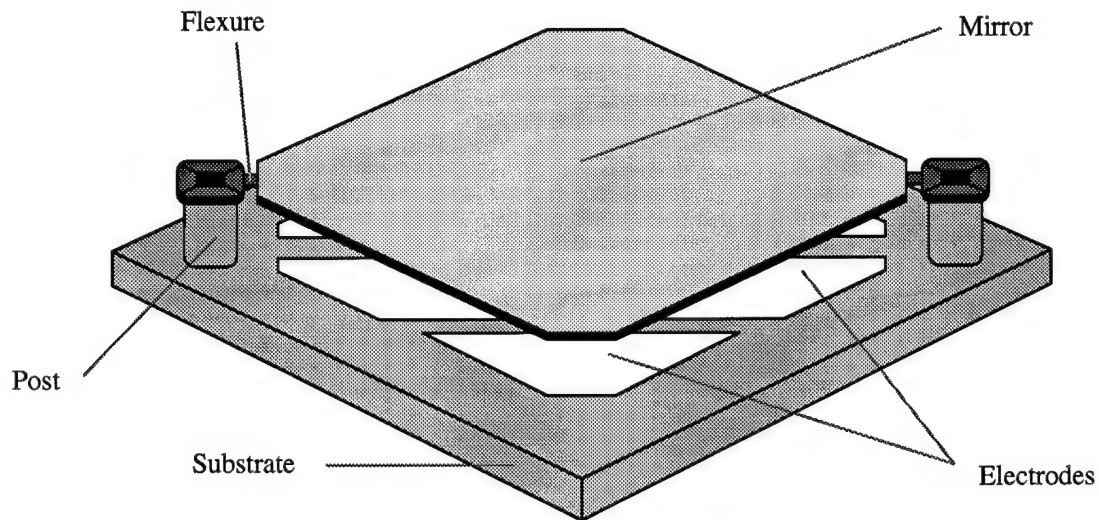


**Figure 2-6.** The Torsion-Beam deformable mirror device [3].

These electrodes, however, must be carefully regulated so that they do not conflict with each other and render the mirror immobile with equal potentials applied to both sides of the device. Likewise, as is common with such tilting designs, the mirror may deflect to the point of touching the supporting substrate. Therefore, "landing" pads may be added to prevent a short between the mirror and address electrodes. This device is already being used in some projection and optical information processing applications due to its wide range of motion and high-speed switching ability [9].

The final deformable micromirror design is the Piston device more commonly known as the Flexure-Beam Micromirror Device (FBMD). This is the primary device being tested and is the focus of micromirror modeling in this thesis. The device is supported along the outer edge of the mirror surface by flexures that are designed to

deform. For best operation, the device is symmetrically designed such that the flexures along one side of the mirror are rotated about the center of the device and are placed along the other sides in the same manner. This creates a more uniform restoring force by the flexures and reduces any undesirable tilting or lateral translation of the mirror. The primary characteristic of the FBMD is that the motion of the device is solely along the vertical axis normal to the reflective surface of the mirror. Figure 2-7 shows a square device with four flexures whose lengths are approximately half the width of the mirror.
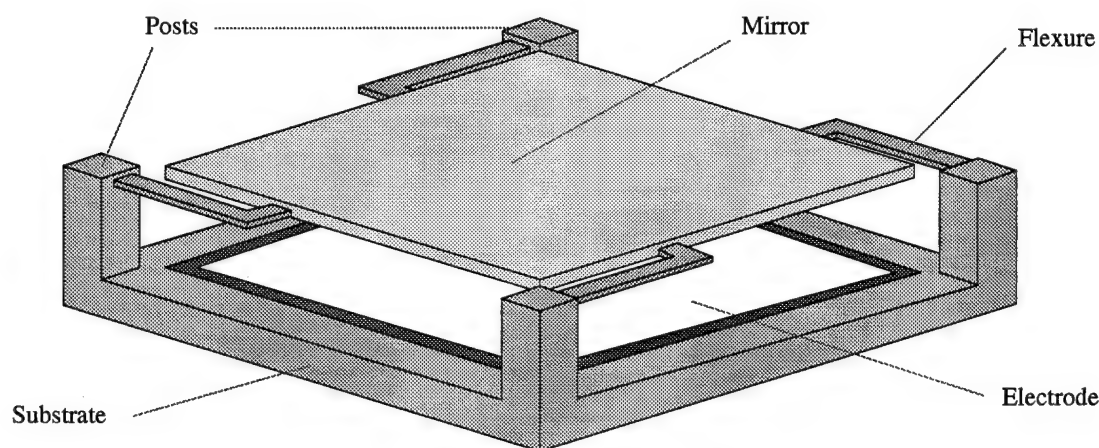


**Figure 2-7.** The square Flexure-Beam Micromirror Device [10].

Flexure-Beam Micromirror Devices are not limited to this form and can be designed with various geometries of flexures and mirrors.

*(2.2) FABRICATION*

The fabrication of deformable micromirrors is quite simple and is based on standard metal-oxide semiconductor (MOS) processing [2]. The micromirror structure is built in layers using either a metal or polymer spacer support post. The polymer spacer is spun on a wafer and baked, followed by a thin layer of metal and a layer of silicon-dioxide which are then patterned as flexures. A thicker layer of metal is then applied

followed by another layer of oxide which are patterned as the mirror. The structures are then etched to remove the polymer spacer and release the micromirror devices. Timing the etch process for the spacer support post devices is critical since the spacer must be completely removed beneath the mirrors while maintaining a reliable amount for the support post. For this purpose, etch holes may be added along the surface of the mirrors so that the spacer beneath the mirrors is removed more quickly. Figure 2-8 demonstrates the fabrication process for both types of support structures.



(a) After Spacer Patterning

(b) After Mirror Oxide Patterning

(c) Released Chip
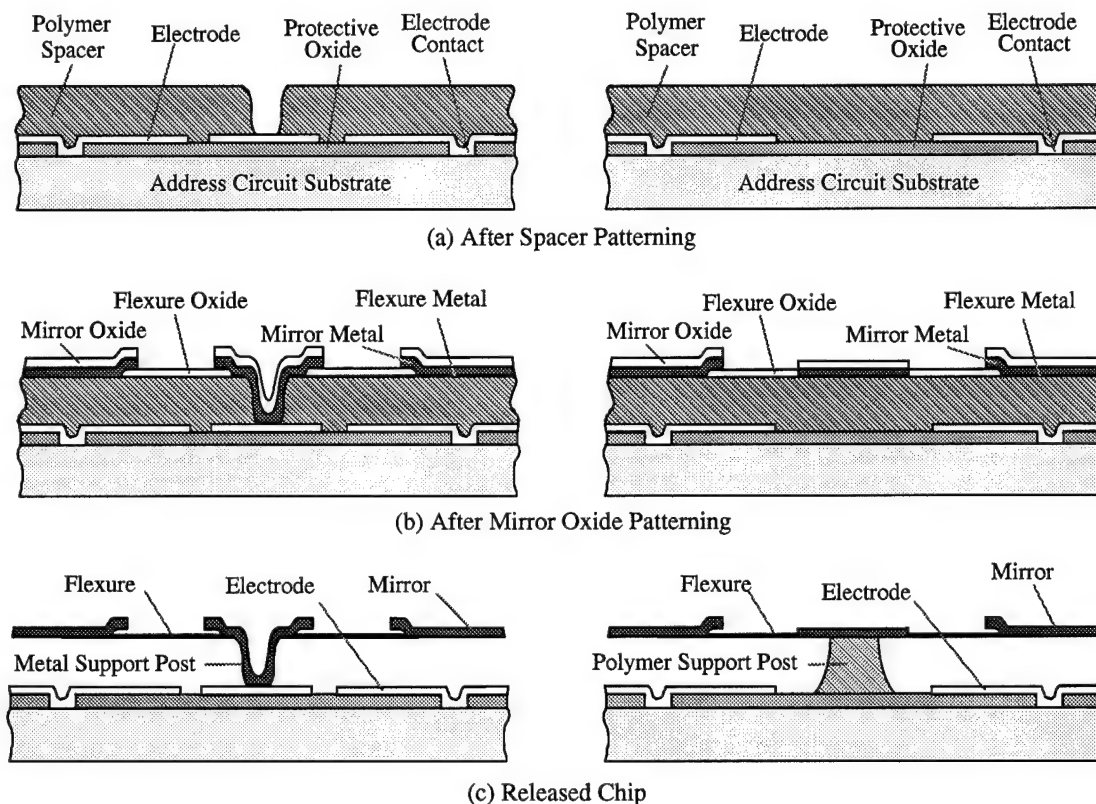
**Figure 2-8.** Fabrication process of the metal and polymer support post devices [2].

The micromirror devices that were designed for testing purposes in this thesis were fabricated commercially using polysilicon support posts. Three distinct layers of polysilicon are used to build the devices while silicon dioxide is used as the sacrificial material. This specific fabrication process is presented in greater detail in Chapter (IV).

## (2.3) DEVICE APPLICATIONS

Given a large number of deformable micromirror applications, none is more immediately available than DMD projection televisions which significantly improve upon the performance of current systems. For example, modern televisions require electron "cannons" to direct a flow of charge within the picture tube to excite the pixels on the screen. This hardware, added to the picture tube itself, constitutes the majority of the volume of a television unit. With an array of torsion micromirror devices, this hardware is no longer necessary since an incident beam of light can be redirected to all points on the screen at a frequency near several MHz, well above that required for the human eye to integrate the pixels into a single image [9].



(a) Torsion-Beam DMD Chip          (b) HDTV Configuration
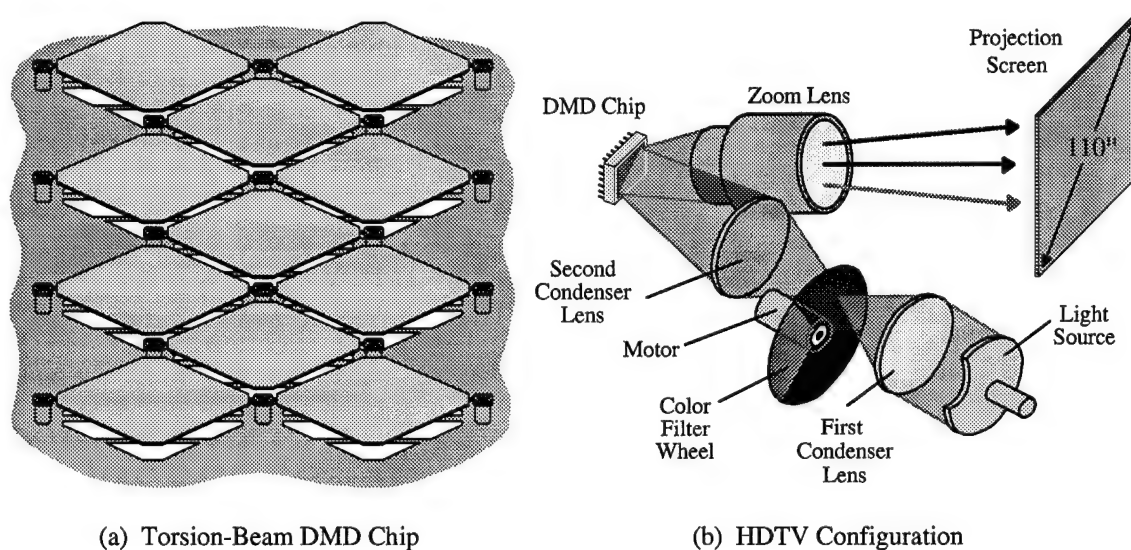
**Figure 2-9.** Torsion-Beam DMD chip and system configuration of the HDTV [9].

Such a device is a High-Definition Television (HDTV), shown in Fig. 2-9, which can provide increased screen size with no loss in resolution or increase in the size of the television. The first condenser lens focuses light from the light source onto the rotating color filter wheel. The wheel is rotated at a rate matched by that of the DMD chip which redirects the light through a projection zoom lens to the screen. The filter wheel contains

the three primary colors and for every one-third revolution, the DMDs will send that colored information to the screen. A complete revolution will create a multicolored image on the screen and the process is repeated to form a working television display.

Several other applications of segmented deformable micromirrors have been suggested and some, as in the case of HDTV, are already being used [11]. In the field of optical communications, micromirror devices offer the distinct capability of bridging the gap between electrical control technology and micromechanical switching. For example, Fig. 2-10(a) shows an array of input fiber optic cables that pass through a wall of micromirrors. It is suggested that these devices be used as the signal generating source for various communication techniques using such optical media as fiber optics.



(a) Signal Generation Network          (b) Optical Switching Network
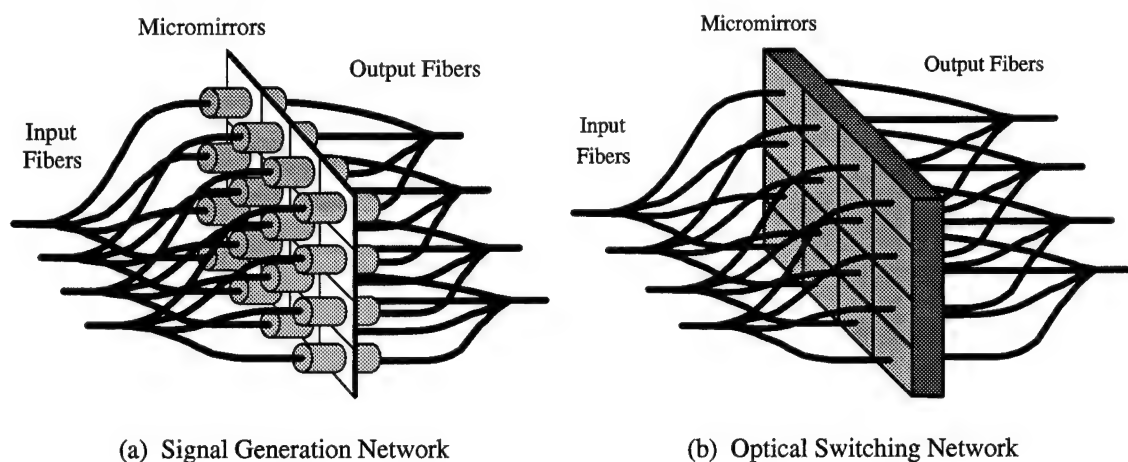
**Figure 2-10.** Suggested signal generation and optical switching networks [11].

Each input fiber is connected to a specific output fiber with a micromirror device placed within the connection interface. A torsion-beam device can be set to interrupt the light from the input fiber at varying intervals so as to create a Pulse Width Modulation (PWM) scheme or, more simply, an On-Off Keying (OOK) scheme.

Likewise, Fig. 2-10(b) depicts a switching network which can be implemented along with the signal generation setup. This network can be comprised of an array of torsion-beam or similar devices that redirect an incident beam of light from an input fiber

to any selected output fiber. If the device range of motion is such that the signal can be sent to any number of output cables, then this network can maintain virtually any combination of input to output signals. Furthermore, such devices, which can operate well into the MHz range, become quite effective for either signal generation or optical switching purposes.

The torsion or cantilever devices could be used in optical imaging systems such as video cameras to provide mechanical stability. A camera mounted on a moving or unstable platform would produce a bumpy and distorted image, but an array of deformable micromirrors could be employed to redirect the incoming light to the film or image sensor to correct for sharp changes in position of the camera.

The proposed application of FBMD is for use in corrective optics in environments that would require a laser beam to be corrected for phase aberrations. For example, the laser communication system described in Chapter (I) employs such a device since the laser signal between two airplanes in rapid relative motion would be limited due to aberrations in the beam caused by airflow around the transmitting and receiving windows of the aircraft. The FBMD combined with a control and sensory unit could correct these aberrations in real time. Other optical imaging systems such as telescopes or video cameras may require the same corrections.

### (2.4) RELATED RESEARCH

The behavioral characterization of deformable micromirrors has only recently been sought and as a result, few papers have been published concerning such research. However, two distinct papers exist that are directly related to research in this thesis. The first presents the development of an ideal characteristic model for FBMDs using basic physical principals [4]. This paper verifies the starting point of a model developed in Chapter (III) which contains the more realistic non-ideal effects of the device.

The second paper is the result of previous thesis work conducted in the same Air Force Institute of Technology laboratory [6]. The research presented in this thesis is an initial characterization of a particular FBMD supplied by a private company interested in FBMD research. The characterization was carried out using the microscope-based laser interferometer mentioned in Chapter (I). As shown in Fig. 2-11, a laser beam is split into a reference beam having a constant amplitude and phase and an object beam that is reflected from the FBMD device under test.
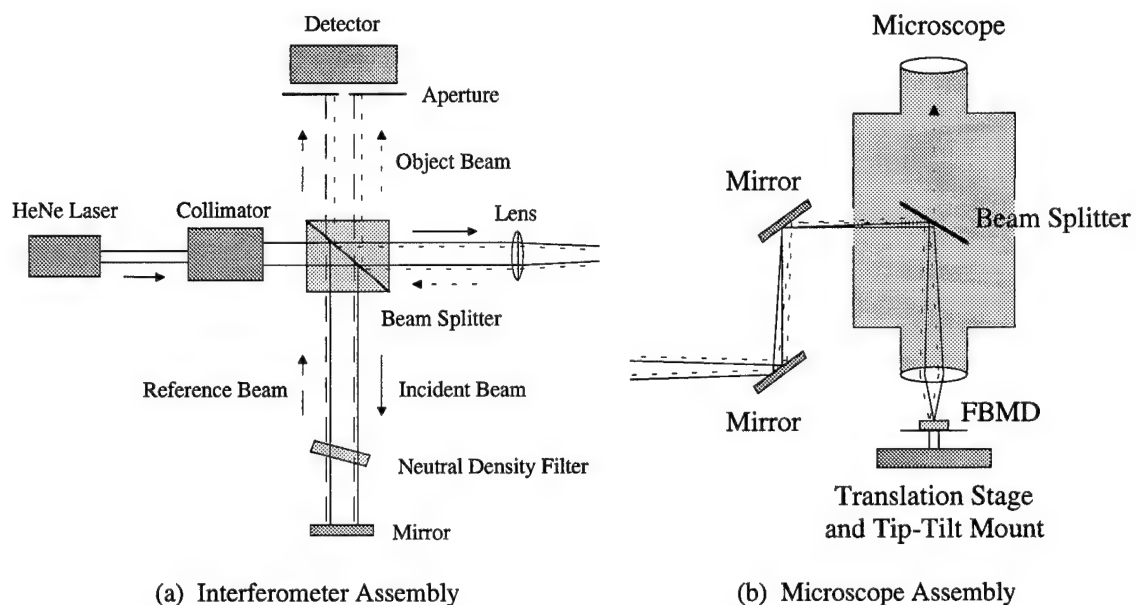


**Figure 2-11.** Experimental setup of microscope-based laser interferometer [6].

The path length of the object beam is discretely lengthened by twice the deflection distance of the micromirror under test. When the reference and object beams are recombined, the resulting beam is modulated such that its intensity as observed by the detector is a function of the relative phase of the two beams and therefore the displacement of the micromirror [6]. The microscope-based laser interferometer is described in greater detail in Chapter (IV).

Using this experimental setup, the FBMD was driven by a 4 kHz signal ranging from zero to 5.8 volts. The resulting detector output signal is shown in Fig. 2-12(a) along

with this input drive signal. The amplitude of the output signal is arbitrary since it is the relative voltage that is used to compare data points. The maximum and minimum values of the output, however, are crucial to the phase calculations of the output waveform [6].



(a) Experimental Signals          (b) Output Phase Representation
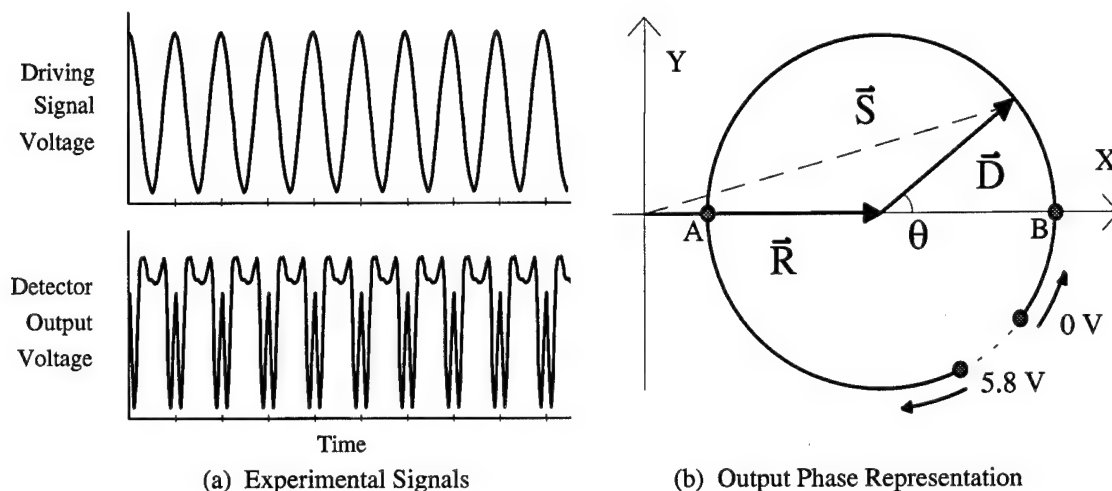
**Figure 2-12.** Experimental signals and phase notation of observed output [6].

The output signal shows that this particular device created nearly a $2\pi$ phase change using a $\lambda = 632.8$ nm HeNe laser. The output signal does not vary as a perfect sinusoid since the system was not calibrated such that the detector output was maximum when no address electrode voltage was applied. The analysis of the experimental setup is discussed in greater detail in Chapter (IV).

The phase-space representation of the output intensity, $\bar{S}$, is shown in Fig. 2-12(b) along with the object and reference beam vectors, $\bar{D}$ and $\bar{R}$, respectively. The upper and lower drive voltage limits, $V_o = 5.8$ V and $V_o = 0$ V, are shown at two different locations along the path of the modulated signal. The arrows indicate that at no time does the path along the circle cross itself in the domain of input voltages. Therefore, the driving signal, which oscillates between these voltages, will produce less than a $2\pi$ phase change and will create a peak in the output voltage at point B and a minimum at point A. These points do not necessarily correspond to the peaks and minima of the driving signal. By

tracing the length of the signal vector, $\bar{S}$, back and forth between these voltage points, it is easy to see that the output voltage waveform is produced.

A set of data reflecting the FBMD motion with respect to the input voltage can be plotted to show the characteristic behavior of the device as shown in Fig. 2-13. The device exhibits the same behavior in both directions of motion indicating that no significant hysteresis effects are present.
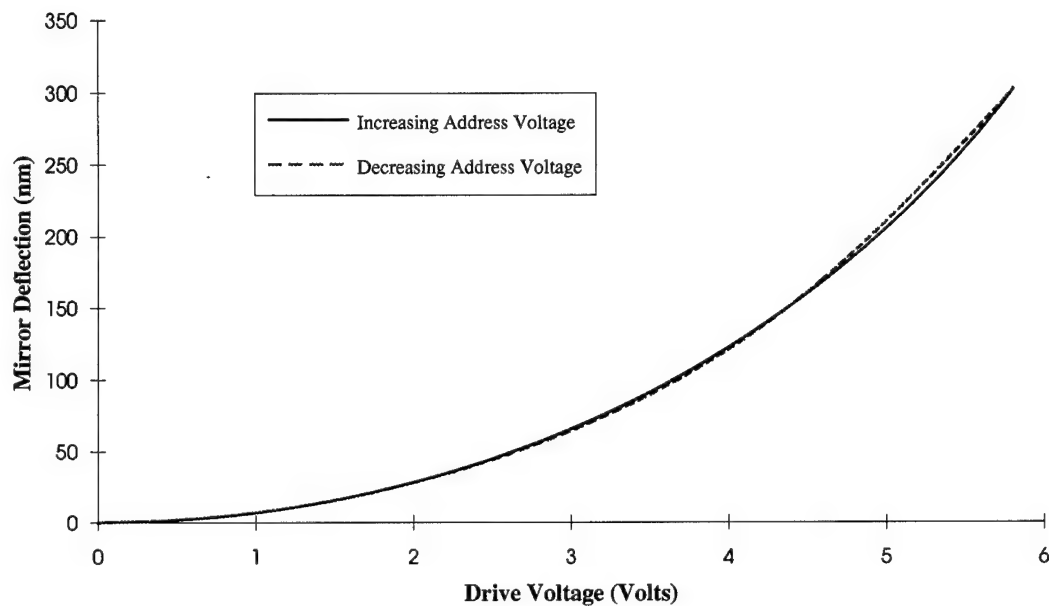


**Figure 2-13.** Experimental behavior of the FBMD under test [6].

The same method of characterization is used in this thesis to verify models of FBMD behavior. This measurement technique is repeated over the entire mirror surface for other devices to verify their deflection and deformation. Devices of various geometries and designs are used to demonstrate the completeness and adaptability of the developed model as well as to present basic behavior traits of these designs. This procedure is presented in greater detail in Chapter (IV) and the results of the measurement techniques described above are presented in Chapter (V).

# (III) Theory of Operation

The actuation of the Flexure-Beam Micromirror Device is electrostatic. A voltage is applied to an address electrode beneath the mirror which creates a potential difference between this electrode and the mirror which is grounded. This creates a downward electrostatic force along the surface of the mirror which is countered by an upward spring force of the flexures. These physical principles dictate the behavior of the device.

In this thesis, ideal characteristic models of the Flexure-Beam and Cantilever micromirror devices are developed by equating the electrostatic force of a parallel plate capacitor with the restoring force of a spring. The models are developed using idealized assumptions of the physical behavior of the devices. For instance, it is assumed that uniform electric fields exist between the mirror and address electrodes of the device which simplifies the analysis of the electrostatic actuation of the mirror.

In addition, a complete characteristic model is developed for Flexure-Beam micromirror devices. The effects of temperature, driving frequency, electric field fringing, mirror surface deformation, and cross-talk from adjacent devices are incorporated into the model to provide an accurate description of Flexure-Beam behavior.

## (3.1) Coordinate System Declaration

A convenient characteristic of most micromirror devices is the symmetry designed about the center of the device. Most micromirror devices are designed in the shape of squares or other polygons that share similar symmetric traits. Therefore, a simple Cartesian coordinate system can be assigned to analyze the behavior of micromirror devices which capitalizes on this symmetry. As shown in Fig. 3-1, the $x$ and $y$ axes lie in the plane of the top of the address electrode and intersect at the center of the device. The

*z* axis defines the vertical dimension within the device. The mirror widths along the *x* and *y* axes, $w_x$ and $w_y$ respectively, are shown such that the coordinates used to describe a position along the mirror surface range from negative to positive values of half the width.
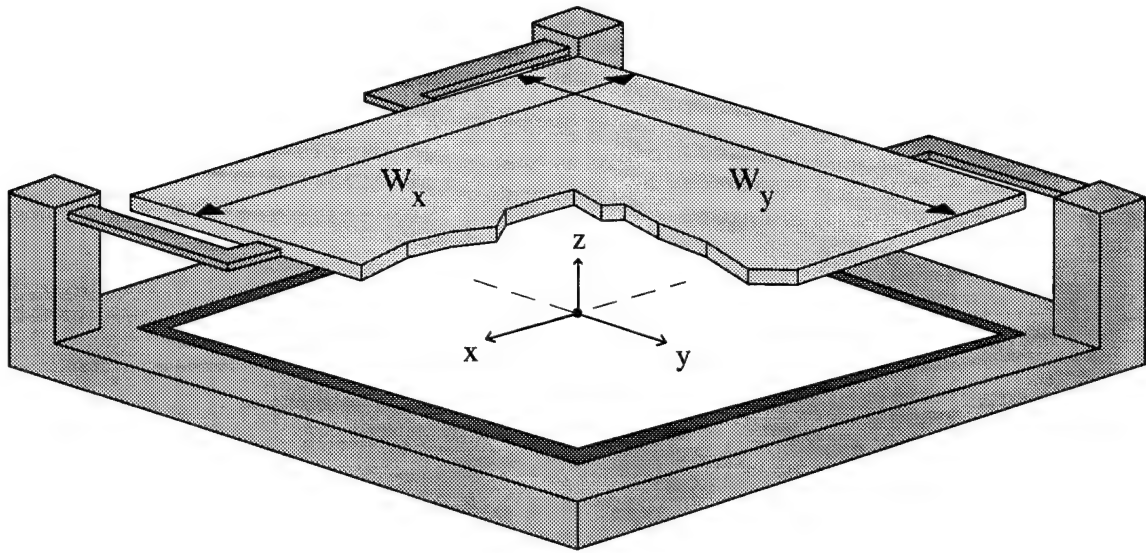


**Figure 3-1.** Cartesian coordinate system used for standard micromirror devices.

This coordinate system will help simplify the solutions of symmetric physical properties such as the electric field intensity which is uniform only at the center of the device.

*(3.1.1) GEOMETRIC VARIABLE DECLARATIONS*

In order to describe the mechanical behavior of micromirror devices, a set of variables must be defined that fully accounts for the physical geometry and motion of the mirrors and flexures. These variables are graphically defined using a simple micromirror device consisting of two flexures supporting the device at opposite ends of the mirror. The flexures and support posts are shown separated from the mirror for the purpose of clarification between the resting and actuated positions of the device.

The flexure variables shown in Fig. 3-2(a) are comprised of the initial deflection due to gravity, $d_g$, the actuated deflection of the device at the end of the flexures, $d_f$, the resting separation distance between the mirror and address electrode, $z_o$, the actuated separation distance at the end of the flexures, $z_f$, and the spacer thickness, $t_s$, used in the fabrication of the device.



(a) Flexure Variables in Actuated and Resting Position      (b) Mirror Variables
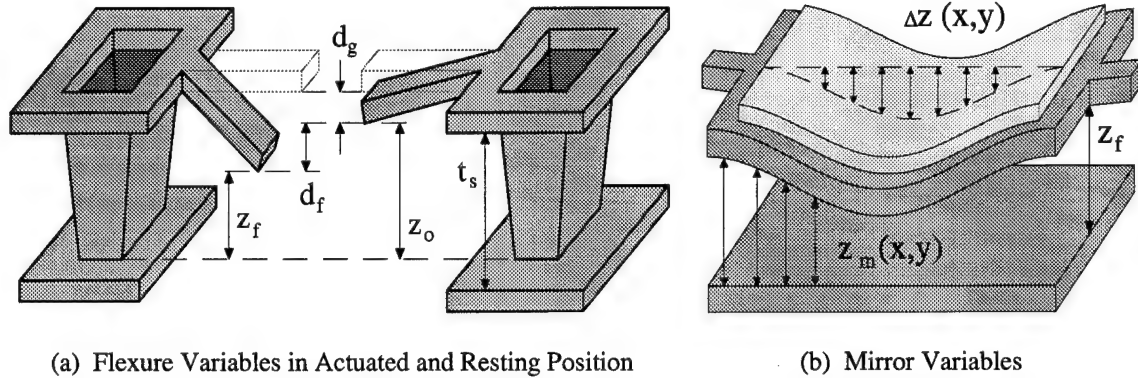
**Figure 3-2.** Graphical identification of micromirror device dimension variables.

The mirror variables shown in Fig. 3-2(b) are a function of position along the surface of the mirror and include the separation distance between the mirror and address electrode, $z_m(x,y)$, and the surface distribution of mirror position relative to the ideal uniform deflection, $\Delta z(x,y)$, which includes mirror surface deformations and tilting of the mirror due to cross-talk interference or variances in flexure behavior.

The initial deflection due to gravity can be found using the combined mass of the mirror, $M$, and the characteristic spring constant of the device, $k$, such that

$$d_g = \frac{Mg}{k} \qquad (3.1)$$

where $g$ is the acceleration constant due to gravity. As shown in Fig. 3-2(a), the resting position of the device at the end of the flexures, $z_o$, is given by:

$$z_o = t_s - d_g = d_f + z_f \qquad (3.2)$$

which describes the vertical separation distance between the address electrode and the

3-3

mirror at the end of the flexures when no address potential is applied. Likewise, as shown in Fig. 3-2(b), the separation of the mirror and address electrode is given as

$$z_m(x,y) = z_o - d_f - \Delta z(x,y) = z_f - \Delta z(x,y) \qquad (3.3)$$

The most important relationship defines the relative deflection as a function of position along the mirror surface, $d(x,y)$, such that

$$d(x,y) = d_f + \Delta z(x,y) \qquad (3.4)$$

which describes the deflection observed for a given voltage at any point *(x,y)* along the surface of the mirror. Ultimately, this is the independent variable used to describe the behavior of a micromirror device such that the voltage is plotted against this deflection.

## *(3.2) ELECTROSTATIC FORCE*

In order to compute the electrostatic force on the mirror, it must first be determined by which means this force will be calculated. More specifically, it must be decided whether the charge distribution, which is not uniform over the mirror surface, will be considered. The charge distribution will change with the position of the mirror surface and will also be altered by any mirror surface deformations or discontinuities such as etch holes. This leads to a complicated solution when integrating across the mirror [12]. As an alternative, since both the charge distribution of the mirror and the applied electrode voltage are related to the electric field within the device, it is possible to express the potential energy, $\xi$, of the electric charge distribution solely in terms of this field:

$$\xi = \frac{1}{2} \int_A \sigma V \, dA = \frac{1}{2} \int_v \varepsilon_o E^2 \, dv \qquad (3.5)$$

where $\sigma$ is the surface charge distribution on the mirror, $V$ is the actuation voltage between the mirror and address electrode, $A$ is the area of the mirror, $\varepsilon_o$ is the free space dielectric constant and $E$ is the electric field intensity at any point in the volume $v$ within

3-4

the device [13]. By assigning an electric energy density of $\frac{1}{2}\varepsilon_o E^2$ to each point in space within the device, the physical effect of the charge distribution on the mirror surface is preserved. From this approach it is easy to see that the non-uniform charge distribution on the mirror surface and the fringing effects of electric fields around the edges of the mirror are complementary descriptions of the same electrical phenomenon.

### (3.2.1) VIRTUAL WORK

With the ability to express the energy of the device in terms of the electric field, the analysis of the electrostatic force on the mirror surface is determined by a method known as virtual work [13]. First, a parallel plate capacitor with conductor separation distance $z$ is connected to a battery supplying a fixed potential, $V$. If some exterior mechanical force, $F$, displaces the mirror by $dz$, the net energy supplied in the course of this displacement is equal to the change in the electrical energy stored in the capacitor. More specifically, the change in electrical energy of the capacitor, $\xi_E$, is equal to the sum of the mechanical work done by the displacement force moving the mirror, $\xi_F$, and the change in the electrical energy supplied by the battery, $\xi_B$, such that

$$\xi_F + \xi_B = \xi_E \qquad (3.6)$$

The mechanical work and the change in the electrical energy of the battery are:

$$\xi_F = F\,dz, \qquad\qquad \xi_B = V\,dQ \qquad (3.7)$$

where $dQ$ represents the net change in electric charge supplied by the battery and is equal to the product of the applied potential, $V$, and the change in capacitance, $dC$. The electrical energy of the battery is then

$$\xi_B = V(V\,dC) = V^2 d\left(\frac{\varepsilon_o A}{z}\right) = -V^2 \varepsilon_o A\,\frac{dz}{z^2} = -\left(\varepsilon_o E^2\right)(A\,dz) \qquad (3.8)$$

Using the electrical energy density within the capacitor, the total electrical energy is

found by integrating Eq. (3.5) using a uniform electric field. The differential change in the electrical energy is given by

$$\xi_E = d\left(\frac{\varepsilon_o E^2}{2} A z\right) = \varepsilon_o \frac{A V^2}{2}\left(\frac{-dz}{z^2}\right) = -\frac{\varepsilon_o E^2}{2} A \, dz \qquad (3.9)$$

Substituting Eqs. (3.8) and (3.9) into Eq. (3.6) yields

$$F \, dz - \varepsilon_o E^2 A \, dz = -\frac{\varepsilon_o E^2}{2} A \, dz \qquad (3.10)$$

which reduces to

$$F = \frac{\varepsilon_o E^2}{2} A \qquad (3.11)$$

Equation (3.11) represents the total force on the surface of the mirror as a function of electric field. It also demonstrates that the force per unit area on the mirror surface is equal to the electrical energy density per unit volume within the device [13].

### (3.3) IDEAL MICROMIRROR MODELS

Before an advanced model is created for the Flexure-Beam Micromirror Device, an ideal model is first developed which is a much simpler account of the physical principles involved in the actuation of a micromirror device. For many devices and operating conditions, this ideal model will be sufficient for the characterization of the micromirror device. For instance, devices having mirror dimensions which are significantly larger than the separation distance between the mirror and address electrode will not demonstrate fringing electric field losses since the actuation of the device is dominated by the uniform electric field within the device.

Ideal models are developed for both the Flexure-Beam and the Cantilever micromirror devices. These models include idealized assumptions of the electric field and mechanical uniformity such as no mirror surface deformations or thermal expansion

effects. A more complete model is later developed for the Flexure-Beam micromirror device which builds upon the ideal model and includes these and other effects.

## (3.3.1) FLEXURE-BEAM MICROMIRROR DEVICES

Since the electric field is symmetric about the center of the cell and the mirror and electrode are assumed to be rigid, the electric field lines along the outer edges of the cell shall be assumed uniform as well, as shown in Fig. 3-3(a). Therefore, the induced electric field is initially assumed to be uniform and orthogonal to both the mirror and electrode at all points along both surfaces. This neglects deformations of the mirror surface during operation as well as fringing effects of the electric field around the edges of the device.



(a) Uniform Field Within Micromirror Device    (b) Two Points Within Uniform Field [14]
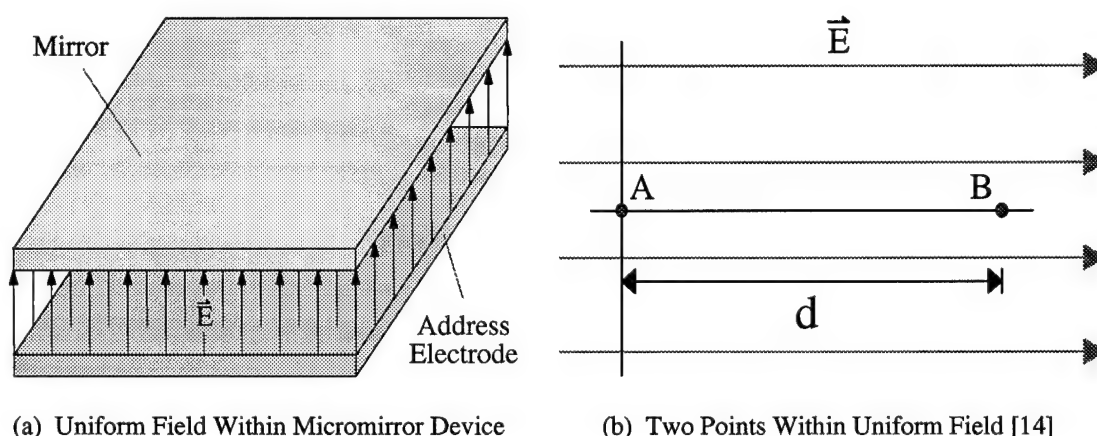
**Figure 3-3.** Uniform electric field analysis of the Flexure-Beam Micromirror Device.

The analysis of a uniform electric field is developed using the interaction between two points, A and B, as shown in Fig. 3-3(b). The potential difference between any two points located within this uniform electric field separated by a distance, $d$, is defined as:

$$\Delta V = V_A - V_B = \int_0^d \vec{E} \cdot d\hat{l} = E d \qquad (3.12)$$

Applying the definition of potential difference between any point along the surface of the address electrode and its opposite point along the surface of the mirror yields the electric

field of a parallel plate capacitor, $E_{PP}$, having a potential, $V$, equal to the voltage difference applied between them:

$$E_{PP} = \frac{V_E - V_M}{z_m} = \frac{V}{z_m}$$

(3.13)

where $V_E$ is the electrode voltage, $V_M$ is the mirror voltage, and $z_m$ is the separation distance between the top of the electrode and bottom of the mirror. Knowing this electric field, the attractive force between the mirror and electrode is given by Eq. (3.11) such that

$$F_{pp} = \frac{\varepsilon_o}{2} E_{pp}^2 A$$

(3.14)

where $Q$ is the total mirror charge, $\varepsilon_o$ is the free space dielectric constant, and $A$ is the surface area of the mirror. The uniform separation distance between the address electrode and the mirror, $z_m$, is given in Eq. (3.3) in which $\Delta z(x,y) = 0$ such that:

$$z_m = z_o - d_f$$

(3.15)

where $z_o$ is the resting separation when no electrode voltage is applied and $d_f$ is the vertical displacement of the mirror at any point along the surface.

The total electrostatic force is found by substituting Eqs. (3.13) and (3.15) into Eq. (3.14) which yields the magnitude of the downward force applied on the mirror:

$$F_{PP} = \frac{\varepsilon_o}{2} \left( \frac{V}{z_0 - d_f} \right)^2 A$$

(3.16)

The restoring force produced by a spring displaced a distance, $d_f$, from its equilibrium position is given by Ficke's Law:

$$F_S = kd_f$$

(3.17)

where $k$ is the characteristic spring constant distinct to a particular spring system. This constant is distinct to each spring and can be measured experimentally or determined using mechanical analysis. It is obvious that the linear response of the restoring force is valid only for a limited range of displacement distances. Forces greater than some critical

force applied to the mirror must be avoided to ensure that the flexures do not deform and that the restoring force exhibits a linear response.

It is expected that the flexures will deform linearly as the rectangular spring described in Chapter (I). Therefore, balancing the upward restoring force of the micromirror flexures against the downward force of the parallel plate capacitor:

$$F_{PP} = F_S, \qquad \frac{\varepsilon_o}{2}\left(\frac{V}{z_0 - d_f}\right)^2 A = kd_f \qquad (3.18)$$

produces an equality that can be solved to determine the necessary voltage, $V$, to vertically displace the mirror a desired distance, $d_f$, from the resting position:

$$V(d_f) = \left(z_0 - d_f\right)\sqrt{\frac{2kd_f}{\varepsilon_o A}} \qquad (3.19)$$

In this ideal model, the deflection along the mirror surface is assumed to be uniform. In a more realistic model, surface deformations invalidate this assumption.

As described above, the characteristic spring constant, k, can be experimentally determined for a specific micromirror device. However, mechanical analysis of the geometry and material properties comprising the flexures can determine this value as well. As a result, the behavior of a Flexure-Beam Micromirror Device can be obtained without the need for experimental observations. Section (3.6) contains this analysis.

### (3.3.2) CANTILEVER MICROMIRROR DEVICES

The Cantilever micromirror device can be modeled using the same ideal conditions assumed for the Flexure-Beam micromirror device. Unlike the FBMD, however, the deflection is not uniform along the surface of the mirror, but a function of position along one dimension since the device tilts away from the support post. Assuming no surface deformations, the deflection becomes a linear function of position.

Figure 3-4 illustrates the motion of the device and defines the dimension variables. It is known that the flexures will deflect according to Ficke's Law given in Eq. (3.17), but another aspect of the Cantilever device is the additional bending of the flexure which determines the angle of deflection, $\theta$, at which the mirror is tilted.
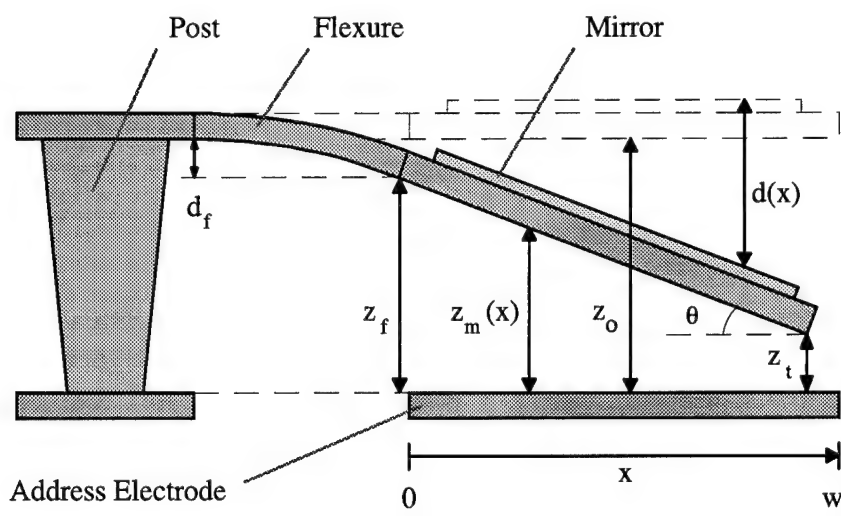


**Figure 3-4.** Side view of Cantilever micromirror deflection with assigned variables.

As the mirror deflects downward, the force distribution along the surface of the mirror is no longer uniform since the end of the mirror is closer to the address electrode than elsewhere along the mirror. As a result, the total electrostatic force applied to the device will change according to the vertical deflection of the flexure, $d_f$, and the angle of deflection, $\theta$. To account for this behavior, two spring constants are introduced such that

$$F_S = k_1 d_f, \qquad \theta = k_2 d_f \qquad (3.20)$$

where $k_1$ describes the vertical deflection at the end of the flexure and $k_2$ describes the angle of deflection of the mirror. Both constants are directly related to the amount of electrostatic force acting on the device since they determine the position of the mirror.

The electrostatic force acting on the mirror is found by integrating the linear force distribution across the surface of the mirror. Since this force distribution is uniform in the $y$ dimension, the force is only dependent on the integral over the $x$ domain. Likewise,

the separation distance between the mirror and address electrode, $z_m$, and the vertical deflection distance of the mirror, $d$, are functions of $x$ and are defined as

$$z_m(x) = z_o - d_f - x\sin(\theta), \qquad d(x) = d_f + x\sin(\theta) \qquad (3.21)$$

The total electrostatic force for a Cantilever micromirror device, $F_C$, is found to be [15]

$$F_C = \frac{\varepsilon_o}{2} w_y V^2 \int_0^{w_x} \frac{dx}{z_m^2(x)} = \frac{\varepsilon_o A V^2}{2 z_f z_t} \qquad (3.22)$$

where the vertical separation distances at the flexure end of the mirror and tip of the device, $z_f$ and $z_t$ respectively, are shown in Fig. 3-4 and are defined as

$$z_f = z_0 - d_f, \qquad z_t = z_f - w_x\sin(\theta) \qquad (3.23)$$

Using the deflection relationship of Eq. (3.20), the deflection angle, $\theta$, becomes

$$\theta = k_2 d_f = k_2[d - x\sin(\theta)] \qquad (3.24)$$

Since the length of the micromirror device is significantly larger than the separation distance between the mirror and address electrode, the angle produced by the actuation of the device is sufficiently small to allow for the $\sin(\theta) \approx \theta$ approximation such that

$$\theta \approx \frac{k_2 d}{(k_2 x + 1)} \qquad (3.25)$$

Equating the electrostatic force in Eq. (3.22) with the restoring force of Eq. (3.20) yields the characteristic model of the Cantilever micromirror device:

$$V(d) = \sqrt{\frac{2k_1[d - x\sin(\theta)]z_f z_t}{\varepsilon_o A}} \qquad (3.26)$$

where the address potential, $V$, is required to deflect a device some distance, $d$, at some position, $x$, along the surface of the mirror. Similar to the FBMD model, the spring constants of the Cantilever micromirror device can be determined from mechanical analysis of the deflection and bending properties of the material comprising the flexure.

## (3.4) ELECTROSTATIC ACTUATION

The relationship in Eq. (3.11) also holds for non-uniform electric fields. The fringing electric fields around the perimeter of the device alter the force per unit area on the mirror as a function of position on the mirror surface. The total electrostatic force acting on the mirror is

$$F = \iint f(x, y)\,dxdy = \frac{\varepsilon_o}{2} \iint E^2(x, y)\,dxdy \qquad (3.27)$$

The fringing electric fields will diminish the force per unit area around the edges of the mirror which will produce an actual total electrostatic force that is slightly less than the ideal force calculated by neglecting fringing effects.

## (3.4.1) SCHWARTZ-CHRISTOFFEL TRANSFORMATION

The electrostatic force of the device is developed using a conformal mapping technique known as the Schwartz-Christoffel transformation. In any map of an electric field, the electric flux and equipotential lines are orthogonal to each other and form curvilinear squares between points of intersection. The sides of these squares will be perfectly linear for uniform electric fields and curved for any non-uniform field. The electric field is taken from a complex plane $\gamma$ as described by some polygon and transformed to a complex plane $W$, where $W$ is an analytic function of $\gamma$. This transformation preserves the orthogonal intersections of the flux and equipotential lines and alters the sides of the curvilinear squares resulting in a mapping of the electric field to the $W$ plane. The Schwartz-Christoffel transformation provides the means to determine the functional relationship between $\gamma$ and $W$ such that any electric field can be mapped about any geometry given the initial polygon [15].

The fringing electric field is analyzed using a parallel plate capacitor whose plates extend to infinity along the y axis and for negative x values. This symmetry approach is valid since the fringing effects of the device are localized at the outer edges of the mirror.



(a) Original $\gamma = x + iz$ Plane     (b) Transformed $W = \Psi + i\Phi$ Plane
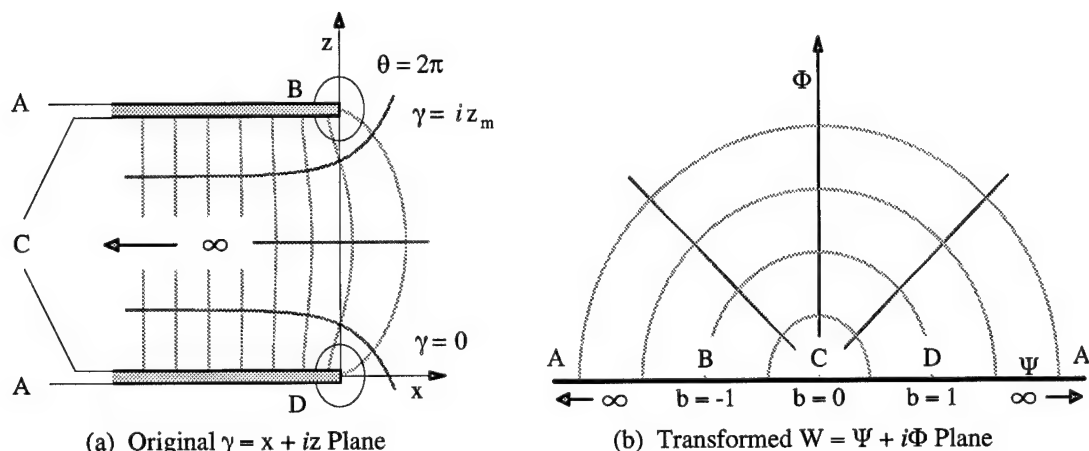
**Figure 3-5.** Schwartz-Christoffel transformation of a parallel plate capacitor [16].

The Schwartz-Christoffel transformation, shown in Fig. 3-5, is a well-developed and widely-accepted tool for such analysis which describes the initial polygon in terms of the exterior angles about which its perimeter traverses and the points at which the angle is located. The conformal mapping equation is given in as:

$$\gamma = x + iz = \gamma_o + A\int (w - b_o)^{\alpha_o}(w - b_1)^{\alpha_1}\ldots(w - b_n)^{\alpha_n}\, dw \qquad (3.28)$$

where $\gamma_o$ and $A$ are constants determined by boundary conditions, $b$ is the value of each point mapped into the $W$ plane, and $n$ is the number of points mapped into finite values. The quantity exponents, $\alpha = \theta/\pi - 1$, are functions of the external angle, $\theta$, of the transformed polygon at each point in the $\gamma$ plane being mapped [15,16].

The electric field of a parallel plate capacitor originally drawn in the $\gamma$ plane is shown in Fig. 3-5(a) where the points being mapped into the $W$ plane are labeled $A$ through $D$ and are enclosed by the polygon drawn around the upper and lower plates of the capacitor. Figure 3-5(b) represents the mapping of these points in the $W$ plane

showing the finite values of points $B$, $C$, and $D$. The constant electric flux lines are mapped into $W$ circularly about point $C$ which produces the relationship:

$$W = \Psi + i\Phi = \left(\frac{V}{i\pi}\right)\ln(w), \qquad w = \exp\left(\frac{i\pi W}{V}\right) \tag{3.29}$$

Where $\Psi$ and $\Phi$ represent electric flux and potential respectively, $V$ is the potential applied between the plates of the capacitor and $w$ represents the $W$ plane in polar form. With $\alpha_B = \alpha_D = 1$ and $\alpha_C = -1$, the Schwartz-Christoffel transformation reduces to

$$\gamma = \gamma_o + A\int \frac{w^2 - 1}{w}\, dw = \gamma_o + A\left[\tfrac{1}{2}w^2 - \ln(w)\right] \tag{3.30}$$

Applying the boundary conditions at points B and D in both planes, the constants of the transformation are $\gamma_o = -\tfrac{1}{2}A$ and $A = -(z_m/\pi)$ which produces the final relationship:

$$\gamma = x + iz = \frac{z_m}{\pi}\left[\frac{i\pi}{V}W + \frac{1}{2}\left(1 - \exp\left\{\frac{2\pi i W}{V_o}\right\}\right)\right] \tag{3.31}$$

which can be solved for the real and imaginary parts to produce the parameterized solution in two dimensions for the edge of a parallel plate capacitor. Doing so yields

$$x = \frac{z_m}{2\pi}\left[\psi + 1 - e^{\psi}\cos(\varphi)\right], \qquad z = \frac{z_m}{2\pi}\left[\varphi - e^{\psi}\sin(\varphi)\right] \tag{3.32}$$

where $z_m$ is the vertical position of the mirror above the address electrode. The index parameters $\psi$ and $\varphi$ are normalized functions of flux and potential respectively, such that

$$\psi = -\frac{2\pi\Psi}{V}, \qquad -\infty \le \psi \le \infty \tag{3.33}$$

and

$$\varphi = \frac{2\pi\Phi}{V}, \qquad 0 \le \varphi \le 2\pi \tag{3.34}$$

where $\Phi$ is the potential variable, $\Psi$ is the electric flux variable, and $V$ is the potential applied between the mirror and electrode. The result of Eq. (3.32) is plotted in Fig. 3-6 which demonstrates that the fringing effects are only present at the edges of the mirror. Moving toward the center of the device, away from the edges of the mirror, the electric

field and equipotential lines approach ideal uniformity . The electric field fringing effects are only considered for field lines on the underside of the mirror ($\psi \leq 0$) since neighboring micromirror devices prevent the extended fringing that would produce field lines emanating from the top of the mirror and underneath the electrode.



**Figure 3-6.** Solution of the Schwartz-Christoffel transformation for two parallel plates.

Micromirror devices standing alone may experience a larger fringing loss than devices positioned within an array due to the existence of these extending electric field lines.

For devices standing alone, the electrostatic force along the electric field lines outside the device acts in the opposite direction as those within the device. Although the arc lengths of these lines are much larger and thus the electric intensity much weaker, the net electrostatic force of these lines should not be neglected. Integrating Eq. (3.27) along the top of the mirror produces a non-zero force in the upward direction which is counterproductive to the actuation of the device. The net electrostatic force acting on devices standing alone is somewhat less than that on devices within an array.

3-15

*(3.4.2) ELECTRIC FIELD ARC LENGTH*

To find the electric field intensity as a function of position along the mirror surface, the length of the arc traced along a constant electric flux value must be determined. Recognizing that differential change in the potential function, $d\varphi$, will result in differential change in position, $dx$ and $dz$, the relation is found to be

$$d\ell = \sqrt{dx^2 + dz^2} = \sqrt{\left(\frac{dx}{d\varphi}\right)^2 + \left(\frac{dz}{d\varphi}\right)^2} \; d\varphi \qquad (3.35)$$

where $d\ell$ is the differential change in the arc length. Using the derivatives of $x$ and $z$ with respect to the potential function, $\varphi$, produces

$$\frac{dx}{d\varphi} = -\frac{z_m}{2\pi}\left(e^{\psi} \sin \varphi\right), \qquad \frac{dz}{d\varphi} = \frac{z_m}{2\pi}\left(1 - e^{\psi} \cos \varphi\right) \qquad (3.36)$$

Substituting these results into Eq. (3.35) and integrating each side yields

$$\ell = \frac{z_m}{2\pi}\sqrt{1+e^{2\psi}} \int_0^{2\pi} \left[1 + \left(\frac{2e^{\psi}}{1+e^{2\psi}}\right)\cos\varphi\right]^{\frac{1}{2}} d\varphi \qquad (3.37)$$

Using basic trigonometric substitution, this is simplified to

$$\ell = \frac{2z_m}{\pi}\left(1 + e^{\psi}\right)\int_0^{\frac{\pi}{2}} \left[1 - m \sin^2 \theta\right]^{\frac{1}{2}} d\theta, \qquad m = \frac{4e^{\psi}}{\left(1 + e^{\psi}\right)^2} \qquad (3.38)$$

which is simply an elliptic integral of the second kind where the need for $m \leq 1$ is valid for all values of $\psi$. Therefore, the elliptic integral series solution is

$$\ell = z_m\left(1 + e^{\psi}\right)\left[1 - \sum_{n=1}^{\infty}\left[\left(\prod_{k=1}^{n}\frac{2k-1}{2k}\right)^2 \frac{m^n}{2n-1}\right]\right] \qquad (3.39)$$

which obviously becomes more accurate as the number of terms increases [17,18].

As an alternative to the elliptic integral series solution, two approximations were developed that are far more efficient and simpler to employ. First, the numerical

integration of Eq. (3.38) produces a series solution that converges much more quickly and requires significantly fewer terms to maintain a certain degree of accuracy. Using the following function declaration for the integrand:

$$f(\theta) = \left[1 - m \sin^2 \theta\right]^{\frac{1}{2}}, \qquad m = \frac{4e^{\psi}}{\left(1 + e^{\psi}\right)^2} \qquad (3.40)$$

the definite integral is then evaluated by summing the areas of $N$ rectangles such that the height of the rectangle is the sample of $f(\theta)$ and width is the corresponding segmentation of the range of integration. Mathematically, this series solution was found to be :

$$\ell = \frac{2 z_m}{\pi} \left(1 + e^{\psi}\right) \left[ \left(\frac{\pi}{2N}\right) \sum_{i=1}^{N} f\left( (i - \tfrac{1}{2}) \left(\frac{\pi}{2N}\right) \right) \right] \qquad (3.41)$$

which requires fewer terms, $N$, to be as precise as Eq. (3.39) and does not require recursive multiplication making this solution much simpler to use.

Another approximation for the electric field arc length is a curve-fitting function which produces a closed-form solution. In the parametric domain, the arc length is found as a function of $\psi$ by solving Eq. (3.39) at various intervals and performing a least squares fit to an exponentially increasing curve. The resulting solution was found to be:

$$\ell = z_m \left(1 + ae^{b\psi}\right), \qquad a = 0.27013, \qquad b = 2.09158 \qquad (3.42)$$

which provides a much simpler evaluation than either of the above series solutions.

To compare the precision of the three solutions, a complete evaluation of the arc length was first obtained for a set of $\Psi$ values. These arc lengths were found by determining the converging limit of Eq. (3.39) with $N = 500$ terms. With this set of data, the sum of the square of differences technique was performed on all three solutions using significantly fewer terms than the converging limit. The precision of the closed-form solution of Eq. (3.42) compares to that of the numerical integration solution of Eq. (3.41) using $N = 6$ terms and the elliptic integral solution of Eq. (3.39) using $N = 11$ terms.

## (3.4.3) FRINGING ELECTRIC FIELD INTENSITY

With the address electrode at some potential, $V$, and the mirror grounded, the electric field intensity at a position, $x$, along the mirror surface becomes

$$E(\psi) = \frac{V}{\ell(\psi)}, \qquad x(\psi) = \frac{z_m}{2\pi}\left[\psi + 1 - e^{\psi}\right] + \frac{w_x}{2} \qquad (3.43)$$

which parametrically represents the electric field intensity as a function of position over half the mirror width ($0 \leq x \leq \frac{1}{2}w_x$) where $w_x$ is the width of the mirror in the $x$ direction and $\ell(\psi)$ is the arc length. In order to maintain the precision of the fringing effects, the arc length was evaluated as the converging limit of the numerical integration series solution given in Eq. (3.41) using $N = 100$ terms. This parametric function is shown in Fig. 3-7(a) which depicts the normalized electric field intensity along the $x$ axis:



(a) Along One Dimension ($x$)    (b) Along Two Dimensions ($x,y$)
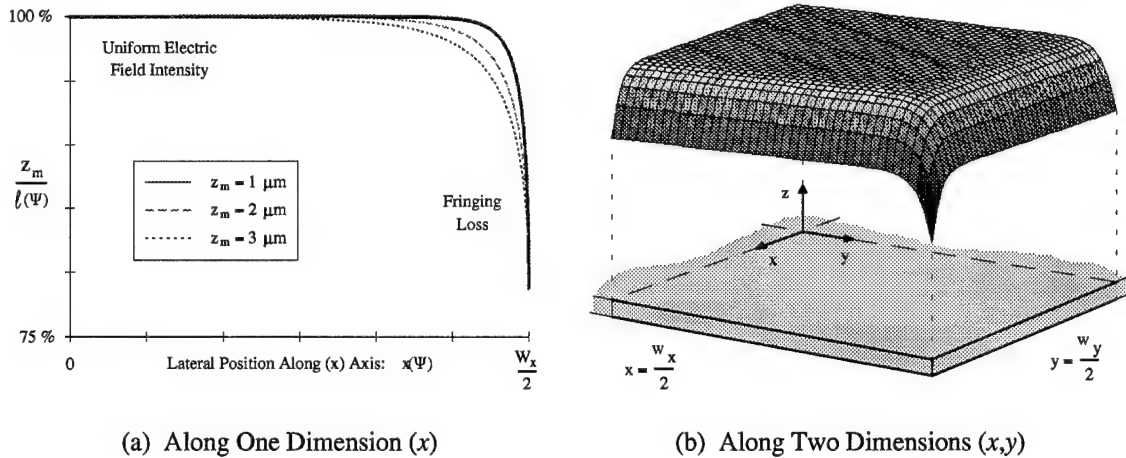
**Figure 3-7.** Electric field intensity as a function of position along the mirror surface.

It should be noted that this is the solution in one dimension. The superposition of this solution in the $x$ and $y$ dimension will produce a surface curve shown in Fig. 3-7(b) in which the solution shown in Fig 3-7(a) does not directly correspond to the cross section of the surface along the $x$ axis. The minimum electric field intensity in one dimension corresponds to that of the corner of the device in two dimensions.

To project this solution into the $y$ domain as well, a method of algebraic averaging was used such that the net electric field intensity at some position along the surface of the mirror is the average of that given by the $x$ and $y$ coordinates:

$$E_{2D}(\psi_x, \psi_y) = \frac{1}{2}[E(\psi_x) + E(\psi_y)] \tag{3.44}$$

where the $x$ and $y$ coordinates are evaluated as:

$$x(\psi_x) = \frac{z_m}{2\pi}[\psi_x + 1 - e^{\psi_x}] + \frac{w_x}{2}, \qquad y(\psi_y) = \frac{z_m}{2\pi}[\psi_y + 1 - e^{\psi_y}] + \frac{w_y}{2} \tag{3.45}$$

Figure 3-7(b) represents the normalized magnitude of the electric field along the surface of the mirror as a function of $x$ and $y$ over one quarter of the mirror surface. At the center of the mirror, no fringing effects exist and the ideal uniform electric field is shown. At the edges, however, the fringing effects are quite significant. At the corners of the mirror and address electrode, the electric field intensity is reduced to 78.7% of the ideal magnitude which corresponds to the intensity shown in Fig. 3-7(a). The solution in one dimension is the cross section along the diagonal of the solution in two dimensions.

To determine the total electrostatic force acting on the mirror in the downward direction, as given in Eq. (3.27), the square of the electric field intensity in Eq. (3.44) must be numerically integrated across the mirror surface using the flux parameter, $\psi$. It is obvious that the total force will be less than the ideal force calculated using an ideal uniform electric field. The total electrostatic force acting on the mirror is

$$F_{PP} = \frac{\varepsilon_o}{2} \int_{-\frac{w_x}{2}}^{\frac{w_x}{2}} \int_{-\frac{w_y}{2}}^{\frac{w_y}{2}} [E_{2D}(\psi_x, \psi_y)]^2 \, dy \, dx = \frac{\varepsilon_o}{2} \int_0^{\frac{w_x}{2}} \int_0^{\frac{w_y}{2}} [E(\psi_x) + E(\psi_y)]^2 \, dy \, dx$$

$$= \frac{\varepsilon_o}{2} \left[ \frac{w_y}{2} \int_0^{\frac{w_x}{2}} E^2(\psi_x) \, dx + 2 \int_0^{\frac{w_x}{2}} \int_0^{\frac{w_y}{2}} E(\psi_x) E(\psi_y) \, dy \, dx + \frac{w_x}{2} \int_0^{\frac{w_y}{2}} E^2(\psi_y) \, dy \right] \tag{3.46}$$

Each of these integrals must be numerically integrated individually due to their distinct integrands. In order to do so, the corresponding parameter, $\psi$, is divided into $N$ segments which are used to evaluate discrete samples of the electric field intensity and position.

The definite integral is evaluated as the sum of the area of rectangles formed in this process. For example, the following integral is numerically integrated such that

$$\int_0^{\frac{w_x}{2}} E(\psi_x)\,dx = \frac{1}{2}\sum_{i=1}^{N}\left[(x(\psi_i) - x(\psi_{i-1}))(E(\psi_i) + E(\psi_{i-1}))\right] \qquad (3.47)$$

where the height of the rectangle is defined as the average of the values of the electric field intensity at each side of the rectangle. The remaining integrals are evaluated using the converging limit of the series solution generated by this technique.

The range of parameter values must be chosen to correspond to the range of integration over position. In order to do so, a relationship must be developed between the index parameter, $\psi$, and the center of the mirror, $x = 0$. Moving away from the edges of the device, the index parameter becomes increasingly negative. Therefore, Eq. (3.45) can be reduced and solved for the index parameter at the center of the device, $\psi_o$, such that

$$x = 0 = \frac{z_m}{2\pi}[\psi_o + 1] + \frac{w_x}{2}, \qquad \psi_o = -\left[\frac{w_x\pi}{z_m} + 1\right] \qquad (3.48)$$

The index parameter at $y = 0$ is determined using the same technique. Since it is known that the value of the index parameter at the edge of the device is zero, the resulting range in the index parameter can be used to describe the desired range of integration with respect to position over the surface of the mirror.

The parametric numerical integration was performed for numerous values of device dimensions, $w_x$ and $w_y$, and mirror separation distance, $z_m$, such that an analytic equivalent of this approach could be determined. It was found that the fringing losses are best described as a fractional loss in the ideal force of a capacitor:

$$\Delta f_{FL} \approx \frac{z_m}{165.4}\left[\frac{2(w_x + w_y)}{w_x w_y}\right], \qquad 0 < \Delta f_{FL} < 1 \qquad (3.49)$$

Figure 3-8 is a plot of this approximation function together with the numerical integration results. It is obvious that as the mirror area increases, the effects of fringing decrease, but

smaller devices are more affected by such losses to the extent that the ideal parallel plate capacitor solution can not be used. The devices fabricated in this thesis have a mirror separation distance, $z_m$, of approximately 2.5 µm when no address potential is applied. As shown in Fig. 3-8, the loss due to fringing becomes a function of mirror surface area.
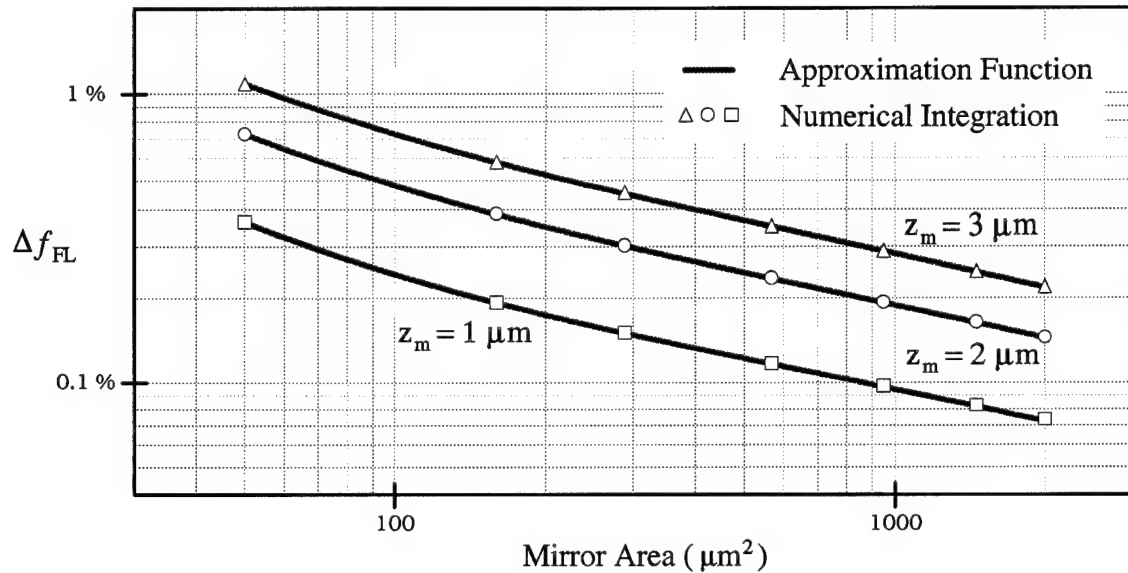


**Figure 3-8.** Plot of fringing loss approximation function with respect to mirror area.

Since the full range of motion of the micromirror device is much smaller than the separation distance, the area of the mirror will have the greatest impact on the loss due to fringing effects. This analysis is valid for devices positioned within an array of similar devices such that the extended fringing shown in Fig. 3-6 does not exist. Devices standing alone are expected to have approximately 65% more loss due to additional fringing electric field lines. It should be noted that Eq. (3.49) is valid for other device geometries such that the quantity in brackets is the ratio of the length of the perimeter to the area of the mirror. The total electrostatic force on the mirror is evaluated by reducing the ideal force given in Eq. (3.14) by the percentage loss in force given in Eq. (3.49).

If etch holes must be added to larger devices, the reduction in mirror area can also be represented as a fractional loss in the ideal force. This fractional loss is determined by the ratio of etch hole area to the total area of the mirror without etch holes:

$$\Delta f_{EH} = \left[ \frac{A_{EH}}{w_x w_y} \right], \qquad\qquad 0 < \Delta f_{EH} < 1 \qquad\qquad (3.50)$$

where $A_{EH}$ is the total area lost in the mirror surface due to etch holes.

The fractional loss in the ideal electrostatic force due to fringing loss and etch holes, $\Delta f_{FL}$ and $\Delta f_{EH}$ respectively, can be summed to produce a net loss in force, $\Delta f$. The net electrostatic force acting on the mirror in the downward direction becomes

$$F = \frac{\varepsilon_o}{2} [1 - \Delta f] \iint \left( \frac{V}{z_m(x, y)} \right)^2 dxdy \qquad\qquad (3.51)$$

where $z_m(x,y)$ represents the separation distance between the electrode and mirror at any position within the device and will not be uniform due to mirror surface deformations.

## (3.5) CROSS-TALK INTERFERENCE

Another characteristic of the electric field within a device is the interference produced by the electric field lines of neighboring devices. This could alter the electrostatic force on the mirror in two ways. First, the fringing field lines of one device can be distorted by partially conforming to those of another which would change the amount of fringing losses as calculated above. However, since the flexures and support posts between each device are grounded with the mirrors and a gap exists between these geometric features, the electric field fringing loss at the edge of an individual mirror is still dominated by the fringing effects within the device itself.

The second cross-talk effect would be the added force on the mirror supplied along additional field lines emanating from the electrode of a neighboring device. This

interference is only present when the primary device is not actuated since the creation of an much stronger electric field within the primary device would prevent the interference field. As shown in Fig. 3-9, the mirror of a primary device experiences a small force along the electric field lines from the first of four neighboring device that are actuated:
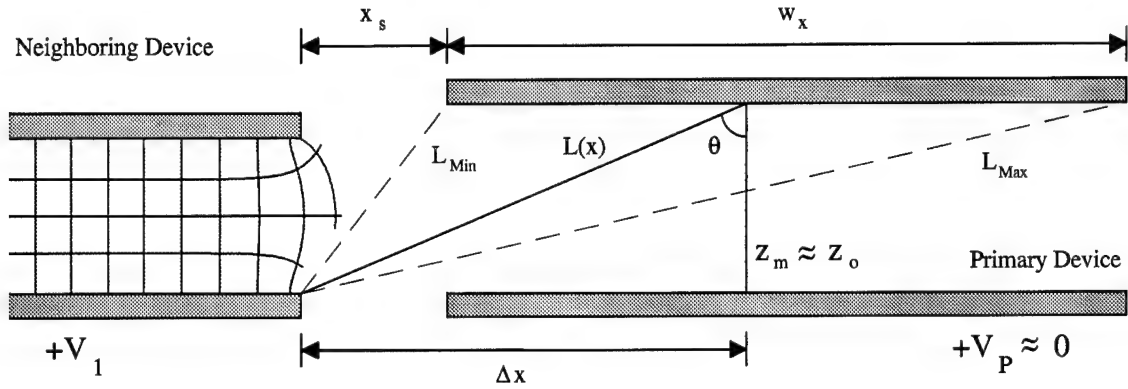


**Figure 3-9.** Cross-talk electric field lines of neighboring micromirror devices.

If the address potential of the primary device, $V_P$, is approximately zero, the net cross-talk force supplied along the electric field lines is simply the integral of the linear force distribution along the surface of the mirror. This distribution is determined by the address potential of the neighboring device, $V_1$, the length of each electric field line, $L$, and the angle of the force vector, $\theta$. The length of the electric field lines is given by

$$L(x) = \sqrt{(\Delta x^2 + z_o^2)} = \sqrt{\left(x + x_s + \frac{w_x}{2}\right)^2 + z_o^2} \qquad (3.52)$$

where $x_s$ is the separation distance between each device as shown in Fig. 3-9 which also shows $\Delta x$ as the horizontal distance between the neighboring address electrode and any point along the surface of the primary mirror. The linear force distribution is found to be

$$f_1(x) = \frac{\varepsilon_o}{2} w_y \left(\frac{V_1}{L(x)}\right)^2 \cos(\theta) = \frac{\varepsilon_o}{2} \frac{w_y V_1^2 z_o}{[L(x)]^3} \qquad (3.53)$$

which is not a function of position in the $y$ direction. Since this distribution is not symmetric about the center of the device, the side of the mirror nearest the neighboring

device will experience a greater force than the opposite side of the mirror. In order to determine the amount of force at both ends of the device, the centroid position, $\bar{x}_1$, and the total force due to cross-talk, $F_1$, must be found and are defined as [17]

$$F_1 = \int_{-w_x/2}^{w_x/2} f_1(x)\, dx = \frac{\varepsilon_o\, w_y\, V_1^2}{2\, z_o} \left[ \frac{(x_s + w_x) L_{min} - x_s L_{max}}{L_{min} L_{max}} \right] \qquad (3.54)$$

and

$$\bar{x}_1 = \frac{1}{F_1} \int_{-w_x/2}^{w_x/2} x f_1(x)\, dx = \frac{z_o^2 (L_{max} - L_{min}) + \left(x_s + \frac{w_x}{2}\right)\left[x_s L_{max} - (x_s + w_x) L_{min}\right]}{(x_s + w_x) L_{min} - x_s L_{max}} \qquad (3.55)$$

where $L_{min}$ and $L_{max}$ are the minimum and maximum arc lengths respectively given as

$$L_{min} = \sqrt{x_s^2 + z_o^2}, \qquad\qquad L_{max} = \sqrt{(x_s + w_x)^2 + z_o^2} \qquad (3.56)$$

It is important to note that the centroid position, $\bar{x}_1$, is not a function of address potential of the neighboring device, $V_1$. Figure 3-10 illustrates the linear force distribution of the cross-talk interference and illustrates the total force at the centroid position:
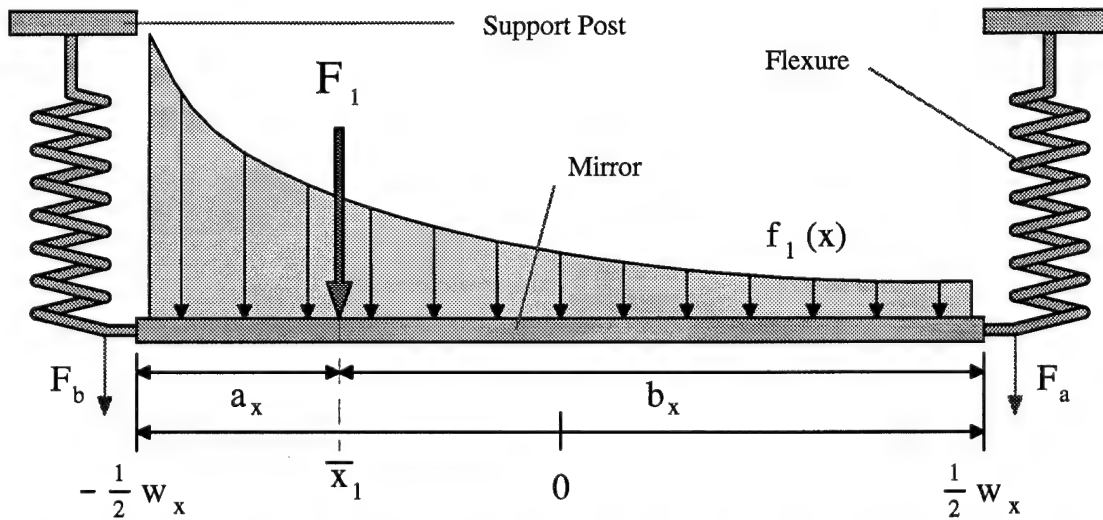


**Figure 3-10.** Cross talk linear force distribution along primary micromirror device.

In one dimension, as shown in Fig. 3-10, the resulting force observed by the flexures supporting each end of the device, $F_a$ and $F_b$, determines the deflection at each end which

3-24

will not be equal. The end of the device nearest the actuated neighbor will deflect more than the opposite end. The force at each flexure is proportional to $F_1$ such that

$$F_a = F_1\left(\frac{a_x}{w_x}\right), \qquad\qquad F_b = F_1\left(\frac{b_x}{w_x}\right) \qquad\qquad (3.57)$$

where

$$a_x = \frac{w_x}{2} + \bar{x}_1, \qquad\qquad b_x = \frac{w_x}{2} - \bar{x}_1 \qquad\qquad (3.58)$$

These forces are related to the deflection at each end by the spring constant of the flexure.

Expanding this analysis into two dimensions, it is known that the $y$ centroid falls on the $x$ axis due to the device symmetry. The total force due to cross talk from the first device, $F_1$, is localized at $(x,y) = (\bar{x}_1, 0)$ and produces a net downward force at each of the four corners of the device. For a square device, the other three neighbors produce similar forces located at the same position, given in Eq. (3.55), relative to each mirror:



(a) Adjacent Micromirror Devices          (b) Tilting Of Mirror Surface
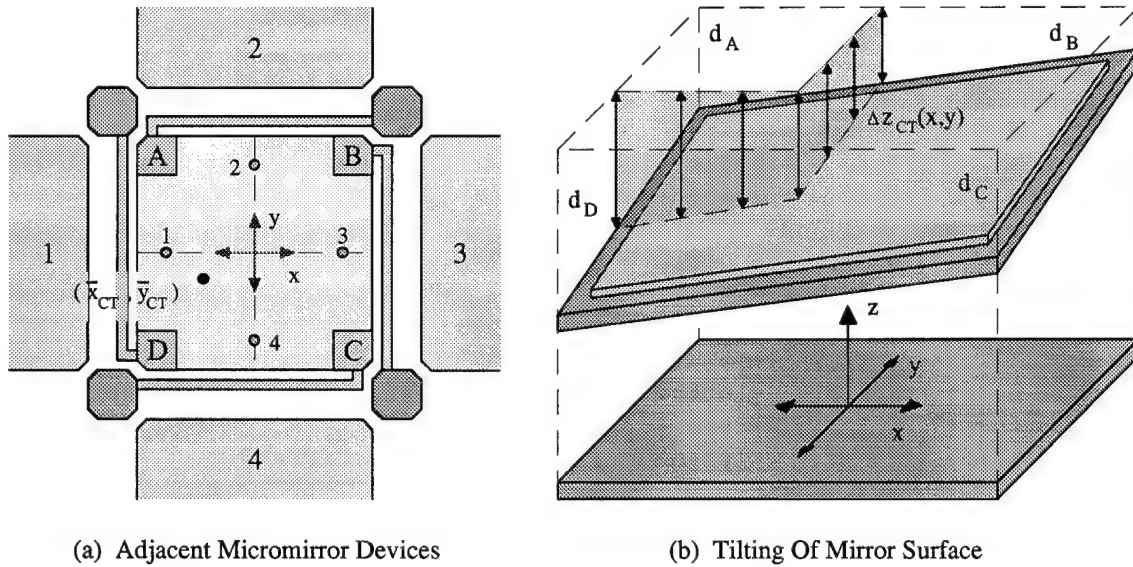
**Figure 3-11.** Cross-talk interference of adjacent devices and resulting mirror surface tilt.

The centroid positions of all four neighbors are shown in Fig. 3-11(a) as circles numbered according to the corresponding device. The total force due to cross talk, $F_{CT}$, is centered at the final centroid position, $(\bar{x}_{CT}, \bar{y}_{CT})$, which is determined by the forces of the

surrounding devices. Figure 3-11(b) illustrates the final effect of cross talk which shows the uneven tilting of the mirror in response to the location of the final centroid. In this example, the first and fourth devices are actuated more than the second and third devices which determines the position of the centroid. Since the spring constants of the flexures are the same, the mirror will tilt toward point D as shown in Fig. 3-11(b).

To determine the position of the final centroid and the total cross talk force, the forces and centroids of all four neighbors are found using Eqs. (3.54) and (3.55) respectively. The centroid coordinates and total force are then given as

$$\overline{x}_{CT} = \frac{1}{F_{CT}}\sum_{n=1}^{4}\overline{x}_n F_n, \qquad \overline{y}_{CT} = \frac{1}{F_{CT}}\sum_{n=1}^{4}\overline{y}_n F_n, \qquad F_{CT} = \sum_{n=1}^{4} F_n \qquad (3.59)$$

where $n$ is the index of the neighboring devices. Similar to the analysis in one dimension given in Eq. (3.57), the force observed at each corner of the device is proportional to the total force, $F_{CT}$, as a function of position relative to the centroid, $(\overline{x}_{CT}, \overline{y}_{CT})$. Since the flexures are only attached at the corners of the square micromirror device, the function that describes the force observed by a given flexure, $F_F$, can be described with normalized position coordinates, $(\hat{x}, \hat{y})$, such that

$$F_F(\hat{x}, \hat{y}) = F_{CT}\left(\frac{\frac{w_x}{2} + \hat{x}\,\overline{x}}{w_x}\right)\left(\frac{\frac{w_y}{2} + \hat{y}\,\overline{y}}{w_y}\right) \qquad (3.60)$$

where $\hat{x} = \pm\hat{y} = \pm 1$ corresponding to the particular corner of the mirror where the flexure is attached. For instance, the force at corner $A$ is found to be

$$F_A = F_F(-1,+1) = F_{CT}\left(\frac{\frac{w_x}{2} - \overline{x}}{w_x}\right)\left(\frac{\frac{w_y}{2} + \overline{y}}{w_y}\right) \qquad (3.61)$$

which is directly proportional to the deflection of the mirror at this corner, $d_A$, such that

$$d_A = \frac{F_A}{k_A}, \qquad\qquad k_A = \tfrac{1}{4}k \qquad (3.62)$$

where $k_A$ is the spring constant of a single flexure which is equal to the total spring

constant of the micromirror, $k$, divided by the number of flexures. Using the same approach, the forces and deflections of corners $B$, $C$, and $D$ can be found which describes the total deflection behavior of the surface of the mirror as shown in Fig. 3-11(b).

The deflection of the mirror due to cross talk is a function of position across the mirror surface and can be obtained by developing an equation of the plane formed by joining the four corners. The function $\Delta z_{CT}$ represents this deflection and was found to be

$$\Delta z_{CT}(x, y) = \tfrac{1}{4} D_{sum} + \tfrac{1}{2} D_x \left( \frac{x}{w_x} \right) + \tfrac{1}{2} D_y \left( \frac{y}{w_y} \right) + D_{xy} \left( \frac{xy}{w_x w_y} \right) \qquad (3.63)$$

where the deflection coefficients are given as

$$D_{sum} = d_A + d_B + d_C + d_D, \qquad D_x = d_B + d_C - d_A - d_D,$$

$$D_y = d_A + d_B - d_C - d_D, \qquad D_{xy} = d_B + d_D - d_A - d_C \qquad (3.64)$$

where $d_B$, $d_C$, and $d_D$ are the deflections at corners $B$, $C$, and $D$ respectively. As given in Eq. (3.53), the significance of the cross-talk deflection, $\Delta z_{CT}$, increases as the distance between devices, $x_s$, decreases. Therefore, arrays containing micromirror devices in close proximity to each other may be significantly affected by neighboring devices.

## (3.6) FLEXURE SPRINGS

The flexures are modeled as simple springs in which the restoring force in the upward direction is linearly related to the vertical deflection of the mirror by a spring constant that can be determined from the geometry and material properties of the hinges. Furthermore, the mirror and flexures of the device comprise an undamped harmonic oscillator when the device is actuated with a periodic voltage at low frequencies. As a result, the restoring force of the flexures is not only a function of geometry and material properties, but also of temperature and driving frequency. At higher frequencies, however, squeeze film damping may become increasingly significant as the mirror must

force air out of the volume of the device during operation. In an operational package of FBMD arrays, a hermetic seal would eliminate this damping as well as prevent particulate matter contamination.

To analyze the behavior of the flexures, another beam is rigidly supported on one end and free-floating on the other. A force, $F$, acts downward at the end of the beam at which point the maximum deflection, $d$, from the horizontal is given as [19]

$$d = \frac{FL^3}{3EI}, \qquad I = \frac{1}{3}wt^3 \qquad (3.65)$$

where $L$, $w$, $t$, and $E$ are the length, width, thickness, and modulus of elasticity for the beam, respectively. Solving for the constant relation between force and deflection yields

$$k_{cs} = \frac{Ewt^3}{L^3} \qquad (3.66)$$

which describes the cross-sectional spring constant. There is also a stress term that can be added to form the complete spring constant for each flexure as

$$k_s = \frac{\sigma(1 - \nu)wt}{2L} \qquad (3.67)$$

where $\sigma$ and $\nu$ are the stress and Poisson ratio of the flexure material, respectively [4]. Since four flexures are used to support the electrostatic force of the device, the net spring constant for the entire device becomes

$$k = 4(k_{cs} + k_s) = 4\left[\frac{Ewt^3}{L^3} + \frac{\sigma(1 - \nu)wt}{2L}\right] \qquad (3.68)$$

which is a function of temperature since the thermal expansion of the flexures will alter the geometry used to evaluate this constant. It should be noted that the modulus of elasticity for thin films of a material is much smaller than that of the bulk material. As a result, the elasticity of the flexures of the micromirror devices must be determined in order to obtain a valid spring constant. The commercial foundry which fabricates the micromirror devices in this thesis provides this information.

## (3.6.1) FREQUENCY RESPONSE

Since the mirror is a harmonic oscillator, the spring constant directly determines the resonant frequency of the mirror given its mass. The time response of any harmonic oscillator can be found by solving a differential equation relating Newton's second law and Hooke's law to a sinusoidal driving force. The solution is given as [20]

$$z(t) = \frac{F_o \cos(\omega t)}{M(\omega_o^2 - \omega^2)}, \qquad \omega_o = \sqrt{\frac{k}{M}} \qquad (3.69)$$

where $z(t)$ is the deflection of the oscillator in time, $F_o$ and $\omega$ are the amplitude and frequency of the driving force respectively, $\omega_o$ is the resonant frequency of the oscillator, $k$ is the spring constant in Eq. (3.17), and $M$ is the combined mass of the mirror as determined from the densities and geometries of the materials comprising it.
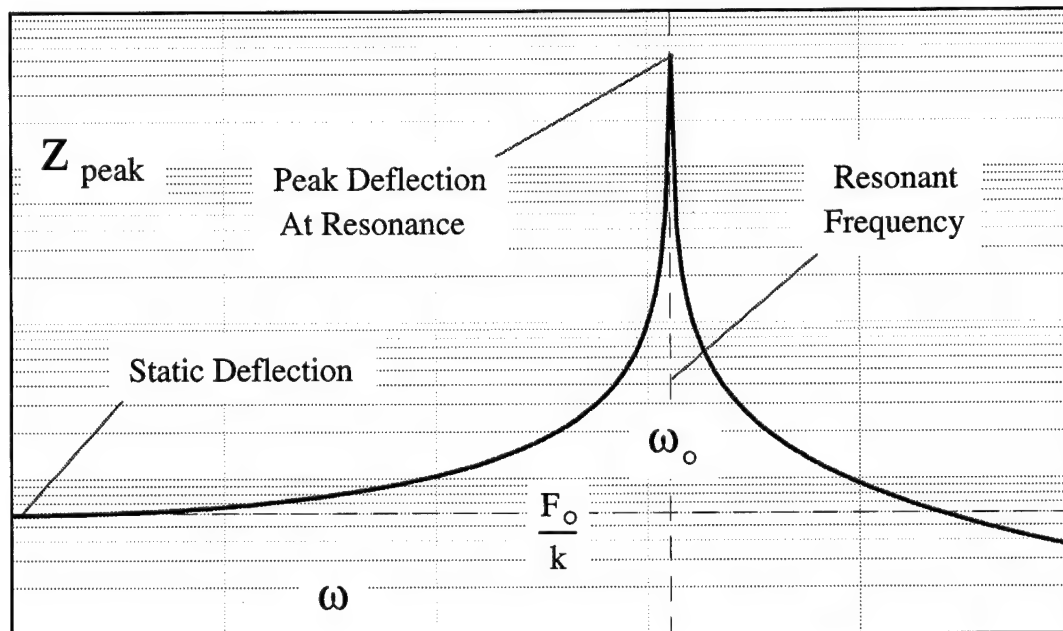


**Figure 3-12.** Frequency response of peak deflection of an undamped harmonic oscillator.

The peak deflection of the oscillator, $z_{peak}$, is a function of frequency such that the deflection sharply increases as the driving frequency approaches the resonant frequency

of the oscillator. This function is the peak positive deflection of Eq. (3.69) such that

$$z_{peak} = \frac{F_o}{M\left|\omega_o^2 - \omega^2\right|}$$  ( 3.70 )

which indicates that the peak deflection approaches infinity as the frequency approaches the resonant frequency of the oscillator. Figure 3-12 illustrates this behavior which illustrates the behavior of the device close to the resonant frequency. The combined restoring force of the flexures becomes

$$F_S = \left[k - M(2\pi f)^2\right]d_f$$  ( 3.71 )

where $d_f$ is the vertical deflection of the mirror at the flexures and $f$ is the driving frequency of the micromirror device in Hertz. For low driving frequencies ($\omega \ll \omega_o$), the peak deflection reduces to the static deflection given by Hooke's Law.

### (3.7 ) MIRROR SURFACE DEFORMATION

Another major factor in the behavior of the device is the inclusion of surface deformations during the actuation of the device. The surface deformation of the mirror is compared to the deformation of a rigid beam supported on each end by ball supports such that the free-floating flexures allow the edges of the mirror to angle upwards as the center of the mirror deflects downward. The maximum deflection, $\delta$, of the beam under a uniform force per unit length, $q$, is at the beam center and is given by

$$\delta = \frac{5qL^4}{384EI}, \qquad q = \frac{F}{L}, \qquad I = \frac{1}{12}wt^3$$  ( 3.72 )

where $L$, $w$, $t$, and $E$ are the length, width, thickness, and modulus of elasticity of the beam, respectively [19].

Although the edges of the beam are allowed to angle upward, the angles produced by very small deflections at the center of the beam compared to its length, $\delta \ll L$, are

negligible and are assumed to be zero. Therefore, the deformation of the mirror can be modeled as a beam rigidly supported at the ends. Figure 3-13(a) represents the deflection of this rigid beam due to some uniform force per unit length, $q$, across the top.



(a)  Beam Deformation                                      (b)  Mirror Surface Deformation
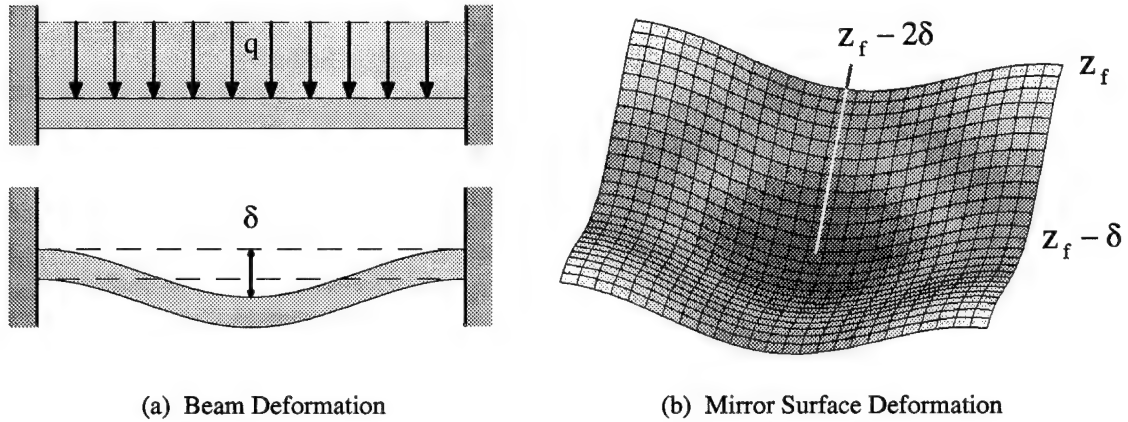
**Figure 3-13.** Use of beam deflection analysis to represent mirror surface deformation.

For small deflections, this deformation as a function of position can be modeled as one period of a cosine wave having an amplitude equal to half the maximum deflection at the center of the beam, $\delta$. For a micromirror device of area $A$, the maximum surface deformation including an initial deformation due to gravity reduces to

$$\delta = \frac{FA}{(6.4)Et^3} = \left[ \frac{\varepsilon_o}{2} \left( \frac{V}{z_m} \right)^2 A + Mg \right] \frac{A}{(6.4)Et^3} \qquad (3.73)$$

where $M$ is the combined mass of the mirror and g is the acceleration constant due to gravity. Although the weight of the hinges adds to the deflection due to gravity, the weight of the mirror is significantly larger.

The surface deformation function is first developed for a micromirror device in which the flexures are attached at the corners. The deformation of such a mirror is illustrated in Fig. 3-13(b) in which the corners of the mirror are rigidly supported by the flexures of the device. In one dimension, the surface deformation can be derived to

describe the mirror along one of the outer edges. Therefore, this deformation can be represented including the above beam analysis such that

$$z_m(x) = z_f - \frac{\delta}{2}\left[1 + \cos\left(\frac{2\pi x}{w_x}\right)\right] \qquad (3.74)$$

where $z_f$ is the vertical position of the flexures at the corners of the mirror. Expanding this into two dimensions, the deformation as a function of $x$ and $y$ becomes:

$$z_m(x,y) = z_f - \Delta z_{SD}(x,y) = z_f - \delta\left[1 + \frac{1}{2}\left(\cos\left(\frac{2\pi x}{w_x}\right) + \cos\left(\frac{2\pi y}{w_y}\right)\right)\right] \qquad (3.75)$$

where $\Delta z_{SD}(x,y)$ represents the change in height across the surface due to deformations. Figure 3-13(b) shows a surface plot of this function which depicts the maximum deflection along the surface ($z_h - 2\delta$) to be at the center of the mirror ($x = y = 0$).

For micromirror devices with the flexures attached at some point along the edge of the mirror, the solution in Eq. (3.75) is simply rotated and scaled down to fit within the dimensions of the mirror. The rotated coordinates of the solution are found to be

$$x' = s_x\left[x\cos(\theta_x) - y\sin(\theta_y)\right], \qquad y' = s_y\left[x\sin(\theta_x) - y\cos(\theta_y)\right] \qquad (3.76)$$

where the scale factors, $s_x$ and $s_y$, are given as

$$s_x = \sqrt{\frac{w_x^2 + w_y^2}{w_x^2 + w_y^2 + 4\left(L_x^2 - w_xL_x\right)}}, \qquad s_y = \sqrt{\frac{w_x^2 + w_y^2}{w_x^2 + w_y^2 + 4\left(L_y^2 - w_yL_y\right)}} \qquad (3.77)$$

where $L_x$ and $L_y$ are the distances between the corners of the mirror and the position at which the flexures are attached and the rotation angles, $\theta_x$ and $\theta_y$, are given as

$$\theta_x = ArcTan\left(\frac{L_x}{w_x - L_x}\right), \qquad \theta_y = ArcTan\left(\frac{L_y}{w_y - L_y}\right) \qquad (3.78)$$

The scale factors are to reduce the mapped solution so that the positions of zero deflection occur within the geometry of the device. If a square is rotated some small angle to one direction, the new position of the corner of the square is outside the

perimeter of the original square. Therefore, the rotated solution must be scaled so that some position along the surface of the mirror is described as having no deformation. Figure 3-14 illustrates the result of this transformation.



(a) Flexures Attached at Corners        (b) Flexures Attached Along Sides
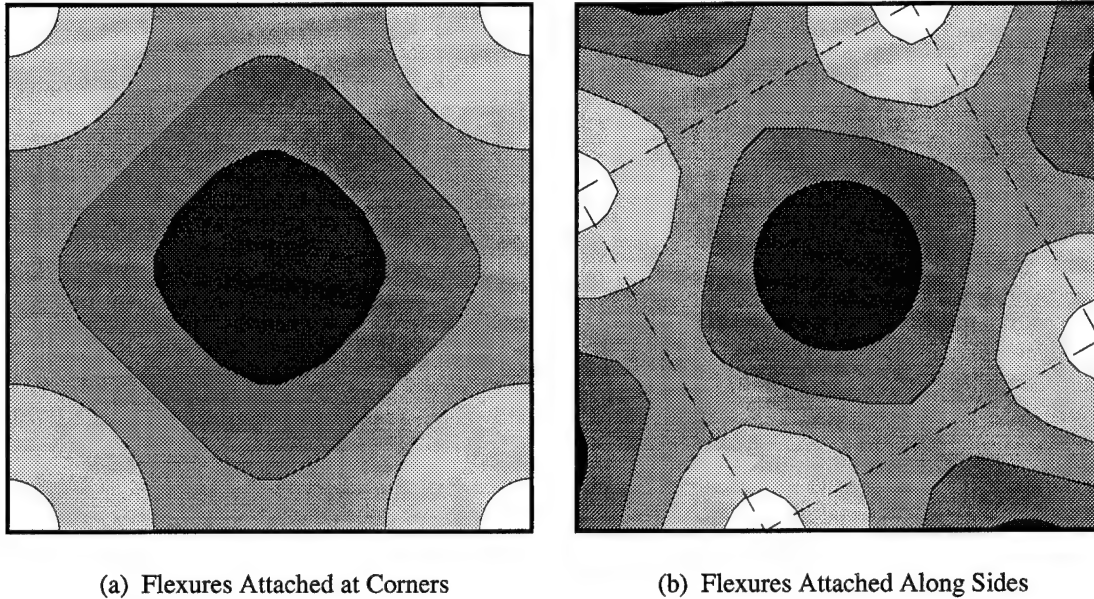
**Figure 3-14.** Plot of surface deformation function for FBMD with two flexure locations.

The surface of the mirror where the flexures are attached has no deformation and is shown as white. The deeper deformations are shown darker relative to the degree of depth. The rotated coordinates given in Eq. (3.76) are used in Eq. (3.75) to produce the contour plot shown in Fig. 3-14(b) in which the original solution is shown within the dashed lines. This contour illustrates the effects of deformations at the corners of the mirror which are free to deform without rigid support by the flexures. In both solutions, the peak deformation is given as $z_f$ -2$\delta$ although the peak deformation of the rotated solution will be slightly less than the original solution shown in Fig. 3-14(a) since the center of the mirror is much closer to the flexures. In this situation, the deflection coefficient, $\delta$, must be reduced so that the peak deflection is also reduced. The surface deformation of any rectangular Flexure-Beam micromirror device can be represented with this solution.

3-33

## (3.8) TEMPERATURE DEPENDENCE

The temperature effects are analyzed by considering the coefficients of thermal expansion for the materials comprising the hinges and mirrors. The length, width and thickness of the device components will increase with temperature which alters such factors as the spring constant of the flexures or the total electrostatic force on the mirror. Consider the length of the flexures as a function of temperature, $T$, in which

$$L = \ell_o\left[1 + \alpha(T - T_o)\right] \tag{3.79}$$

where $\ell_o$ is any length at temperature $T_o$ and $\alpha$ is the coefficient of thermal expansion for the flexure material [14]. The temperature dependence of the entire device can then be predicted by applying this analysis to all dimensions of length in the final model.

## (3.9) FLEXURE-BEAM CHARACTERISTIC MODEL

To develop the overall characteristic model for the device, the electrostatic force given in Eq. (3.51) is set equal to the spring force in Eq. (3.71) such that

$$F = \left[k - M(2\pi f)^2\right]d_f = \frac{\varepsilon_o}{2}\left[1 - \Delta f_{FL}\right] \iint \left(\frac{V}{z_m(x,y)}\right)^2 dxdy \tag{3.80}$$

Solving for $V$ while incorporating mirror surface deformation yields

$$V = \sqrt{\left[\frac{2\left[k - M(2\pi f)^2\right]d_f}{\varepsilon_o\left[1 - \Delta f_{FL}\right]}\right]\left[\frac{1}{\iint z_m^{-2}(x,y)\,dxdy}\right]}$$

$$\approx \sqrt{\left[\frac{2\left[k - M(2\pi f)^2\right]d_f}{\varepsilon_o\left[1 - \Delta f_{FL}\right]}\right]\tan\left[\frac{(z_f - \delta)^2}{w_x w_y}\right]} \tag{3.81}$$

Recognizing that $\delta$ is a function of address potential $V$, this creates a circular reference when calculating the voltage required to deflect the device a desired distance. Therefore,

the spring force is used to replace the electrostatic force given in this equation since these

forces are ideally equal. The temperature effects then can be added such that:

$$V = \sqrt{\frac{2[k_o - M(2\pi f)^2](d - \Delta z(x,y))}{\varepsilon_o[1 - \Delta f_{FL}]} \tan\left[\frac{(z_o - d - \Delta z(x,y) - \delta)^2}{w_x w_y[1 + \alpha_M(T - T_o)]^2}\right]} \qquad (3.82)$$

where

$$k_o = \frac{k}{[1 + \alpha_F(T - T_o)]}, \qquad (3.83)$$

$$\delta = \left[\frac{[k_o(d - \Delta z(x,y)) + Mg]w_x w_y}{(6.4)Et^3}\right][1 + \alpha_M(T - T_o)], \qquad (3.84)$$

$$\Delta z(x,y) = \Delta z_{CT}(x,y) + \Delta z_{SD}(x,y) \qquad (3.85)$$

and where $\alpha_F$ and $\alpha_M$ are the coefficients of linear expansion for the flexures and mirror

respectively, $d$ is the desired deflection distance at some location $(x,y)$ along the surface

of the mirror, and $z_o$ is the height of the hinges when no voltage is applied. This model is

valid as long the desired deflection distance of the mirror is greater than the surface

deformation due to gravity at that point. In this case, a complex voltage will be evaluated

since it would require a repulsive force to achieve the desired deflection and the

electrostatic force is not capable of doing so.

# *(IV)* EXPERIMENTAL SETUP AND PROCEDURE

The micromirror devices studied in this thesis were designed in the Very Large Scale Integration (VLSI) Laboratory at AFIT using the Cadence layout editor [21]. The layout files were sent to a commercial foundry which returned the completed dice packed in a photoresist for shipping. After releasing, packaging, and wire bonding these dice at AFIT, the micromirror test structures were characterized using the microscope-based laser interferometer mentioned in Chapter (I). This chapter describes the fabrication process, design considerations, additional micromirror designs, test equipment, experimental procedures, and software analysis used in this thesis.

## *(4.1)* FABRICATION

The micromirror devices studied in this thesis were fabricated by the Microelectronics Corporation of North Carolina (MCNC) using the ARPA-sponsored Multi-User Mems ProcesS (MUMPS) fabrication service. This is a three-layer polysilicon process which uses silicon dioxide as the sacrificial material and an initial layer of silicon nitride for substrate isolation. The first polysilicon layer, Poly-0, is non-releasable and is used for address electrodes and local wiring while the second and third layers, Poly-1 and Poly-2 respectively, can be released to form mechanical devices.

The MUMPS process allows metal to be deposited only on the top of Poly-2. The metal is the last deposited layer of the fabrication process since it is non-refractory and the polysilicon layers are annealed at 1100°C to reduce stress. In the past, MCNC has experimented with various metals in this process. In the most recent fabrication run, MUMPS6, gold (with a thin adhesion layer of chromium) was used to reduce corrosive damage to reflective surfaces and to allow for easy and reliable wire bonding.

The MUMPS fabrication process is well defined and uses several structural and sacrificial layers, each having a very specific target thickness that is distinct to each layer. Although each fabrication run produces actual dimensions which may vary slightly from those shown below, each layer remains the same relative thickness in proportion to the other layers. Figure 4-1 illustrates the various layers of the MUMPS fabrication process in order of deposition with their corresponding target thicknesses.
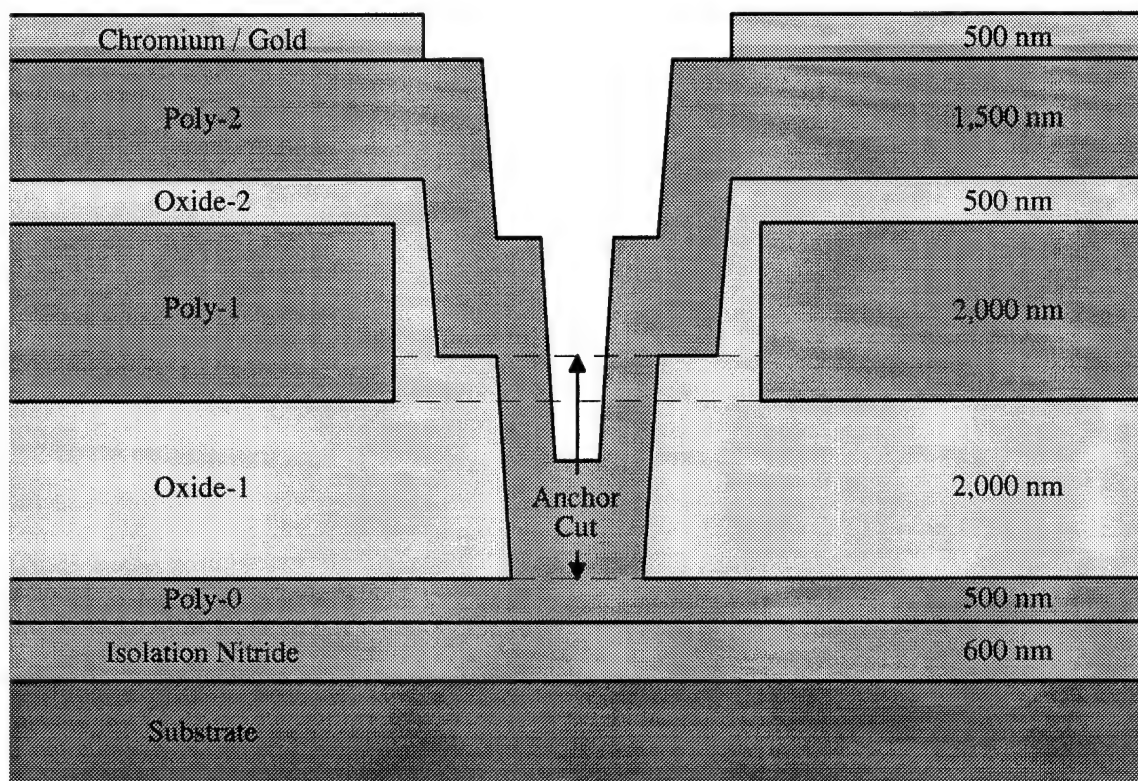


**Figure 4-1.** Proportional cross-section of MUMPS layers with each target thickness.

Due to the deposition of these layers, the foundry provides several design rules for the layout of MEMs devices such as a minimum spacing of 2 μm between Poly-2 structures. Although the suggested rules for a variety of layers and combinations thereof may vary, it has been found that 2 μm satisfies most of the rules such as the margin around the inside of a Poly-2 structure in which gold can not be deposited. Likewise, the flexure width of all micromirror devices was designed to be 2 μm which is the minimum allowed.

The fabrication process is illustrated using a simple device consisting of a single metallized mirror, one flexure, and one support post. Note that this design does not use the second polysilicon layer, Poly-1. Figure 4-2(a) shows a cross-section of this design prior to metallization. After fabrication, the sacrificial layers must be etched away to release the mechanical layers. Figure 4-2(b) shows the released structure after the metal has been deposited and the sacrificial material has been removed.



(a) Annealed Micromirror Device        (b) Released Micromirror Device
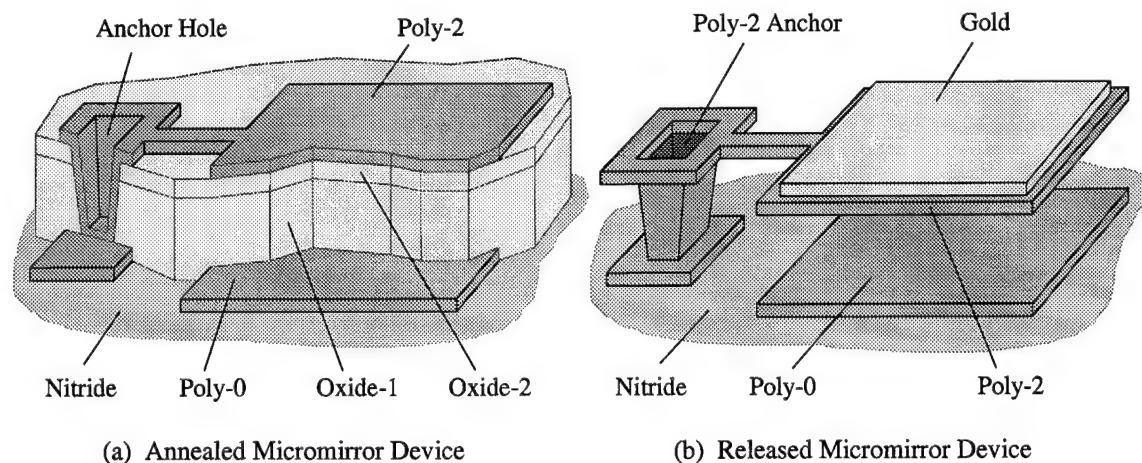
**Figure 4-2.** Fabrication process of a basic cantilever micromirror device.

Designs utilizing Poly-1 have the second polysilicon layer between the two oxides. This layer, however, is much thicker than Poly-2 and cannot be used to support metallized surfaces. Therefore, Poly-2 is used to form the flexures of the micromirror devices due to its greater flexibility. Other micromechanical devices are fabricated with this same process using various combinations of these structural and sacrificial layers.

To fabricate micromechanical devices, certain "negative" layers must be utilized to form the necessary support for the structures. The MCNC fabrication process uses an Anchor layer which actually specifies the removal of a material rather than the deposition of another. An Anchor cut will remove all the oxide spacer beneath it so that the next polysilicon layer deposited will be attached to Poly-0. Figure 4-2(a) shows a cross

section of the resulting support post which illustrates the effect of the Anchor cut. Likewise, Poly-Via cuts exist for removing portions of individual oxide layers.

The die containing the unreleased devices are delivered from MCNC with a protective coating of photoresist which is stripped off in a three minute acetone bath. The die are then rinsed in deionized water for two minutes. The etch that releases the micromirror devices is a two minute dip in concentrated (49%) hydrofluoric acid. The die are then rinsed for five minutes in gently stirred deionized water. After the rinse, they are soaked for five minutes in 2-propanol and baked dry in a 150°F oven for five minutes. The propanol displaces the water and evaporates when the die are removed from the rinse. Propanol also has a lower surface tension than water which prevents the pull-down and destruction of the released polysilicon structures.

After the devices are released, the die are placed in standard integrated circuit packages of various sizes depending on the number of bonding pads designed on a particular die. Once the die are glued within the package frame, bond wires are attached between the pads on the die and the wire pads located around the frame of the package which are connected to the package pins. After wire bonding, a schematic diagram must be generated which relates each pin to the devices connected to it. Once the schematic diagram is completed, the micromechanical devices on the chip are ready for testing.

The mirrors are tested on a probe station before the wire-bonded structures are tested on the laser table. This ensures that the expected range of address potentials will not damage the packaged devices since these are much harder to replace. The mirrors are tested with an electrometer rather than a regular power supply. This allows a large range of drive voltages and the low source current of the electrometer prevents the mirror flexures from burning out if the mirror is pulled into contact with the address electrode. More recent mirror designs have bumps fabricated in the mirror to prevent such contact when the mirror is fully deflected.

## (4.2) DESIGN CONSIDERATIONS

The square FBMD micromirror arrays were designed to be individually addressed in order to test a wide variety of device behavior. The micromirrors tested contain only eight devices arranged in a 2×4 array due to extensive routing difficulties incurred using larger arrays. The address electrodes are limited to the lowest polysilicon layer, Poly-0, and running address lines to the micromirror devices inside larger arrays requires some of the area that would otherwise be used for active devices. Eventually too much area would be devoted to wiring and not enough would remain for micromirror devices.

Another design consideration is the effect the underlying wires have on the topology of the upper layers. The thin films used in the MUMPS process conform closely to the topology of the layers below them.
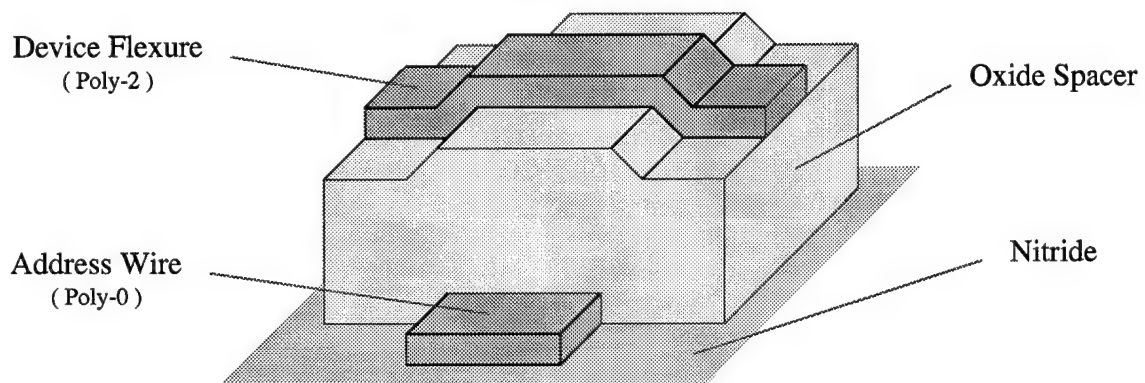


**Figure 4-3.** Conformal effects of deposited layers on surface topology.

The uneven topology created by masking Poly-0 address wires adversely affects the surface uniformity of the flexures and reflective surfaces of the micromirrors. Figure 4-3 illustrates these conformal effects using a portion of a flexure from a micromirror device in which the flexure conforms to the address wire that is routed below it. Such effects change the physical properties of the flexures and alter the behavior of the device. Likewise, an uneven topology on the reflective surface of the device due to conforming

layers may cause adverse effects during operation or complete device failure in which the desired response is not observed or the device is locked in a stationary position.

To maintain uniform operation of the square FBMD, dummy Poly-0 address wires were added beneath the flexures of each micromirror device. These wires are identical to the actual address wire connected to the electrode. This is to ensure that all four flexures behave exactly the same since they all posses the same geometric design and topology. Therefore, the device should maintain its phase-only characteristic since the identical flexures will exhibit the same deflection behavior for any address potential.
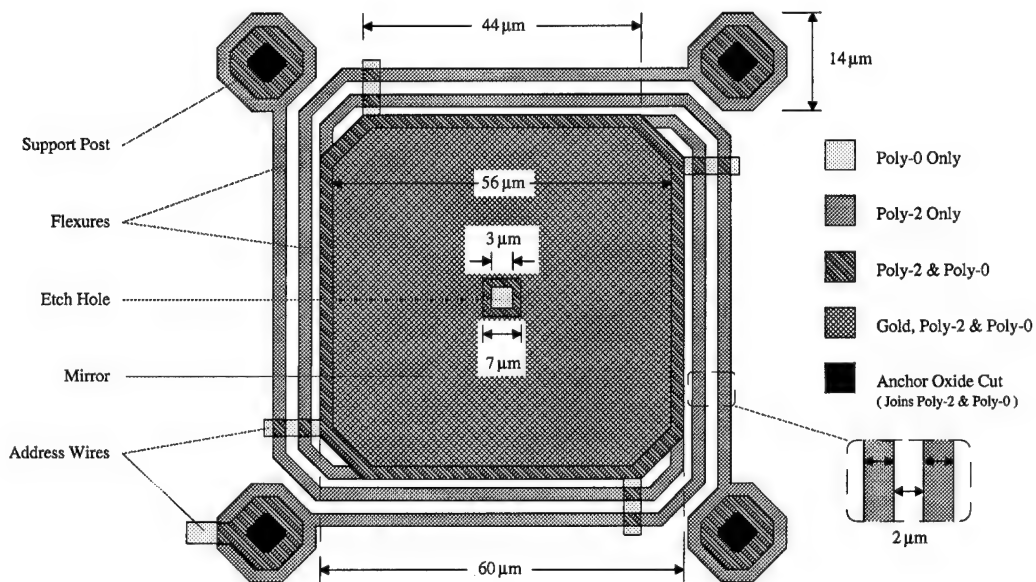


**Figure 4-4.** Overhead view of square FBMD micromirror design as seen in layout editor.

Each Poly-2 flexure crosses an underlying Poly-0 wire twice, once on each side of the micromirror device. The dummy wires are placed in exactly the same location relative to the original wire so that the deformation of each flexure occurs in the same position as the others. Figure 4-4 shows the square FBMD, as observed in the Cadence layout editor, which illustrates the use of the dummy address wires for flexure uniformity [21].

Each of the support posts consists of a layer of Poly-0 bonded with the upper layer of Poly-2 via the Anchor hole. The array of micromirrors is created by simply joining

additional devices at the corners such that adjacent devices share the support posts between them. Once joined, the Poly-2 support posts, flexures, and mirrors are all conductive such that only one address wire must be attached to the support posts to supply the ground plane for the entire array.

The most significant design consideration was to make the flexures long enough to keep the drive voltage reasonably low. Also, since the flexures and mirrors are made from the same polysilicon layer, another consideration was to minimize the layout area required for the flexures so the reflective surfaces could be packed closely together. Thus, a tradeoff exists between the lower drive voltage and greater optical efficiency.
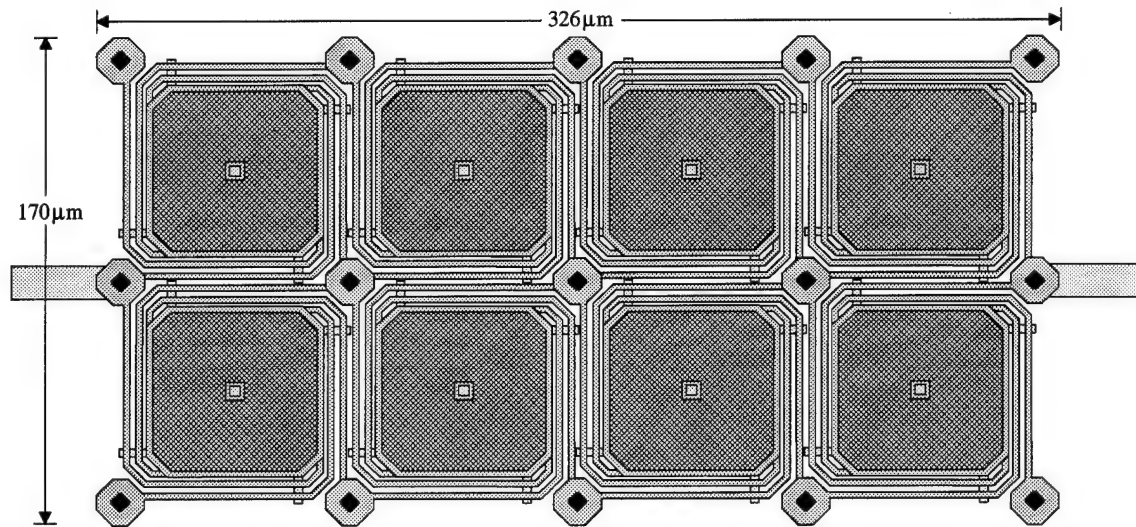


**Figure 4-5.** Experimental array of square Flexure-Beam Micromirror Devices.

The corners of the square FBMD had to be rounded to allow for the maximum density of devices and support posts. This design successfully achieves the desired lower address potential while maximizing the amount of reflective surface available to each micromirror device. When packed together, the devices use all the available space allowed by the design rules and offer large reflective surfaces. The micromirror devices in the array shown in Fig. 4-5 can be individually addressed along the outside of each device. This allows for experimental measurements of cross-talk effects in addition to the

standard deflection and deformation observations. Each array has two ground electrodes attached to the support posts at each end.

The size of the square FBMD was chosen as the largest that could be reliably released without requiring more than one etch hole in the mirror surface. The design rules specify that the release etch can safely remove the oxide spacer as far as 20-25 μm within a device without damaging the structure. Without etch holes, however, the device would require a longer release etch which may stretch the margin of safety for the structure. Additionally, larger mirrors tend to deform in the center due to their weight and larger separation distance between support posts. To maximize the optical efficiency of the device, the widths of the flexures and the gaps between adjacent flexures are 2 μm which is the smallest dimension allowed by the design rules.

## (4.3) *ADDITIONAL MICROMIRROR DESIGNS*

Additional square and hexagonal FBMD designs were fabricated along with the initial device described above. Similar devices were designed with a combination of geometric variations to test the effect of geometry on device behavior. Arrays of square FBMDs were designed which contain mirrors of varying sizes and flexures of varying lengths. The size of the mirror determines the significance of such effects as cross-talk, fringing losses, surface deformations, and resonant frequency. Likewise, the length of the flexures significantly impacts the voltage required to fully deflect the device. The various device geometries offer a wide range of experimental data for the analysis of FBMD behavior. These and all other devices are presented in greater detail in Chapter (V) along with the fabrication results of each micromirror design.

Other devices were designed for the purpose of gaining a better understanding of micromirror devices in general. Although these designs are not the focus of advanced modeling, their behavior can be predicted using the same physical principles. Among the

other designs were numerous styles of Cantilever devices as well as a new style of Axial rotation device in which the support post is located in the center of the device.

The Cantilever micromirror devices, shown in Fig. 4-6(a), are designed to bend along one flexure supporting the mirror. One support post and ground wire are shared by three devices which can be actuated independently.



(a) Cantilever Micromirror Devices          (b) Axial Micromirror Device
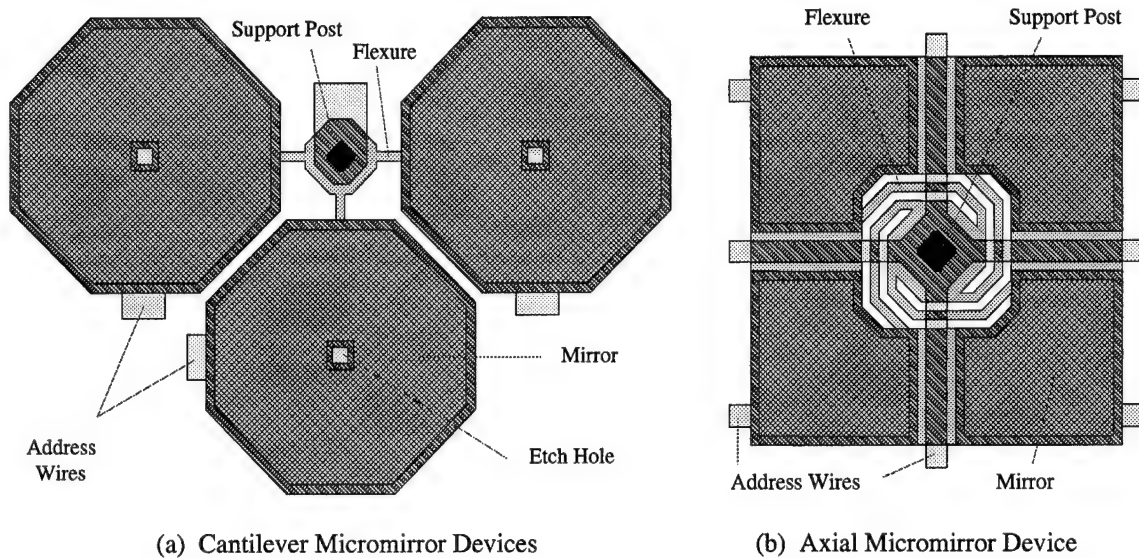
**Figure 4-6.** Overhead view of two styles of additional micromirror designs.

These devices are similar to those reviewed in Chapter (II) in which the operation of the Cantilever device is described. This design of micromirror devices was fabricated with a variety of flexure and mirror sizes to again test the effect of geometry on device behavior.

The Axial rotation device, shown in Fig. 4-6(b), is a new micromirror design in which the support post and ground electrode are located at the center of the device. Each device has four individually actuated address electrodes located under each corner of the mirror. This allows the mirror to bend toward any direction along the surface of the substrate by applying varying potentials to each of the address electrodes according to the desired direction and amount of deflection. If the same potential is applied to all four address electrodes, the mirror deflects downward in the same manner as the FBMD.

4-9

*(4.4)* EXPERIMENTAL SETUP

The experimental setup is shown in Fig. 4-7 in which a microscope-based laser interferometer is used to combine a fixed reference beam with the object beam reflected from the micromirror device under test. An incident laser beam is split into reference and object beams and each is allowed to travel some distance before they are joined together at an aperture creating an interference pattern.
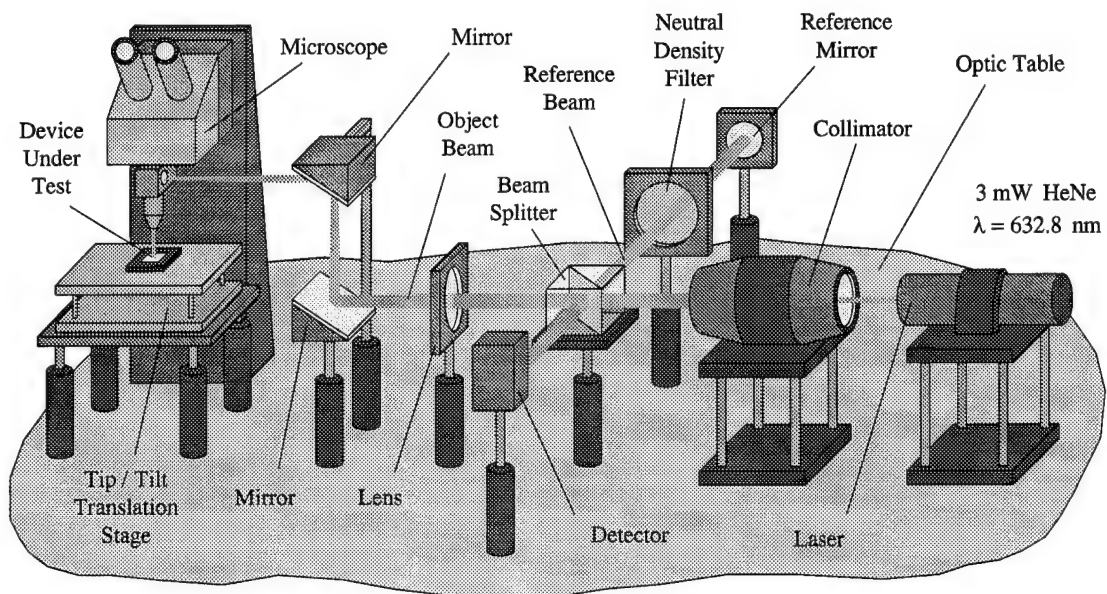


**Figure 4-7.** Experimental setup of the microscope-based laser interferometer.

A photo-detector is placed behind the aperture to measure the relative intensity of the interference pattern and produce a current linearly proportional to the pattern intensity. A neutral density filter must be added along the reference beam path to reduce its intensity since some of the object beam intensity is lost when reflected from the microscope optics and micromirror device under test. The reference and object beams must be maintained at the same intensity in order to maximize the interference signal seen by the detector.

The collimator is required to expand the initial laser beam. Basic optics theory suggests that the diameter of a beam focused by a lens is inversely proportional to its

diameter before passing through the lens. Therefore, as the collimated beam expands, the lens can focus the object beam to a smaller spot size on the device, allowing for more precise measurements along the surface of the mirror. The spot size is less than 4 μm in diameter and the translation stage can move in the *(x,y)* plane in 0.1 μm increments which allows for measurements of displacement at any location along the mirror surface. Deformations and tilting of the device can be observed by comparing the behavior at one point on the mirror to similar measurements taken elsewhere along the mirror surface.

The schematic diagrams of the drive signal generator and output transimpedance amplifier of the laser interferometer are shown in Figs. 4-8(a) and 4-8(b), respectively:



(a) Drive Signal Generator          (b) Output Transimpedance Amplifier
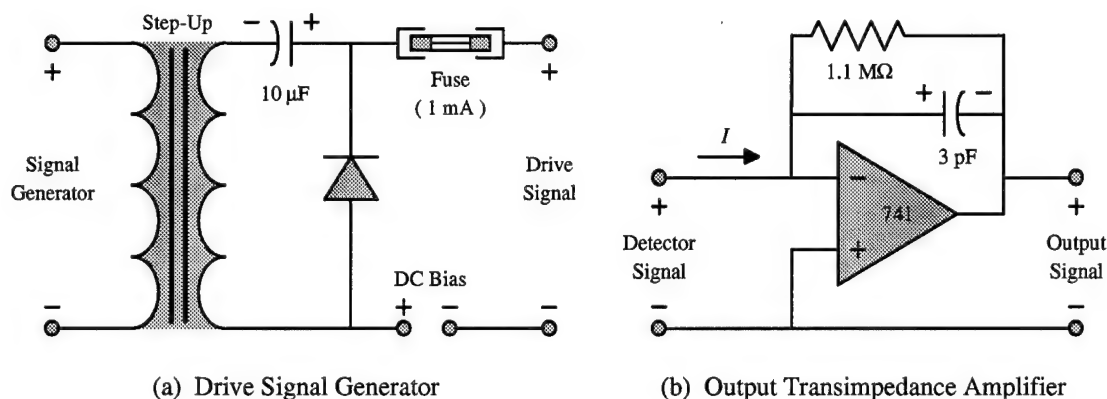
**Figure 4-8.** Schematic diagrams of the input and output signal processors.

The drive signal generator actuates the micromirror device and the output transimpedance amplifier converts the current produced by the photo-detector to a relative voltage. Both signals are sent to an oscilloscope which graphically displays them as the input and output waveforms of the device. The oscilloscope is connected to a computer via a GPIB cable such that the traces can be captured and analyzed using customized software.

In the drive signal generator, a step-up transformer is used for voltage amplification because many devices require actuation potentials much greater than can be produced by a standard signal generator or operation amplifier circuit. At low frequencies, below 5 kHz, the transformer exhibits no significant hysteresis or saturation

that would otherwise add noise to an ideal sine wave. A fuse is placed in the line of the drive signal to protect the devices under test. In the event that a mirror is pulled into contact with the address electrode, the fuse will prevent a rush of current that would normally destroy the device. If desired, an additional DC bias can be added to shift the drive signal further above the standard operating range.

The capacitor and diode form a voltage shifter in which a DC offset is added to the sine wave from the transformer that is equal to the peak positive voltage. The result is a shifted sine wave which varies between zero and some new maximum voltage equal to the peak-to-peak voltage of the original signal less the voltage drop of the diode, $V_D$.



(a) Negative Input Voltage    (b) Positive Input Voltage    (c) Input and Output Signals
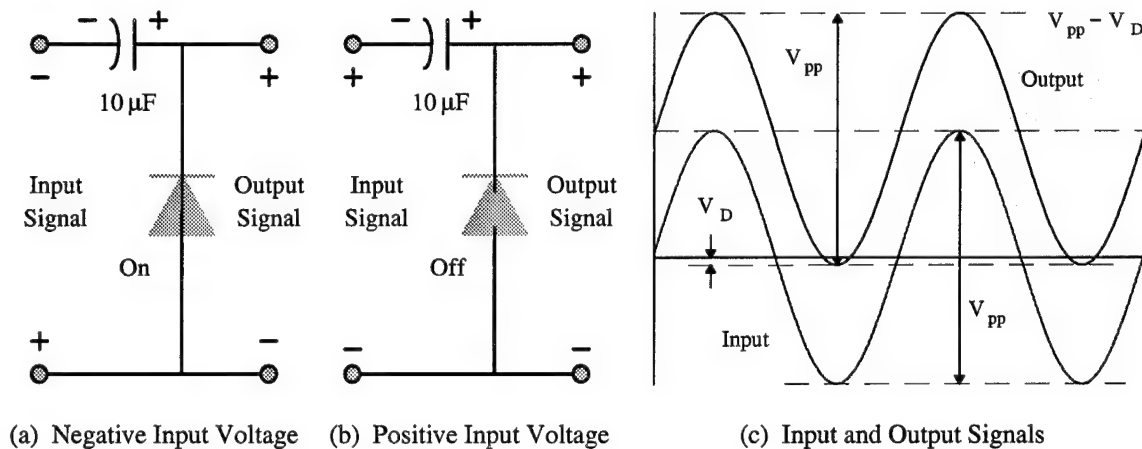
**Figure 4-9.** Two-stage operation and signal manipulation of the input voltage shifter.

When the input signal is negative, as shown in Fig. 4-9(a), the diode is on which charges the output node of the capacitor. When the input signal switches polarity, as shown in Fig. 4-9(b), the diode cuts off and the output signal is shifted by the residual voltage on the output node of the capacitor. The charging and shifting cycle repeats for every period of the input signal. This design was verified using the SPICE® simulation software package [22] in which this circuit produces the output signal shown in Fig. 4-9(c) which swings from a new minimum voltage, $-V_D$, to some new peak voltage, $V_{pp} - V_D$. The effect of the diode voltage drop is actually desirable because the step-up transformer

produces a slight deformation in the sine wave at the low voltage peak. Therefore, the voltage margin produced by $V_D$ helps eliminate noise from the positive actuation signal.

The transimpedance amplifier shown in Fig. 4-8(b) uses a capacitor to reduce noise in the signal from the photo-detector. This circuit is a single time constant low-pass filter in which the resistor and capacitor have a cutoff frequency of $f_c = 48.2$ $kHz$ for the values shown [23]. Since the devices are actuated at very low frequencies, $f << f_c$, the output signal is amplified while the noise is shorted around the feedback resistor.

Along the path of the object beam, the path length increases in relation to the vertical displacement of the device under test. Figure 4-10 illustrates this relationship.
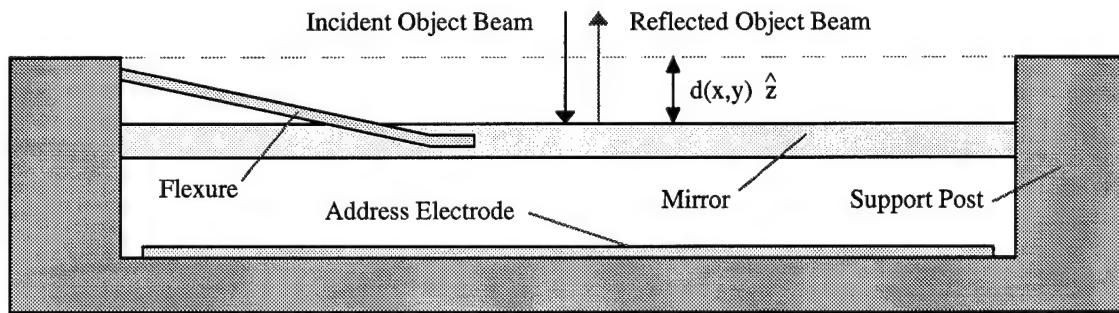


**Figure 4-10.** Beam path extension as a function of mirror displacement.

It is obvious that the beam must travel an extended distance equal to twice the downward mirror deflection, $d(x,y)$, which results in a phase change of the reflected plane wave relative to the reference beam. It is this relative phase change that creates the interference pattern whose intensity is measured by the detector.

Using a periodic drive signal and knowing the exact wavelength of the laser beam, a continuous sample of the detector output signal yields an accurate measurement of the displacement of the micromirror surface. Comparing this displacement waveform with the input signal yields the response characteristics of the device in which the measured deflection of the micromirror is plotted against its corresponding address potential [6].

Shown in Fig. 4-11 is the modulated phase representation of the combined reference and object beams, $\bar{R}$ and $\bar{D}$ respectively. The resulting interference signal, $\bar{S}$, is the vector sum of these beams. At point A, the beams are $\pi$ radians out of phase. It is at this point that the signal vector is minimized and the minimum intensity is observed by the detector. Similarly, at point B, the beams are exactly in phase with each other. At this point, the signal vector is maximized and the maximum intensity is observed.
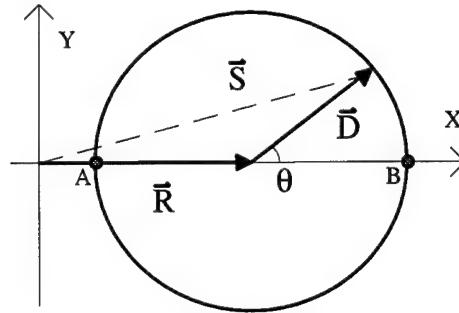


**Figure 4-11.** Relative phase of reference, $\bar{R}$, and object, $\bar{D}$, beam interference [6].

The intensity of the interference pattern as seen by the detector is given by:

$$I = \left|\bar{S}\right|^2 = \left|\bar{R} + \bar{D}\right|^2 \tag{4.1}$$

Where the reference and object beams, $\bar{R}$ and $\bar{D}$ respectively, are represented as:

$$\bar{R} = \hat{x}R, \qquad \bar{D} = \hat{x}D\cos\theta + \hat{y}D\sin\theta \tag{4.2}$$

The observed intensity as a function of phase difference, $\theta$, is then found to be:

$$I = \left|\hat{x}(R + D\cos\theta) + \hat{y}D\sin\theta\right|^2 = R^2 + 2RD\cos\theta + D^2 \tag{4.3}$$

The minimum and maximum intensities observed by the detector, $I_{min}$ and $I_{max}$, are found by evaluating Eq. (4.3) with $\theta = \pi$ and $\theta = 0$ radians, respectively:

$$I_{min} = R^2 + 2RD\cos\pi + D^2 = R^2 - 2RD + D^2 \tag{4.4}$$

$$I_{max} = R^2 + 2RD\cos0 + D^2 = R^2 + 2RD + D^2 \tag{4.5}$$

These intensities, $I_{min}$ and $I_{max}$, are measured constants of the experimental system. Treating them as such, Eqs. (4.4) and (4.5) reduce to two unknown variables, $R$ and $D$.

Solving these equations simultaneously yields the amplitude values of the intensities of the reference and object beams.

$$R = \frac{\sqrt{I_{max}} + \sqrt{I_{min}}}{2}, \qquad D = \frac{\sqrt{I_{max}} - \sqrt{I_{min}}}{2} \qquad (4.6)$$

Substituting these into Eq. (4.3) and solving for $\theta$ yields an equation for phase difference as a function of observed intensity, $I$.

$$\theta = \arccos\left(\frac{2I - I_{max} - I_{min}}{I_{max} - I_{min}}\right) \qquad (4.7)$$

If the phase data is calibrated such that the phase is zero when no address potential is applied, the measured deflection distance of the mirror becomes:

$$d(x, y) = z_o - z_m(x, y) = \frac{\lambda}{2}\left(\frac{\theta}{2\pi}\right) \qquad (4.8)$$

where $\lambda$ is the wavelength of the incident laser beam. This equation is used to record displacement distances corresponding to a domain of electrode voltages.

## *(4.5)* *SOFTWARE ANALYSIS*

The first step in gathering and analyzing the data is to capture the input and output signal traces from the oscilloscope. The LeCroy 7200 oscilloscope, used in these experiments, has the capability to export data via a GPIB cable to a standard personal computer equipped with a GPIB interface. The software necessary to do so is included with the oscilloscope manuals and consists of two main programs [24]. First, the *ACQUIRE.EXE* utility captures all traces which are visible on the screen of the oscilloscope and saves them as binary data files. Finally, the *WAVETRAN.EXE* utility converts the binary files into ASCII text files and generates a separate header file containing important information about the current oscilloscope panel settings such as the voltage versus time spans and the total number of points captured.

The number of points used in sampling the traces on the oscilloscope can be selected according to the capabilities of the software used in processing the data. The discrete signal-to-noise ratio improves as the number of sample points increases until some critical number of points where the software can no longer process extremely long arrays of real numbers. The optimum number of data points per acquired signal trace was determined to be 4,000 points for either the input or output waveforms.

Once the data is captured from the oscilloscope and converted to ASCII text files, the traces can be loaded into a standard spreadsheet using a comma-separated-variable file designation. Figure 4-12 shows typical input and output waveforms.
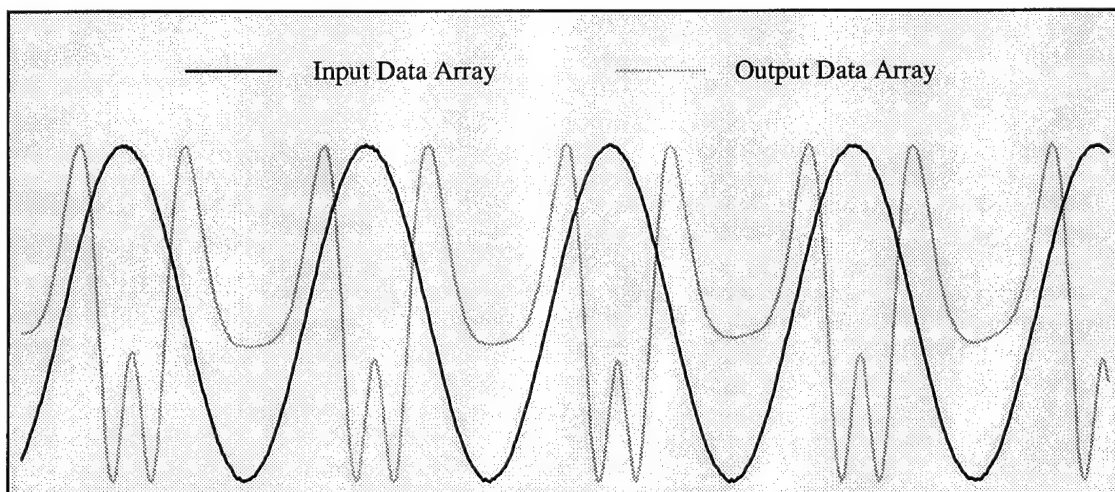


**Figure 4-12.** Data arrays of input and output signals captured from the oscilloscope.

In order to improve the signal-to-noise ratio of the setup and to remove noise associated with drift in the interference pattern, it is necessary to capture between four and six periods of input and output traces. Once certain information is gathered from the original array, these periods will be averaged together to remove noise distinctions between them.

A significant problem in the analysis of the data arrays is the effect of noise from the drive signal generator on an otherwise ideal drive signal. In order to successfully process the input and output signals, it is necessary to identify the indices at which the

maximum and minimum drive voltages are located in the data array. Unfortunately, the signal noise prevents simply scanning the array for the largest and smallest values since their index may not correspond to those of an ideal sine wave.

The regions of the input signal in which the slope is nearly zero are dominated by noise whereas the regions of large positive or negative slopes are dominated by the sinusoidal drive signal. Therefore, the input array is scanned for its maximum and minimum values solely to determine the midpoint line which is their numerical average. Now, the input array is scanned for the index of each midpoint and taking the average of the points between every other index produces the number of points per period, $N_{Period}$. As shown in Fig. 4-13, the indices of the maximum and minimum drive voltages can be determined simply by adding or subtracting the appropriate number of one-quarter periods from the index of the corresponding midpoint.
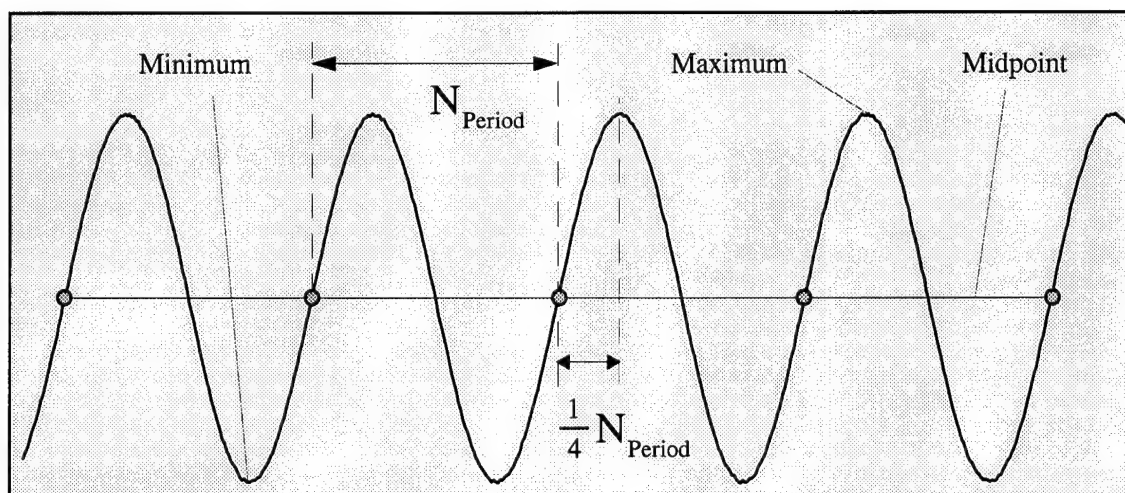


**Figure 4-13.** Data array of input signal waveform illustrating period analysis.

To reduce noise, the input and output waveforms are averaged between all captured periods to form one complete period of data for each array. The exact frequency of the drive signal can be determined using the time span stored in the header file, the total number of points captured, and the number of points per period.

Another problem to overcome in software is to correct for a capacitance delay associated with the output transimpedance amplifier and wire connections for the output signal. The relative peak in the output signal lags the peak of the input signal by some number of points, $N_{Shift}$. This shift is illustrated in Fig. 4-14 and must be corrected in order to establish a direct correlation between the input and output waveforms. First, the index of the peak input voltage is determined as described above and the output signal is evaluated at that index, point A. Then, the indices are found for the first equal value prior and second equal value following the current output sample, B and C, respectively.
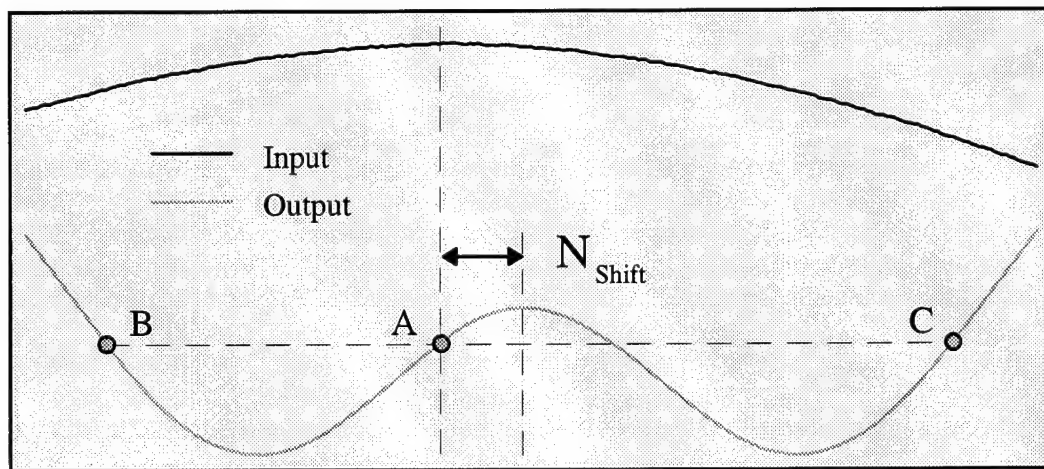


**Figure 4-14.** Input and output waveforms illustrating capacitance delay correction.

Finally, the index of the relative output peak is found to be the numerical average of these two indices, points B and C. The output shift is simply the difference between the index of the input peak and the index of the relative output peak.

The next step in analyzing the data traces is to translate them into a calibrated position within each data array. The data points of the input signal array are translated such that the first data point corresponds to the starting voltage. The signal array starts at the minimum drive voltage, rises to the peak drive voltage at the center of the array, and then returns to the minimum voltage at the end of the array. Likewise, the output signal array is translated according to the input array, and then further translated by $N_{Shift}$ to

correct for its capacitive time delay. The purpose of translating the arrays is to provide a simplified range of data points when plotting the final behavior of the device. The failure to do so results in a segmented plot that is difficult to understand.

Once the input and output arrays have been translated, the relative phase array can be calculated. After scanning the output data array for its maximum and minimum values, Eq. (4.7) is used to determine a relative phase for each data point. Two distinct characteristics of the relative phase array must be corrected. First, a $\pi$ ambiguity in the inverse cosine function creates an error in determining the absolute phase modulation of the device. In addition, the relative phase of the data point corresponding to the resting position of the device is non-zero. This is due to drift in the experimental system in which the object and reference beams are not exactly in phase when the address potential is zero. Figure 4-15 shows the relative phase array along with the translated output array.
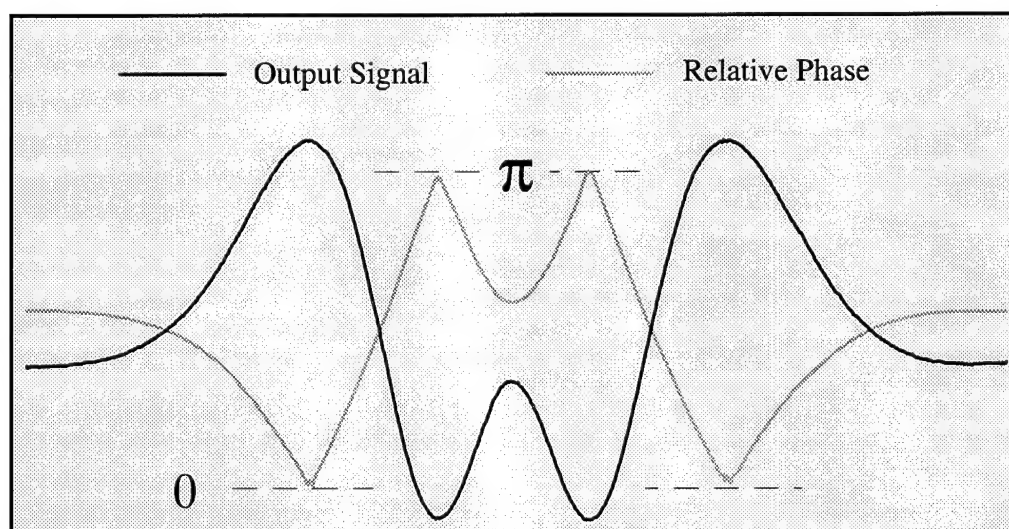


**Figure 4-15.** Relative phase array calculated from the translated output signal array.

The $\pi$ ambiguity in the relative phase array requires additional software correction as well as correction for the non-zero values of the starting and ending points of the array.

To overcome these effects, an absolute phase array is calculated from the relative phase array in which the first point is set equal to zero. The following points are

4-19

recursive in nature such that the evaluation of any point in the absolute phase array is based on the previous value plus some change in the relative phase array. Mathematically, this can be represented with a recursion relation given as:

$$AP_1 = 0, \qquad\qquad AP_{n+1} = AP_n + c_s \left| RP_{n+1} - RP_n \right| \qquad\qquad (4.9)$$

where $AP$ and $RP$ are the absolute and relative phase arrays respectively, the array index range is $1 \leq n \leq N_{Period} - 1$, and $c_s = \pm 1$ depending on the slope of the input data array. When the input voltage is increasing, the index, $n$, is less than half $N_{Period}$ and $c_s = 1$ since the phase is also increasing. Likewise, $c_s = -1$ for the second half of the array since the phase decreases along with the input voltage. Figure 4-16 illustrates these results.
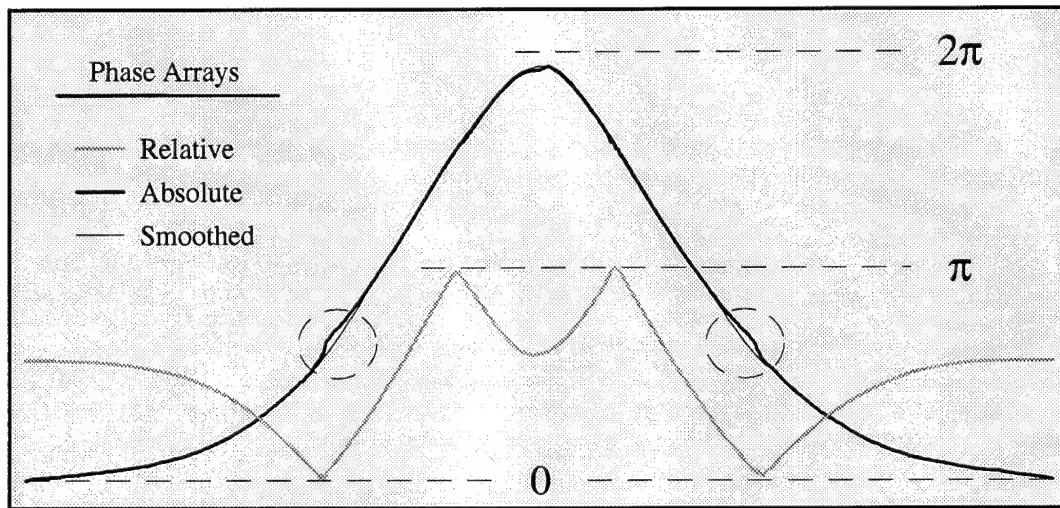


**Figure 4-16.** Absolute phase array calculated from relative phase array.

The absolute phase array is smoothed with a standard box algorithm using linear regression in which a point in the array evaluated according to the best-fit line formed with its surrounding points. The number of points used in the algorithm is quite significant relative to the change in the output array. Various plots of the effects of this smoothing algorithm are attached in Appendix (E) which compare the outcome of several waveforms using different numbers of points. The circles shown in Fig. 4-16 highlight the regions of the absolute phase array in which the noise of the relative phase array has

produced some erroneous characteristics. The smoothed phase array partially corrects these errors and reduces compounding noise effects as further calculations are made.

The last step in developing the characteristic behavior of the FBMD is to calculate the deflection of the device from the smoothed phase array. Using Eq. (4.8), the deflection array is calculated and, when plotted against the original input drive signal, yields the behavior characteristics of the device. Figure 4-17 illustrates this result.
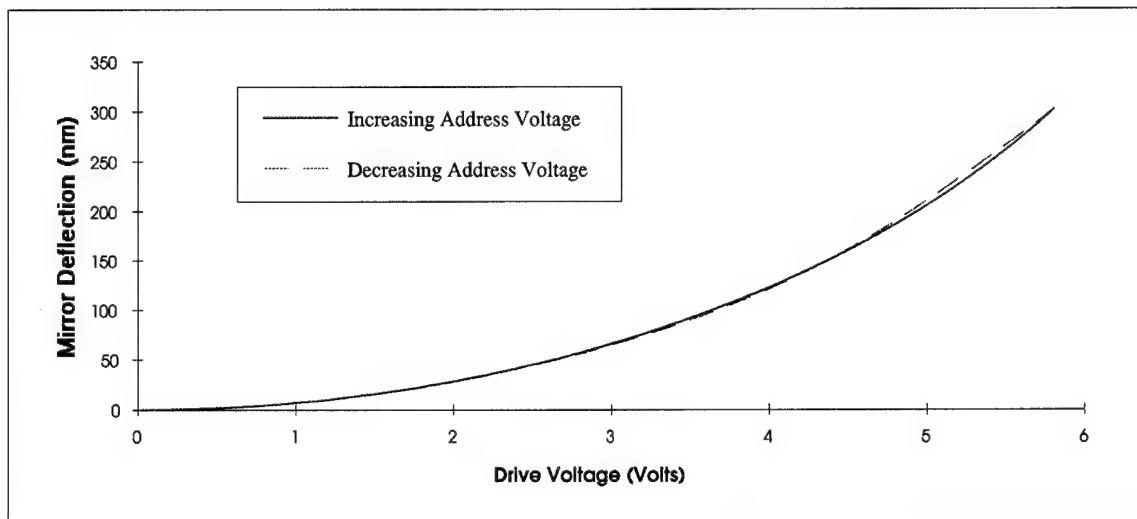


**Figure 4-17.** Plot of device behavior for increasing and decreasing address potentials [6].

Since no significant hysteresis effects are present, the increasing and decreasing potential curves can be averaged together to form one behavior curve. It is this behavior curve that can be used to operate the device according to a desired deflection. The same procedures are followed to obtain quantitative data for specific devices in which a desired deflection can be achieved by applying the corresponding address potential.

The software to execute these procedures was written in the Pascal programming language using a standard Turbo Pascal® editor [25]. The programs used in the acquisition and analysis of the data are designed to operate in the MicroSoft Windows® environment such that the data can be immediately observed in the MicroSoft Excel® spreadsheet [26]. Printed copies of this software are included in Appendix (A).

# (V) RESULTS

The experimental results of this thesis are very similar to the theory and experimental design presented in Chapters (III) and (IV), respectively. It was found that the fabricated devices behave very similar to expected and are very well characterized by the models developed to describe their behavior. This chapter presents the fabrication results of each micromirror device compared to its layout design and compares the experimental data collected with the microscope-based laser interferometer to the theoretical models developed for each device. The effects of various parameters and operating conditions on the behavior of micromirror devices are also presented.

## (5.1) FABRICATION RESULTS

The fabrication results of the micromirror devices in this thesis were outstanding in the sense that all devices functioned exactly as designed. The quality of the fabrication process appears to be quite high as can be seen in the scanning electron microscope (SEM) micrographs of the devices fabricated by MCNC. The photographs of the devices are shown along with the original editor layout designs so that the effect of the fabrication process can be observed. Enlarged figures are attached in Appendices (C), (D), and (E) which include the SEM micrographs, editor layout designs, and data plots, respectively, so that details of these figures referenced in the text can be more easily observed.

No significant errors or geometric variations in the design layout were observed in the fabricated devices with the exception of the flexures of the hexagonal Flexure-Beam devices. Due to the geometry of the device, portions of at least one flexure of each device are positioned at a thirty degree angle to the coordinate system. The micromirror devices

were designed using a 0.1 μm grid spacing while the foundry used a 0.25 μm spacing in its automated mask fabrication routine. The resulting rounding error produced wider flexures for these portions that were not perfectly snapped into the 0.25 μm grid. As a result, the hexagonal Flexure-Beam micromirror device does not deflect uniformly across the surface of the mirror and requires slightly more address potential than anticipated.

All micromirror designs studied in this thesis were included as part of the MUMPS6 fabrication run. The foundry provides a list of film data for each layer of the fabrication process which includes the actual thicknesses of each layer as well as any residual stress. Table 5-1 lists this data in reverse order of film deposition.

**Table 5-1.** Film data from the MUMPS6 fabrication run provided by the foundry.

| Film | Thickness (nm) | Stress (MPa) | Resistivity (Ω-cm) |
|------|----------------|--------------|--------------------|
| Metal (Cr/Au) | 554 | 30 (T) | $3.39 \times 10^{-6}$ |
| Poly-2 | 1,565 | 5.1 (C) | $2.72 \times 10^{-3}$ |
| Oxide-2 | 523 | - - | - - |
| Poly-1 | 2,022 | 5.1 (C) | $2.58 \times 10^{-3}$ |
| Oxide-1 | 2,015 | - - | - - |
| Ploy-0 | 520 | 19.7 (C) | $1.84 \times 10^{-3}$ |
| Nitride | 621 | 19.2 (T) | - - |

The thickness of each layer is close to the corresponding target thickness described in greater detail in Chapter (IV). All micromirror flexures are made from the Poly-2 layer having a thickness of 1.565 μm which provides one of the necessary dimensions for the spring constant analysis. Since the flexures of every device were designed to be the same width, 2 μm, it is expected that the spring constant will vary between devices as a

function of flexure length. It was found that the width of the flexures was less than designed as a result of an over-etch used by the foundry. Fortunately, this process has the same effect on all flexures such that each device still shares the same flexure width.

### (5.1.1) FLEXURE-BEAM DEVICES

The primary devices of interest in this thesis are the various shapes and sizes of Flexure-Beam micromirror devices. Several sizes of rectangular devices were designed to test the effects of various geometries on the behavior of the device. An array of devices was fabricated in which the flexures of each device are identical to those of the other devices. The only variation between micromirror devices is the size of the mirror:



(a) Editor Layout Design         (b) SEM Micrograph
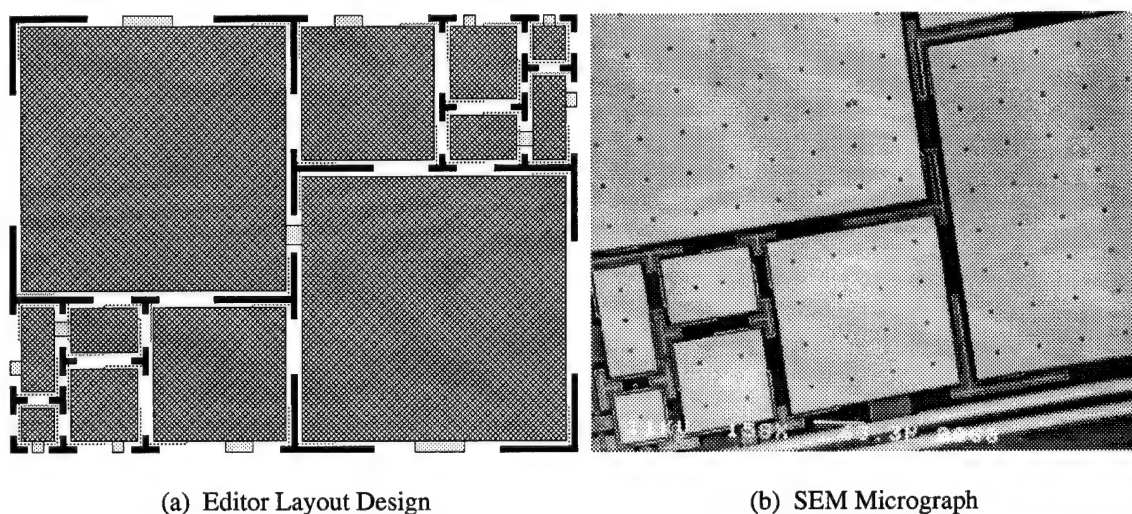
**Figure 5-1.** Layout design and fabricated test array of rectangular Flexure-Beam devices.

The largest of these devices is partially deflected downward at the center of the mirror due to gravity. As shown in Fig. 5-1(b), the edges of this device are deflected upward as a result of this deformation in the surface of the mirror. This observation is useful in evaluating the modulus of elasticity of the mirror, $E_m$, which will be used to determine the magnitude of surface deformation for the remaining devices.

Among the Flexure-Beam micromirror devices fabricated in this thesis, the square device shown in Fig. 5-2 is the primary focus of Flexure-Beam modeling and testing. It is this device that is used to verify the advanced model developed in Chapter (III).



| (a) Editor Layout Design | (b) SEM Micrograph |
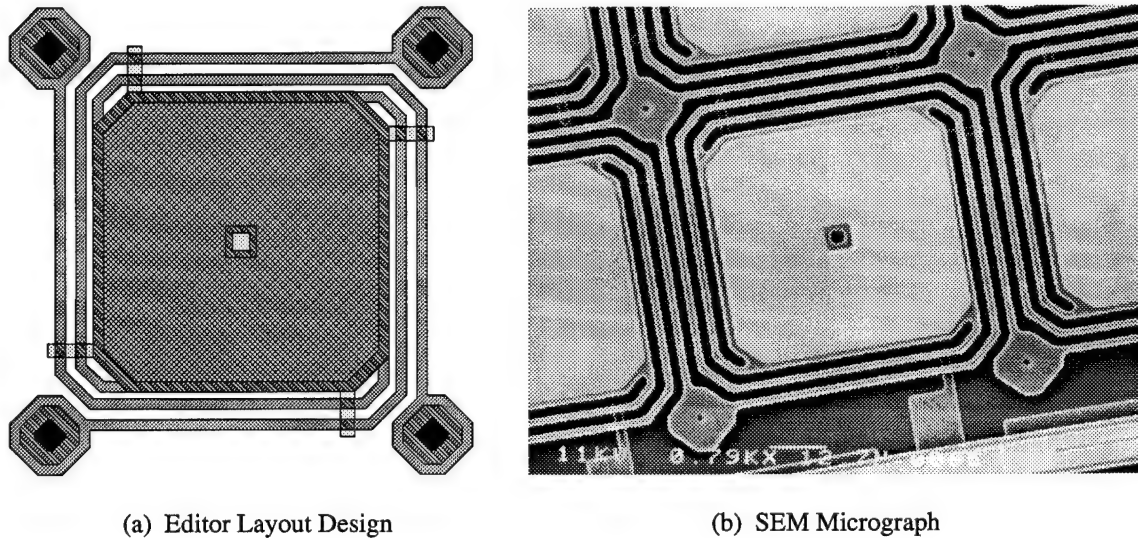
**Figure 5-2.** Layout design and fabricated square Flexure-Beam micromirror device.

The design of this device was described in Chapter (IV) in which the addition of dummy wires was explained as a means of maintaining deflection uniformity among the four flexures. As shown in Fig. 5-2(b), these dummy wires cause a disruption of the surface topology in the Poly-2 flexures at the same relative location as the address wire attached to the address electrode. Since no other discontinuities exist in the flexures, it is expected that this device will deflect uniformly at the four corners of the mirror.

Using the same image of the device under much higher magnification, it was observed that the flexures were much thinner than designed. The flexures were designed with a width of 2 µm, but the foundry uses an over-etch of 200% to remove excess Poly-2 from the wafers. Therefore, the edges of the devices are slightly etched from underneath the oxide that is used to mask the features of mirror and flexures. The ruler on the SEM micrograph showed the width of the flexures to be 1.65 µm which will produce a significantly different response than originally anticipated.

Another of the Flexure-Beam micromirror devices used for model verification is the hexagonal device that was developed as an attempt to maximize the effective area of an array of micromirrors. It was found that geometric properties of a hexagon were most effective for this purpose and allowed the micromirrors to be closely packed relative to each other in the array.



(a) Editor Layout Design                    (b) SEM Micrograph
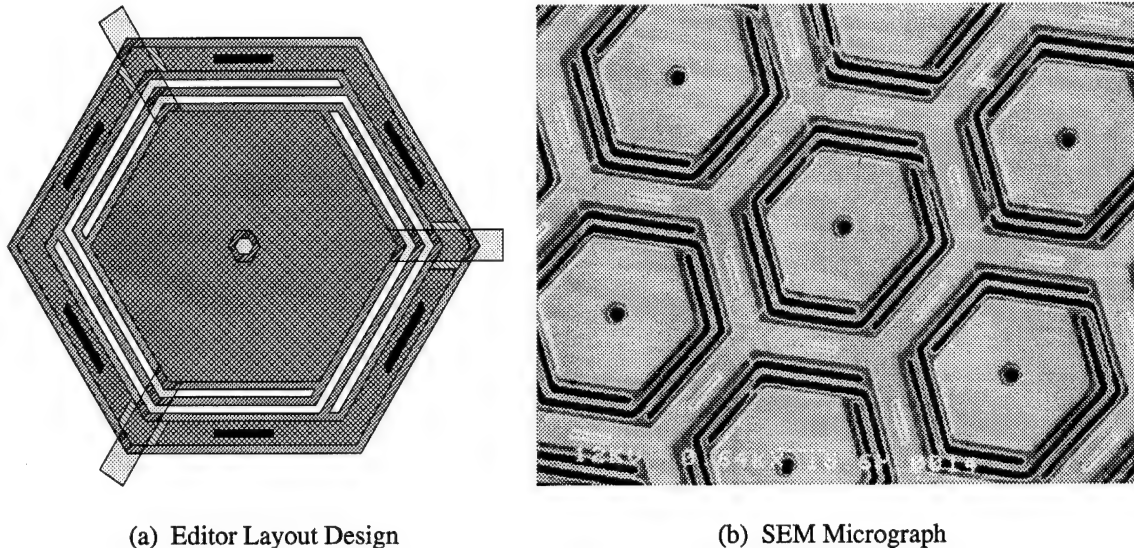
**Figure 5-3.** Layout design and fabricated hexagonal Flexure-Beam micromirror device.

The three flexures of this device were designed to span one-third of the perimeter of the mirror to maximize the use of space surrounding it. Figure 5-3 shows this device which also shows the addition of two dummy wires for flexure uniformity. The reflective surface surrounding each device is used as the support post and maximizes the amount of reflective area of the array.

As shown in Fig. 5-3(b), some of the flexures are poorly fabricated due to the grid spacing error described above. Since the flexure along the right side of the device has two segments at an angle to the coordinate system rather than just one, this flexure will resist the electrostatic actuation of the device more than the other two flexures. As a

result, it is expected that this device will not deflect uniformly, but will tilt away from the corner at which this flexure is attached.

### (5.1.1.1) DESIGN VARIATIONS

The standard Flexure-Beam micromirror device was slightly altered in an attempt to maximize the effective area of an array of devices. In a new design, the support post was placed in the location where an etch hole must normally be placed, thereby using the space more efficiently since the corners of the device no longer require support posts. This Axial rotation device is shown in Fig. 5-4 which illustrates the center support post.



(a)  Editor Layout Design                                  (b)  SEM Micrograph
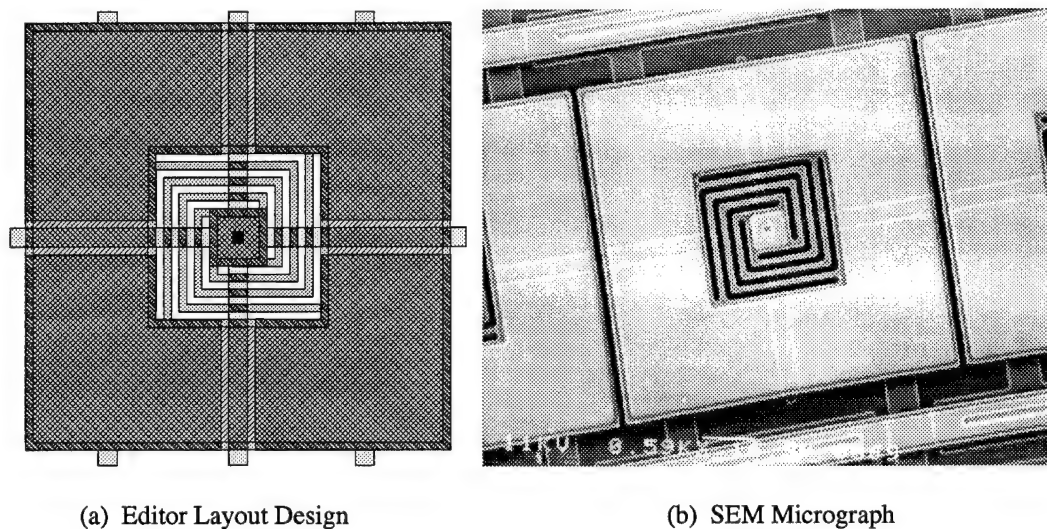
**Figure 5-4.** Layout design and fabricated Axial rotation micromirror device.

In addition, each device has four address electrodes, one beneath each corner of the device. By applying a range of address potentials to these electrodes, the device can be actuated such that its motion combines properties of the Flexure-Beam and Cantilever devices. The device will tilt toward the address electrode at the highest potential or it will deflect downward similar to the Flexure-Beam micromirror device if all four electrodes are at the same potential.

## (5.1.2) CANTILEVER DEVICES

Besides the Flexure-Beam devices, two styles of Cantilever devices were designed and fabricated to test the Cantilever model developed in Chapter (III). The purpose of this modeling is to verify the basic principles used in the advanced model of the Flexure-Beam devices. Since the same principles act on the Cantilever devices, validating the model of their behavior serves to verify the validity of other models as well.

The first style of Cantilever micromirror is the paddle-style device in which the mirror is supported by one flexure which bends downward as the mirror deflects. This is the primary style of Cantilever devices as described in Chapter (II).



(a) Editor Layout Design                    (b) SEM Micrograph
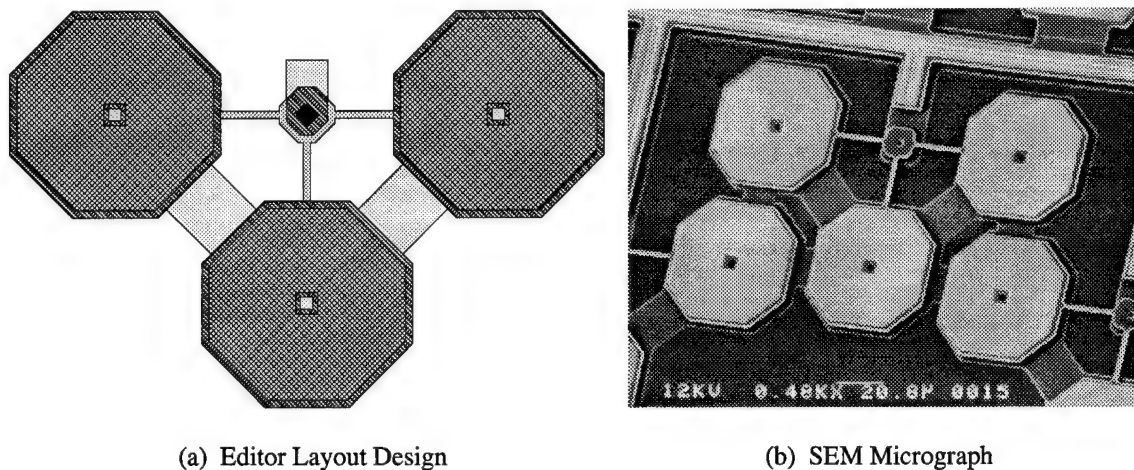
**Figure 5-5.** Layout design and fabricated paddle-style Cantilever micromirror device.

Two test arrays of this device were fabricated in which only the flexure length was altered. As shown in Fig. 5-5, the mirror will tilt away from the support post as it deflects which creates a dependence on position along the surface of the mirror. The length of the flexure determines the address potential that will be required to deflect the mirror to a desired distance at a specific position on the mirror. One array of devices was fabricated with 15 μm long flexures while the second array has 25 μm long flexures. These arrays provide a set of data that describes the effect of the length of flexures.

Another style of Cantilever micromirrors is the torsion-style device in which two flexures support the mirror and are attached along one side of the device. When the device is actuated, it will also tilt to one direction away from the flexures that will twist to provide the necessary deflection.



(a) Editor Layout Design        (b) SEM Micrograph
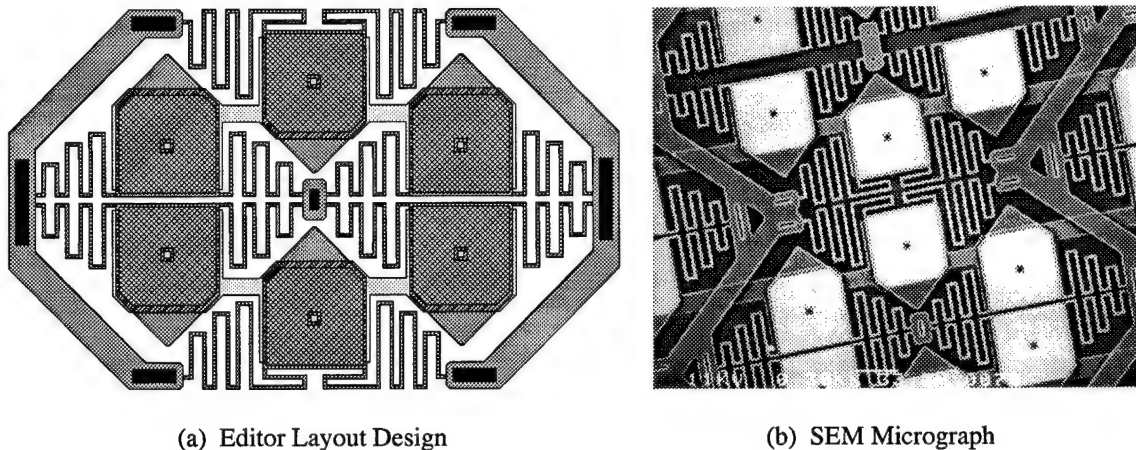
**Figure 5-6.** Layout design and fabricated torsion-style Cantilever micromirror device.

The flexures are designed to rotate in the direction that the mirror deflects to reduce the voltage required for a desired deflection. Figure 5-6 shows the flexures that are folded several times to provide the equivalence of a very long flexure on the paddle-style device.

Another feature of this device is the pointed end of the mirror which serves two purposes. First, the extra weight on the ends of the mirror reduce the voltage required for a desired deflection due to an initial torque on the flexures due to gravity. Second, these points prevent a short-circuit in the event that the device is driven with an address potential that would otherwise pull the end of the mirror into the address electrode. The extension of the end of the mirror is designed to rest against the substrate in the event of such a deflection so that the mirror remains a safe distance above the address electrode.

The torsion-style Cantilever device was also designed with three lengths of flexures to test the effect of the flexure geometry on device behavior. Unlike the paddle-style devices, however, the flexures of the torsion-style device include several corners in

which the flexure is wrapped in a zig-zag pattern. This may additionally affect the characteristic behavior of the device such that the spring constant is not only a function of the length of the flexure, but of the shape as well.



(a) 208.5 μm Flexures      (b) 108.5 μm Flexures      (c) 66 μm Flexures
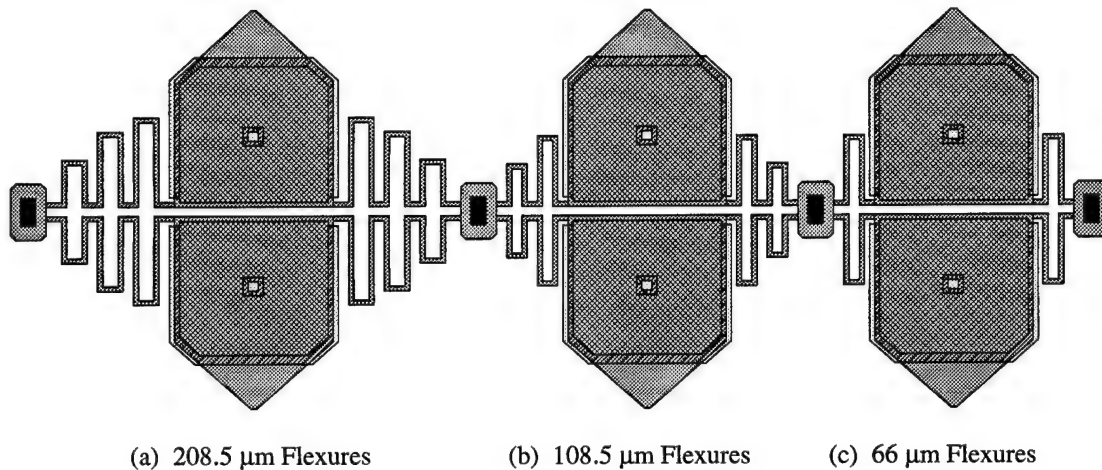
**Figure 5-7.** Torsion-style Cantilever micromirror devices with various flexure lengths.

The different lengths of flexures will help determine the effect of the sharp turns on the behavior of the flexures. Figure 5-7 illustrates three micromirror devices having the same surface area and different lengths of flexures which also shows the number of corners per design. It is not clearly known how these turns will affect the spring constant of the flexures and therefore how the devices will behave.

## (5.2) IDEAL MODEL VERIFICATION

The first step in validating the advance model of the Flexure-Beam micromirror device is to evaluate the ideal model that describes the basic principles involved in the operation of the device. Both the Flexure-Beam and Cantilever devices are used to evaluate their respective models in which the experimental data is fit to the theoretical behavior curves using the spring constants described in Chapter (III). These constants are determined experimentally from the observed behavior of the devices which allows for a

closer fit of the theory. The advanced model, however, requires that the spring constants be determined from the geometry and material properties of the flexures which creates the possibility of discrepancies between the model and observed behavior.

### (5.2.1) FLEXURE-BEAM DEVICES

The behavior curves shown in Fig. 5-8 depict the ideal theoretical model for Flexure-Beam devices given in Eq. (3.19) and the corresponding experimental data for one device of each design. This data was taken from a single square Flexure-Beam device of Fig. 5-2 and two sizes of hexagonal devices of Fig. 5-3 and is shown with the best-fit spring constants for each set of data.
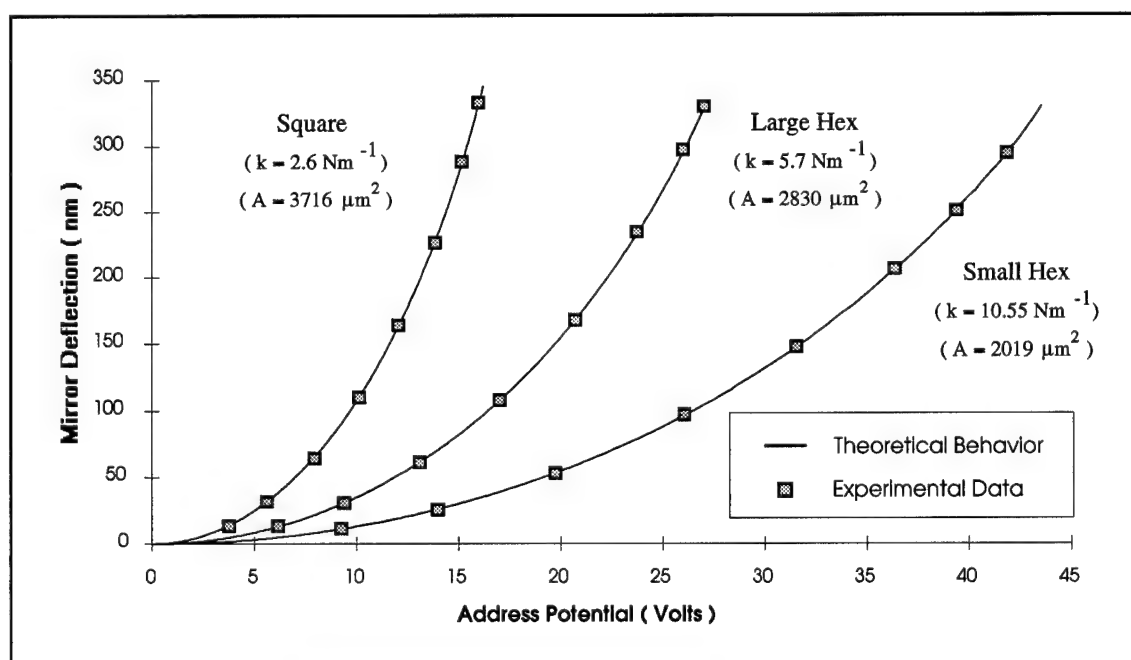


**Figure 5-8.** Ideal characteristic behavior of various Flexure-Beam micromirror devices.

The data was taken at a position on the mirror surface immediately adjacent to one of the flexures to minimize the effects of surface deformations on the data. Therefore, the mirror deflection observed is directly related to the spring constant of the micromirror.

These best-fit spring constants will be used to extract the values of the thin film modulus of elasticity for polysilicon which will be used in the advanced model to predict the spring constants of the flexures given their geometry and material properties.

The ideal theoretical behavior curves in Fig. 5-8 appear to fit the data quite well for each of the three Flexure-Beam devices. It should be noted that the data is simply fit to a curve given by the model which does not verify the model, but only the form of the model in which the square of the voltage is proportional to a third-order polynomial of the deflection distance. In order to use this model, the spring constant for each device must be experimentally measured which defeats the purpose of a model. The advanced Flexure-Beam model serves to remove this requirement of experimental observations.

## (5.2.2) CANTILEVER DEVICES

The analysis of the Cantilever devices designed in this thesis is two-fold. First, the experimental data gathered from both the paddle and torsion-style devices is best-fit to the model by the two constants in Eq. (3.20) in order to verify the basic principles of the model. Second, the torsion-style Cantilever is used to study the effects of right angles on the behavior of the flexures supporting the device. As shown in Fig. 5-7, the three designs of this device have various lengths of flexures that also have various numbers of corners. For devices fabricated on the same chip, the material properties are the same for each device such that the relative spring constant becomes a function solely of the length of the flexure. Therefore, the data from one device can be normalized to that of another based on the two lengths of the flexures. Any significant discrepancies in the behavior of the flexures can be attributed to the effect of sharp corners along its length. In addition, the ideal Flexure-Beam model is also used to describe the observed data for a particular Cantilever device in order to illustrate the distinctness of the Cantilever behavior curve.

The behavior curves shown in Fig. 5-9 depict the ideal theoretical model for Cantilever micromirror devices given in Eq. (3.26) and the corresponding experimental data. This data was measured at a position on the mirror surface at the far end of the mirror opposite the flexure on the paddle-style Cantilever devices of Fig. 5-5 and is shown with the best-fit spring constants for both sets of data.
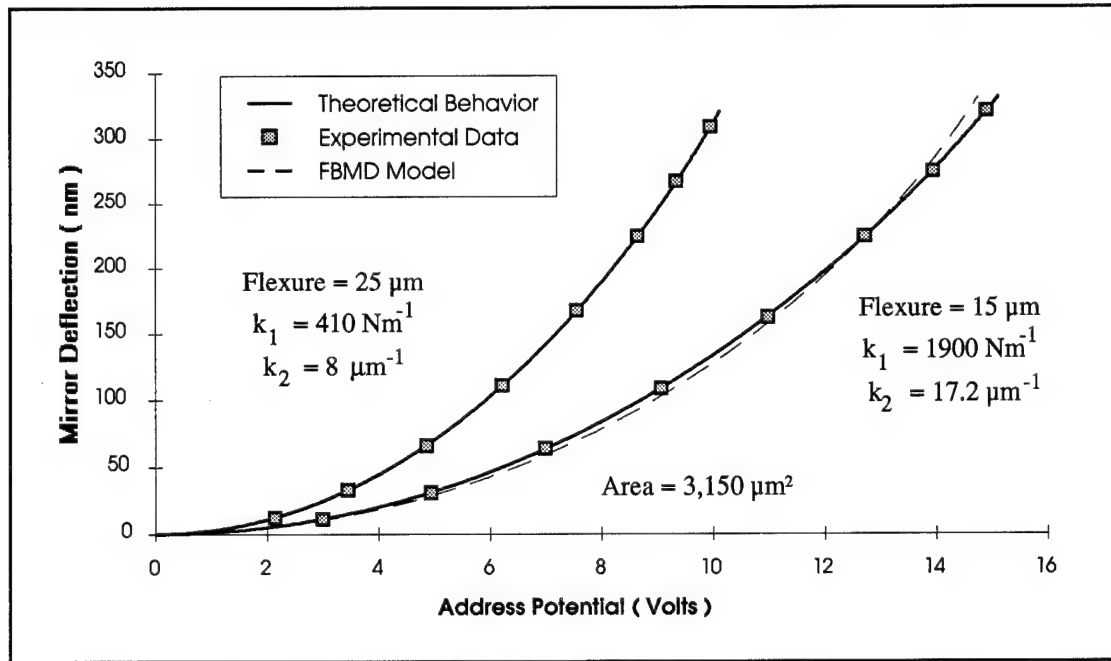


**Figure 5-9.** Ideal characteristic behavior of two paddle-style Cantilever devices.

The Cantilever model appears to fit the data well, but the data is simply fit to the curve as was the Flexure-Beam data which does not directly validate the model as described above. Again, the calibration of the spring constant was required in order to describe the behavior of the device. As a means of comparison, the best-fit Flexure-Beam curve is shown for one of the devices in Fig. 5-9 which illustrates the slight variation in the behavior of the Cantilever device. Although the Flexure-Beam model closely approximates the curve at any one point on the surface of the mirror, a different spring constant is required to fit this model elsewhere along the mirror surface. Once the

Cantilever constants are determined, however, the model becomes a function of position such that no new calibration is required to describe the behavior of the device.

The constants determined for the paddle-style Cantilever device with the shorter flexure were used in the model in which the deflection at other points on the surface of the mirror was measured. Figure 5-10 illustrates the result of this measurement which shows the model and experimental data at the end and center of the mirror.
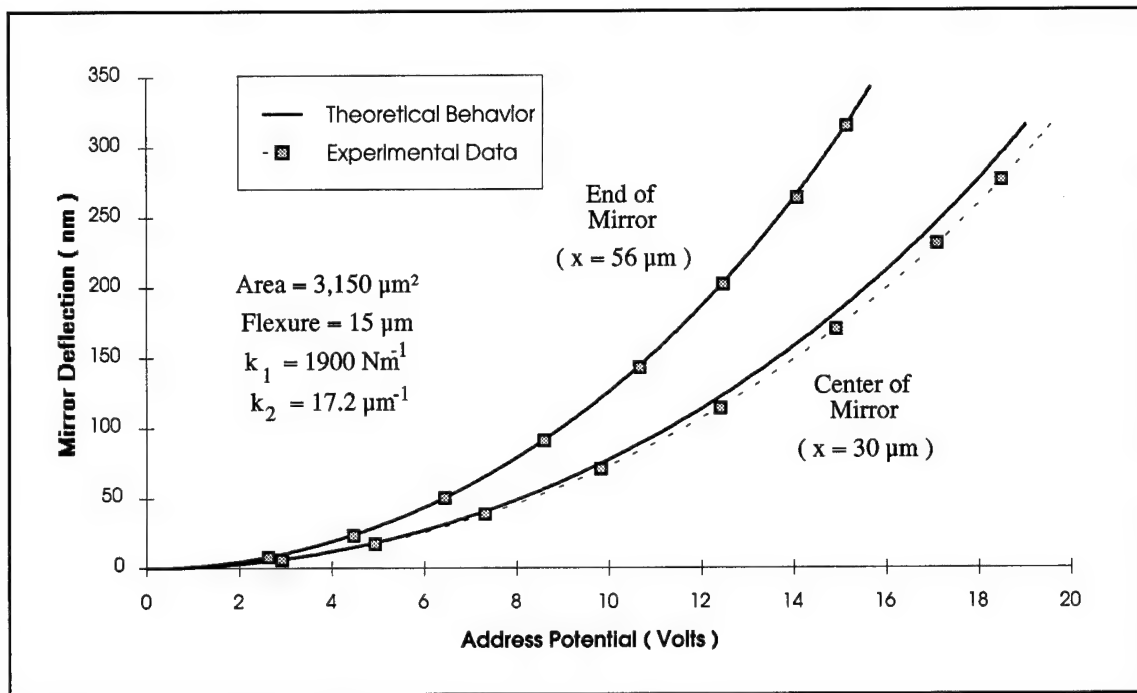


**Figure 5-10.** Behavior curves for two locations on the paddle-style Cantilever device.

The behavior curve for the data taken at the center of the mirror is slightly erroneous due to as many as three primary reasons. First, it was noted that the curves could be fit to a wide range of constants at a particular point along the mirror surface, but since these constants determine the amount of tilting of the mirror, and therefore the slope along the surface, only a precise set of constants could describe the entire surface of the mirror. It is necessary to take several sets of curves at various intervals along the surface of the mirror and find the constants that satisfy them simultaneously.

Secondly, the constants were determined for a position at the end of the mirror for which the coordinate was approximated due to the size of the laser spot focused on the mirror. This coordinate could contain a significant amount of error which would produce erroneous values of the fitting constants. Likewise, the position coordinate of the center of the mirror could be equally inaccurate such that a combination of the two approximations leads to the theoretical behavior curve shown in Fig. 5-10 in which the model does not exactly describe the data. Ultimately, however, the Cantilever model describes the behavior of this device fairly well with the current spring constants.

## (5.3) SPRING CONSTANT EVALUATION

Micromirror devices fabricated on the same wafer typically share the mechanical properties of the layers from which they are fabricated such that the elastic modulus and stress due to fabrication can be assumed uniform between similar devices. For this reason, the spring constant of Eq. (3.68) reduces to a function of geometry of the flexures of a micromirror device. If the flexures are all designed to be of common width, the spring constant becomes a function solely of the length of the flexure. Therefore, without knowing the exact modulus of elasticity of the flexures, a relation between two or more sets of spring constants can be determined based on an experimentally determined value of one constant and the lengths of two or more flexures. Solving Eq. (3.68) for two micromirror devices, A and B, whose modulus of elasticity are set identically equal to each other yields the following spring constant relationship:

$$ k_B = \frac{k_A L_A^3 + b\left(L_B^2 - L_A^2\right)}{L_B^3}, \qquad b = 2\sigma(1 - \upsilon)wt \qquad (5.1) $$

such that the deflection spring constant for a second device, $k_1 = k_B$, can be determined from the calibration of the first device constant, $k_1 = k_A$, and the relative length of their

flexures, $L_B$ and $L_A$, respectively. The paddle-style devices characterized in Fig. 5-9 were found the obey this relationship well within one percent error indicating that the beam analysis used to develop the spring constant relationship was valid. For flexures that contain bends or sharp corners in their layout, however, this relationship may be affected by additional stress or torque produced in the flexures based on their geometry.

### (5.3.1) PROPERTIES OF SHAPED FLEXURES

The three versions of torsion-style devices shown in Fig. 5-7 were characterized at a position at the end of each mirror. Figure 5-11 shows the ideal theoretical model and the data taken for each device having the flexure lengths given next to each curve.
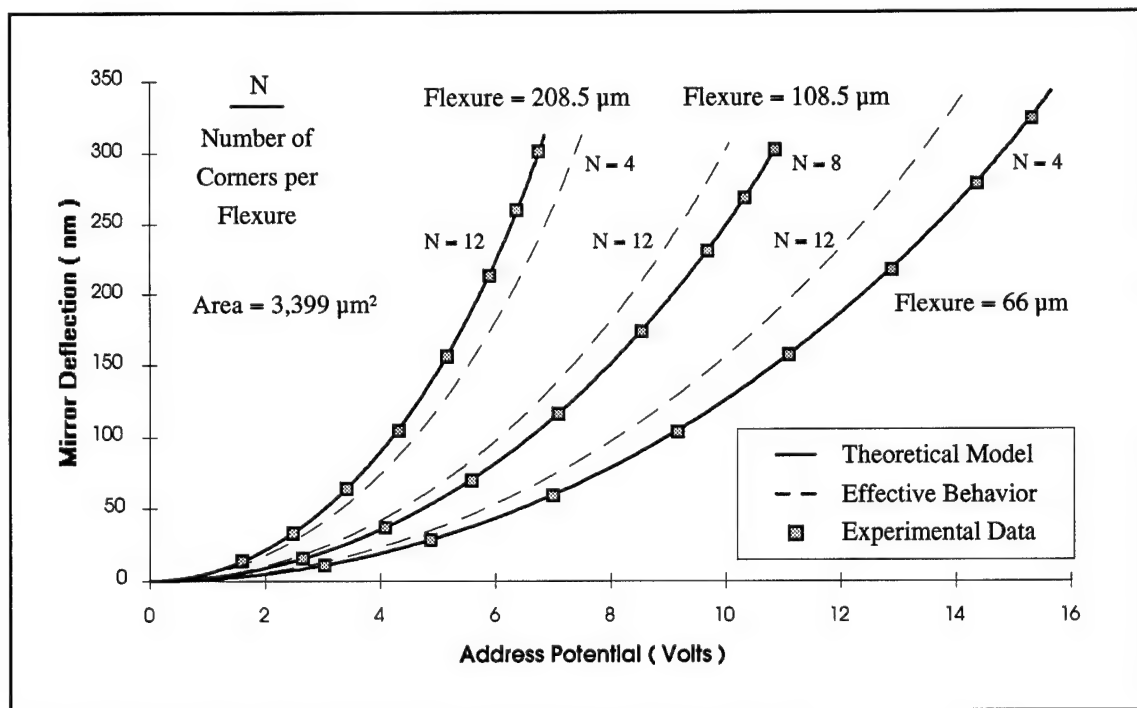


**Figure 5-11.** Ideal characteristic behavior of three torsion-style Cantilever devices.

Also shown with each data curve is the effective behavior of each device given the spring constants evaluated from the relationship in Eq. (5.1) for the three lengths of flexures.

The number of corners per flexure of a given device is also shown adjacent to the corresponding behavior curve. For straight flexures containing no sharp corners in their layout, it is expected that the effective behavior for a device as calculated by another would be very similar to the experimental behavior observed for that device. As shown in Fig. 5-11, however, the zig-zag wrapping of the flexures alters the spring constant of the device regardless of the net length of the flexure.

It appears that the spring constant decreases with the increase in the number of corners in the layout of the flexures. This is reasonable since the majority of the length of the flexures lies in the direction of the deflection of the mirror which allows the flexures to deform more easily to actuation. This indicates that the observed behavior may not entirely be the result of the corners in the flexure layout, but also the direction in which the flexures are positioned relative to the deflection of the device. For this reason, the spring constant data collected from the torsion-style Cantilever devices is inconclusive. Chapter (VI) contains several suggested improvements and recommended test structures from which the effect of shaped hinges can more accurately be analyzed.

## (5.3.2) ELASTIC MODULUS EXTRACTION

The spring constant that describes the behavior of the Flexure-Beam micromirror devices is given in Eq. (3.68) in which all dimensions and variables are known except the value of the thin-film modulus of elasticity for the flexures. In order to extract the elasticity of the flexures, an observed behavior curve must first be fit to a model of the device to experimentally determine a spring constant describing their behavior. Since the behavior of the Cantilever devices is dependent on two constants, these devices can not be used because the degree of bending associated with the device affects their values. Therefore, only Flexure-Beam devices can be used since their flexures deflect without extreme bending as well. Unfortunately, the rounding effects of the grid spacing during

fabrication created uneven flexures for the two sizes of hexagonal micromirrors which does not permit the use of these devices to directly evaluate the flexure elasticity. As a result, the only devices remaining for this purpose are the square micromirrors which are the focus of the advanced model. This would seem to defeat the purpose of extracting parameters from other devices to describe its behavior.

As an alternative, however, the elastic modulus is found using all three designs and then averaged to remove the error due to the widened flexures. Equation (3.68) is solved for the elastic modulus which is evaluated using the spring constants in Fig. 5-8 that were previously determined to fit the model to the observed data of the devices. The modulus was found to be 210 GPa for the square Flexure-Beam device, 152 GPa for the small hexagonal device, and 125 GPa for the large hexagonal device.
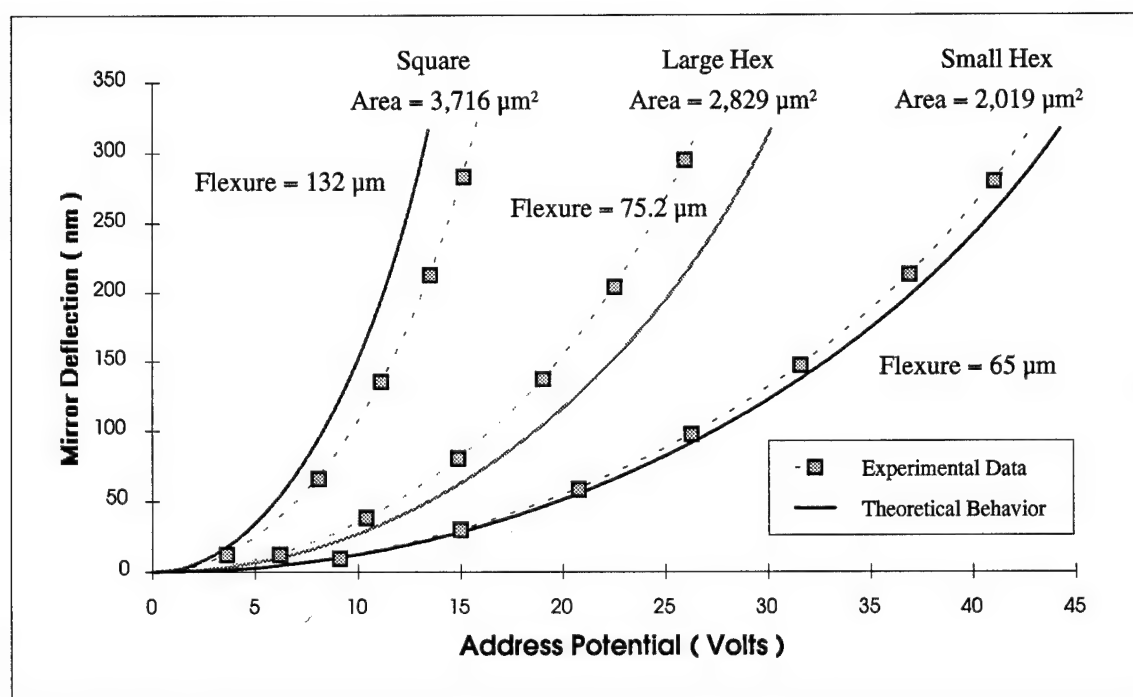


**Figure 5-12.** Comparison of behavior curves using extracted modulus of elasticity.

The average of these values yields a reasonable approximation of the thin-film elastic modulus for Poly-2 found to be 162.3 GPa which produces the characteristic behavior

curves shown in Fig. 5-12 for the three devices. The value of 162.3 GPa compares favorably to other sources in which values of 168 GPa, 169 GPa, and 173 GPa were experimentally determined [27,28,29]. Knowing the elastic modulus of the Poly-2 flexures, the advanced model does not require experimental observations to predict the behavior of the devices.

In order to gain a more accurate value of the elastic modulus, however, other effects of the geometry of the flexures must be studied. It was observed that the shape of the flexures of the torsion-style Cantilever devices altered the behavior of the device such that the spring constant of the flexures was not only a function of geometric proportions, but also of the shape and position in which the flexures are designed. Therefore, the spring constants between the square and hexagonal devices may produce different values of the elastic modulus because the flexures of the square mirror are angled more than those of the hexagonal mirrors. In order analyze and extract the exact value of the thin film modulus of elasticity, the spring constant must be made to account for the shape of the flexures which may include any angles in the flexures or the direction in which the flexures lie relative to the motion of the mirror. Suggested experiments are presented in Chapter (VI) which should help determine such effects on device behavior.

## (5.4) ADVANCED FLEXURE-BEAM MODEL VERIFICATION

For the square Flexure-Beam micromirror device, the ideal characteristic model appears to be accurate for low frequencies and temperatures because the device is large enough that no significant electric field fringing losses are present. The surface deformations observed for this device, however, require a more complete model that will allow for slight modifications based on the physical behavior of the device and for more extreme operating conditions.

The elastic modulus of the mirror surface is determined from observations of a large Flexure-Beam device that is partially deflected due to gravity in which the center of the device is deflected further than the edges. This modulus is then used to quantify the amount of surface deformation observed from the square Flexure-Beam device used to test the advanced model. In addition, the net effect of cross-talk is found to be negligible for these devices due to the spacing between adjacent micromirrors. The effects of temperature, frequency, and fringing losses are analyzed using simulated devices or conditions and applying the advanced model to them since the capabilities of the experimental setup are such that these effects can not be directly measured with the equipment and devices currently available.

### (5.4.1) MIRROR SURFACE DEFORMATION

The elastic modulus of the micromirrors fabricated in the MUMPS6 run can be obtained from the behavior of a particular device and used to predict and analyze the behavior of others. The large square Flexure-Beam device shown in Fig. 5-1 exhibits partial surface deformations due to its own weight. This observation is very useful since the mass of the mirror can be precisely determined from the volume and densities of the materials comprising it. Therefore, the modulus of elasticity of the mirror can be found that will describe the degree of surface deformations that can be expected from micromirror devices that are actuated at a given address potential.

### (5.4.1.1) MIRROR ELASTICITY

To obtain the modulus of elasticity of the mirror, the deformation at the center of the mirror must first be measured. However, due to the extreme size of the device, its motion can not be measured using the laser interferometer because the mirror of the

device would come into contact with the address electrode and short circuit the device. As a result, the deformation at the center of the device must be estimated. Since the separation distance between the mirror and address electrode is much smaller than the width of the mirror, estimating the deformation distance will produce an estimated elastic modulus that is well within an order of magnitude of the actual value.

It is first assumed that the center of the mirror is fully deflected by its own weight such that $\delta = d_{2\pi} = 316.4 \ nm$. Although the mirror may appear to be significantly more deflected, it must be noted that the stress in the Gold layer is tensile while the stress in the Poly-2 layer is compressive such that large mirrors will partially deform downward due to this bimetallic actuation. The elastic modulus is found using Eq. (3.73) such that

$$E_m = \frac{MgA}{(6.4)\delta \ t_m^3} \qquad (5.2)$$

where $M$ is the mass of the mirror, $g$ is the gravitational acceleration constant, $A$ is the area of the mirror, and $t_m$ is the total thickness of the mirror given as the sum thickness of Poly-2 and Gold. The elastic modulus of the mirror, $E_m$, is found to be 268.4 MPa which is several orders of magnitude less than the bulk elastic modulus for both silicon and gold, 112 GPa and 74.5 GPa, respectively [17]. Although this seems unreasonable, the surface deformation theory and experimental results will verify this magnitude.

Since the bulk modulus of elasticity of silicon is much greater than that of gold and the Poly-2 layer is much thicker than the Gold layer, it is expected that the polysilicon will dominate the elasticity of the mirror. If the thickness of the Poly-2 layer is used as the thickness of the mirror, the produced modulus of elasticity is somewhat larger than initially calculated. The elastic modulus of the mirror, $E_m$, in this case is found to be 704.97 MPa which is more closely verified by observed data. The following section contains this analysis which uses the square Flexure-Beam micromirror device to depict the effects of surface deformations on the behavior of the mirror.

## (5.4.1.2) SURFACE DEFORMATION VERIFICATION

The deflection of the square Flexure-Beam device of Fig. 5-2 was measured at the four corners and center of the mirror in order to test the deformation of the mirror. Since the hinges were designed for uniform behavior and are attached at the corners of the mirror, it is anticipated that the corners of the mirror will deflect along very similar behavior curves. Figure 5-13 shows these curves along with that from the mirror center.
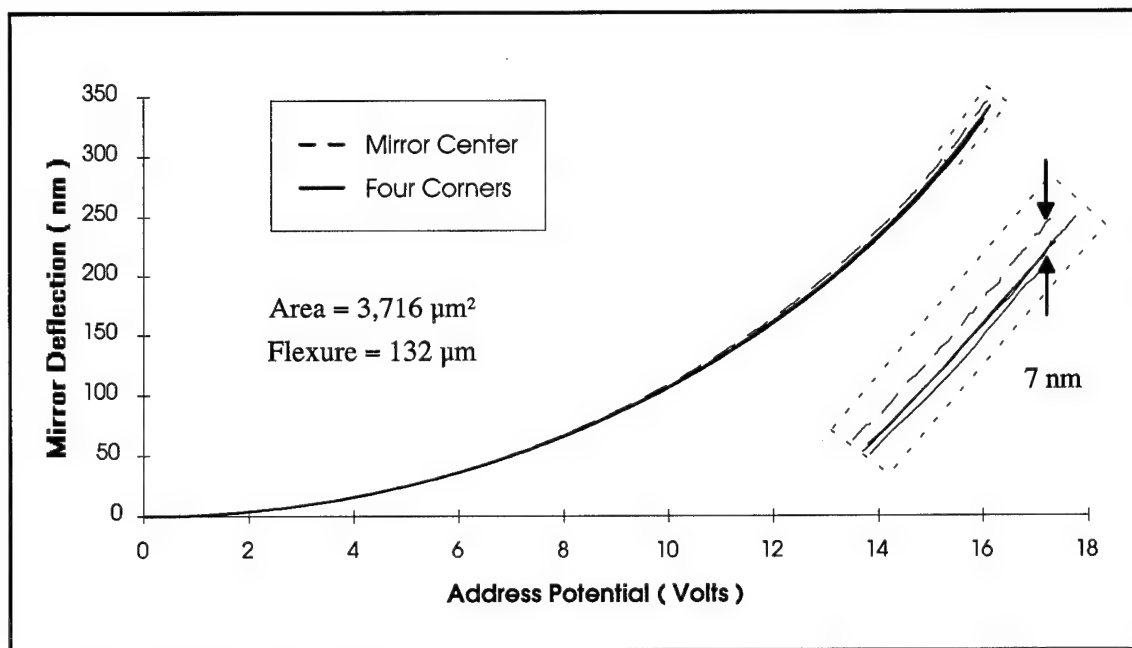


**Figure 5-13.** Characteristic behavior of the square Flexure-Beam micromirror surface.

As expected, the four corners deflected uniformly relative to each other to the extent that their behavior curves are almost indistinguishable. The characteristic behavior of the center of the mirror, however, shows that the mirror deformed as it deflected. The difference between the deflection of the mirror at the center of the device and the deflection at the flexures is given in Eq. (3.75) and is experimentally determined to be approximately 7 nm at the peak address potential. Using the mirror elastic modulus

determined from the large Flexure-Beam device of Fig. 5-1, the calculated deformation at the center of this device should be approximately 5 nm at the same potential.

Using the elastic modulus of 705 MPa, the advance model is updated to include a relative degree of surface deformation using Eq. (3.75) for micromirror devices in which the flexures are attached at the corners of the device. Since this deformation is a function of position, the experimental data shown in Fig. 5-13 is reproduced by the model to include similar behavior of the four corners of the mirror and an additional deflection at the center of the device of approximately 5 nm at the peak address potential.
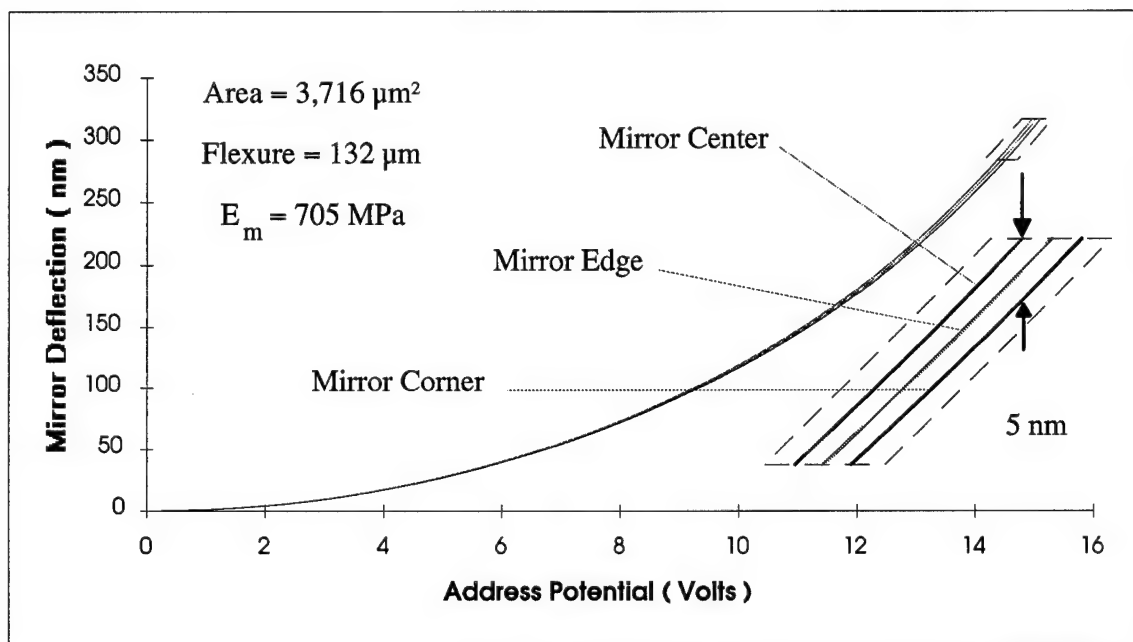


**Figure 5-14.** Surface deformation behavior curves of the square Flexure-Beam device.

The theoretical behavior of the device at three positions on the surface of the mirror is shown in Fig. 5-14 which shows the peak deformation to be 5 nm between the curve at the center of the device and the curve at the corner. As illustrated in Fig. 3-13, the edge of the mirror is expected to deform half the distance as that of the center of the device. Since the peak deformation at the peak address potential is approximately the same as the

experimental value observed with the data shown in Fig. 5-13, the value of the extracted mirror elasticity, 705 MPa, is assumed to be reasonably accurate.

### (5.4.2) CROSS-TALK

In order to evaluate the magnitude of cross-talk interference relative to the actuation of a primary device, the maximum possible interference is evaluated by assuming that all four adjacent mirrors in an array of square Flexure-Beam devices are fully actuated. The peak actuation potential, $V_{2\pi}$, is defined as the voltage required to deflect the mirror of any device to a peak deflection distance, $d_{2\pi}$, which is relative to the wavelength of the incident beam of light. If all four neighbors are fully actuated, the total force due to cross-talk on the primary mirror is given in Eqs. (3.54) and (3.59) such that

$$F_{CT} = \frac{2\varepsilon_o w V_{2\pi}^2}{z_o}\left[\frac{(x_s + w)L_{min} - x_s L_{max}}{L_{min}L_{max}}\right] = k\, d_{max} \qquad (5.3)$$

where $w$ is the width of the square mirror, $z_0$ is the resting height of the mirror, $x_s$ is the separation distance between adjacent devices, $l_{min}$ and $l_{max}$ are the minimum and maximum arc lengths of the cross-talk interference, respectively, and $d_{max}$ is defined as the maximum deflection of the primary mirror due to cross-talk. Using the ideal model in Eq. (3.19), the peak actuation potential is given as

$$V_{2\pi}^2 = (z_o - d_{2\pi})^2\left(\frac{2k\, d_{2\pi}}{\varepsilon_o A}\right), \qquad A = w^2 \qquad (5.4)$$

which can be substituted into Eq. (5.3) to yield the maximum deflection such that

$$d_{max} = \frac{4 d_{2\pi}(z_o - d_{2\pi})^2}{z_o w}\left[\frac{(x_s + w)L_{min} - x_s L_{max}}{L_{min}L_{max}}\right] \qquad (5.5)$$

where $L_{min}$ and $L_{max}$ are given in Eq. (3.56) and are functions of the geometry of the device and the distance between the adjacent mirrors. Since the peak address potential is

a function of the spring constant, the peak deflection due to cross-talk is normalized to all devices independent of the spring constant provided that the adjacent mirrors have the same spring constant. Figure 5-15 shows a plot of $d_{max}$ for various device geometries.
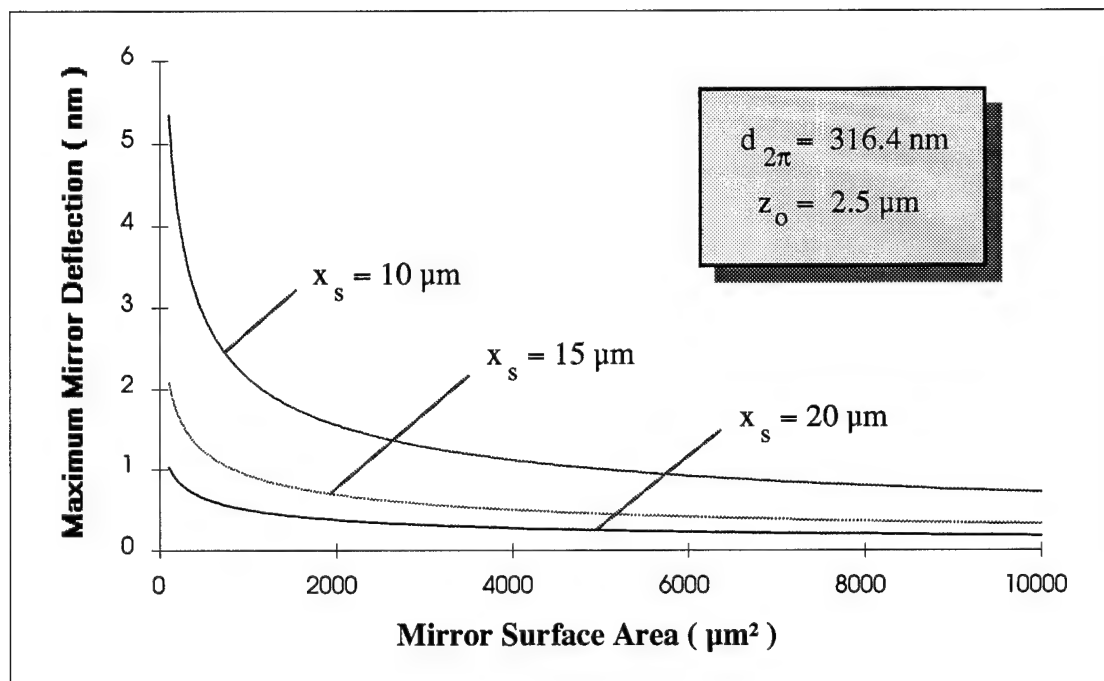


**Figure 5-15.** Plot of maximum deflection due to cross-talk versus micromirror area.

The square Flexure-Beam micromirror devices used to evaluate the advanced model are spaced 18 µm between adjacent devices and are 3,716 µm² in area. This corresponds to a maximum deflection of approximately 0.5 nm which is on the order of noise in the experimental system. Therefore, it is expected that no significant change in the behavior of the device will be observed when the adjacent mirrors are actuated.

To test this assumption, three of the adjacent devices in the array of square Flexure-Beam devices shown in Fig. 5-2(b) were actuated with a constant address potential of approximately 15 Volts which is very close to the peak address potential. A behavior curve was generated for the primary device along the edge of the mirror nearest the neighboring devices which was compared to the same curve generated when the

adjacent devices were not actuated. As expected, no measurable changes were observed which validates the assumption that cross-talk can be ignored for these particular mirrors. For smaller devices that are more closely packed together within an array, however, the peak deflection due to cross-talk can be quite significant.

## (5.4.3) SIMULATED BEHAVIOR

Although the temperature and frequency effects on the behavior of micromirror devices was not directly measured, the theory developed in Chapter (III) provides adequate information to predict the behavior of micromirror devices at various temperatures and driving frequencies. For both cases, the square Flexure-Beam micromirror device shown in Fig. 5-2 will be used to study these effects. The data collected at room temperature and at low frequencies will be used as a comparison for the theoretical behavior of the device under extreme operating conditions.

## (5.4.3.1) TEMPERATURE RESPONSE

Before the effect of temperature is simulated on the square Flexure-Beam device, it should be noted that this model only accounts for the ideal change in the elastic modulus of the device materials as the temperature changes. At extremely low or high temperatures, the elastic modulus may be significantly altered to the point where the analysis of simple thermal expansion effects are no longer valid. At these temperatures, however, the device is most likely to deform or become brittle due to melting or freezing temperatures respectively and will therefore most likely not be operated in these regions. For most applications, the temperature effects of the advanced model remain valid.

The effect of operating temperature on micromirror devices in general was developed in Chapter (III) in which the thermal expansion coefficients of the materials

comprising a device dictated a change in geometry with respect to temperature. This change in geometry in turn created new properties in the actuation of the device which altered the characteristic behavior curve. Figure 5-16 illustrates the effect of ambient temperature on the behavior curve of the square Flexure-Beam micromirror device.
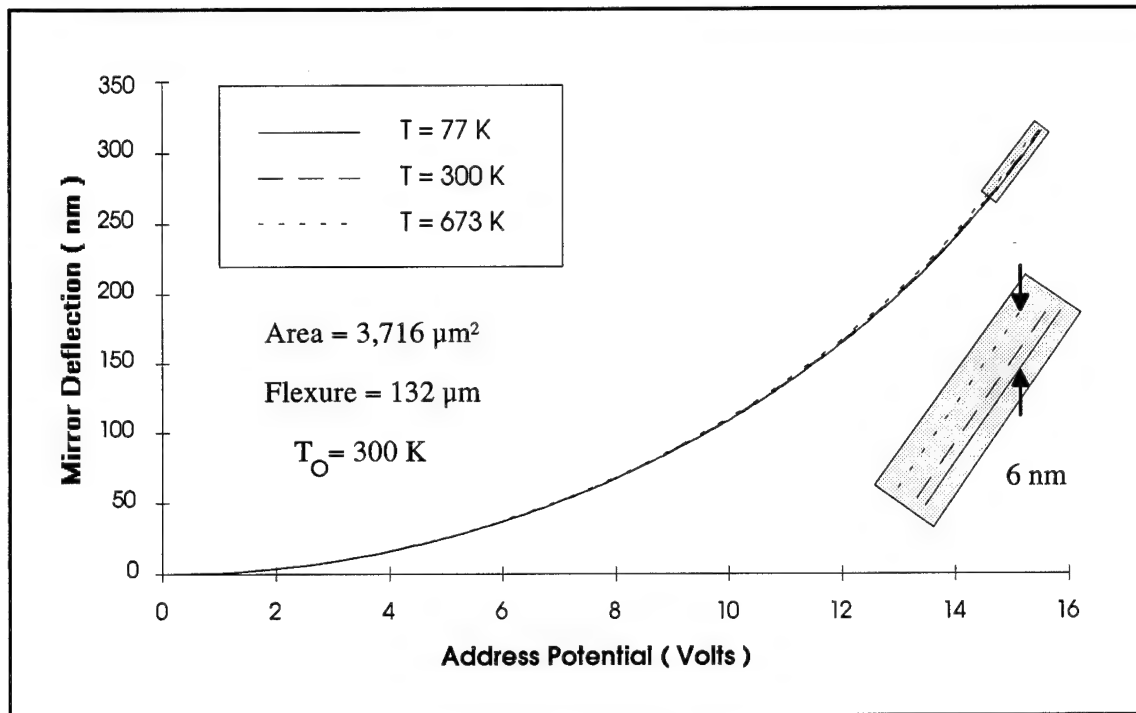


**Figure 5-16.** Simulated temperature response of the square Flexure-Beam device.

These behavior curves are simulated using the advanced model because the experimental setup did not allow for changes in ambient temperature large enough to produce measurable changes in the behavior of the micromirror devices under test. It is easy to see, however, that the device will become more flexible as the temperature increases such that lower voltages are required to achieve a desired deflection distance. The effect of this temperature dependence does not appear to be a significant portion of the advanced model since only 6 nm of variance is predicted for typical operational temperatures ranging from 77°K to 673°K for the square Flexure-Beam device. However, smaller devices may exhibit proportionately greater effects due to the operating temperature.

## (5.4.3.2) FREQUENCY RESPONSE

Similarly, the frequency effects of the advanced model had to be simulated because the experimental setup does not provide accurate behavior curves for devices actuated at frequencies above 5 kHz which is much less than the resonant frequency of the square Flexure-Beam micromirror device. Therefore, no significant characteristics of the effects of driving frequency would be observed. Figure 5-17 illustrates the simulated effects generated by the advanced model which demonstrate that the address potential decreases as the driving frequency approaches resonance.
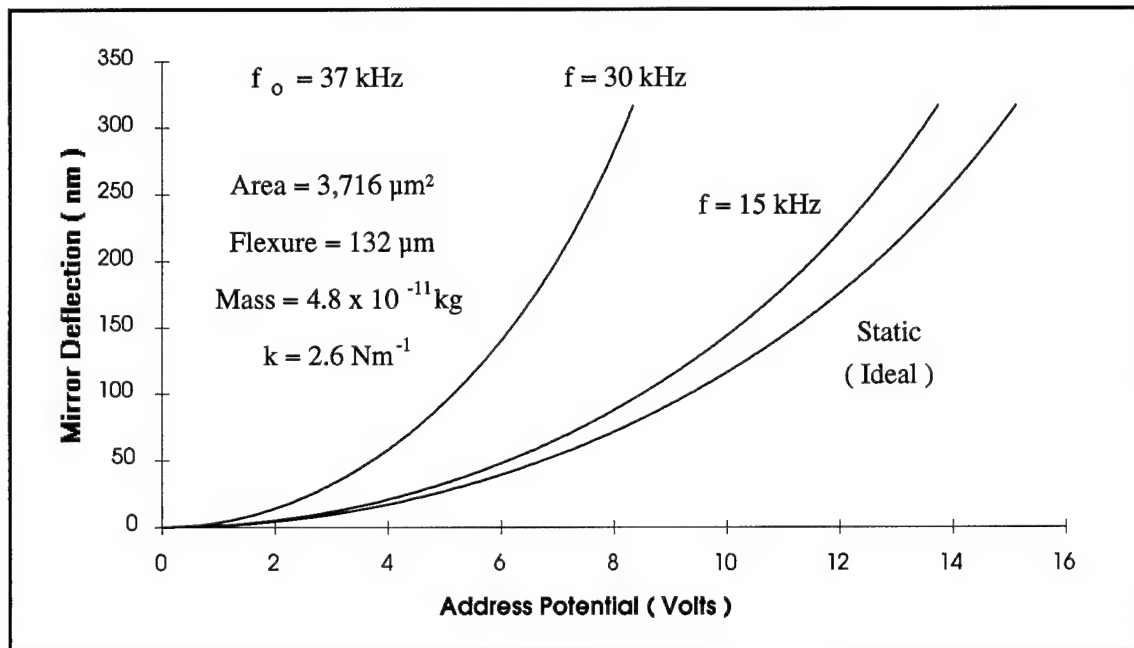


**Figure 5-17.** Simulated frequency response of the square Flexure-Beam device.

The resonant frequency of the device is calculated using Eq. (3.69) in which the total mass of the mirror, $M$, is found to be $4.80 \times 10^{-11}$ kg as calculated from the volume and densities of the polysilicon and gold that comprise the mirror. Using the spring constant that was experimentally evaluated for this device, $k = 2.6$ Nm$^{-1}$, the resonant frequency, $f_o$, is found to be approximately 37 kHz which is well within the operating limits of many

applications of micromirror devices. Therefore, precautions must be taken to prevent excessive responses from similar devices such that the driving frequency is maintained below resonance. For higher frequency applications, the mass of the mirror or the spring constant of the device must be altered to increase the operating range of frequency.

### (5.4.3.3) FRINGING LOSSES

Due to the size of the square Flexure-Beam device, no significant fringing losses were observed. However, for smaller devices with relatively long flexures, the difference between the ideal and advanced model becomes more significant as shown in Fig. 5-18.



**Figure 5-18.** Simulated fringing losses of a small Flexure-Beam micromirror device.

It is easy to see that as the mirror area of the device decreases, the ideal behavior model given in Eq. (3.19) becomes less accurate. Therefore, the advanced model must be used to incorporate fringing losses in the characteristic behavior of the device.

## (5.5)  VARIANCE OF FLEXURE-BEAM BEHAVIOR

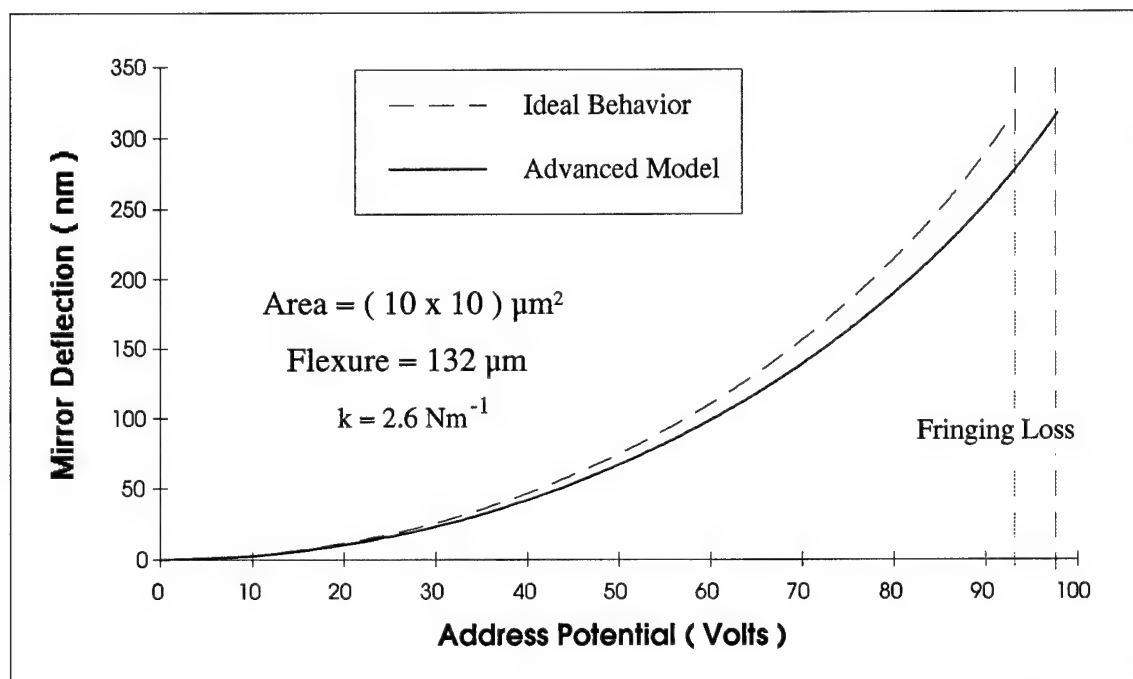The models used to describe the behavior of micromirror devices incorporate a statistical assumption that all the devices with the same design will exhibit similar behavior characteristics.   The standard deviation of the behavior of these devices decreases as the quality of the fabrication process increases such that an ideal fabrication process would produce devices that behaved identically to those of the same design.

Unfortunately, variances in the fabrication process or other uncontrollable conditions create discrepancies in the behavior of similar devices.  In order to apply a model based on this statistical assumption, it is desirable to determine how well the behaviors of similar devices conform to some average behavior for a given design.  To do so, several sets of observations were made that would ideally produce no variation between measurements.  Realistically, however, this is known to be erroneous and deviation analysis must be performed on the set of experimental data to determine the relative coherence of the observations.

The deviation analysis performed on the characteristic behavior curves of the Flexure-Beam micromirror devices was simply a tracing of the maximum and minimum deflection distances observed for a range of address potentials.  Since each characteristic curve represents a continuos set of behavior for a particular device, error bars depicting the standard deviation at a known potential are not applicable since hundreds of points are used to construct each curve and the exact values of each address potential are not necessarily shared between characteristic curves.  As a result, the range of experimental data must be shown together with the averaged behavior curve in order to depict the result of averaging these samples.  Furthermore, the observed behavior curves illustrate the standard deviation of these samples by outlining the highest and lowest deflection distances observed throughout the entire range of address potentials.   Therefore, the coherence of the experimental data decreases as the behavior curves spread apart.

## (5.5.1) VARIANCE OF THE EXPERIMENTAL SYSTEM

In order to accurately evaluate the variance of micromirror device behavior, the variance due to noise in the experimental system must first be established. To do so, five measurements were made within a several seconds at the flexures of a single device. The variance of these behavior curves represents the noise of the measurements. As illustrated in Fig. 5-19, the range of experimental data is tightly grouped together about the averaged behavior of the measurement.
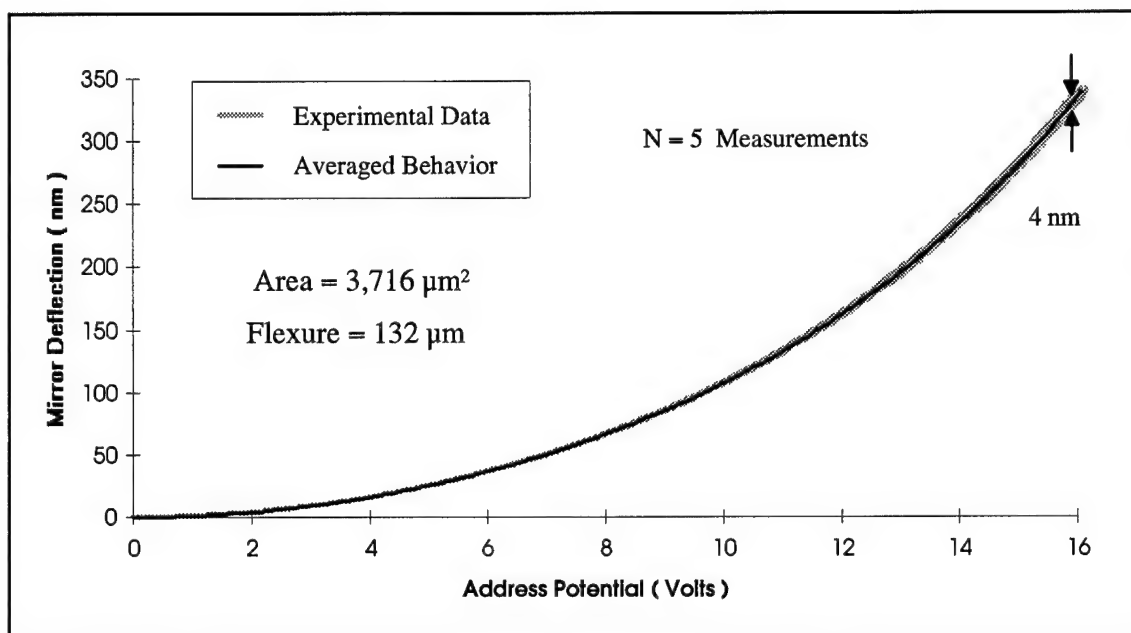


**Figure 5-19.** Range of experimental data from a single square Flexure-Beam device.

The deviation of the observed behavior at the peak address potential is relatively small, approximately 4 nm, which indicates the precision of the setup. Much of the noise induced in these measurements stems from the limitations of the software to process the input and output signals from the oscilloscope. The effects of high frequency noise are compounded by the numerical precision of the analysis software which propagates very low amplitude perturbations in the signals. Although the captured traces are averaged

between periods to reduce noise, the software remains quite sensitive to the minimum and maximum output values which are used to evaluate the remainder of the deflection array.

## *(5.5.2) VARIANCE OF THE SQUARE FLEXURE-BEAM DEVICE*

Similarly, one measurement was made at a flexure on the mirror surface of five square Flexure-Beam devices in order to test the variance of an array of these micromirrors. Figure 5-20 shows these measurements along with the average behavior.
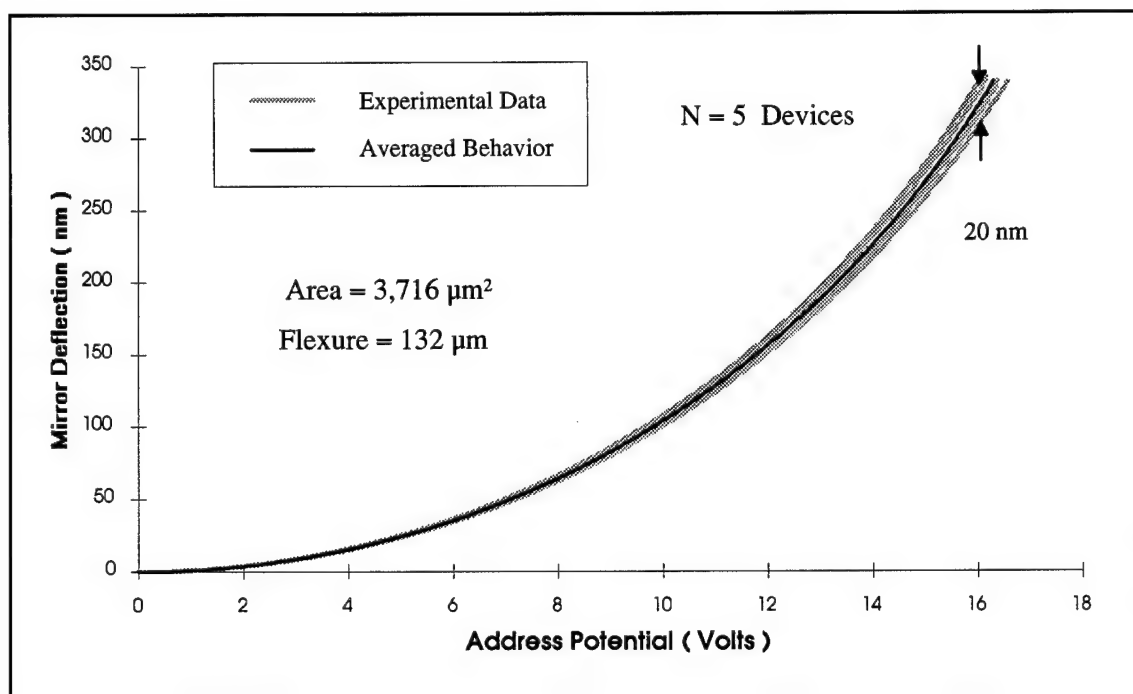


**Figure 5-20.** Range of experimental data for several square Flexure-Beam devices.

The range of data is more spread out which indicates that the mirrors do not conform to identical behavior. At the peak actuation potential, a span of nearly 20 nm was observed between the maximum and minimum deflections. Since the flexures of these device were adequately adapted to the fabrication grid, this degree of error can be expected for all devices fabricated in this process since the cause of this variance is most likely the sum of

several uncontrollable factors such as fabrication material residues or inhomogeneous distributions of stress due to thermal annealing of the material layers forming the devices.

### (5.5.3) VARIANCE OF THE HEXAGONAL FLEXURE-BEAM DEVICE

Since the flexures of the hexagonal micromirrors were observed to be noticeably distorted along one side of the device, it is expected that these micromirrors will display a significant degree of variation. It is also anticipated that these mirrors will not deflect uniformly along the surface of the mirror. Figure 5-21 shows the deflection measured at the three corners of a hexagonal micromirror at which the flexures are attached.
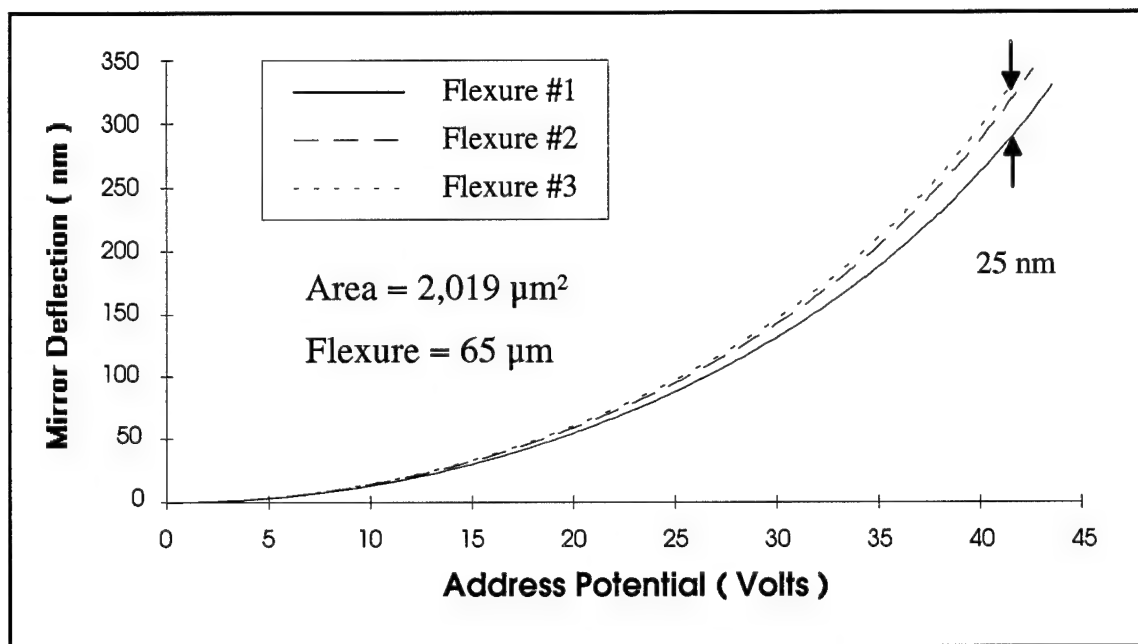


**Figure 5-21.** Behavior of a hexagonal FBMD at the position of each flexure.

As expected, the corner of the mirror attached to the widened flexure requires significantly more address potential to achieve the same deflection as the other two corners which are also unequally deflected. Since the distortion of the flexures was due to a systematic rounding of the grid spacing used to fabricate the devices, it is expected

that the majority of hexagonal devices will exhibit this behavior since the other flexures supporting them are distorted in a similar manner. Six other devices were tested which also tilt to some degree as the mirror is deflected downward.

The experimental data observed from these seven hexagonal micromirrors was used to compare the variance of the deflection between different devices. As illustrated in Fig. 5-22, the deflection of these devices is significantly spread out such that the peak address potential produces a span of more than 50 nm between the high and low values.
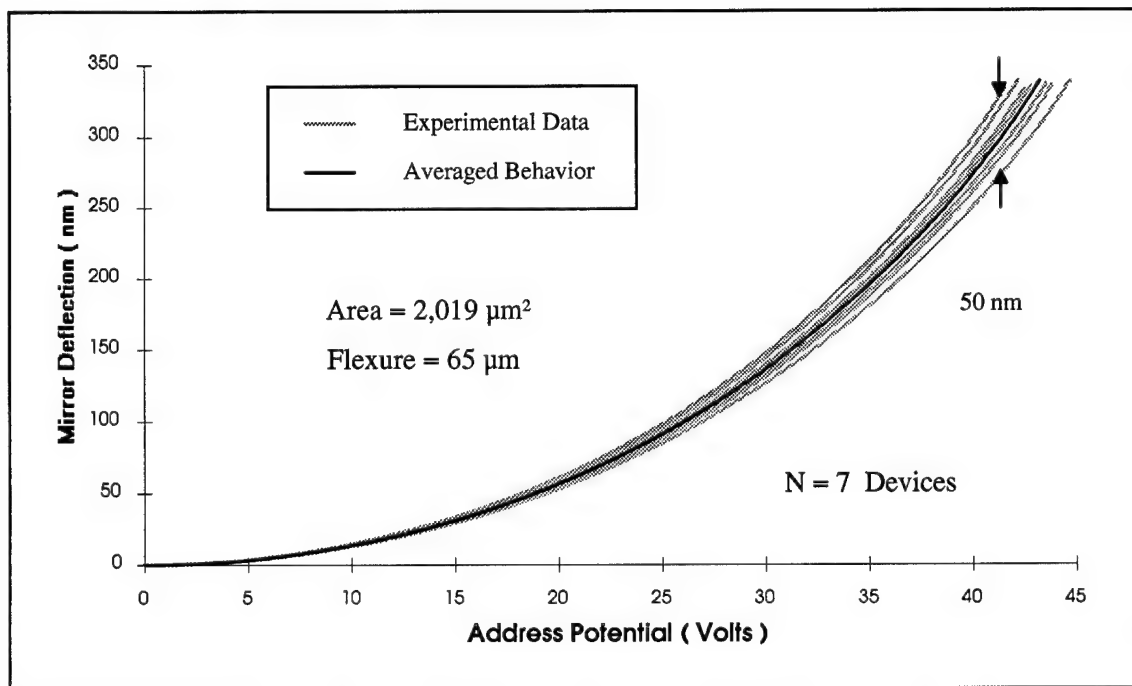


**Figure 5-22.** Range of experimental data for several hexagonal Flexure-Beam devices.

Using a $\lambda$ = 632.8 nm laser, the error associated with the peak address potential is approximately 18 % of the active deflection range of the device. Under these conditions, it is most likely that this device would not be used in the application for which it was designed and would be considered a fabrication failure. Since only seven out of hundreds of similar devices were sampled, it is likely that numerous other devices demonstrate behavior curves of equal or greater variance than those observed.

## (5.6) DEVICE RELIABILITY

The reliability of micromirror devices was tested by obtaining initial characteristic behavior curves for specific devices and comparing them to curves obtained after some actuation period. The square Flexure-Beam micromirror device shown in Fig. 5-2 was driven with a variety of sinusoidal input signals through the full range of motion for the device. The frequency of the actuation ranged from 5 kHz to 45 kHz for a duration of approximately 7½ hours which generated between 135 million and 1.2 billion oscillations of the device. A comparison of the two characteristic curves for each driving frequency indicates that the behavior of the device is unchanged such that the curves were within the deviation of the experimental system. Similar experiments were conducted on all other designs of micromirrors in this thesis which produced the same results.

# (VI) SUMMARY AND CONCLUSIONS

The research of this thesis has produced several models and characterizations of micromirror devices including an advanced model for Flexure-Beam devices that includes the physical effects of the devices and operating conditions. This chapter summarizes the findings of this research by highlighting the most significant observations concerning the design, fabrication, modeling, and testing of micromirror devices. Several suggested improvements and future research ideas are also presented.

## (6.1) THESIS SUMMARY

In the design of surface-micromachined micromirror devices, several key considerations emerged that affect the operation and capability of the devices. It was found that the surface topology was significantly interrupted by the sharp edges created by the masking of lower layers. As the intermediate layers were deposited, they conformed to the previous layer such that dips in the surface of the mirrors relative to the thickness of the previous layer were observed where the Poly-0 had been removed in the forming of address wires and electrodes. This effect can alter the behavior of micromirror devices by changing the physical properties of the flexures such that one may behave differently from another which would cause the mirror to tilt as it deflected. Likewise, the mirror itself can be affected by the conforming nature of deposited layers such that the reflective surface appears discontinuous.

The primary concern in designing micromirror devices is the desire to achieve a specified range of deflection with low address potentials. The voltage required to actuate some devices can be extremely high such that the device is virtually unusable in many

applications. In order to overcome this problem, the micromirrors in this thesis were designed with a large surface area ($\sim$ 3,000 $\mu m^2$) and very long flexures ($\sim$ 100 $\mu m$) so that the address potential required to actuate them remained on the order of several or tens of volts rather than hundreds as would be the case for much smaller mirrors or flexures. Devices of this size, however, are quite massive such that the resonant frequency is significantly lower ($\sim$ 30 kHz) than that of much smaller devices ($\sim$ 1 MHz).

It was observed that the interference due to cross-talk did not significantly affect the behavior of the square Flexure-Beam micromirrors, shown in Fig. 5-2, that were the primary focus of the advanced model. For other devices, however, reducing the mirror surface area can increase the interference between devices as will reducing the spacing between them. Before an array of micromirror devices can be designed, the maximum cross-talk tolerance should be identified which corresponds to a minimum separation distance between devices of a given surface area.

The micromirror devices studied in this thesis were fabricated by the Microelectronics Corporation of North Carolina (MCNC) using the ARPA-sponsored Multi-User Mems ProcesS (MUMPS) fabrication service. This polysilicon process has one address layer, Poly-0, two releasable layers, Poly-1 and Poly-2, and uses silicon dioxide as the sacrificial material. All micromechanical devices are fabricated on an initial layer of silicon nitride for substrate isolation. The fabrication results of the devices designed in this thesis were excellent such that all devices behaved as anticipated. The only exception was the effect of the grid spacing on the flexures of the hexagonal mirrors which caused the devices to resist the electrostatic actuation more than expected since the flexures were slightly widened from 2 $\mu m$ to approximately 2.2 $\mu m$. This problem can be corrected in future fabrication runs by simply snapping the devices to the proper grid spacing in the layout editor and shaping the angles of the flexures within the grid.

The ideal models developed in this thesis appear to describe the behavior of the Flexure-Beam and Cantilever devices quite well. Unfortunately, these models require a

calibration of the device in order to establish the spring constant that describes its behavior. As a result, the advanced model was designed to determine this constant from the information provided by the foundry such that no measurements must be taken. The model includes the realistic effects of fringing electric fields, cross-talk between devices, ambient temperature, driving frequency, and surface deformations of the mirror. Although the model properly includes the effects of these physical principles, the formula which determines the spring constant of the flexures does not include the effects of how the flexures are shaped. According to this formula, all flexures having the same length, width, thickness, and material properties should behave the same. As observed with some of the torsion-style Cantilever devices, however, this may not be true if the flexures are shaped differently. As a result, the model falls short of completeness based on the determination of the spring constant for a given device. Similarly, the extraction of the thin-film elastic modulus for the flexures contains the same error in the measurement.

The experimental setup used to measure the behavior of the devices in this thesis seems to work quite well such that the characteristic curve can be generated from the interference pattern observed by the detector with a 50 dB signal-to-noise ratio. This corresponds to less than one percent error in the generation of the deflection curve versus address potential using a $\lambda = 632.8$ nm laser which was verified with a measured variance of approximately 4 nm for a given measurement. Several problems created by the nature of the system must be corrected in the software used to compute the behavior curves such as calibrating the deflection curve so that the deflection is zero when no address potential is applied. All significant problems were adequately corrected in the analysis software.

## (6.2) SUGGESTED IMPROVEMENTS

After nearly two years of micromirror research, it has become evident that certain factors in the design, fabrication, modeling, and testing of micromirror devices are far

more important than others or are simply vital to the success of the research. The expertise gained throughout the completion of this research and others must be passed to the follow-on researchers so that the net accumulation of knowledge of the subject matter continues to expand rather than be recreated. For this reason, suggested improvements are provided as a beginning for other engineers continuing micromirror research.

## *(6.2.1) CONTROL OF THE FABRICATION PROCESS*

In the design and implementation of micromirror devices, probably the most significant means of improvement for the future would be to gain control of the fabrication process. In the past, the fabrication of devices was dependent upon a single foundry in which no manipulation of the fabrication process is allowed. As a result, the ability to design micromirror devices with specific capabilities and features is limited.

For instance, one of the most common considerations in the design process of micromirror devices is the desire to keep the address potential low while maximizing the active area of an array of devices. In order to lower the voltage required to actuate many devices, however, the flexures supporting them had to be significantly lengthened to the extent that much of the layout was devoted to the flexures rather than to the mirrors. With no control of the fabrication process, this sacrifice had to be made in order to avoid very large address potentials. However, if the thickness of the flexures was even slightly reduced, the resulting change in the spring constant of the device would be such that much smaller flexures could be used to support the device which would require significantly less voltage to achieve a desired deflection. Therefore, by reducing the thickness of only one deposited layer in the fabrication process, two significant design considerations can be met. Control of other factors such as the number of releasable layers or the type of metal used in the fabrication process could be equally advantageous.

### (6.2.2) BETTER TEST EQUIPMENT

One of the main sources of noise in the experimental system is the test equipment such as the signal generator and the input and output signal amplifiers. The WaveTek signal generator has a maximum wave form amplitude of only 11 volts making the input amplifier necessary. Furthermore, the DC bias control on the generator is limited such that the signal does not achieve a completely positive wave form making the voltage shifter within the amplifier necessary. A high-voltage signal generator would make the input amplifier obsolete and would allow for direct manipulation of the DC offset of the signal. This would reduce much of the noise and capacitive delay of the test signals by eliminating its primary source, the transformer and voltage shifter of the input amplifier.

Likewise, the transimpedance amplifier used to convert the detector current to the output signal is a home-made circuit that possesses somewhat limited characteristics. It would be desirable to acquire a commercially-made amplifier that has a pre-amp stage for noise reduction. It is hoped that this amplifier would not display some of the capacitive side-effects observed in the existing circuit which must be corrected in the software.

Finally, the objective used on the microscope has a beam splitter within its optical path in order to let light enter from an aperture located on the side of the objective. It has been observed that this objective contains some amount of particulate matter that could possibly alter the properties of a portion of the light passing through the splitter. A new or rebuilt objective would be a good improvement for the system.

### (6.2.3) FOURIER TRANSFORM NOISE ANALYSIS

In order to obtain better characteristic curves of device behavior, it is suggested that a discrete Fourier transform be used to convert the time domain data to its frequency transform at which point the high-frequency noise and other discontinuities can be removed. These transforms could easily be added to the analysis software.

First, several periods of the input and output traces are captured from the oscilloscope and averaged within each period as previously described. After translating and shifting the traces so that the first point corresponds to the starting test voltage, the arrays of points are then concatenated with themselves so that a new array exists for each signal that contains ten identical periods forming a continuous trace. With these new data arrays, the first transform is used to convert the points to the frequency domain such that

$$F(n) = \sum_{k=0}^{N-1} f(k) \left[ \exp\left(-i\frac{2\pi}{N}\right) \right]^{nk} = \sum_{k=0}^{N-1} f(k) \left[ \cos\left(\frac{2nk\pi}{N}\right) - i\sin\left(\frac{2nk\pi}{N}\right) \right] \quad (6.1)$$

where $F(n)$ is the frequency data array and its index, $f(k)$ is the time data array and its index, and $N$ is the total number of points in each index. The frequency arrays contain complex numbers whose magnitude represents the significance of a given frequency on the original signal. The frequency step between each point in the new arrays is given by

$$\Delta F = \frac{1}{N\Delta t} = \frac{1}{T_{Span}} \quad (6.2)$$

where $\Delta t$ is the time step between points in the time array and $T_{Span}$ is the total time span represented in the original arrays. Since the time domain arrays contain ten identical periods, the frequency arrays will contain peaks at every tenth frequency interval. The high frequency peaks represent noise in the signal while non-zero values at frequencies other than multiples of ten are indicative of random discontinuities. By defining a frequency threshold above which the points are set to zero, the noise is filtered from the data. Likewise, the points at frequencies other than multiples of ten are also set to zero. At this point, the reverse transform is used to return the data to the time domain such that

$$f(k) = \frac{1}{N} \sum_{n=0}^{N-1} F(n) \left[ \exp\left(i\frac{2\pi}{N}\right) \right]^{nk} = \frac{1}{N} \sum_{n=0}^{N-1} F(n) \left[ \cos\left(\frac{2nk\pi}{N}\right) + i\sin\left(\frac{2nk\pi}{N}\right) \right] \quad (6.3)$$

which will most likely produce complex numbers since the frequency domain data was manually altered. The magnitude of these arrays represents the time domain data which is then averaged between the ten periods of the array to produce a final period of input and output data. This data should maintain the primary characteristics of the original traces

with only sharp discontinuities and high-frequency noise removed. It should be noted that this analysis on an ideal sine wave input signal will produce only one non-zero point in the frequency domain. This technique can be used to idealize the drive signal to generate more continuous plots of deflection versus address potential.

### (6.2.4) USING A DC BIAS

In the operation and testing of micromirror devices, the best range of actuation does not necessarily start at zero voltage. Since the full range of motion of most micromirror devices is significantly greater than the range of desired deflection distance, a bias can be added to the address signal to shift the operation up the behavior curve.
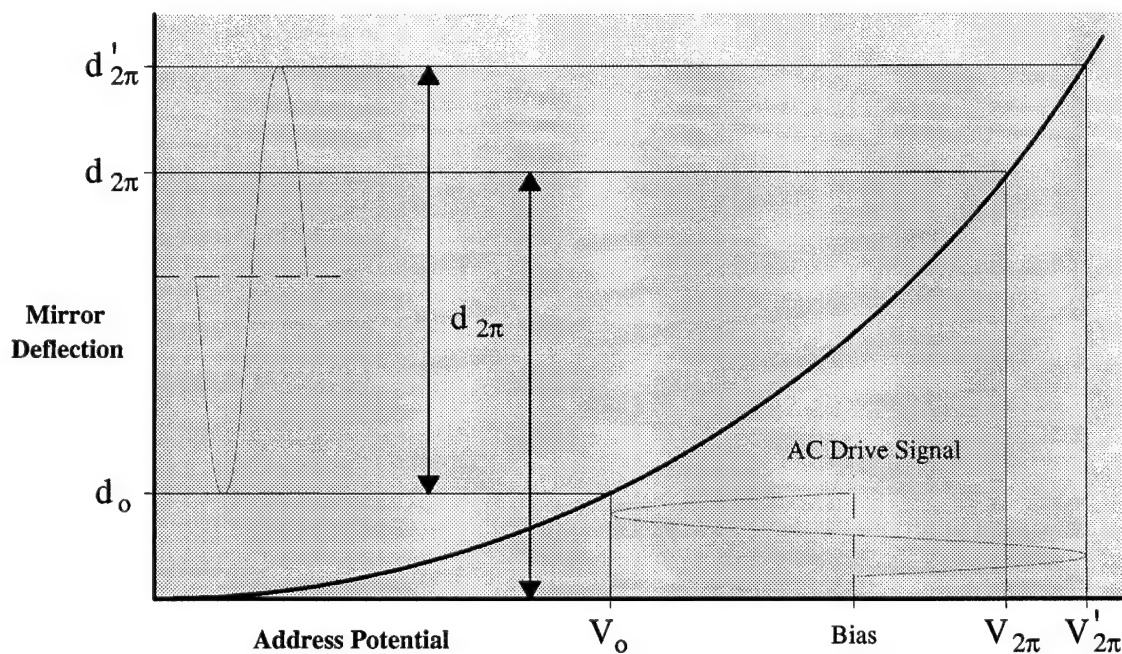


**Figure 6-1.** Shifting the operating range of a micromirror device up the behavior curve.

The resulting range of deflection of the device still provides $2\pi$ modulation, but the starting deflection is no longer at the resting position. At some new starting voltage, $V_o$, the resting deflection is $d_o$ which can be calibrated simply by setting the bias level. The

most significant change in the operational characteristics of the device is the reduction of the amplitude of the drive signal. The original address potential ranged from zero to $V_{2\pi}$ which requires a large sinusoidal drive signal. After adding a bias, the drive signal is shifted to a range from $V_o$ to $V'_{2\pi}$ which significantly reduces the amplitude of the signal. In addition, the effects of cross-talk and device instability which are only present at very low address potentials can be eliminated since the device remains actuated.

## (6.3) SUGGESTED FUTURE RESEARCH

As is typical in most fields of engineering, the number of possible research endeavors significantly outnumbers those than can be adequately studied with the resources available. For this reason, several specific research topics are highlighted which are considered the most significant of those under consideration. The suggested research described in this chapter is intended to provide an idea of what is considered important if this research is to continue in the near future.

## (6.3.1) HIDDEN FLEXURE DEVICES

As described above, gaining control of the fabrication process is most likely the single greatest improvement which can be made of the current micromirror research. In doing so, the possibility arises to design and fabricate devices that have new modes of operation and significantly more benefits than current designs. Among these devices are hidden flexure micromirrors in which the flexures supporting the mirrors are located beneath the mirror. As a result, neighboring devices can be placed immediately adjacent to each other such that no active area of the chip is lost to support posts or flexures. The optical efficiency of an array of these micromirrors would be significantly greater than those of current device.

The commercial fabrication process currently used has only two releasable layers from which to form the device. Therefore, the hidden flexures must be made from the Poly-1 layer which is the second layer of polysilicon. The mirror is attached to the flexures at the corner of the device by a Poly1-2 Via that removes the oxide spacer immediately after the deposition and masking of the Poly-1 layer. As the Poly-2 is deposited, it conforms to the via cut thereby joining with the flexure. Figure 6-2 shows a hypothetical device as it would look using the current fabrication process from MCNC.
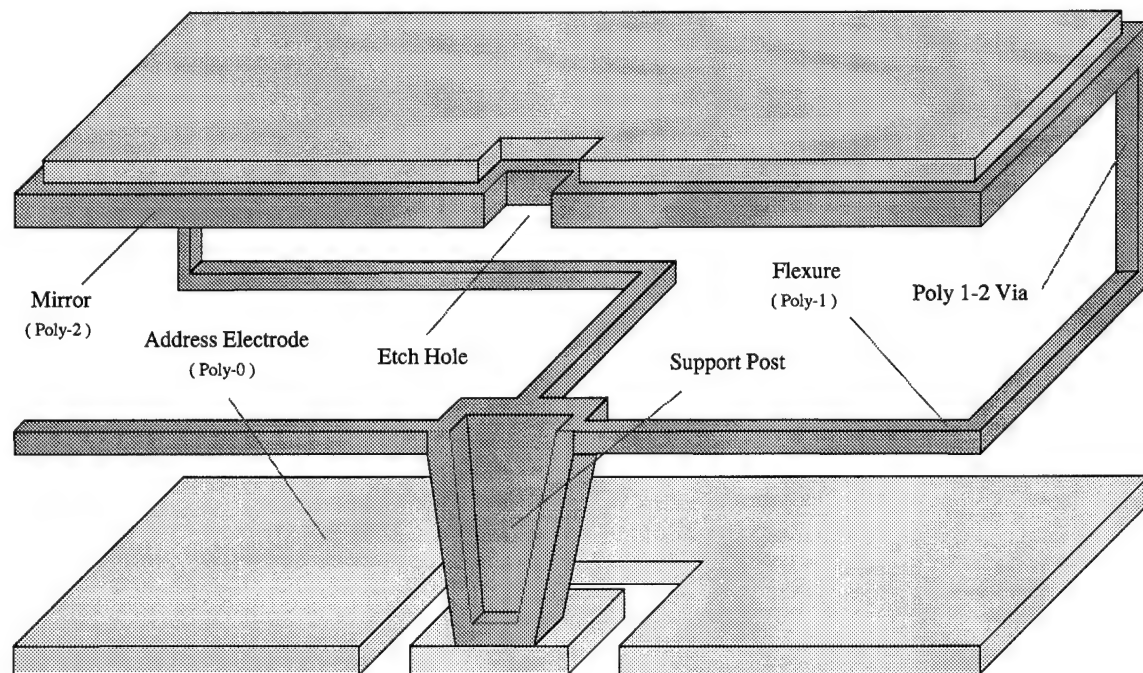


**Figure 6-2.** Suggested use of Poly-1 flexures for a hidden flexure micromirror device.

The thickness of the Poly-1 layer is much greater than Poly-2 which is normally used to make the flexures. As given in Eq. (3.68), the spring constant of the device is significantly greater since it is a third-order function of the flexure thickness. Therefore, the potential required to activate this device would be much greater. Control of the fabrication process, however, would provide the freedom to make this layer thinner by which hidden flexure devices could easily be made.

*(6.3.2) TEMPERATURE AND FREQUENCY EFFECTS*

Since the experimental setup did not allow for the direct testing of the temperature and frequency effects on the behavior of micromirror devices, some other means of observing them should be obtained. For this purpose, a variation of the experimental setup could be made in which the device under test rests in a temperature controlled chamber with a window through which the laser will pass. Likewise, new signal generation and amplification techniques could remove the frequency limit on the current setup in order to actuate the device near resonance.

*(6.3.3) SHAPE OF FLEXURES AND THIN-FILM ANALYSIS*

As observed with the torsion-style Cantilever devices, flexures of the same length do not necessarily behave the same if they are shaped differently. For this reason, it is expected that the behavior of the devices in Fig. 6-3 would vary according to their shape.
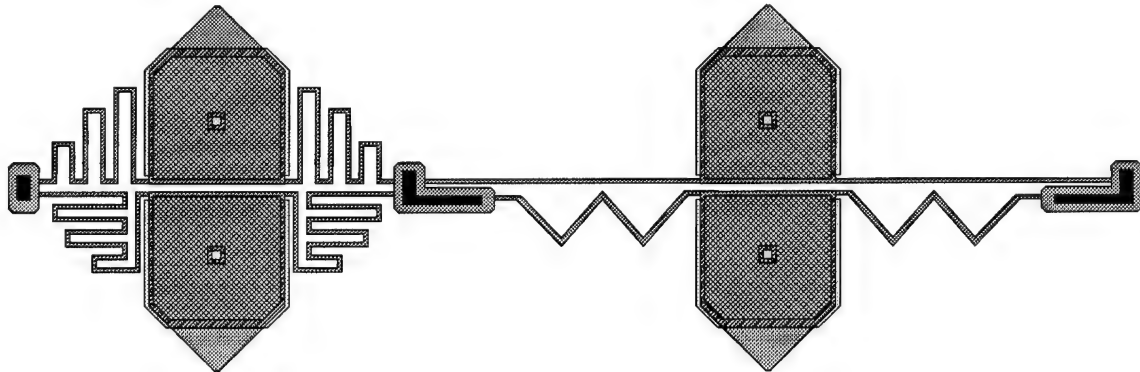


Figure 6-3. Cantilever devices with various shapes of flexures having the same length.

The flexures shown in Fig. 6-3 are intended to depict a variety of shapes and are assumed to be the same length. Since the extraction of the thin-film modulus of elasticity depends on observations of a particular device, the effects of the shape of the flexures can be propagated through the extracted value such that an error is introduced between devices.

In order to remove this error and allow for the accurate use of the advanced Flexure-Beam model, the spring constant must be determined as a function of the shape of the flexure as well as its geometric proportions. This should include the analysis of each segment of the flexure such that the compound effect of all forces and torques produced within the flexure due to actuation of the device can be accounted for. For this reason, a simplified method of finite element analysis would be beneficial such that the behavior of each segment of the flexure is dependent on the behavior of that segment given the conditions at its end points. As a result, the analysis of each segment can be reduced to the beam theory used to develop the current spring constant relationships. The final value of the spring constant would then become a function of the conditions at each node of the flexure which includes the length, angle, and direction of its layout.

Once the actual spring constant is determined based on the design of the flexures, the extraction of the thin-film elastic modulus becomes a trivial observation. As a result, the modulus can be measured using various devices from different fabrication runs so that a function of the thin-film effects on the value of the modulus of elasticity of the flexure material can be determined. This function will include such parameters as the exact density of the flexure material, the temperature at which the device was annealed, and the resulting stress induced in the structure due to the various steps of the fabrication process. This information can be provided by the foundry for each fabrication run.

# References

[1]     R. H. Freeman and J. E. Pearson, *"Deformable mirrors for all seasons and reasons,"* Applied Optics, vol. 21, pp. 580-588, Feb. 15, 1982.

[2]     L. J. Hornbeck, *"Deformable mirror spatial light modulators,"* in Proc. SPIE , vol. 1150, pp. 86-102, 1990.

[3]     J. M. Florence, T. H. Lin, and W. R Wu, *"Improved DMD configurations for image correlation,"* in Proc. SPIE, vol. 1296, pp. 101-109, 1990.

[4]     T. H. Lin, *"Implementation and characterization of a flexure-beam micromirror spatial light modulator,"* in Optical Engineering, vol. 33, pp. 3643-3648, Nov. 1994.

[5]     R. W. Cohn and J. B. Sampsell, *"Random phase errors and pseudo-random phase modulation of deformable mirror spatial light modulators,"* in Proc. SPIE, vol. 1772, pp. 34-42, 1992.

[6]     T. A. Rhoadarmer, V. M. Bright, B. M. Welsh, S. C. Gustafson, and T. H. Lin, *"Interferometric characterization of the flexure beam micromirror device,"* in Proc. SPIE, Vol. 2291, 1994, pp. 13-23.

[7]     D. A. Gregory and R. D. Juday, *"Optical characteristics of a deformable-mirror spatial light modulator,"* Optics Letters, vol. 13, pp. 10-12, Jan. 1988.

[8]     D. R. Pape and L. J. Hornbeck, *"Characteristics of the deformable mirror device for optical information processing,"* Optical Engineering, vol. 22, pp. 675-681, Nov./Dec., 1983.

[9]     J. M. Younse, *"Mirrors on a chip,"* IEEE Spectrum, pp. 27-31, Nov., 1993.

[10]    R. M. Boysel, J. M. Florence, and W. R. Wu, *"Deformable mirror light modulators for image processing."* in Proc. SPIE, vol. 1151, pp. 183-194, 1989.

[11]    H. S. Hinton. An Introduction to Photonic Switching Fabrics. Plenum Press, New York, 1993.

[12]    M. R. Boyd, S. B. Crary, and M. D. Giles, *"A heuristic approach to the electromechanical modeling of MEMs beams,"* Solid-State Sensors and Actuator Workshop, 1994.

[13] P. Lorrain, D. R. Corson, and F. Lorrain. Electromagnetic Fields and Waves. 3rd Ed. W. H. Freeman and Company, New York, 1988.

[14] R. A. Serway. Physics for Scientists and Engineers. 2 ed. Suanders College Publishing, Philadelphia, 1986.

[15] H. B. Palmer, *"The Capacitance of a parallel-plate capacitor by the Schwartz-Christoffel transformation,"* in Electrical Engineering, pp. 363-366, March 1937.

[16] P. M. Morse and H. Feshbach. Methods of Theoretical Physics. McGraw-Hill, New York, 1953.

[17] D. R. Lide, ed. CRC Handbook of Chemistry and Physics. 71 ed. CRC Press, Boston, 1990.

[18] M. Abramowitz and I. A. Stegun. Handbook of Mathematical Functions. Dover Publications, New York, 1972.

[19] K. K. Stevens. Statics & Strength of Materials. 2 ed. Prentice-Hall, Englewood Cliffs, New Jersey, 1987.

[20] J. B. Marion and S. T. Thornton. Classical Dynamics of Particles & Systems. 3 ed. Harcourt Brace Jovanovich, San Diego, 1988.

[21] Cadence Layout Editor, ver. 9201, Cadence Design Systems, San Jose, CA.

[22] SPICE Simulation Software, ver. H92, Meta-Software, Inc. Campbell, CA.

[23] A. S. Sedra and K. C. Smith. Microelectronic Circuits. 3 ed. Harcourt Brace College Publications, Fort Worth, TX, 1991.

[24] LeCroy 7200 Oscilloscope, PC Connect Software, LeCroy, Inc, Kansas City, MO.

[25] Turbo Pascal, ver. 5.5, Borland Corporation, Santee, CA.

[26] Microsoft Excel, ver. 4.0, Microsoft Corporation, Seattle, WA.

[27] P. M. Osterberg, R. K. Gupta, J. R. Gilbert, and S. D. Senturia, *"Quantitative models for the measurement of residual stress, Poisson ratio and Young's modulus using electrostatic pull-in of beams and diaphrams,"* Solid-State Sensors and Actuator Workshop, pp. 184-188, 1994.

[28] P. Osterberg, H. Yie, X. Cai, J. White, and S. Senturia, "Self-consistent simulation and modeling of electrostatically deformed diaphrams," in Proc. MEMS, Oiso, Japan, 1994

[29] W. A. Brantley, "*Calculated elastic constants for stress problems associated with semiconductor devices*," Journal of Applied Physics, vol. 44, pp 534-535, 1973.

[30] D. C. Giancoli. Physics Principles with Applications. 2 ed. Prentice-Hall, Englewood Cliffs, New Jersey, 1985.

[31] D. Halliday and R. Resnick. Fundamentals of Physics. 3 ed. Wiley and Sons, New York, 1988.

[32] G. B. Arfken and D. F. Griffing. University Phyisics. Academic Press, New York, 1984.

[33] S. E. Koonin and D. C. Meredith. Computational Physics. Addison-Wesley, New York, 1990.

[34] L. J. Hornbeck, "*128 x 128 deformable mirror device*," IEEE Transactions on Electronic Devices, vol. ED-30, pp. 539-545, May 5, 1983.

[35] J. E. Cravatt and M. K. Giles, "*An improved model for the TI deformable mirror device*," in Proc. SPIE, vol. 1296, pp. 110-124, 1990.

[36] J. M. Florence, M. K. Giles, and J. Z. Smith, "*Operation of a deformable mirror device as a Fourier plane phase modulating filter*," in Proc. SPIE, vol. 938, pp. 2-10, 1988.

[37] W. R. Wu, R. O. Gale, L. J. Hornbeck, and J. B. Sampsell, "*Electro-optical performance of an improved deformable mirror device*," in Proc. SPIE, vol. 825, pp. 24-31, 1987.

[38] R. W. Cohn and J. B. Sampsell, "*Deformable mirror device uses in frequency excision and optical switching*," Applied Optics, vol. 27, pp. 937-940, Mar. 1, 1988.

[39] P. B. Zhou. Numerical Analysis of Electromagnetic Fields. Springer, Berlin, 1993.

[40] D. H. Trevena. Static Fields in Electricity and Magnetism. Butterworths, London, 1961.

[41] K. Polivanov. The Theory of Electromagnetic Fields. Mir Publishers, Moscow, 1983.

[42] P. Lorrain and D. R. Corson. Electromagnetic Fields and Waves. 2nd Ed. W. H. Freeman and Company, New York, 1962.

[43] M. Zahn. Electromagnetic Field Theory: A Problem Solving Approach. Wiley and Sons, New York, 1979.

[44]   H. A. Haus and J. R. Melcher. <u>Electromagnetic Fields and Energy</u>. Prentice Hall, New Jersey, 1989.

[45]   M. V. K. Chari and P. P. Silvester. <u>Finite Elements in Electrical and Magnetic Field Problems</u>. Wiley and Sons, New York, 1980.

[46]   R. K. Wangsness. <u>Electromagnetic Fields</u>. Wiley and Sons, New York, 1979.

[47]   J. M. Crowley. <u>Fundamentals of Applied Electrostatics</u>. Wiley and Sons, New York, 1986.

[48]   K. J. Binns and P. J. Lawrenson. <u>Analysis and Computation of Electric and Magnetic Field Problems</u>. 2nd Ed. Pergamon Press, New York, 1973.

[49]   R. F. Graf. <u>Encyclopedia of Electronic Circuits.</u> vol. I, Tab Books, Blue Ridge Summit, PA, 1985.

# *APPENDIX*

# (A)

## Analysis Software

```pascal
PROGRAM ScopeTraces;

Uses CRT, DOS;

CONST

  MaxChartPoints = 250;

  WaveLength = 632.8;          { Deflection is calculated in nano-meters! }

  OpsDirectory      = 'C:\ADRIAN\DMD\OPS';
  RawDataDirectory  = 'C:\ADRIAN\DMD\RAWDATA';
  AnalysisDirectory = 'C:\ADRIAN\DMD\ANALYSIS';

  InputSignalFileName  = 'INPUT.TXT';
  OutputSignalFileName = 'OUTPUT.TXT';
  HeaderFileName       = 'HEADER.TXT';

  MaxNumberOfPoints  = 4000;                { Points Per Acquired Trace  }
  MaxNumberPerPeriod = 1250;                { Points Per Averaged Period }
  MaxNumberOfPeriods = 8;                   { Periods Per Acquired Trace }

  { Error Check These During Operation - Exit If Violated! }

TYPE

  DataArrayType = ARRAY [ 1 .. MaxNumberOfPoints + 1 ] of REAL;

VAR

  Input, Output                              : DataArrayType;

  Time, FileName, FileDirectory,
  TestChip, TestStructure, PixelLocation     : STRING[12];


  NumberPoints, PointsCaptured,
  OutputShift, NumberPerPeriod,
  FunctionalPoints, NegativeInputPoints      : INTEGER;

  TimeSpan, TimePerPoint, InputFrequency     : REAL;

  MemoryPointer                              : POINTER;

  GlobalIndex, TempIndex : INTEGER;

(*********************************************************************)

FUNCTION ArcCos ( InValue : REAL ) : REAL;

VAR
  Delta, TempValue  : REAL;

BEGIN

  Delta := SQR( InValue );
  If Delta > 1 then TempValue := 99
  ELSE If Delta = 1 then
    TempValue := InValue * ( PI / 2 )
  ELSE TempValue := ArcTan( InValue / SQRT( 1 - Delta ) );
  ArcCos := ( PI / 2 ) - TempValue;

END;

(*********************************************************************)
```

```
(*************************************************************************)

PROCEDURE GetOpsInformation;

  { This program evaluates the Date, Time, and output FileName that }
  { will be used by the other procedures throughout this program.   }

VAR

  Year, Month, Day, DayofWeek,
  Hour, Minute, Second, Sec100           : WORD;

  DayString, MonthString, YearString     : STRING[4];

BEGIN

  GetDate(Year,Month,Day,DayofWeek);
  GetTime(Hour,Minute,Second,Sec100);
  Year := Year - 1900;
  Case Month of
     1 : MonthString := 'JAN';        2 : MonthString := 'FEB';
     3 : MonthString := 'MAR';        4 : MonthString := 'APR';
     5 : MonthString := 'MAY';        6 : MonthString := 'JUN';
     7 : MonthString := 'JUL';        8 : MonthString := 'AUG';
     9 : MonthString := 'SEP';       10 : MonthString := 'OCT';
    11 : MonthString := 'NOV';       12 : MonthString := 'DEC';
  END;

  STR(Hour*100+Minute,Time);
  STR(Year,YearString);
  STR(Day,DayString);
  If Length(DayString) = 1 then Insert('0',DayString,1);

  FileDirectory := CONCAT(DayString,MonthString,YearString);

END;

(*************************************************************************)

PROCEDURE SelectOutputFile;

VAR TraceLetter    : CHAR;
    FileInfo       : SearchRec;  { Internally Declared DOS Record Type }

  { This procedure searches for files with the current output file name }
  { to avoid overwriting them, selects the new file name, and searches  }
  { for the appropriate file directory.  If the directory is not found, }
  { it is created using the file name under the RAWDATA root directory.  }

BEGIN

  WRITELN;
  WRITE('Selecting Output File Name ... ');
  Delay(1000);

  ChDir(AnalysisDirectory);

  FindFirst(FileDirectory,Directory,FileInfo);
  If DosError <> 0 then
    BEGIN
      MkDir(FileDirectory);
      ChDir(RawDataDirectory);
      MkDir(FileDirectory);
    END;
```

```pascal
    ChDir(FileDirectory);

    FileName := FileDirectory;
    FindFirst(CONCAT(FileName,'?.CSV'),AnyFile,FileInfo);
    Case DosError of
       0 : BEGIN

                { The TraceLetter is assigned as the the character found   }
                { immediately after the date of the filename.  For example, }
                { the file '10JAN95a.CSV' would return the 'a' character.    }

                { The following WHILE loop searches all the files in the    }
                { given directory to find the highest trace letter index.   }

                TraceLetter := FileInfo.Name[8];
                While DosError = 0 DO
                  BEGIN
                    FindNext(FileInfo);
                    If FileInfo.Name[8] > TraceLetter then
                      TraceLetter := FileInfo.Name[8];
                  END;
                INC(TraceLetter);
             END;
      18 : TraceLetter := 'A';
    END;

    FileName := CONCAT(FileName,TraceLetter,'.CSV');

END;

(**************************************************************************)

PROCEDURE GetHeaderData;

VAR HeaderFile            : TEXT;
    TimeUnitMagnitude     : REAL;
    DataTransferValue     : STRING;
    HeaderIndex, Error    : INTEGER;

 { This procedure evaluates the PointsCaptured and TimeSpan by reading }
 { the values from the header file generated by the WAVETRAN program.  }

BEGIN

  WRITELN;
  WRITELN;
  WRITE('Reading Header Information ... ');
  Delay(1000);

  ChDir(RawDataDirectory);

  Assign(HeaderFile,HeaderFileName);
  RESET(HeaderFile);

  For HeaderIndex := 1 to 6 DO READLN(HeaderFile);
  READLN(HeaderFile,DataTransferValue);
  Delete(DataTransferValue,1,59);
  HeaderIndex := 1;
  REPEAT
    If DataTransferValue[HeaderIndex] = ' ' then
      Delete(DataTransferValue,HeaderIndex,1)
    ELSE INC(HeaderIndex);
  Until HeaderIndex = Length(DataTransferValue) + 1;

  VAL(DataTransferValue,PointsCaptured,Error);
```

```
   For HeaderIndex := 1 to 11 DO READLN(HeaderFile);
   READLN(HeaderFile,DataTransferValue);
   Delete(DataTransferValue,1,59);
   TimeUnitMagnitude := 0;
   HeaderIndex := 1;
   REPEAT
     Case DataTransferValue[HeaderIndex] of
       '_' : BEGIN
               Case DataTransferValue[HeaderIndex+1] of
                 's' : TimeUnitMagnitude := 1;
                 'm' : TimeUnitMagnitude := 1e-3;
                 'u' : TimeUnitMagnitude := 1e-6;
                 'n' : TimeUnitMagnitude := 1e-9;
                 'p' : TimeUnitMagnitude := 1e-12;
               END;
               DataTransferValue := COPY(DataTransferValue,1,HeaderIndex-1);
             END;
       '.' : If HeaderIndex = 1 then Insert('0',DataTransferValue,0);
     END;
     INC(HeaderIndex);
   Until DataTransferValue[HeaderIndex-1] = '_';
   VAL(DataTransferValue,TimeSpan,Error);
   TimeSpan := TimeSpan * 10 * TimeUnitMagnitude;

   Close(HeaderFile);

END;

(*********************************************************************)

PROCEDURE FixInputSignal;

VAR FixIndex                           : INTEGER;
    DiodeVoltageDrop, Minimum          : REAL;

 { This procedure is only used when the input signal is AC coupled to }
 { the oscilloscope due to the limiting range of the vertical shift.  }

BEGIN

  WRITELN;
  WRITELN;
  WRITE('Diode Voltage Drop:  ');
  READLN(DiodeVoltageDrop);
  WRITELN;
  WRITE('Shifting AC Input To DC Signal . . . ');

  DiodeVoltageDrop := ABS(DiodeVoltageDrop);

  Minimum := Input[100];
  For FixIndex := 100 to NumberPoints - 100 DO
    If Input[FixIndex] < Minimum then Minimum := Input[FixIndex];

  WRITELN;
  WRITELN;
  WRITELN('Old Min :   ', Minimum:8:8);
  WRITELN;

  For FixIndex := 1 to NumberPoints DO
    Input[FixIndex] := Input[FixIndex] - Minimum - DiodeVoltageDrop;

  Minimum := Input[100];
  For FixIndex := 100 to NumberPoints - 100 DO
    If Input[FixIndex] < Minimum then Minimum := Input[FixIndex];
```

A-5

```
      WRITELN('New Min :    ', Minimum:8:8);
      WRITELN;

      Delay(250);

   END;

   (********************************************************************)

   PROCEDURE GetSignalData;

   VAR SignalFile                         : TEXT;
       DataTransferValue                  : STRING;
       TimePerPoint, MinimumInput         : REAL;
       SignalIndex, Error, DataPoint      : INTEGER;

       { This procedure opens the input data file and reads the text value }
       { of each data point.  Each value is first converted to its numeric }
       { representation and then loaded into the RawTimeData array.         }

   BEGIN

      MinimumInput := 0;

      WRITELN;
      WRITELN;
      WRITE('Reading Signal Data ... ');
      Delay(1000);

      ChDir(RawDataDirectory);

      Assign(SignalFile,InputSignalFileName);
      RESET(SignalFile);

      DataPoint := 0;
      While (NOT(EOF(SignalFile))) and (DataPoint < MaxNumberOfPoints) DO
        BEGIN
          INC(DataPoint);
          READLN(SignalFile,DataTransferValue);
          SignalIndex := 1;
          REPEAT
            If DataTransferValue[SignalIndex] = ' ' then
              Delete(DataTransferValue,SignalIndex,1)
            ELSE INC(SignalIndex);
          Until SignalIndex = Length(DataTransferValue) + 1;
          VAL(DataTransferValue,Input[DataPoint],Error);
          If Error <> 0 then
            BEGIN
              WRITELN;
              WRITELN('    **** Error In Variable Conversion! ****');
              WRITELN;
              WRITELN('    STRING type variable read from text file not ');
              WRITELN('    converted to REAL type numeric representation!');
              WRITELN;
            END
          ELSE If Input[DataPoint] < MinimumInput then
            MinimumInput := Input[DataPoint];
        END;

      Close(SignalFile);

      NumberPoints := DataPoint;

      If MinimumInput < - 1 then FixInputSignal;
```

A-6

```
      Assign(SignalFile,OutputSignalFileName);
      RESET(SignalFile);

      DataPoint := 0;
      While (NOT(EOF(SignalFile))) and (DataPoint < MaxNumberOfPoints) DO
        BEGIN
          INC(DataPoint);
          READLN(SignalFile,DataTransferValue);
          SignalIndex := 1;
          REPEAT
            If DataTransferValue[SignalIndex] = ' ' then
              Delete(DataTransferValue,SignalIndex,1)
            ELSE INC(SignalIndex);
          Until SignalIndex = Length(DataTransferValue) + 1;
          VAL(DataTransferValue,Output[DataPoint],Error);
          If Error <> 0 then
            BEGIN
              WRITELN;
              WRITELN('    **** Error In Variable Conversion! ****');
              WRITELN;
              WRITELN('    STRING type variable read from text file not ');
              WRITELN('    converted to REAL type numeric representation!');
              WRITELN;
            END;
        END;

      Close(SignalFile);

      If DataPoint < NumberPoints then NumberPoints := DataPoint;

      TimePerPoint := TimeSpan / PointsCaptured;

      WRITELN;
      WRITELN;
      WRITE('Storing Raw Data ...');
      Delay(1000);

      ChDir(FileDirectory);

      ASSIGN(SignalFile,FileName);
      REWRITE(SignalFile);

      WRITELN(SignalFile);
      WRITELN(SignalFile,'Time,Input,Output');
      WRITELN(SignalFile,'(ms),(Volts),(Volts)');
      WRITELN(SignalFile);

      For SignalIndex := 1 to NumberPoints DO
        BEGIN
          WRITE(SignalFile,SignalIndex*TimePerPoint*1000:6:6,',');
          WRITE(SignalFile,Input[SignalIndex]:6:6,',');
          WRITELN(SignalFile,Output[SignalIndex]:6:6);
        END;

      Close(SignalFile);

END;

(**********************************************************************)

PROCEDURE WriteOutputHeader;

VAR
  OutputFile  : TEXT;
```

```
    NumberPeriods : REAL;

    { This procedure writes the header information to the output file.    }
    { The output file will later be appended with the experimental data. }

BEGIN

  WRITELN;
  WRITELN('Writing Output Header Data ... ');
  Delay(1000);

  ChDir(CONCAT(AnalysisDirectory,'\',FileDirectory));

  NumberPeriods := NumberPoints / NumberPerPeriod;

  Assign(OutputFile,FileName);
  REWRITE(OutputFile);

  WRITELN(OutputFile);
  WRITELN(OutputFile,'M Adrian Michalicek');
  WRITELN(OutputFile);
  WRITELN(OutputFile,'Test Chip:,,',TestChip);
  WRITELN(OutputFile,'Test Structure:,,',TestStructure);
  WRITELN(OutputFile,'Pixel Location:,,',PixelLocation);
  WRITELN(OutputFile);
  WRITELN(OutputFile,'Sample Date:,,',FileDirectory);
  WRITELN(OutputFile,'Sample Time:,,',Time);
  WRITELN(OutputFile);
  WRITELN(OutputFile,'Points Captured:,,',PointsCaptured);
  WRITELN(OutputFile,'Points Averaged:,,',NumberPoints);
  WRITELN(OutputFile,'Points Per Period:,,',NumberPerPeriod);
  WRITELN(OutputFile,'Points Analyzed:,,',FunctionalPoints);
  WRITELN(OutputFile,'Points Shifted:,,',OutputShift);
  WRITELN(OutputFile);
  WRITELN(OutputFile,'Time Span (ms):,,',TimeSpan*1000:4:4);
  WRITELN(OutputFile,'Frequency (Hz):,,',InputFrequency:2:2);
  WRITELN(OutputFile,'Periods Averaged:,,',NumberPeriods:2:2);
  WRITELN(OutputFile);
  WRITE(OutputFile,',Period,Period,Functional,Functional');
  WRITELN(OutputFile,',Chart,Chart,Chart,Smooth');
  WRITE(OutputFile,'Time,Input,Output,Input,Deflection');
  WRITELN(OutputFile,',Input,Output,Deflection,Deflection');
  WRITE(OutputFile,'(ms),(Volts),(Volts),(Volts),(nm)');
  WRITELN(OutputFile,',(Volts),(Volts),(nm),(nm)');
  WRITELN(OutputFile);

  Close(OutputFile);

END;

(*********************************************************************)

PROCEDURE WriteOutputData;

CONST  SigFigs : WORD = 6;

VAR
  OutputFile             : TEXT;
  DataTransferValue      : STRING;
  WriteIndex, Index      : WORD;

BEGIN

  WRITELN;
  WRITE('Writing Analysis Data To ',FileName,' ... ');
```

```
    Delay(1000);

    Assign(OutputFile,FileName);
    APPEND(OutputFile);

    For Index := 1 to NumberPerPeriod DO
      BEGIN

        { Time }

        STR(Index*TimePerPoint*1000:SigFigs:SigFigs,DataTransferValue);
        WRITE(OutputFile,DataTransferValue,',');

        { Period Input / Output }

        STR(Input[Index]:SigFigs:SigFigs,DataTransferValue);
        WRITE(OutputFile,DataTransferValue,',');
        STR(Output[Index]:SigFigs:SigFigs,DataTransferValue);
        WRITE(OutputFile,DataTransferValue,',');

        If Index = 1 then
          BEGIN
            WRITE(OutputFile,'   { Negative Input Points Neglected:');
            WRITE(OutputFile,',,,,',NegativeInputPoints,',');
            WRITE(OutputFile,'Points }');
          END
        ELSE If ( Index > 2 ) and ( Index <= FunctionalPoints + 2 ) then
          BEGIN

            { Functional Phase / Deflection }

            WriteIndex := Index + NumberPerPeriod - 2;
            STR(Input[WriteIndex]:SigFigs:SigFigs,DataTransferValue);
            WRITE(OutputFile,DataTransferValue);
            STR(Output[WriteIndex]:SigFigs:SigFigs,DataTransferValue);
            WRITE(OutputFile,',',DataTransferValue);

            { Chart Data }

            If Index <= ( MaxChartPoints + 2 ) then
              BEGIN
                WriteIndex := Index + NumberPerPeriod + FunctionalPoints;
                INC(WriteIndex,( ROUND( FunctionalPoints / 2 ) - 2 ) );
                STR(Input[WriteIndex]:SigFigs:SigFigs,DataTransferValue);
                WRITE(OutputFile,',',DataTransferValue);
                STR(Output[WriteIndex]:SigFigs:SigFigs,DataTransferValue);
                WRITE(OutputFile,',',DataTransferValue);
                INC(WriteIndex,MaxChartPoints);
                STR(Input[WriteIndex]:SigFigs:SigFigs,DataTransferValue);
                WRITE(OutputFile,',',DataTransferValue);
                STR(Output[WriteIndex]:SigFigs:SigFigs,DataTransferValue);
                WRITE(OutputFile,',',DataTransferValue);
              END;
          END;

        WRITELN(OutputFile);

      END;

    Close(OutputFile);

END;

(*********************************************************************)
```

```pascal
(*************************************************************************)

PROCEDURE ChopOffEndPoints;

VAR

  Index, ChopPoints : WORD;

BEGIN

  WRITELN;
  WRITELN;
  WRITE('Performing Numerical Analysis ... ');
  Delay(1000);

  { The first and last two percent of the points of each waveform are }
  { discarded to remove the transient effects of the scope waveforms. }

  ChopPoints := ROUND( 0.02 * PointsCaptured );
  NumberPoints := NumberPoints - 2 * ChopPoints;
  For Index := 1 to NumberPoints DO
    BEGIN
      Input[Index] := Input[Index + ChopPoints];
      Output[Index] := Output[Index + ChopPoints];
    END;

END;

(*************************************************************************)

PROCEDURE GetAverageWaveForms;

TYPE

  IndexArrayType = Array[ 1..( 2 * MaxNumberofPeriods + 1 ) ] of WORD;

VAR

  IndexArray                           : IndexArrayType;

  MidPointsFound, NumberSamples,
  Delta, Index, PeriodIndex            : WORD;

  VinMin, VinMax, VinMidPoint,
  ThisDelta, NextDelta, RunningSum     : SINGLE;

BEGIN

  { The input signal trace is scanned to find the maximum and minimum }
  { values.  The midpoint value is then calculated as their average.  }

  VinMin := Input[1];
  VinMax := Input[1];
  For Index := 2 to NumberPoints DO
    BEGIN
      If Input[Index] < VinMin then VinMin := Input[Index];
      If Input[Index] > VinMax then VinMax := Input[Index];
    END;
  VinMidPoint := ( VinMax + VinMin ) / 2;

  { The number of points between each sample of the input midpoint are }
  { counted.  The number of points between every other sample are then }
  { averaged to determine the number of points per period.  The input  }
  { signal frequency and the time between points are then calculated.  }
```

```
   MidPointsFound := 0;
   For Index := 1 to NumberPoints DO
     BEGIN
        ThisDelta := Input[Index] - VinMidPoint;
        NextDelta := Input[Index+1] - VinMidPoint;
        If ( ThisDelta * NextDelta ) <= 0 then
          BEGIN
            INC(MidPointsFound);
            If ABS(ThisDelta) > ABS(NextDelta) then INC(Index);
            IndexArray[MidPointsFound] := Index;
          END;
     END;
   NumberSamples := ROUND( ( MidPointsFound - 2 ) / 2 );
   RunningSum := 0;
   For Index := 1 to NumberSamples DO
     BEGIN
        Delta := IndexArray[(Index-1)*2+3] - IndexArray[(Index-1)*2+1];
        RunningSum := RunningSum + Delta;
     END;
   NumberPerPeriod := ROUND( RunningSum / NumberSamples );
   TimePerPoint := TimeSpan / PointsCaptured;
   InputFrequency := NumberSamples / ( RunningSum * TimePerPoint );

   { The input and output waveforms are averaged between each period  }
   { and placed in the second period of the corresponding array.      }

   For Index := 1 to NumberPerPeriod DO
     BEGIN
        RunningSum := 0;
        NumberSamples := 0;
        PeriodIndex := Index;
        REPEAT
          INC(NumberSamples);
          RunningSum := RunningSum + Input[PeriodIndex];
          INC(PeriodIndex,NumberPerPeriod);
        Until PeriodIndex > NumberPoints;
        Input[Index+NumberPerPeriod] := RunningSum / NumberSamples;
     END;
   For Index := 1 to NumberPerPeriod DO
     BEGIN
        RunningSum := 0;
        NumberSamples := 0;
        PeriodIndex := Index;
        REPEAT
          INC(NumberSamples);
          RunningSum := RunningSum + Output[PeriodIndex];
          INC(PeriodIndex,NumberPerPeriod);
        Until PeriodIndex > NumberPoints;
        Output[Index+NumberPerPeriod] := RunningSum / NumberSamples;
     END;

END;

(******************************************************************)

PROCEDURE GetOutputShift;

VAR

   Index, SampleIndex, Span,
   QuarterPeriod, ThreeQuarterPeriod               : WORD;

   Slope, OutputSample,
   VinMin, VinMax, VoutMin, VoutMax,
   VinMidPoint, ThisDelta, NextDelta               : REAL;
```

```
   { The output waveform must be shifted ahead in the time domain to   }
   { compensate for the delay due to the capacitance of the system.    }

BEGIN

   QuarterPeriod := ROUND( NumberPerPeriod / 4 );
   ThreeQuarterPeriod := ROUND( 3 * NumberPerPeriod / 4 );

   { The index of the first peak in the averaged input signal is found }
   { from the index and slope of the first midpoint.  The maximum and  }
   { minimum values of the input and output signals must also be found. }

   VinMin := Input[1];
   VinMax := Input[1];
   VoutMin := Output[1];
   VoutMax := Output[1];
   For Index := 2 to NumberPerPeriod DO
     BEGIN
        If Input[Index] < VinMin then VinMin := Input[Index];
        If Input[Index] > VinMax then VinMax := Input[Index];
        If Output[Index] < VoutMin then VoutMin := Output[Index];
        If Output[Index] > VoutMax then VoutMax := Output[Index];
     END;
   VinMidPoint := ( VinMax + VinMin ) / 2;

   Index := 0;
   REPEAT
     INC(Index);
     ThisDelta := Input[Index] - VinMidPoint;
     NextDelta := Input[Index+1] - VinMidPoint;
   Until ( ThisDelta * NextDelta ) <= 0;
   If ABS(ThisDelta) > ABS(NextDelta) then INC(Index);

   Slope := Input[Index+10] - Input[Index-10];
   If Slope > 0 then INC(Index,QuarterPeriod)
   ELSE If Index >= QuarterPeriod then DEC(Index,QuarterPeriod)
   ELSE INC(Index,ThreeQuarterPeriod);

   { At this index the output value and the slope are used to determine }
   { the output sample value which is given as the average between this }
   { point and the previous relative maximum or minimum of the output.  }

   Slope := Output[Index] - Output[Index-10];
   If Slope > 0 then
     OutputSample := ( Output[Index] + VoutMin ) / 2
   ELSE OutputSample := ( Output[Index] + VoutMax ) / 2;

   SampleIndex := Index;
   REPEAT
     DEC(SampleIndex);
     ThisDelta := Output[SampleIndex] - OutputSample;
     NextDelta := Output[SampleIndex+1] - OutputSample;
   Until (ThisDelta * NextDelta) <= 0;
   If ABS(ThisDelta) > ABS(NextDelta) then INC(SampleIndex);

   Span := Index - SampleIndex;
   Index := SampleIndex;
   SampleIndex := Index + Span;
   REPEAT
     INC(SampleIndex);
     ThisDelta := Output[SampleIndex] - OutputSample;
     NextDelta := Output[SampleIndex+1] - OutputSample;
   Until (ThisDelta * NextDelta) <= 0;
   If ABS(ThisDelta) > ABS(NextDelta) then INC(SampleIndex);
```

A-12

```
      OutputShift := ROUND( ( SampleIndex - Index ) / 2 - Span );

END;

(**********************************************************************)

PROCEDURE TranslateWaveForms;

VAR

   Index, PeriodIndex, Translate,
   QuarterPeriod, ThreeQuarterPeriod            : WORD;

   Slope, Amplify,
   VinMin, VinMax, VoutMin, VoutMax,
   VinMidPoint, ThisDelta, NextDelta            : REAL;

BEGIN

   QuarterPeriod := ROUND( NumberPerPeriod / 4 );
   ThreeQuarterPeriod := ROUND( 3 * NumberPerPeriod / 4 );

   { The index of the first valley of the averaged input waveform is  }
   { found from the index and slope of the first input midpoint.  The }
   { maximum and minimum values are again scanned for both waveforms.  }

   VinMin := Input[1];
   VinMax := Input[1];
   VoutMin := Output[1];
   VoutMax := Output[1];
   For Index := 2 to NumberPerPeriod DO
     BEGIN
       If Input[Index] < VinMin then VinMin := Input[Index];
       If Input[Index] > VinMax then VinMax := Input[Index];
       If Output[Index] < VoutMin then VoutMin := Output[Index];
       If Output[Index] > VoutMax then VoutMax := Output[Index];
     END;
   VinMidPoint := ( VinMax + VinMin ) / 2;

   Index := 0;
   REPEAT
     INC(Index);
     ThisDelta := Input[Index] - VinMidPoint;
     NextDelta := Input[Index+1] - VinMidPoint;
   Until ( ThisDelta * NextDelta ) <= 0;
   If ABS(ThisDelta) > ABS(NextDelta) then INC(Index);

   Slope := Input[Index+10] - Input[Index-10];
   If Slope < 0 then INC(Index,QuarterPeriod)
   ELSE If Index >= QuarterPeriod then DEC(Index,QuarterPeriod)
   ELSE INC(Index,ThreeQuarterPeriod);

   { The averaged input and output traces are translated into the first }
   { period of the corresponding array such that the first point of the }
   { input array is the minimum value of the ideal input.  The output   }
   { trace is also translated by the additional amount of OUTPUTSHIFT.   }

   PeriodIndex := Index;
   For Index := 1 to NumberPerPeriod DO
     BEGIN
       Translate := ( (PeriodIndex+Index-2) MOD NumberPerPeriod ) + 1;
       Input[Index] := Input[Translate+NumberPerPeriod];
       Translate := ((Translate+OutputShift-1) MOD NumberPerPeriod)+1;
       Output[Index] := Output[Translate+NumberPerPeriod];
```

A-13

```
      END;

   { The output array is amplified to match the positive input range. }
   { This minimum value is zero and the maximum value is PEAKVALUE.    }

   Amplify := VinMax / ( VoutMax - VoutMin );
   For Index := 1 to NumberPerPeriod DO
     Output[Index] := Amplify * ( Output[Index] - VoutMin );

END;

(*********************************************************************)

PROCEDURE IdealizeInputSignal;

VAR

   Index                    : WORD;

   VinMin, VinMax, Temp,
   VinMidPoint, Amplify     : REAL;

BEGIN

   { Due to the clipping effects of the transformer voltage generator }
   { of the voltage multiplier, the input waveform is replaced with a }
   { cosine wave given by the input frequency and time span.          }

   { This procedure is used only when the raw data is unusable! }

   VinMin := Input[NumberPerPeriod + 1];
   VinMax := Input[NumberPerPeriod + 1];
   For Index := ( NumberPerPeriod + 2 ) to ( 2 * NumberPerPeriod ) DO
     BEGIN
       If Input[Index] < VinMin then VinMin := Input[Index];
       If Input[Index] > VinMax then VinMax := Input[Index];
     END;

   Amplify := ( VinMax - VinMin ) / 2;
   VinMidPoint := ( VinMax + VinMin ) / 2;

   For Index := 1 to NumberPerPeriod DO
     BEGIN
       Temp := Cos( 2 * PI * Index / NumberPerPeriod );
       Input[Index] := -1 * Amplify * Temp + VinMidPoint;
     END;

END;

(*********************************************************************)

PROCEDURE GetPositiveInputPoints;

VAR Index : WORD;

BEGIN

   { The number of positive input points are found so as to determine  }
   { the range of functional data.  The phase and deflection arrays are }
   { calculated only from positive input points.  The functional input  }
   { and output arrays are placed in the second period of their array.  }

   NegativeInputPoints := 0;
   REPEAT
     INC(NegativeInputPoints);
```

A-14

```
      Until Input[NegativeInputPoints] >= 0;
      Index := NegativeInputPoints;

      DEC(NegativeInputPoints);

      FunctionalPoints := 0;
      While Input[Index] >= 0 DO
        BEGIN
          INC(FunctionalPoints);
          Input[NumberPerPeriod+FunctionalPoints] := Input[Index];
          Output[NumberPerPeriod+FunctionalPoints] := Output[Index];
          INC(Index);
        END;

END;

(*********************************************************************)

PROCEDURE GetResponseData;

VAR

  Sign : INTEGER;

  Index, PeriodIndex, ArrayIndex              : WORD;

  VoutMin, VoutMax, NewPhase, PreviousPhase,
  DeltaPhase, FirstSample, SecondSample,
  TotalPhaseChange, ReversalPhase             : REAL;

BEGIN

  { The output signal is scanned to determine the maximum and minimum }
  { values which will be used to determine the phase calculations.    }

  VoutMin := Output[1];
  VoutMax := Output[1];

  For Index := 2 to NumberPerPeriod DO
    BEGIN
      If Output[Index] < VoutMin then VoutMin := Output[Index];
      If Output[Index] > VoutMax then VoutMax := Output[Index];
    END;

  { The phase array is placed in the second period of the input array  }
  { and deflection is placed in the second period of the output array. }
  { Both arrays are calculated using only the positive input points.    }

  For Index := 1 to FunctionalPoints DO
    BEGIN
      NewPhase := 2*Output[Index+NumberPerPeriod]-VoutMax-VoutMin;
      NewPhase := NewPhase / ( VoutMax - VoutMin );
      Input[Index+NumberPerPeriod] := ArcCos( NewPhase );
    END;

  PreviousPhase := Input[NumberPerPeriod+1];
  TotalPhaseChange := 0;
  For Index := 2 to FunctionalPoints DO
    BEGIN
      NewPhase := Input[Index+NumberPerPeriod];
      DeltaPhase := ABS( NewPhase - PreviousPhase );
      PreviousPhase := NewPhase;
      TotalPhaseChange := TotalPhaseChange + DeltaPhase;
    END;
```

A-15

```
      TotalPhaseChange := TotalPhaseChange / 2;

      PreviousPhase := Input[NumberPerPeriod+1];

      Input[NumberPerPeriod+1] := 0;
      Output[NumberPerPeriod+1] := 0;

      Sign := 1;

      For Index := 2 to FunctionalPoints DO
        BEGIN
          PeriodIndex := Index + NumberPerPeriod;
          DeltaPhase := ABS( Input[PeriodIndex] - PreviousPhase );

      { METHODS: Finding the point at which to reverse the phase array. }

{#1}    { If Sign * NewPhase >= TotalPhaseChange then Sign := -1;
          NewPhase := Input[PeriodIndex-1] + Sign * DeltaPhase;   }

          { Method #2 works best with the idealized input signal! }

{#2}      If Index <= ( ( FunctionalPoints / 2 ) + 1 ) then
              NewPhase := Input[PeriodIndex-1] + DeltaPhase
          ELSE NewPhase := Input[PeriodIndex-1] - DeltaPhase;

          PreviousPhase := Input[PeriodIndex];
          Input[PeriodIndex] := NewPhase;
          Output[PeriodIndex] := ( NewPhase * WaveLength ) / ( 4 * PI );
        END;

      { Overwrite intermediate phase data with functional input data. }

      For Index := 1 to FunctionalPoints DO
        BEGIN
          ArrayIndex := NumberPerPeriod + Index;
          PeriodIndex := NegativeInputPoints + Index;
          Input[ArrayIndex] := Input[PeriodIndex];
        END;

      { The input trace and the deflection array are averaged about their  }
      { central points to produce arrays that are half a period in length. }
      { These traces are placed in the third section of their arrays.      }

      For Index := 1 to ROUND( FunctionalPoints / 2 ) DO
        BEGIN
          PeriodIndex := FunctionalPoints - Index + 1;
          ArrayIndex := Index + NumberPerPeriod + FunctionalPoints;
          FirstSample := Input[ NumberPerPeriod + Index ];
          SecondSample := Input[ NumberPerPeriod + PeriodIndex ];
          Input[ArrayIndex] := ( FirstSample + SecondSample ) / 2;
          FirstSample := Output[ NumberPerPeriod + Index ];
          SecondSample := Output[ NumberPerPeriod + PeriodIndex ];
          Output[ArrayIndex] := ( FirstSample + SecondSample ) / 2;
        END;

END;

(*********************************************************************)

PROCEDURE GetChartWaveForms;

VAR

   ArrayLimit, Index,
   PeriodIndex, Translate      : INTEGER;
```

```pascal
    DeltaIndex, Average           : REAL;

BEGIN

  WRITELN;
  WRITELN;
  WRITE('Generating Chart Data ... ');

  ArrayLimit := ROUND( FunctionalPoints / 2 );
  DeltaIndex := ( ArrayLimit - 1 ) / ( MaxChartPoints - 1 );
  Average := ( MaxChartPoints - ArrayLimit ) / ( MaxChartPoints - 1 );
  For Index := 1 to MaxChartPoints DO
    BEGIN
      PeriodIndex := Index+ArrayLimit+NumberPerPeriod+FunctionalPoints;
      Translate := ROUND(DeltaIndex*Index+Average)+NegativeInputPoints;
      Input[PeriodIndex] := Input[Translate];
      Output[PeriodIndex] := Output[Translate];
      DEC(Translate,NegativeInputPoints);
      INC(Translate,NumberPerPeriod);
      INC(PeriodIndex,MaxChartPoints);
      Input[PeriodIndex] := Output[Translate];
    END;

END;

(***********************************************************************)

PROCEDURE SmoothChartData;

CONST N = 15;           { Number of points used in linear regression fit. }

VAR StartIndex, EndIndex, PointIndex,
    Index, ArrayIndex, FirstPoint          : WORD;

    SumProduct, SumXSquared, NewPoint,
    SumX, SumY, Slope, Intercept           : REAL;

BEGIN

  StartIndex := ROUND( ( N + 1 ) / 2 );
  EndIndex := ROUND( MaxChartPoints - ( N - 1 ) / 2 );

  Index := NumberPerPeriod+FunctionalPoints+ROUND(FunctionalPoints/2);

  For PointIndex := 1 to MaxChartPoints DO
    If PointIndex in [ StartIndex .. EndIndex ] then
      BEGIN
        SumProduct := 0;
        SumX := 0;
        SumY := 0;
        SumXSquared := 0;
        FirstPoint := PointIndex - StartIndex + 1;
        For ArrayIndex := FirstPoint to ( FirstPoint + N - 1 ) DO
          BEGIN
            SumProduct := SumProduct + Input[Index+ArrayIndex] *
                          Input[Index+ArrayIndex+MaxChartPoints];
            SumX := SumX + Input[Index+ArrayIndex];
            SumY := SumY + Input[Index+ArrayIndex+MaxChartPoints];
            SumXSquared := SumXSquared + SQR(Input[Index+ArrayIndex]);
          END;

        If ( N * SumXSquared - SQR( SumX ) ) = 0 then
          BEGIN
            Sound(1256);
```

```pascal
                  Delay(100);
                  NoSound;
                  WRITELN;
                  WRITELN('*** Error Smoothing Data Curve! ***');
                  WRITELN;
                  EXIT;
               END;

            Slope := N * SumProduct - SumX * SumY;
            Slope := Slope / ( N * SumXSquared - SQR( SumX ) );
            Intercept := SumY / N - Slope * SumX / N;
            NewPoint := Slope * Input[Index+PointIndex] + Intercept;
            Output[Index+MaxChartPoints+PointIndex] := NewPoint;
          END
        ELSE
          BEGIN
            ArrayIndex := Index + PointIndex + MaxChartPoints;
            Output[ArrayIndex] := Input[ArrayIndex];
          END;

END;

(**********************************************************************)

BEGIN

  Mark(MemoryPointer);

  CLRSCR;

  { Current Test Data: }

  TestChip := 'MUMPS6';
  WRITELN;
  WRITE('Enter Mirror Number:  ');
  READLN(TestStructure);
  WRITELN;
  WRITE('Enter Pixel Location:  ');
  READLN(PixelLocation);
  CLRSCR;

  GetOpsInformation;
  SelectOutputFile;
  GetHeaderData;
  GetSignalData;

  ChopOffEndPoints;

  GetAverageWaveForms;
  GetOutputShift;
  TranslateWaveforms;

{  IdealizeInputSignal;}

  GetPositiveInputPoints;
  GetResponseData;
  GetChartWaveForms;
  SmoothChartData;

  WRITELN;
  WRITELN;
  WRITELN('Points Captured    :  ',PointsCaptured);
  WRITELN('Points Averaged    :  ',NumberPoints);
  WRITELN('Points Per Period  :  ',NumberPerPeriod);
  WRITELN('Points Analyzed    :  ',FunctionalPoints);
```

A-18

```
WRITELN('Output Shift      :   ',OutputShift);
WRITELN('Frequency (Hz)    :   ',InputFrequency:1:1);

Delay(50);

WriteOutputHeader;
WriteOutputData;

ChDir(OpsDirectory);

WRITELN;
WRITELN;
WRITE('DONE!  Returning to Windows ... ');

Delay(5000);

Release(MemoryPointer);

END.
```

*APPENDIX*

# (B)

MathCAD Worksheets

# Arc Length Approximations

**_Exact Solution:_**

$$\text{ArcLength}\left(\psi, z_m\right) := \frac{z_m}{\pi} \cdot \int_0^\pi \left(1 + 2 \cdot e^\psi \cdot \cos(\phi) + e^{2 \cdot \psi}\right)^{\frac{1}{2}} d\phi$$

$$x\left(\psi, z_m, w\right) := \frac{z_m}{2 \cdot \pi} \cdot \left(\psi + 1 - e^\psi\right) + \frac{w}{2}$$

**_Numerical Integration:_**

$$f(\phi, \psi) := \sqrt{1 + 2 \cdot e^\psi \cdot \cos(\phi) + e^{2 \cdot \psi}} \qquad N := 5 \qquad n := 1, 2 .. N$$

$$\Delta\phi := \frac{\pi}{N} \qquad L_{ni}\left(\psi, z_m\right) := \frac{z_m \cdot \Delta\phi}{\pi} \cdot \sum_n f\left[\left(n - \frac{1}{2}\right) \cdot \Delta\phi, \psi\right]$$

$$f_2(\theta, \psi) := \sqrt{1 - \frac{4 \cdot e^\psi}{\left(1 + e^\psi\right)^2} \cdot \sin(\theta)^2}$$

$$L_{ni2}\left(\psi, z_m\right) := 2 \cdot \frac{z_m}{\pi} \cdot \left(1 + e^\psi\right) \cdot \frac{\pi}{2 \cdot N} \cdot \sum_n f_2\left[\left(n - \frac{1}{2}\right) \cdot \frac{\pi}{2 \cdot N}, \psi\right]$$

$$\Delta AL_{ni}\left(\psi, z_m\right) := \frac{L_{ni}\left(\psi, z_m\right) - \text{ArcLength}\left(\psi, z_m\right)}{\text{ArcLength}\left(\psi, z_m\right)}$$

**_Elliptic Solution:_**

$$a_0 := 1 \qquad N := 10 \qquad n := 1, 2 .. N \qquad a_n := \left(\frac{2 \cdot n - 1}{2 \cdot n}\right)^2 \cdot a_{n-1}$$

$L_{ni}(0, 2 \cdot \mu m) = 2.557 \cdot \mu m$

$L_{ni2}(0, 2 \cdot \mu m) = 2.557 \cdot \mu m$

$$m(\psi) := \frac{4 \cdot e^\psi}{\left(1 + e^\psi\right)^2} \qquad L_{es}\left(\psi, z_m\right) := z_m \cdot \left(1 + e^\psi\right) \cdot \left[1 - \sum_n \left[a_n \cdot \left(\frac{m(\psi)^n}{2 \cdot n - 1}\right)\right]\right]$$

$$\Delta AL_{es}\left(\psi, z_m\right) := \frac{L_{es}\left(\psi, z_m\right) - \text{ArcLength}\left(\psi, z_m\right)}{\text{ArcLength}\left(\psi, z_m\right)}$$

**_Curve-Fitting Solution:_**

$$a := 0.27013 \qquad b := 2.09158 \qquad L_{cf}\left(\psi, z_m\right) := z_m \cdot (1 + a \cdot \exp(b \cdot \psi))$$

$$\Delta AL_{cf}\left(\psi, z_m\right) := \frac{L_{cf}\left(\psi, z_m\right) - \text{ArcLength}\left(\psi, z_m\right)}{\text{ArcLength}\left(\psi, z_m\right)}$$

# *Arc Length Approximations*   ( Continued )

*Plotting Specifications:*          $\psi := -1.5, -1.48 .. 0$        $z_m := 3 \cdot \mu m$        $x_f := 0.2 \cdot \mu m$
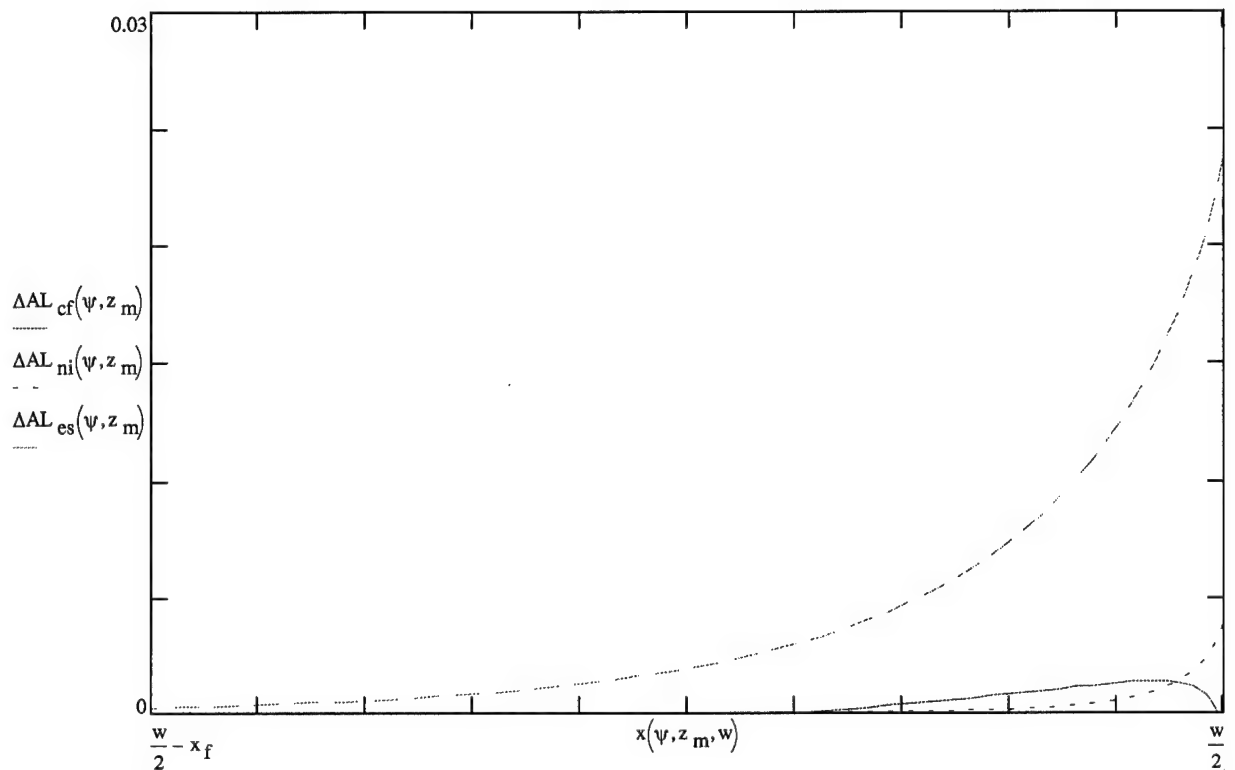


The Elliptical Solution method using N = 10 points is clearly the most erroneous of the three solutions. The Numerical Integration method using only N = 5 points produces the least overall error as can be seen by integrating the above curves through the range of x shown. However, the Curve-Fitting solution has the lowest maximum error out of the three curves and offers a much simpler function. It should be noted that different values of zm produce exactly the same traces, but xf must change proportional to zm so that larger zm values will create fringing effects further into the mirror from the edge. The maximum error of the Curve-Fitting function is about 0.2% of the actual value given by the definite integral.

# *Curve-Fitting Approximation*

*Fitting Indices:*     $w_x := 16 \cdot \mu m$     $z_m := 4 \cdot \mu m$     $NumPoints := 100$     $i := 0, 1 .. NumPoints$

*Basic Functions:*     $\psi_i := \dfrac{\psi_0(z_m, w_x)}{2} \cdot \left(1 - \dfrac{i}{NumPoints}\right)$     $L_\psi(\psi, z_m, a, b) := z_m \cdot (1 + a \cdot \exp(b \cdot \psi))$

*Fitting Function:*     $SLS(a, b) := \sum_i \left(ArcLength(\psi_i, z_m) - L_\psi(\psi_i, z_m, a, b)\right)^2$

*Initial Guesses:*     $a := 0.2701$     $b := 2.0918$

*Solve Block:*     Given     $SLS(a, b) = 0 \cdot \mu m^2$     $1 = 1$     $\begin{pmatrix} a \\ b \end{pmatrix} := MinErr(a, b)$

$a = 0.27$     $b = 2.092$
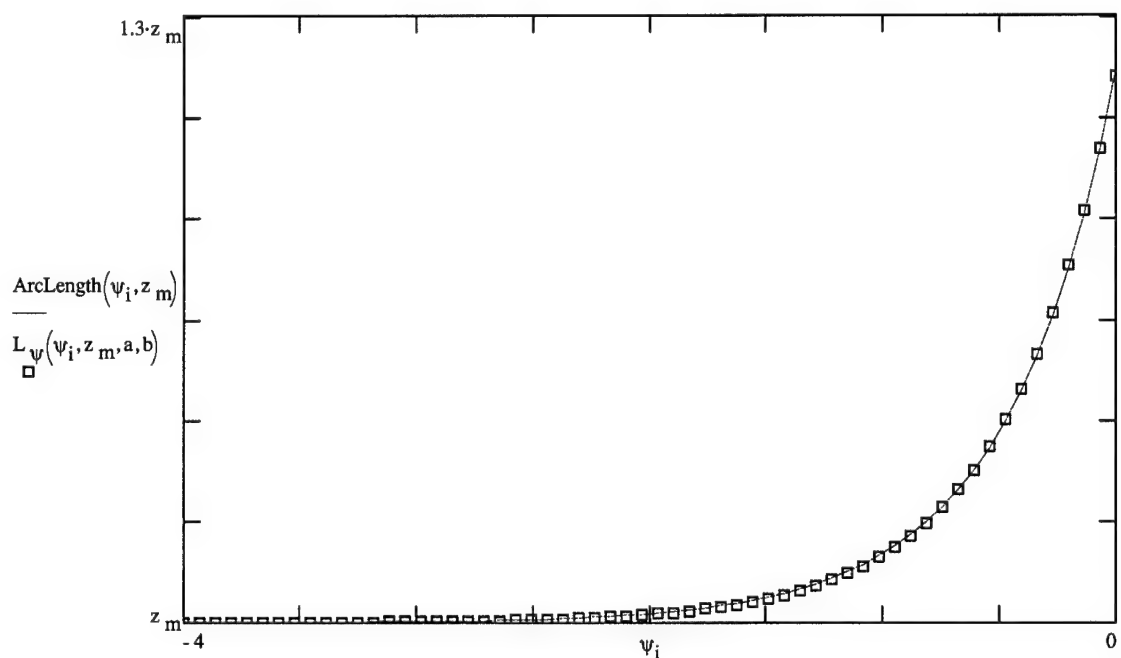
# Inverse Cosine Function

$\text{NumberPerPeriod} := 1000$      $i := 1, 2 .. \text{NumberPerPeriod}$      $\text{InValue} := -0.99843$

$\text{CosineIndex}_i := 2 \cdot i - 1$      $\text{NewTerm}_1 := \text{InValue}$      $\text{TempValue}_1 := 0$

$$\text{NewTerm}_{(i+1)} := \frac{\text{NewTerm}_i \cdot (\text{InValue})^2 \cdot (\text{CosineIndex}_i)^2}{(\text{CosineIndex}_i + 1) \cdot (\text{CosineIndex}_i + 2)}$$      $\text{ArcCos} := \frac{\pi}{2} - \sum_i \text{NewTerm}_i$

$\text{TempValue}_{(i+1)} := \text{TempValue}_i + \text{NewTerm}_i$

$\text{ArcCos} = 0.982133 \cdot \pi$

$\text{acos}(\text{InValue}) = 0.982161 \cdot \pi$

$\dfrac{\pi}{2} - \text{TempValue}_{\text{NumberPerPeriod}} = 0.982133 \cdot \pi$

$\dfrac{\pi}{2} - \text{asin}(\text{InValue}) = 0.982161 \cdot \pi$
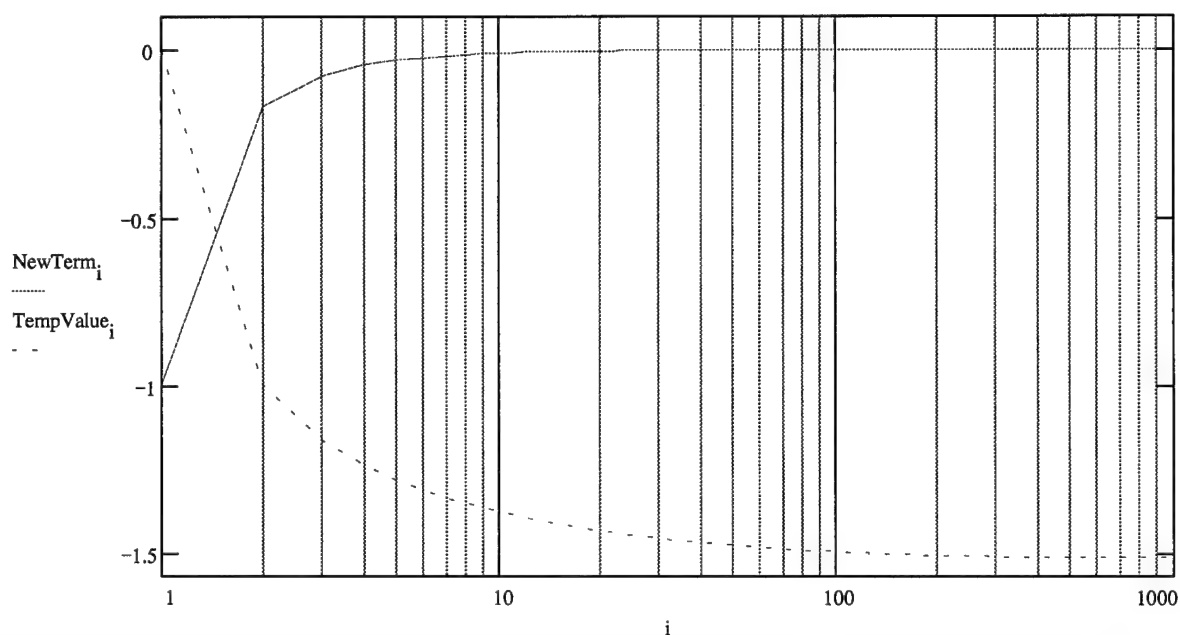
# *Total Electric Field*

*Device Parameters:*     $w_x := 16 \cdot \mu m$     $w_y := 16 \cdot \mu m$     $z_m := 4 \cdot \mu m$     $V_o := 10 \cdot volt$

*Field Parameters:*     $\psi_o(w, z_m) := -\left(\dfrac{w \cdot \pi}{z_m} + 1\right)$     $E_{2D}(\psi, z_m, V_o) := \left(\dfrac{V_o}{ArcLength(\psi, z_m)}\right)$

*Parameterized Solution:*     $E_1(\psi_x, \psi_y, z_m, V_o) := \dfrac{1}{2} \cdot \left(E_{2D}(\psi_x, z_m, V_o) + E_{2D}(\psi_y, z_m, V_o)\right)$

$$E_2(\psi_x, \psi_y, z_m, V_o) := \sqrt{E_{2D}(\psi_x, z_m, V_o) \cdot E_{2D}(\psi_y, z_m, V_o)}$$

*Total Electric Field:*     $PointSpan := 20$     $x := 0, 1 .. PointSpan$     $y := 0, 1 .. PointSpan$

$$\psi_x := \frac{\psi_o(w_x, z_m) \cdot (PointSpan - x)}{PointSpan} \qquad \psi_y := \frac{\psi_o(w_y, z_m) \cdot (PointSpan - y)}{PointSpan}$$

$$E1_{x,y} := E_1(\psi_x, \psi_y, z_m, V_o) \qquad E2_{x,y} := E_2(\psi_x, \psi_y, z_m, V_o)$$



E1



E2

*Field Functions:*

$$L(\psi) := z_m \cdot (1 + 0.27013 \cdot \exp(2.09158 \cdot \psi)) \qquad E(\psi_x, \psi_y) := \frac{V_o}{2} \cdot \left( \frac{1}{L(\psi_x)} + \frac{1}{L(\psi_y)} \right)$$

*Total Electric Field:*     NumPoints := 40     $x := 0, 1 .. NumPoints$     $y := 0, 1 .. NumPoints$

$$\psi_x := \frac{\psi_o(w_x, z_m) \cdot (NumPoints - x)}{NumPoints} \qquad \psi_y := \frac{\psi_o(w_y, z_m) \cdot (NumPoints - y)}{NumPoints} \qquad EField_{x,y} := E(\psi_x, \psi_y)$$

*Electric Field Fringing Losses:*

$$ELoss_{x,y} := \frac{V_o}{z_m} - EField_{x,y}$$
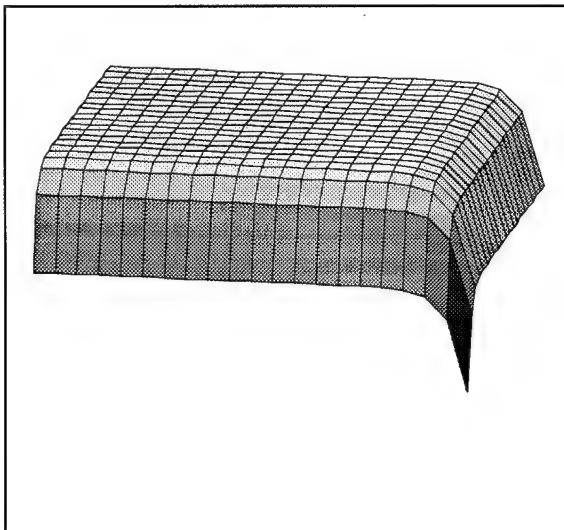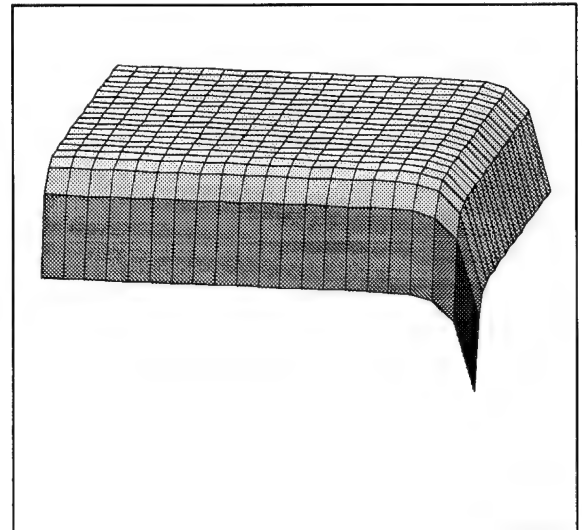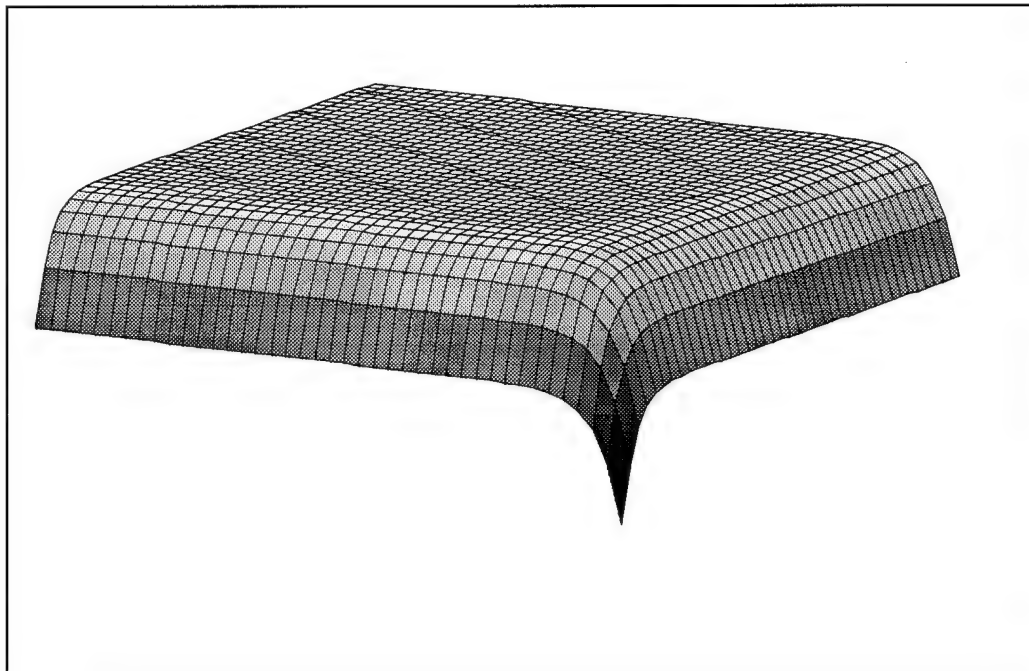


EField

# *Total Electric Field*    ( Continued )

*Field Functions:*        $L(\psi) := z_m \cdot (1 + 0.27013 \cdot \exp(2.09158 \cdot \psi))$        $E\left(\psi_x, \psi_y\right) := \dfrac{V_o}{2} \cdot \left(\dfrac{1}{L\left(\psi_x\right)} + \dfrac{1}{L\left(\psi_y\right)}\right)$

*Field Parameters:*        $\text{NumPoints} := 50$        $x := 0, 1 .. \text{NumPoints}$        $y := 0, 1 .. \text{NumPoints}$

$$f_x(x) := \frac{\psi_o\left(w_x, z_m\right) \cdot (\text{NumPoints} - x)}{\text{NumPoints}} \qquad \psi_x := \text{if}\left(x < \frac{\text{NumPoints}}{2}, f_x(\text{NumPoints} - x), f_x(x)\right)$$

$$f_y(y) := \frac{\psi_o\left(w_y, z_m\right) \cdot (\text{NumPoints} - y)}{\text{NumPoints}} \qquad \psi_y := \text{if}\left(y < \frac{\text{NumPoints}}{2}, f_y(\text{NumPoints} - y), f_y(y)\right)$$

*Total Electric Field:*        $\text{EField}_{x,y} := E\left(\psi_x, \psi_y\right)$
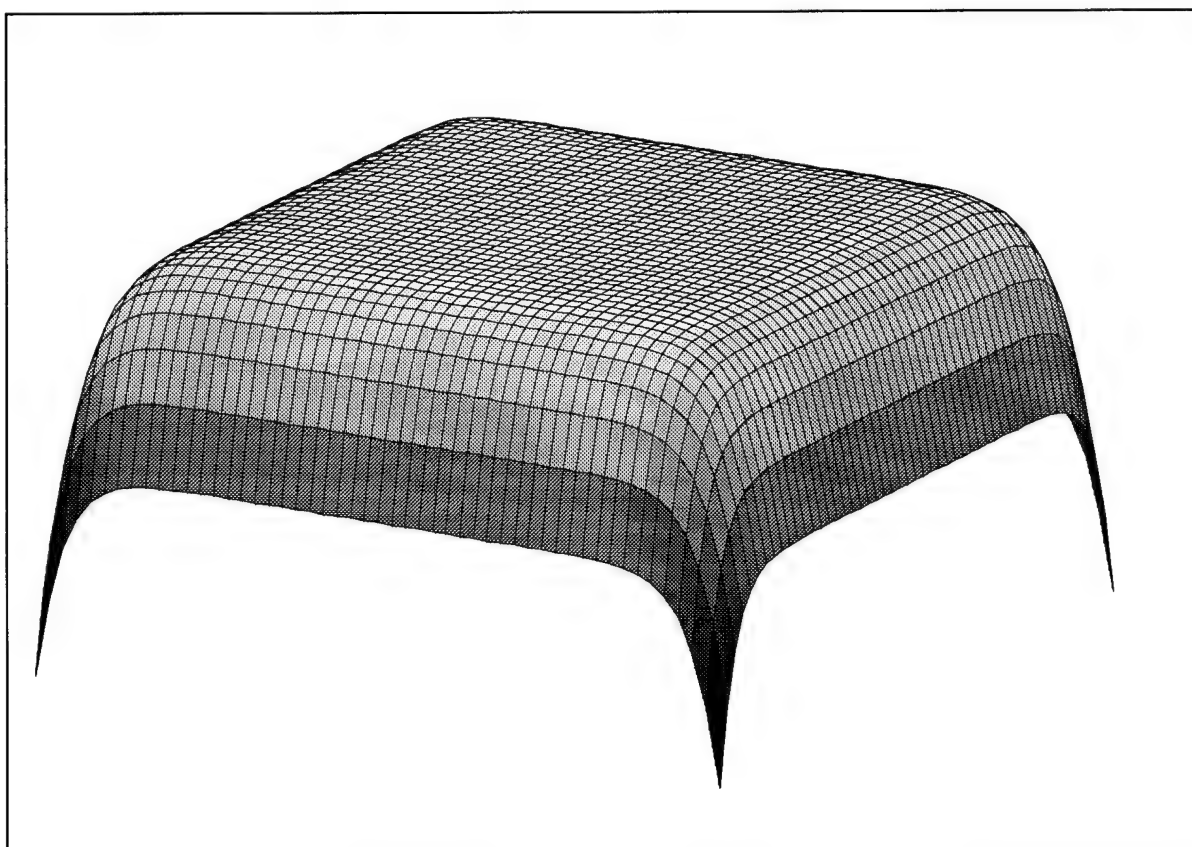


EField

# *Normalized Force Magnitude Contours*

**_Device Parameters:_** $\qquad\qquad$ $w := 8 \cdot \mu m, 16 \cdot \mu m .. 24 \cdot \mu m \qquad z_m := 1 \cdot \mu m, 3 \cdot \mu m .. 5 \cdot \mu m$

**_Flux Line Range:_** $\qquad\qquad$ $\psi := -8, -7.98 .. 0$

**_Arc Length:_** $\qquad\qquad$ $\mathrm{ArcLength}(\psi, z_m) := \dfrac{z_m}{\pi} \cdot \displaystyle\int_0^\pi \left(1 + 2 \cdot e^\psi \cdot \cos(\phi) + e^{2 \cdot \psi}\right)^{\frac{1}{2}} d\phi$

**_Parameterized Solutions:_** $\qquad$ $x(\psi, z_m, w) := \dfrac{z_m}{2 \cdot \pi} \cdot \left(\psi + 1 - e^\psi\right) + \dfrac{w}{2}$

$$\mathrm{NForce}(\psi, z_m) := \left(\dfrac{z_m}{\mathrm{ArcLength}(\psi, z_m)}\right)^2$$
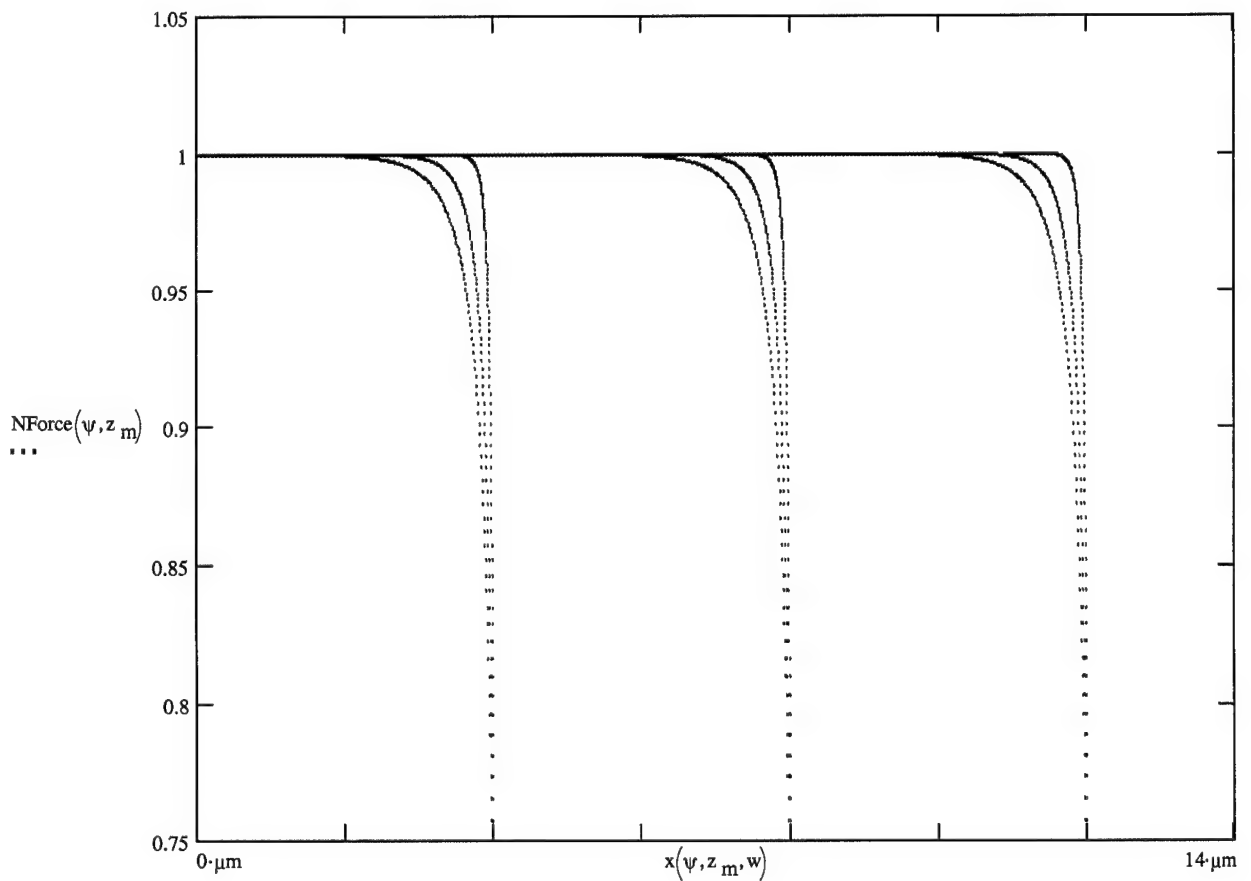
# *Parametric Numerical Integration*

**_Device Parameters:_**  $w_x := 100 \cdot \mu m$    $w_y := 20 \cdot \mu m$    $z_m := 3 \cdot \mu m$    $V_o := 10 \cdot volt$

**_Index Range:_**  $NumPoints := 1000$    $i := 1, 2 .. NumPoints$

**_Field Functions:_**  $L(\psi) := z_m \cdot (1 + 0.27013 \cdot \exp(2.09158 \cdot \psi))$    $E(\psi) := \dfrac{V_o}{L(\psi)}$

**_Initial Parameters:_**  $x_0 := 0 \cdot \mu m$    $y_0 := 0 \cdot \mu m$    $\psi_{x_0} := \psi_o(z_m, w_x)$    $\psi_{y_0} := \psi_o(z_m, w_y)$

**_Parameteric Ranges:_**  

$$\psi_{x_i} := \psi_o(z_m, w_x) \cdot \left(1 - \frac{i}{NumPoints}\right) \qquad x_i := \frac{z_m}{2 \cdot \pi} \cdot \left(\psi_{x_i} + 1 - e^{\psi_{x_i}}\right) + \frac{w_x}{2}$$

$$\psi_{y_i} := \psi_o(z_m, w_y) \cdot \left(1 - \frac{i}{NumPoints}\right) \qquad y_i := \frac{z_m}{2 \cdot \pi} \cdot \left(\psi_{y_i} + 1 - e^{\psi_{y_i}}\right) + \frac{w_y}{2}$$

**_Integral Solutions:_**  

$$X_{Int} := \frac{w_y}{4} \cdot \left[ \sum_i \left[ x_i - x_{(i-1)} \right] \cdot \left[ E\left(\psi_{x_i}\right)^2 + E\left[\psi_{x_{(i-1)}}\right]^2 \right] \right]$$

$$Y_{Int} := \frac{w_x}{4} \cdot \left[ \sum_i \left[ y_i - y_{(i-1)} \right] \cdot \left[ E\left(\psi_{y_i}\right)^2 + E\left[\psi_{y_{(i-1)}}\right]^2 \right] \right]$$

$$XY_{Int} := \frac{1}{2} \cdot \left[ \sum_i \left[ x_i - x_{(i-1)} \right] \cdot \left[ E\left(\psi_{x_i}\right) + E\left[\psi_{x_{(i-1)}}\right] \right] \right] \cdot \left[ \sum_i \left[ y_i - y_{(i-1)} \right] \cdot \left[ E\left(\psi_{y_i}\right) + E\left[\psi_{y_{(i-1)}}\right] \right] \right]$$

**_Force Calculations:_**  

$$F_{Ideal} := \frac{\varepsilon_o}{2} \cdot \left(\frac{V_o}{z_m}\right)^2 \cdot w_x \cdot w_y \qquad F_{Ideal} = 98.333333 \cdot nN$$

$$F_{Actual} := \frac{\varepsilon_o}{2} \cdot \left(X_{Int} + Y_{Int} + XY_{Int}\right) \qquad F_{Actual} = 98.118341 \cdot nN$$

$$\Delta F := \frac{F_{Ideal} - F_{Actual}}{F_{Ideal}} \qquad \Delta F = 0.002186$$

# *Force Loss Due To Fringing Effects*

Given the two-dimensional loss profile, it is expected that the loss due to fringing effects will be proportional to the mirror separation distance, $z_m$, and the length of the mirror perimeter. To normalize to the ideal force, the loss should be divided by the device area, ( $w_x * w_y$ ).

<u>*Function Information:*</u>  $\qquad i := 1, 2 .. 10 \qquad w_y := 16 \cdot \mu m \qquad Fringe\left(w_x, z_m\right) := \dfrac{z_m}{82.7} \cdot \left(\dfrac{w_x + w_y}{w_x \cdot w_y}\right)$

## <u>*Mirror Width Dependence:*</u>

$$\Delta F_i := \frac{F_{Ideal_i} - F_{Actual_i}}{F_{Ideal_i}} \qquad z_m := 2 \cdot \mu m$$

| $w_{x_i} :=$ | $F_{Ideal_i} :=$ | $F_{Actual_i} :=$ |
|---|---|---|
| 50·μm | 88.5·nN | 88.322658·nN |
| 45·μm | 79.65·nN | 79.486114·nN |
| 40·μm | 70.8·nN | 70.649567·nN |
| 35·μm | 61.95·nN | 61.813017·nN |
| 30·μm | 53.1·nN | 52.976464·nN |
| 25·μm | 44.25·nN | 44.139908·nN |
| 20·μm | 35.4·nN | 35.303349·nN |
| 15·μm | 26.55·nN | 26.466787·nN |
| 10·μm | 17.7·nN | 17.630222·nN |
| 5·μm | 8.85·nN | 8.793654·nN |
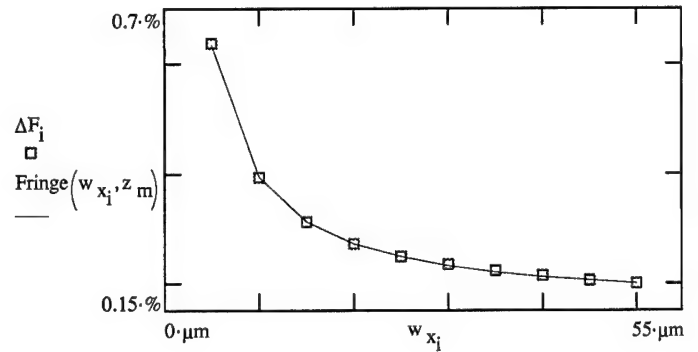


## <u>*Mirror Height Dependence:*</u>

$$\Delta F_i := \frac{F_{Ideal_i} - F_{Actual_i}}{F_{Ideal_i}} \qquad w_x := 16 \cdot \mu m$$

| $z_{m_i} :=$ | $F_{Ideal_i} :=$ | $F_{Actual_i} :=$ |
|---|---|---|
| 5·μm | 4.5312·nN | 4.496871·nN |
| 4.5·μm | 5.594·nN | 5.555926·nN |
| 4·μm | 7.08·nN | 7.037079·nN |
| 3.5·μm | 9.247·nN | 9.198288·nN |
| 3·μm | 12.5867·nN | 12.529423·nN |
| 2.5·μm | 18.1248·nN | 18.056095·nN |
| 2·μm | 28.32·nN | 28.234099·nN |
| 1.5·μm | 50.347·nN | 50.232088·nN |
| 1·μm | 113.28·nN | 113.107977·nN |
| 0.5·μm | 453.12·nN | 452.77441·nN |
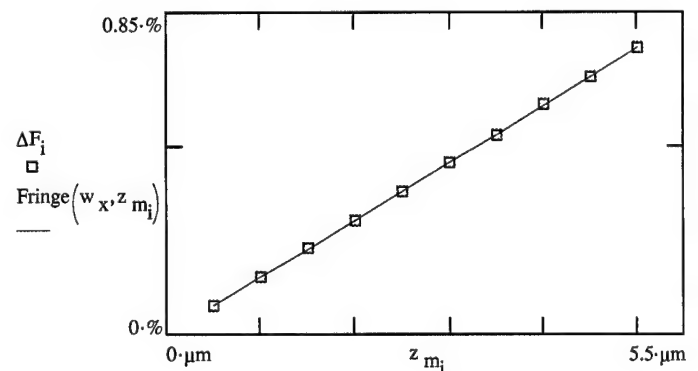


The loss due to fringing effects can directly be calculated with the device geometry. The fringefunction determines the loss as a percentage of the ideal force which increases with the mirror separation distance, $z_m$, and decreases with the mirror area, ( $w_x * w_y$ ).

# *Force Loss By Fringing*    ( Continued )

*Device Information:*
$$w_x := 8 \cdot \mu m, 8.1 \cdot \mu m .. 50 \cdot \mu m \qquad z_m := 1 \cdot \mu m, 2 \cdot \mu m .. 3 \cdot \mu m$$

$$V_o := 20 \cdot volt \qquad w_y(w_x) := w_x \qquad Area(w_x, w_y) := w_x \cdot w_y$$

*Force Functions:*
$$F_{Ideal}(w_x, w_y, z_m, V_o) := \frac{\varepsilon_o}{2} \cdot \left(\frac{V_o}{z_m}\right)^2 \cdot w_x \cdot w_y$$

$$\Delta F_{Fringing}(w_x, w_y, z_m) := \frac{z_m}{82.7} \cdot \left(\frac{w_x + w_y}{w_x \cdot w_y}\right)$$

$$F_{Actual}(w_x, w_y, z_m, V_o) := F_{Ideal}(w_x, w_y, z_m, V_o) \cdot \left(1 - \Delta F_{Fringing}(w_x, w_y, z_m\right.$$
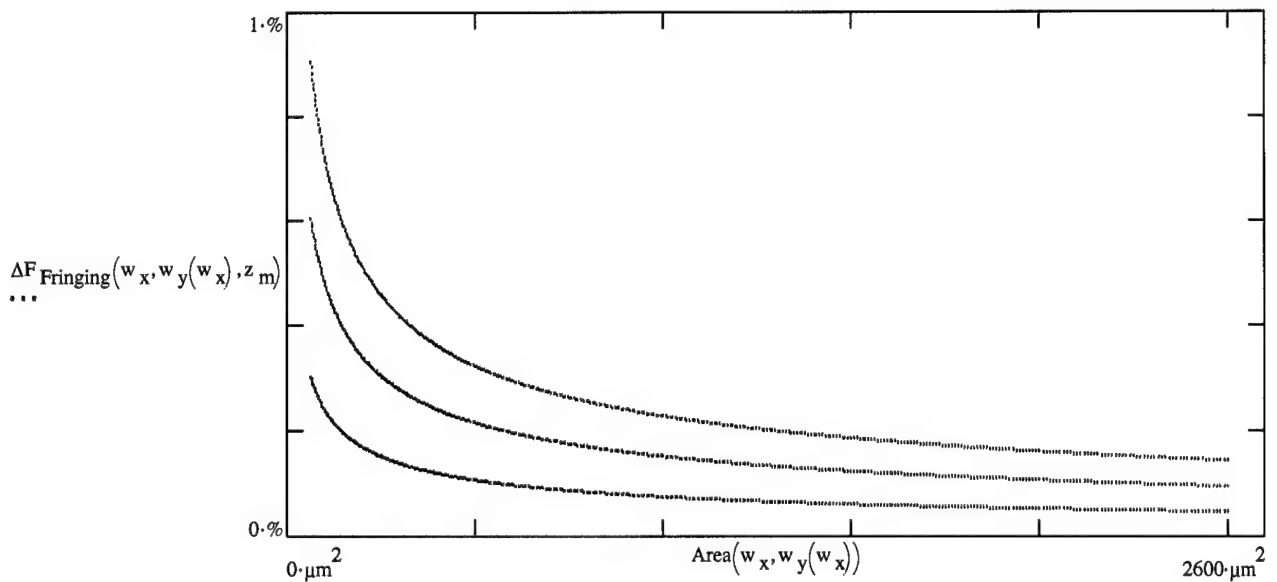


The $z_m = 3$ μm curve exhibits the largest percent error of the ideal force throughout the range of the device area. Likewise, smaller mirror separations exhibit less significant losses. The loss becomes less affected by the device area as the size of the mirror increases and is independent of the electric potential, $V_o$, between the mirror and the addressing electrode.

# Conformal Mapping Solution

*Flux Line Parameters:*

$$\psi := -6, -5 .. 2 \qquad \phi' := 0, \frac{\pi}{100} .. 2 \cdot \pi$$

*Potential Line Parameters:*

$$\psi' := -6, -5.99 .. 2 \qquad \phi := 0, \frac{\pi}{3} .. 2 \cdot \pi$$

*Parameterized Solutions:*

$$x(\phi, \psi, z_m) := \frac{z_m}{2 \cdot \pi} \cdot \left( \psi + 1 - e^{\psi} \cdot \cos(\phi) \right)$$

$$z(\phi, \psi, z_m) := \frac{z_m}{2 \cdot \pi} \cdot \left( \phi - e^{\psi} \cdot \sin(\phi) \right)$$
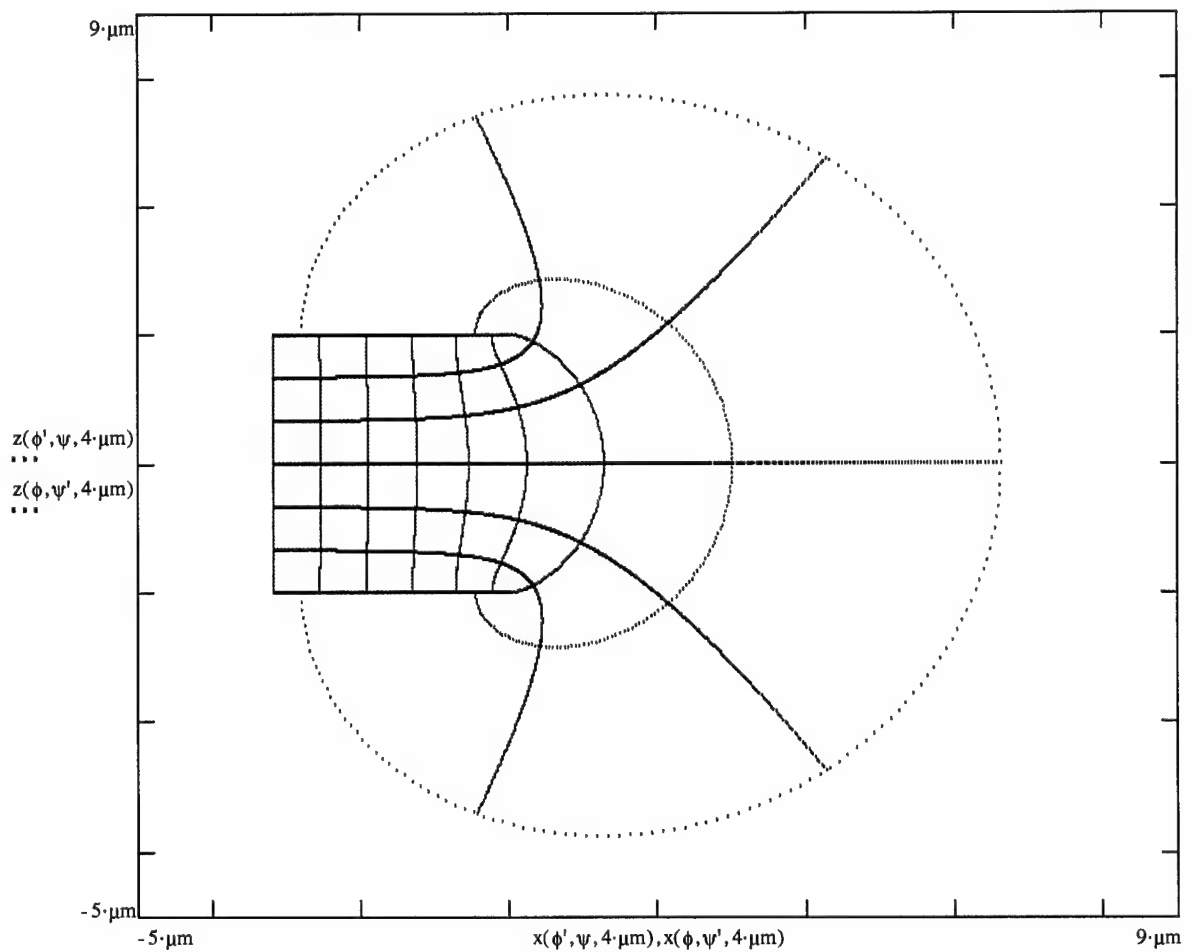
# Parallel Plate Capacitor Solution

*Device Specifications:* $\qquad$ $w := 16 \cdot \mu m$ $\qquad$ $z_m := 4 \cdot \mu m$ $\qquad$ $\psi_o := \dfrac{w \cdot \pi}{z_m} + 1$

*Flux Line Parameters:* $\qquad$ $\psi := -1.2 \cdot \psi_o, -1.1 \cdot \psi_o \, .. \, 1.2 \cdot \psi_o$ $\qquad$ $\phi' := 0, \dfrac{\pi}{100} \, .. \, 2 \cdot \pi$

*Potential Line Parameters:* $\qquad$ $\psi' := -1.2 \cdot \psi_o, -1.19 \cdot \psi_o \, .. \, 1.2 \cdot \psi_o$ $\qquad$ $\phi := 0, \dfrac{\pi}{3} \, .. \, 2 \cdot \pi$

*Parameterized Solutions:* $\qquad$ $x(\phi, \psi) := \dfrac{z_m}{2 \cdot \pi} \cdot \left( \psi - \psi_o + 1 - 2 \cdot e^{-\psi_o} \cdot \sinh(\psi) \cdot \cos(\phi) \right) + \dfrac{w}{2}$

$$z(\phi, \psi) := \dfrac{z_m}{2 \cdot \pi} \cdot \left( \phi - 2 \cdot e^{-\psi_o} \cdot \cosh(\psi) \cdot \sin(\phi) \right)$$
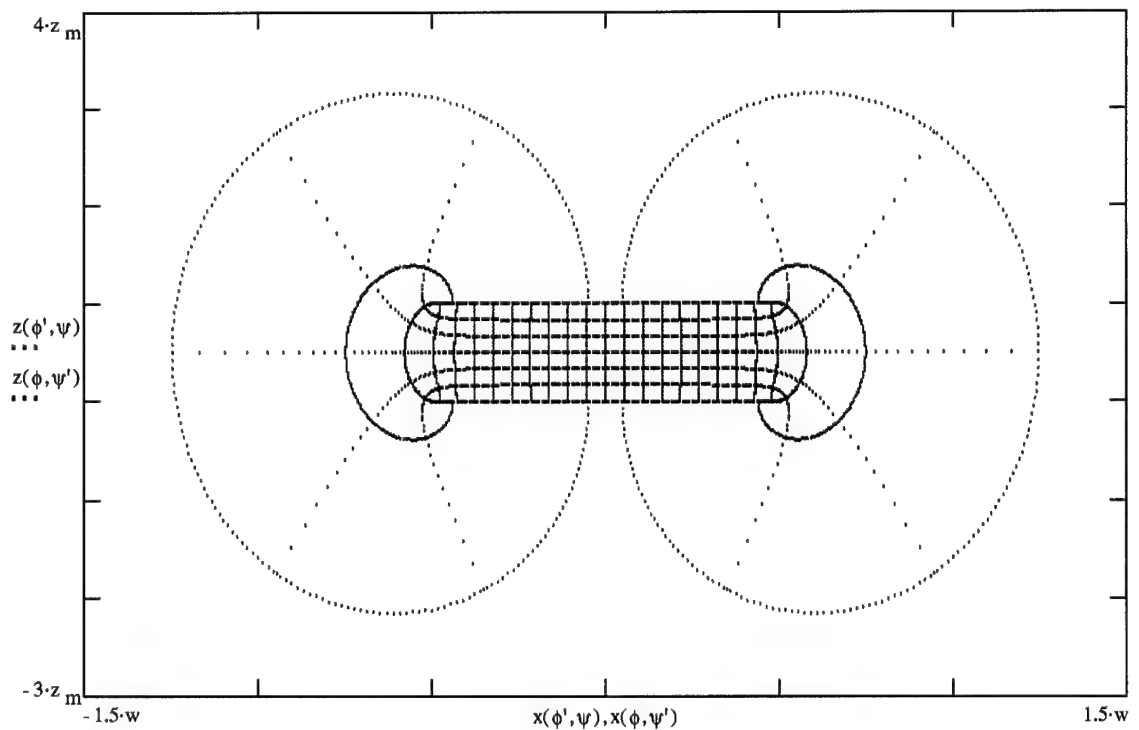
# Harmonic Oscillators

$M := 10^{-12} \cdot kg$ $\qquad$ $\beta := 0.01 \cdot Hz$ $\qquad$ $A := 1 \cdot nN$ $\qquad$ $k := 0.5 \cdot \dfrac{newton}{m}$ $\qquad$ $\omega_o := \sqrt{\dfrac{k}{M}}$ $\qquad$ $f_o := \dfrac{\omega_o}{2 \cdot \pi}$

$f_o = 112.54 \cdot kHz$ $\qquad$ $f := 112 \cdot kHz$ $\qquad$ $\omega := 2 \cdot \pi \cdot f$ $\qquad$ $\delta := atan\left(\dfrac{2 \cdot \omega \cdot \beta}{\omega_o^2 - \omega^2}\right)$ $\qquad$ $\delta = 2.943 \cdot 10^{-6}$

$t := 0 \cdot sec, \dfrac{5}{1000 \cdot f} .. \dfrac{5}{f}$ $\qquad$ $x_p(t) := \dfrac{A}{M} \cdot \dfrac{\cos(\omega \cdot t - \delta)}{\sqrt{\left(\omega_o^2 - \omega^2\right)^2 + 4 \cdot \omega^2 \cdot \beta^2}}$ $\qquad$ $x_{peak}(f) := \dfrac{A}{M} \cdot \dfrac{1}{\sqrt{\left[\omega_o^2 - (2 \cdot \pi \cdot f)^2\right]^2 + 4 \cdot (2 \cdot \pi \cdot f)^2 \cdot \beta^2}}$
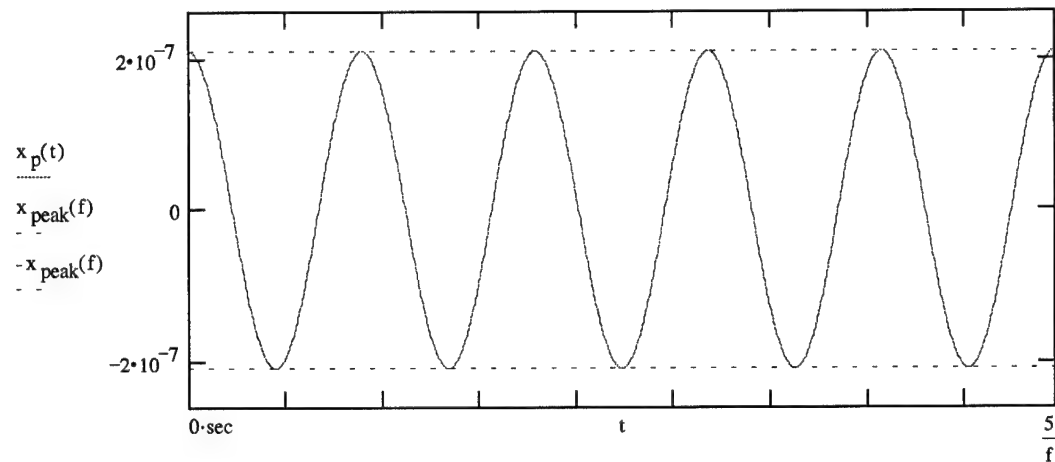


$f := 0 \cdot Hz, \dfrac{f_o}{500} .. 2 \cdot f_o$ $\qquad$ $x_{peak}(f_o) = 70.711 \cdot m$
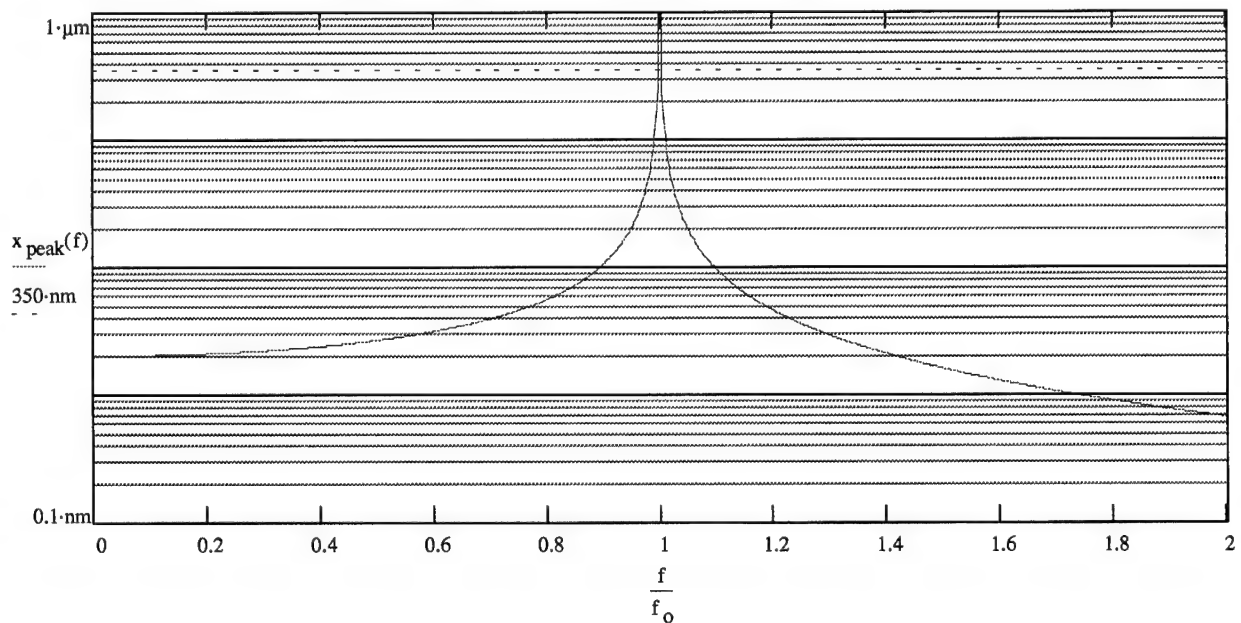
# Cross Talk

_Device Dimensions_:

$$z_o := 2.5 \cdot \mu m \qquad w_x := 61 \cdot \mu m \qquad w_y := 61 \cdot \mu m \qquad x := -\frac{w_x}{2}, -\frac{w_x}{2.1} \, .. \, \frac{w_x}{2}$$

_Cross-Talk Parameters_:

$$x_s := 18 \cdot \mu m \qquad\qquad V_{ct} := 15 \cdot volt$$

_Cross-Talk Functions_:

$$L(x) := \sqrt{\left(x + x_s + \frac{w_x}{2}\right)^2 + z_o{}^2} \qquad\qquad f(x) := V_{ct}{}^2 \cdot \left(\frac{\varepsilon_o \cdot w_y \cdot z_o}{2}\right) \cdot \left(\frac{1}{L(x)}\right)^3$$

$$x_{c\_actual} := \left[\int_{-\frac{w_x}{2}}^{\frac{w_x}{2}} x \cdot f(x) \, dx\right] \cdot \left[\int_{-\frac{w_x}{2}}^{\frac{w_x}{2}} f(x) \, dx\right]^{-1} \qquad\qquad F_{ct\_actual} := \int_{-\frac{w_x}{2}}^{\frac{w_x}{2}} f(x) \, dx$$

_Closed-Form Soluctions_:

$$L_{max} := \sqrt{\left(w_x + x_s\right)^2 + z_o{}^2} \qquad\qquad L_{min} := \sqrt{x_s{}^2 + z_o{}^2}$$

$$x_c := \frac{z_o{}^2 \cdot \left(L_{max} - L_{min}\right) + \left(x_s + \frac{w_x}{2}\right) \cdot \left[x_s \cdot L_{max} - \left(w_x + x_s\right) \cdot L_{min}\right]}{\left(w_x + x_s\right) \cdot L_{min} - x_s \cdot L_{max}} \qquad x_c = 1 \cdot x_{c\_actual}$$

$$F_{ct} := V_{ct}{}^2 \cdot \left(\frac{\varepsilon_o \cdot w_y}{2 \cdot z_o}\right) \cdot \left[\frac{\left(w_x + x_s\right) \cdot L_{min} - x_s \cdot L_{max}}{L_{min} \cdot L_{max}}\right] \qquad\qquad F_{ct} = 1 \cdot F_{ct\_actual}$$
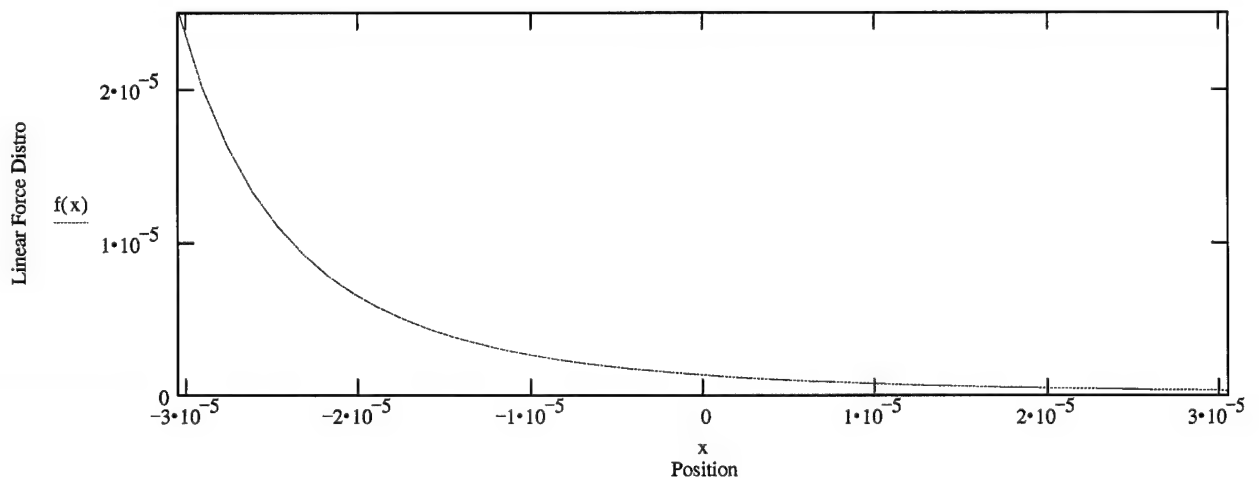
$$k := 2.5 \cdot \frac{newton}{m} \qquad \Delta z_{near} := \left(\frac{w_x}{2} - x_c\right) \cdot \left(\frac{F_{ct}}{k \cdot w_x}\right) \qquad \Delta z_{far} := \left(\frac{w_x}{2} + x_c\right) \cdot \left(\frac{F_{ct}}{k \cdot w_x}\right)$$

$$\Delta z_{near} = 0.071 \cdot nm \qquad \Delta z_{far} = 0.016 \cdot nm \qquad \Delta z(x) := \left(\frac{\Delta z_{far} - \Delta z_{near}}{w_x}\right) \cdot x + \left(\frac{\Delta z_{near} + \Delta z_{far}}{2}\right)$$
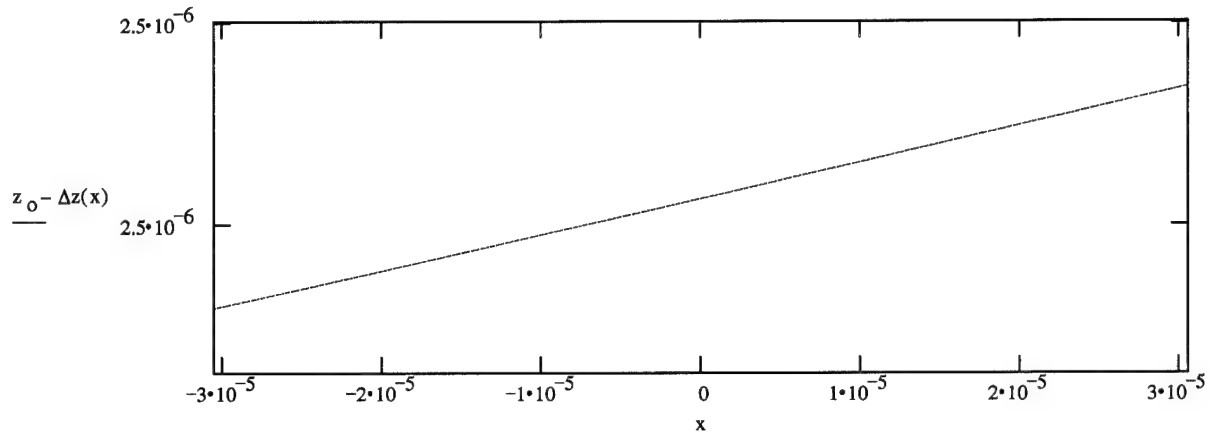


$$V_o(d) := (z_o - d) \cdot \sqrt{\frac{2 \cdot k \cdot d}{\varepsilon_o \cdot w_x \cdot w_y}} \qquad\qquad F_{pp}(d) := \frac{\varepsilon_o}{2} \cdot \left[\frac{V_o(d)}{(z_o - d)}\right]^2 \cdot w_x \cdot w_y$$

$$d := 0 \cdot nm, 0.0025 \cdot nm .. 4 \cdot nm \qquad V_{2\pi} := V_o\left(\frac{632.8 \cdot nm}{2}\right) \qquad V_{2\pi} = 15.135 \cdot volt$$

$$F_{ct}(V_{ct}) := V_{ct}^2 \cdot \left(\frac{\varepsilon_o \cdot w_y}{2 \cdot z_o}\right) \cdot \left[\frac{(w_x + x_s) \cdot L_{min} - x_s \cdot L_{max}}{L_{min} \cdot L_{max}}\right] \qquad \%F(V_{ct}, d) := \frac{F_{ct}(V_{ct})}{F_{ct}(V_{ct}) + F_{pp}(d)}$$
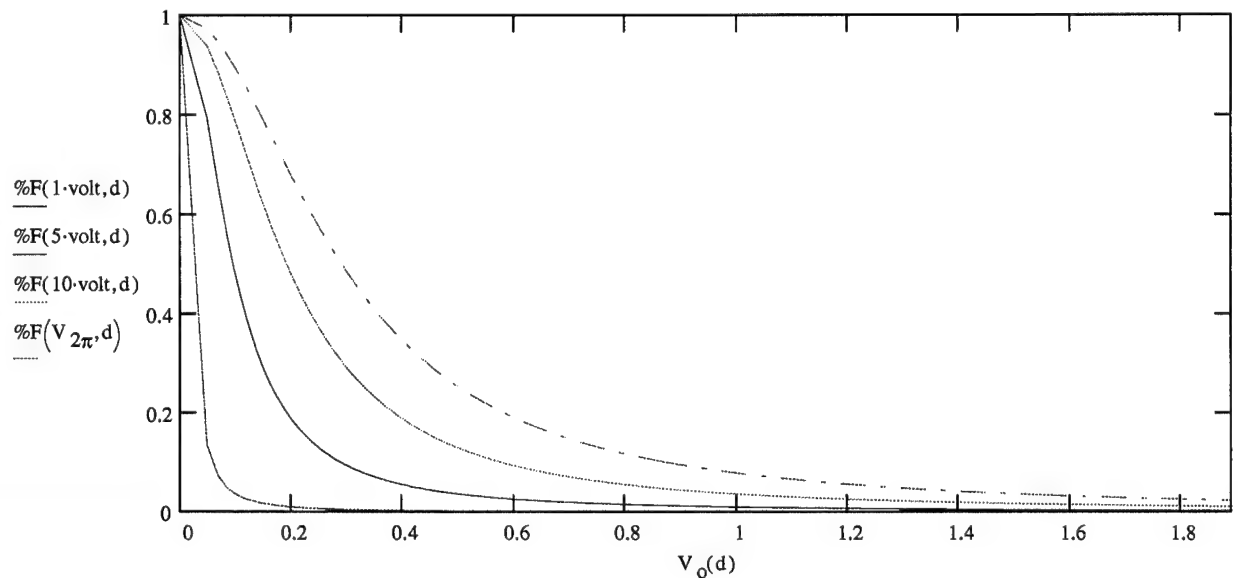
# Frequency Band Filter Design

Frequency Range of Interest for Detector Signal: $\qquad \omega_S := 1 \cdot Hz \cdot (2 \cdot \pi), 2 \cdot Hz \cdot (2 \cdot \pi) .. 1 \cdot kHz \cdot (2 \cdot \pi)$

Frequency Range of Interest for Amplifier Noise: $\qquad \omega_N := 1 \cdot kHz \cdot (2 \cdot \pi), 2 \cdot kHz \cdot (2 \cdot \pi) .. 1 \cdot MHz \cdot (2 \cdot \pi)$

### *Low Pass Filter:*

( Noise Block )

$C_H := 0.022 \cdot \mu F$

$R_{HP} := 33 \cdot k\Omega$

$R_{HS} := 220 \cdot \Omega$
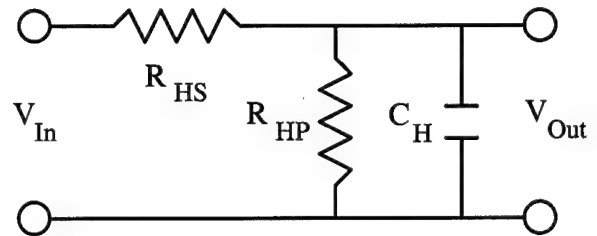


$$\omega_H := \frac{1}{C_H} \cdot \left( \frac{R_{HS} + R_{HP}}{R_{HS} \cdot R_{HP}} \right) \qquad LPF(\omega) := \left( \frac{R_{HP}}{R_{HP} + R_{HS}} \right) \cdot \left( \frac{1}{1 + \dfrac{i \cdot \omega}{\omega_H}} \right) \qquad LM(\omega) := 20 \cdot \log( |LPF(\omega)| )$$



$LM(\omega_N) \cdot dB$

$\dfrac{\omega_N}{2 \cdot \pi} \cdot Hz$
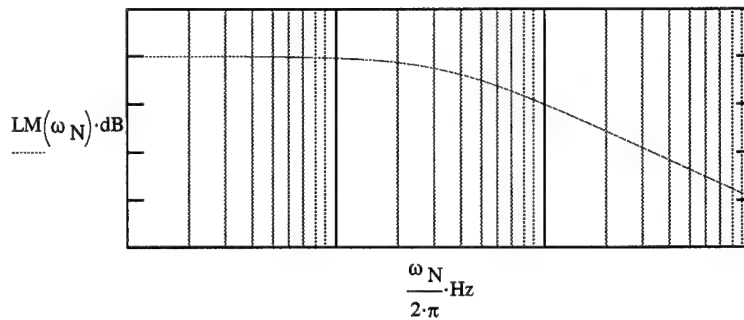
### High Frequency Limit:

$$\frac{\omega_H}{2 \cdot \pi} = 33.102 \cdot kHz$$

### *High Pass Filter:*

( DC Block )

$C_L := 10 \cdot \mu F$

$R_{LP} := 1 \cdot k\Omega$

$R_{LS} := 0 \cdot \Omega$
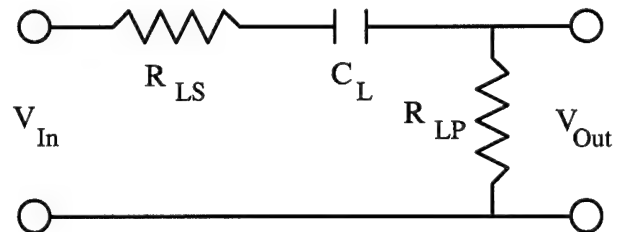


$$\omega_L := \frac{1}{C_L \cdot (R_{LS} + R_{LP})} \qquad HPF(\omega) := \left( \frac{R_{LP}}{R_{LP} + R_{LS}} \right) \cdot \left( \frac{1}{1 + \dfrac{\omega_L}{i \cdot \omega}} \right) \qquad LM(\omega) := 20 \cdot \log( |HPF(\omega)| )$$



$LM(\omega_S) \cdot dB$

$\dfrac{\omega_S}{2 \cdot \pi} \cdot Hz$
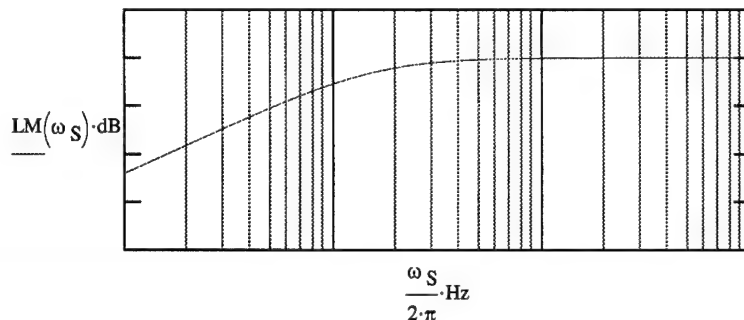
### Low Frequency Limit:

$$\frac{\omega_L}{2 \cdot \pi} = 15.915 \cdot Hz$$

**_Amplification:_**  $A := 400$  Two stages with approximate gain of 20 each.

**_Band Pass Filter:_**  $i := 1, 2 .. 5000$  $\omega_i := \left(\dfrac{i}{5}\right)^2 \cdot 2 \cdot \pi$  $LM(\omega) := 20 \cdot \log\left(\left| LPF(\omega) \cdot HPF(\omega) \cdot A \right|\right)$

**_Amplifier Characteristics:_**  $NoLoss := 20 \cdot \log(A)$  $NoLoss = 52.041 \cdot dB$



$$\dfrac{LM\left(\omega_i\right) \cdot dB}{NoLoss \cdot dB}$$

$$\dfrac{\omega_i}{2 \cdot \pi} \cdot Hz$$
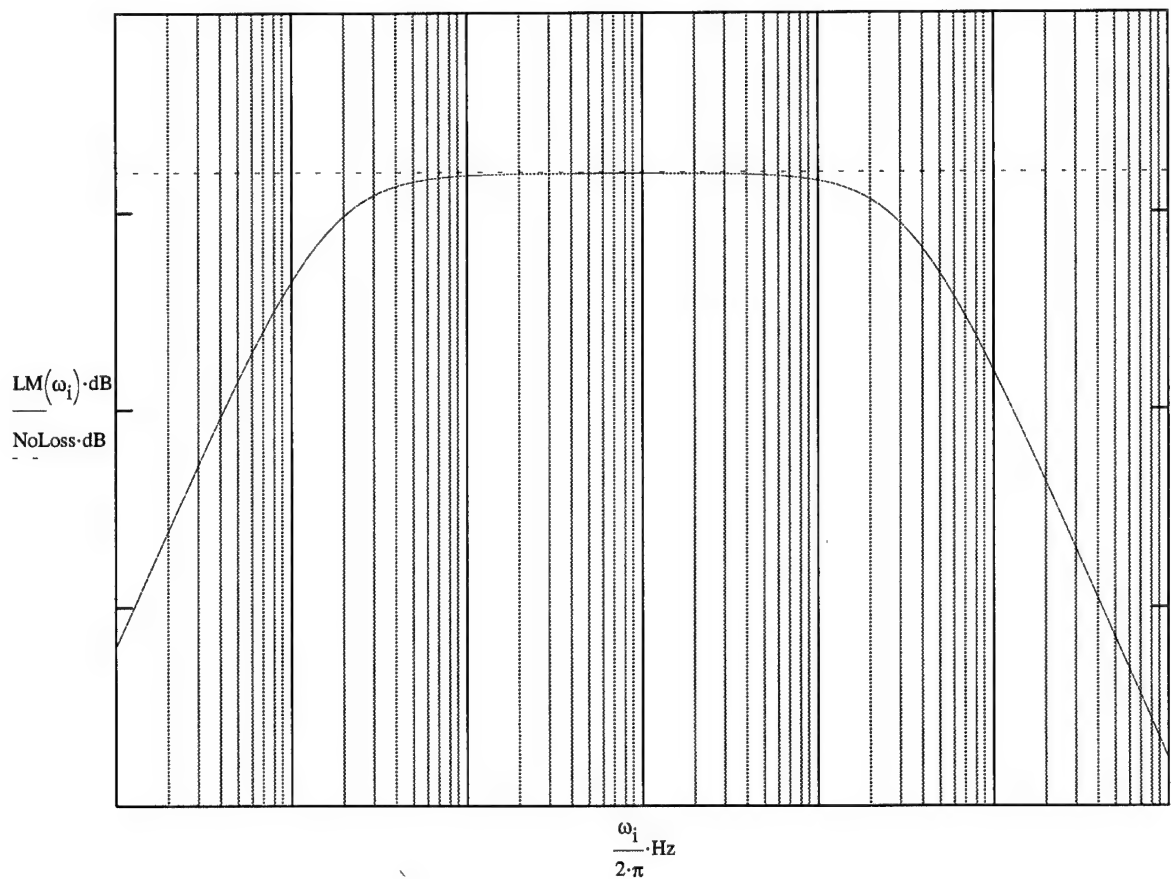
# Mirror Surface Deformations

$$w_x := 16 \cdot \mu m \qquad w_y := 16 \cdot \mu m \qquad \text{Amplitude} := 10 \cdot nm$$

$$d_1(x,y) := -\text{Amplitude} \cdot \sqrt{\left(\cos\left(\frac{2 \cdot \pi \cdot x}{w_x}\right) + 1\right) \cdot \left(\cos\left(\frac{2 \cdot \pi \cdot y}{w_y}\right) + 1\right)}$$

$$d_2(x,y) := \frac{-\text{Amplitude}}{2} \cdot \left[1 + \frac{1}{2} \cdot \left(\cos\left(\frac{2 \cdot \pi \cdot x}{w_x}\right) + \cos\left(\frac{2 \cdot \pi \cdot y}{w_y}\right)\right)\right]$$

$$\text{NumberPoints} := 20 \qquad i := 0, 1 .. \text{NumberPoints} \qquad j := 0, 1 .. \text{NumberPoints}$$

$$x_i := \frac{i \cdot w_x}{\text{NumberPoints}} - \frac{w_x}{2} \qquad\qquad y_j := \frac{j \cdot w_y}{\text{NumberPoints}} - \frac{w_y}{2}$$

$$D1_{i,j} := d_1(x_i, y_j) \qquad\qquad\qquad D2_{i,j} := d_2(x_i, y_j)$$
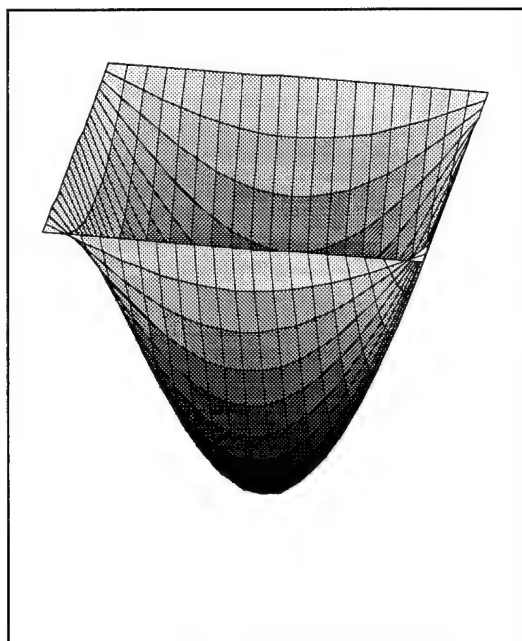


D1



D2
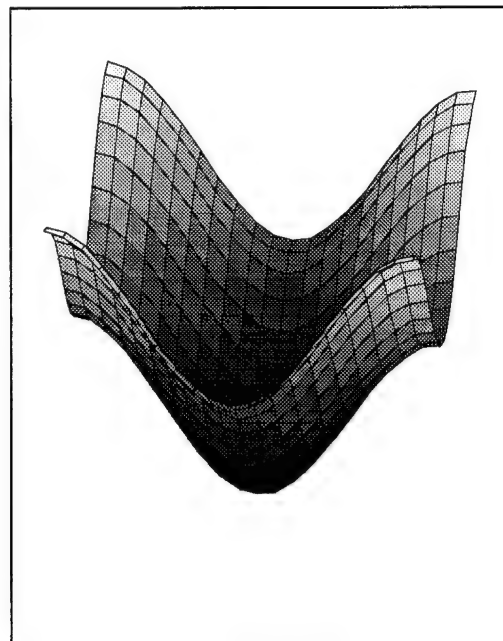
Mirror surface deformations for mirrors in which the hinges are attached at some length, $L_h$, from the corners of the mirror.

$$L_h := 5 \cdot \mu m \qquad L_x := w_x - L_h \qquad L_y := w_y - L_h$$

$$\theta_x := atan\left(\frac{L_h}{L_x}\right) \qquad \theta_y := atan\left(\frac{L_h}{L_y}\right) \qquad Scale := \sqrt{\frac{w_x^2 + w_y^2}{w_x^2 + w_y^2 + 4 \cdot \left(L_h^2 - w_x \cdot L_h\right)}}$$

$$x'(x,y) := \left(x \cdot \cos\left(\theta_x\right) - y \cdot \sin\left(\theta_y\right)\right) \cdot Scale \qquad y'(x,y) := \left(x \cdot \sin\left(\theta_x\right) + y \cdot \cos\left(\theta_y\right)\right) \cdot Scale$$

$$D_{i,j} := d_2\left(x'\left(x_i, y_j\right), y'\left(x_i, y_j\right)\right) \qquad \theta_x \cdot \frac{180}{\pi} = 24.444 \qquad \theta_y \cdot \frac{180}{\pi} = 24.444$$

White areas represent the location of the hinges while the darker areas represent the location of the deeper deflections.
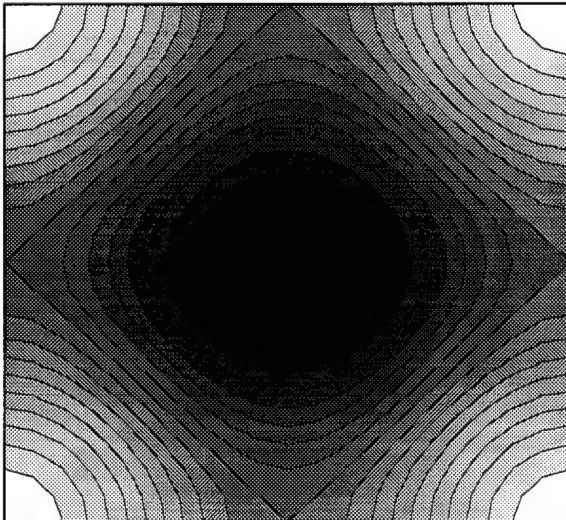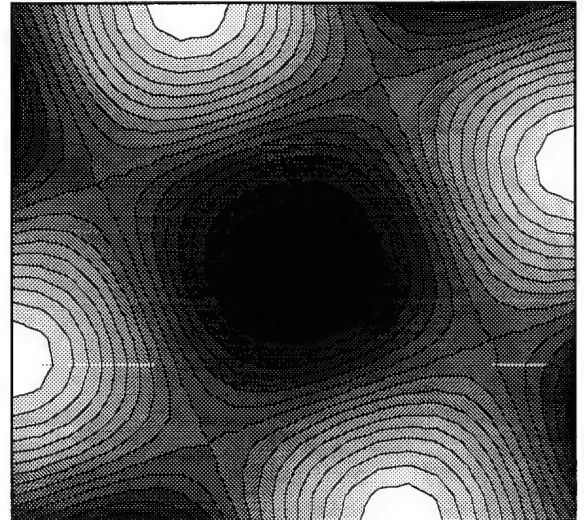


D2                                          D

# Mirror Surface Deformations With Corner Flexures
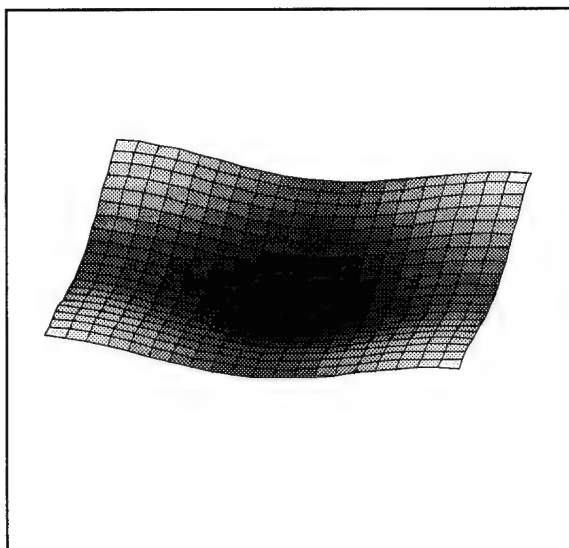


D2



D2
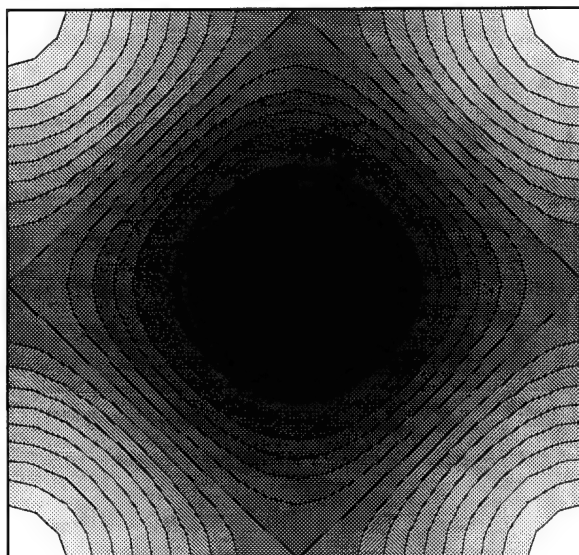
# Mirror Surface Deformations With Side Flexures
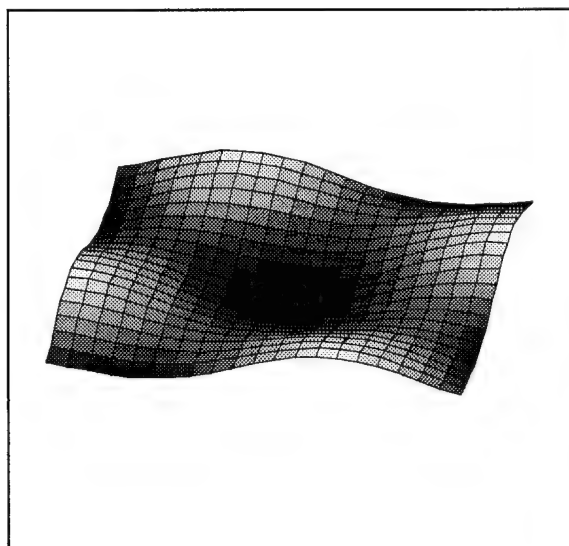


D



D
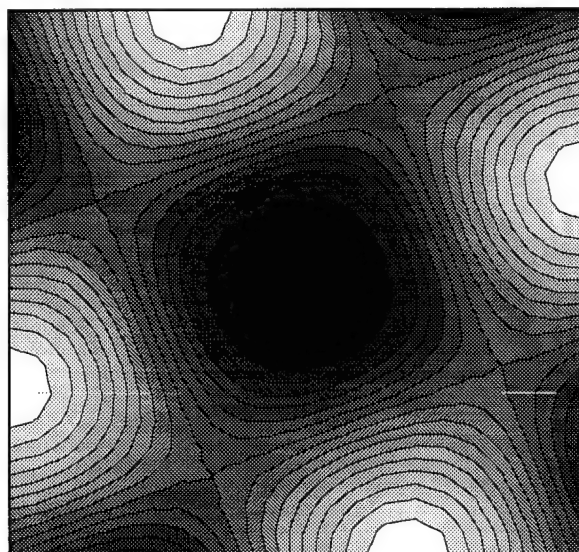
# Surface Deformation Integral Verification

$$j := 0, 1 .. 2 \qquad \text{Amplitude}_j := 50 \cdot j \cdot nm \qquad z_i := \left( \frac{i}{10} + 1 \right) \cdot \mu m$$

$$\Delta z(x, y, Amp) := \frac{Amp}{2} \cdot \left[ 1 + \frac{1}{2} \cdot \left( \cos\left( \frac{2 \cdot \pi \cdot x}{w_x} \right) + \cos\left( \frac{2 \cdot \pi \cdot y}{w_y} \right) \right) \right]$$

$$\text{Value}_{i,j} := \int_{-\frac{w_x}{2}}^{\frac{w_x}{2}} \int_{-\frac{w_y}{2}}^{\frac{w_y}{2}} \frac{1}{\left( z_i - \Delta z(x, y, \text{Amplitude}_j) \right)^2} \, dy \, dx \qquad \text{Fit}_{i,j} := \frac{1}{\tan\left[ \dfrac{\left( z_i - \dfrac{\text{Amplitude}_j}{2} \right)^2}{w_x \cdot w_y} \right]}$$

$$\begin{array}{l} \text{Value}_{i,j} \\ \square \\ \text{Fit}_{i,0} \\ \underline{\hphantom{xxxx}} \\ \text{Fit}_{i,1} \\ \cdots\cdots \\ \text{Fit}_{i,2} \\ \cdots\cdots \end{array}$$
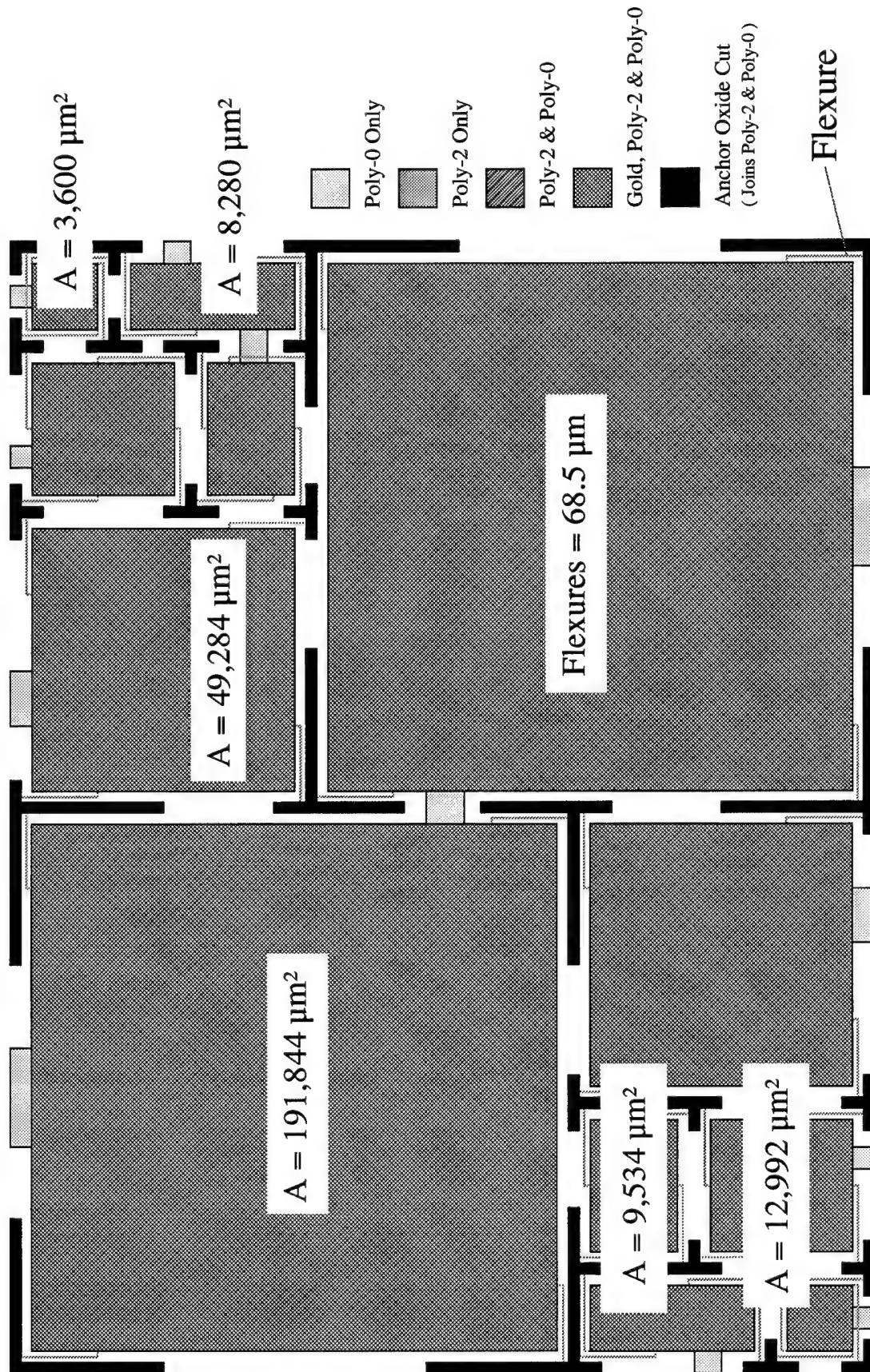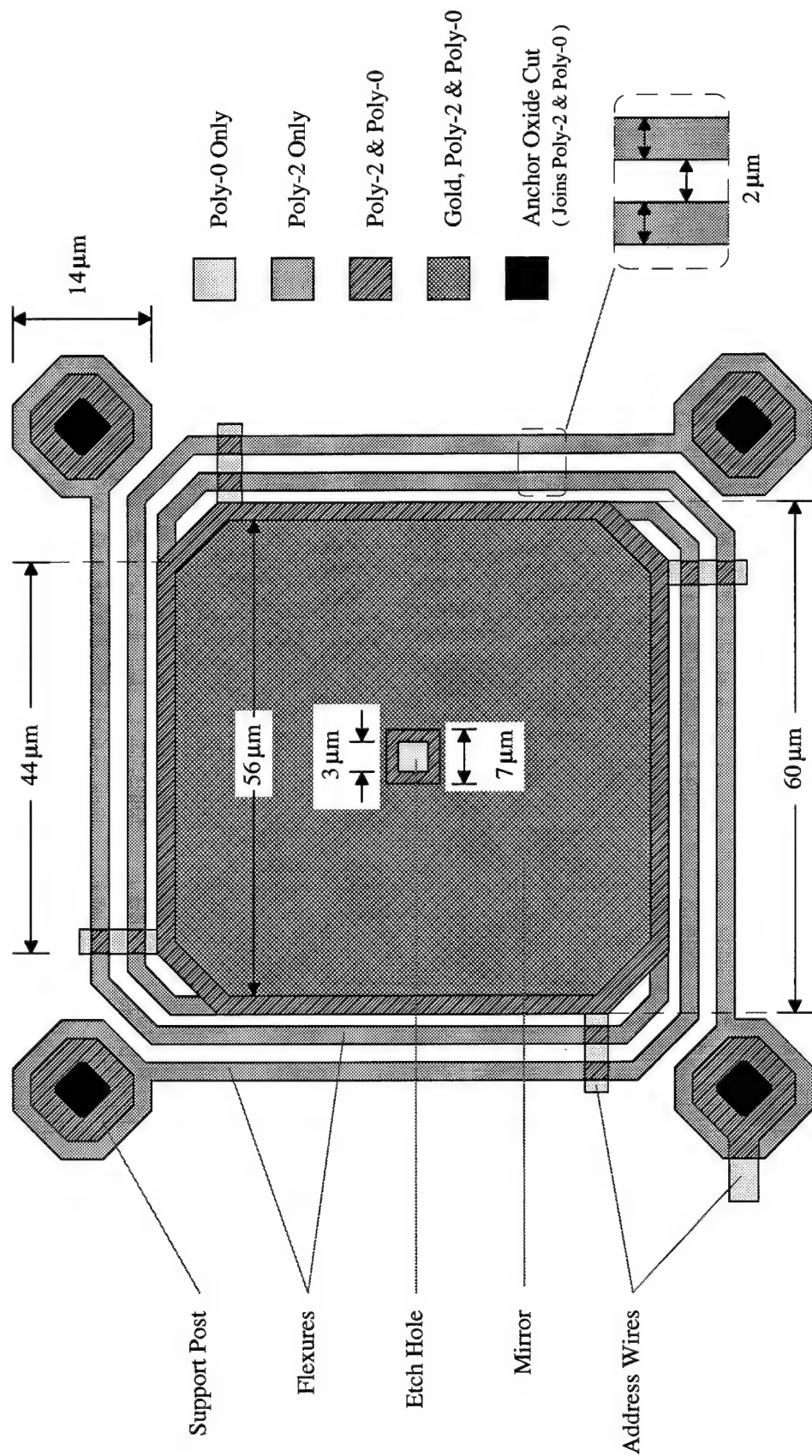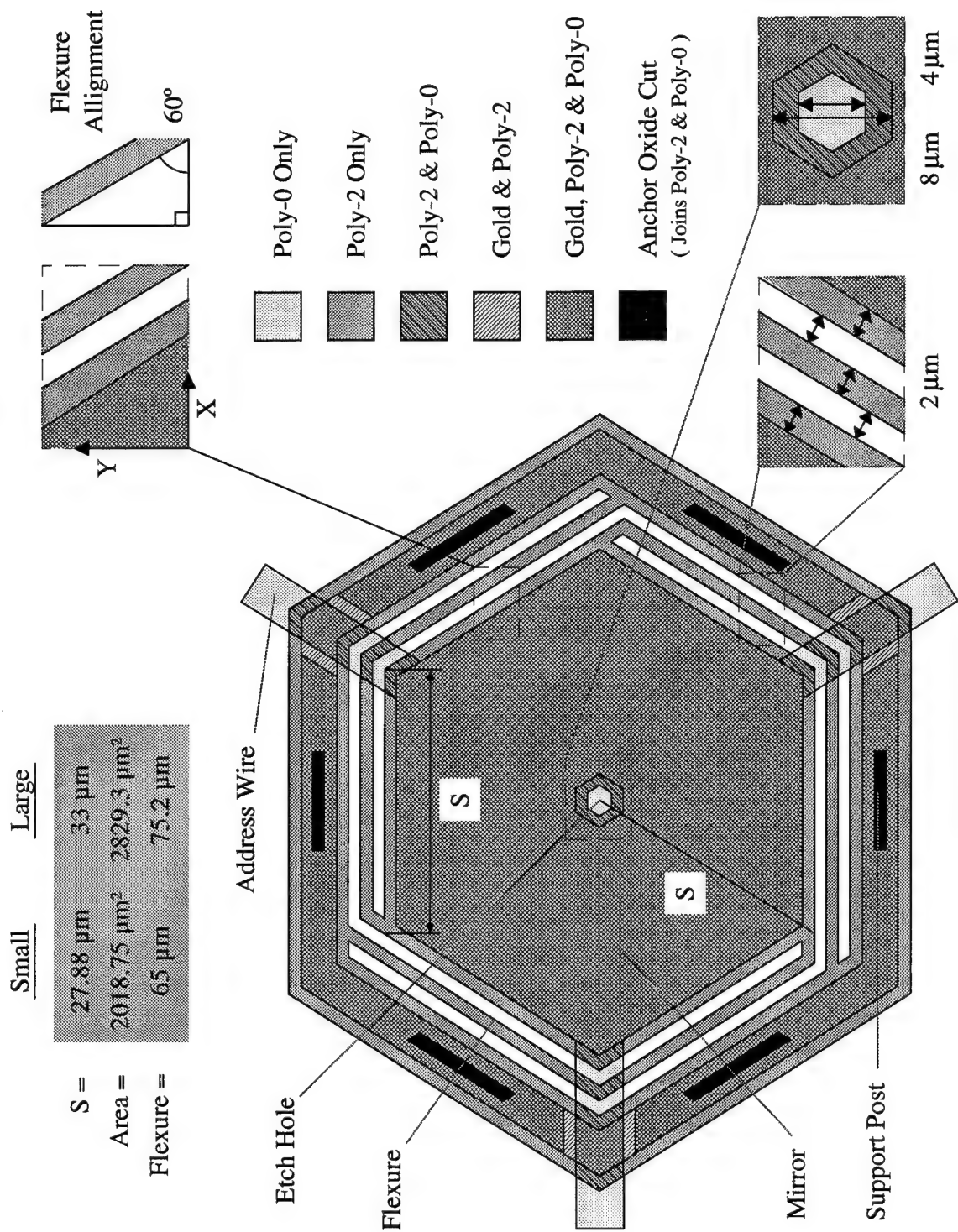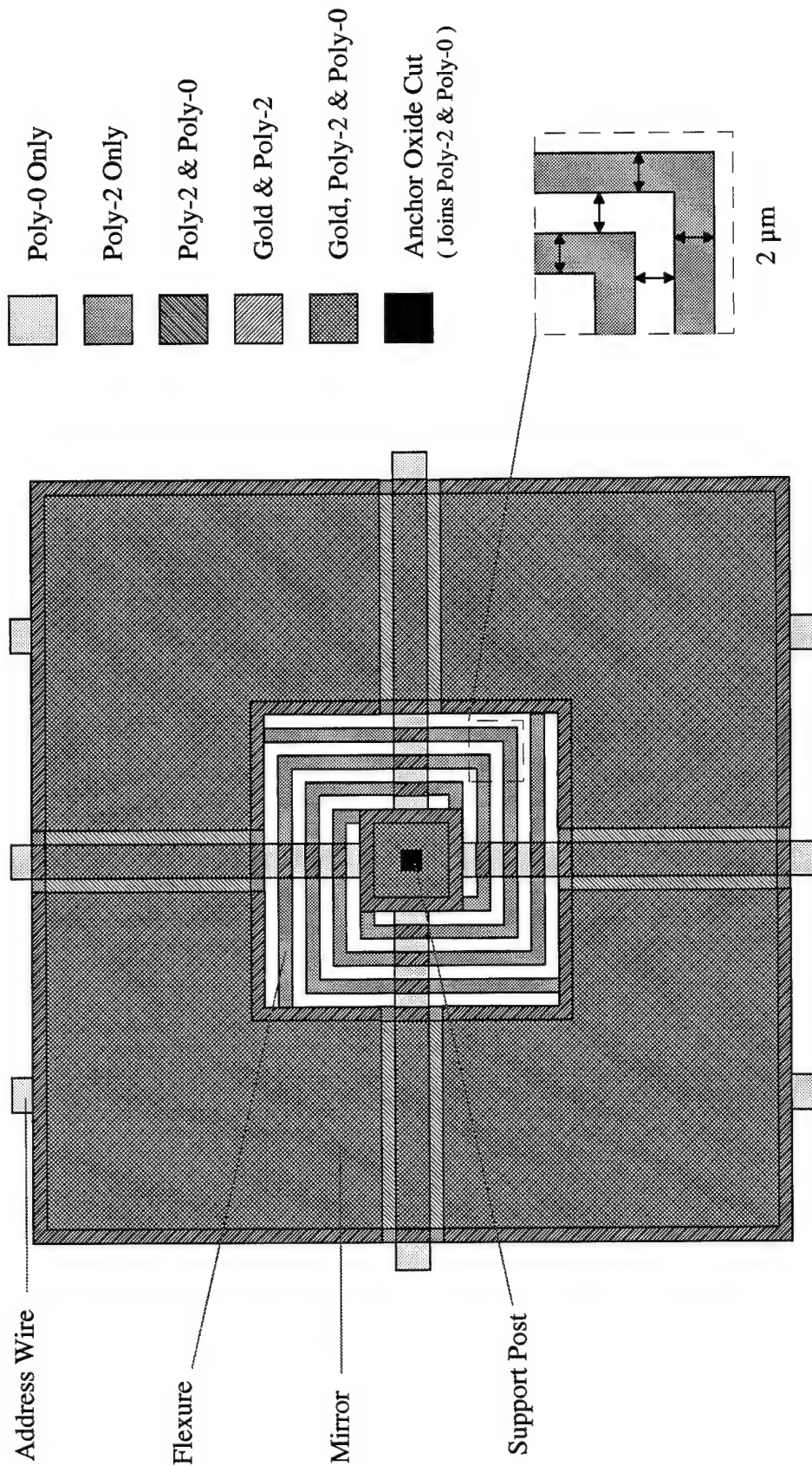


$z_i$

# *APPENDIX*

# (C)

# SEM Micrographs

# APPENDIX

# (D)

## Micromirror Device Layouts

$A = 3,600\ \mu m^2$

$A = 8,280\ \mu m^2$

Poly-0 Only

Poly-2 Only

Poly-2 & Poly-0

Gold, Poly-2 & Poly-0

Anchor Oxide Cut
( Joins Poly-2 & Poly-0 )

Flexure

$A = 49,284\ \mu m^2$

Flexures = 68.5 µm

$A = 191,844\ \mu m^2$

$A = 9,534\ \mu m^2$

$A = 12,992\ \mu m^2$

D-2

Poly-0 Only

Poly-2 Only

Poly-2 & Poly-0

Gold, Poly-2 & Poly-0

Anchor Oxide Cut
( Joins Poly-2 & Poly-0 )

14 μm

44 μm

60 μm

56 μm

3 μm

7 μm

2 μm

Support Post

Flexures

Etch Hole

Mirror

Address Wires

Flexure
Allignment

60°

Y
X

Poly-0 Only
Poly-2 Only
Poly-2 & Poly-0
Gold & Poly-2
Gold, Poly-2 & Poly-0
Anchor Oxide Cut
( Joins Poly-2 & Poly-0 )

8 μm     4 μm

2 μm

Address Wire

Etch Hole

Flexure

S

S

Mirror

Support Post

| | Small | Large |
|---|---|---|
| S = | 27.88 μm | 33 μm |
| Area = | 2018.75 μm² | 2829.3 μm² |
| Flexure = | 65 μm | 75.2 μm |

D-4

Flexures = 89 µm      Area = (113 µm)² - (43 µm)² = 10,920 µm²

Poly-0 Only

Poly-2 Only

Poly-2 & Poly-0

Gold & Poly-2

Gold, Poly-2 & Poly-0

Anchor Oxide Cut
( Joins Poly-2 & Poly-0 )

2 µm

Address Wire

Flexure

Mirror

Support Post

Flexure =

| Small | Large |
|-------|-------|
| 15 μm | 25 μm |

Support Post

Etch Hole

Mirror

Flexure

Area = 3,150 μm²

3 μm    7 μm

60 μm

30 μm

Poly-0 Only

Poly-2 Only

Poly-2 & Poly-0

Gold, Poly-2 & Poly-0

Anchor Oxide Cut
( Joins Poly-2 & Poly-0 )

D-6

Poly-0 Only
Poly-2 Only
Poly-2 & Poly-0
Gold, Poly-2 & Poly-0
Anchor Oxide Cut
( Joins Poly-2 & Poly-0 )

Etch Hole

Support Post

Flexure

Mirror

Area = 3,399 μm²
Flexure = 208.5 μm

60 μm
7 μm
3 μm
29 μm
53 μm

Poly-0 Only

Poly-2 Only

Poly-2 & Poly-0

Gold, Poly-2 & Poly-0

Anchor Oxide Cut
( Joins Poly-2 & Poly-0 )

Etch Hole

Support Post

Flexure

Mirror

7 μm

3 μm

60 μm

29 μm

53 μm

Area = 3,399 μm²

Flexure = 108.5 μm

Poly-0 Only

Poly-2 Only

Poly-2 & Poly-0

Gold, Poly-2 & Poly-0

Anchor Oxide Cut
( Joins Poly-2 & Poly-0 )

7 µm

3 µm

60 µm

29 µm

53 µm

Area = 3,399 µm²

Flexure = 66 µm

Etch Hole

Support Post

Flexure

Mirror

*APPENDIX*

# (E)

Enlarged Data Plots
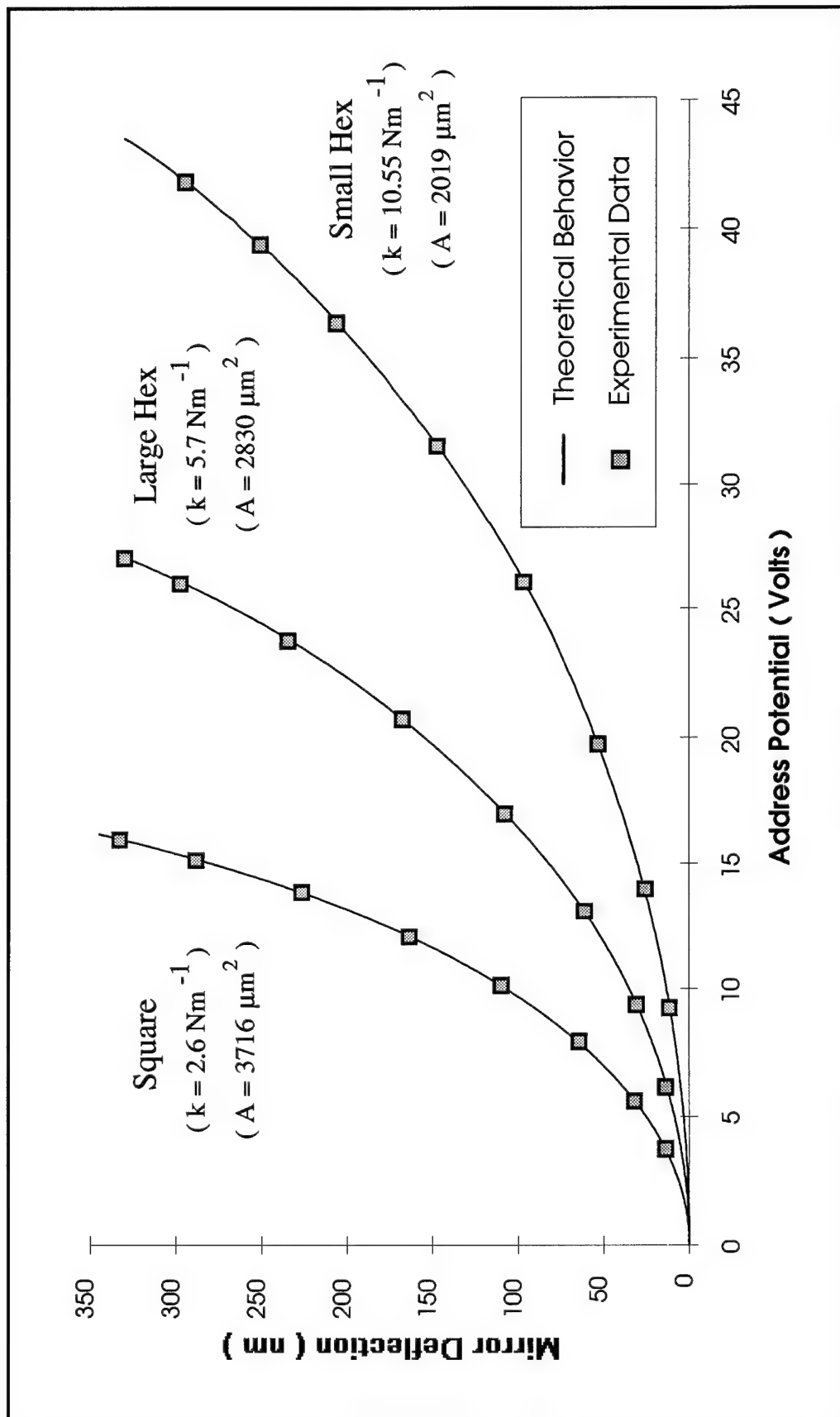
**Figure 5-8**
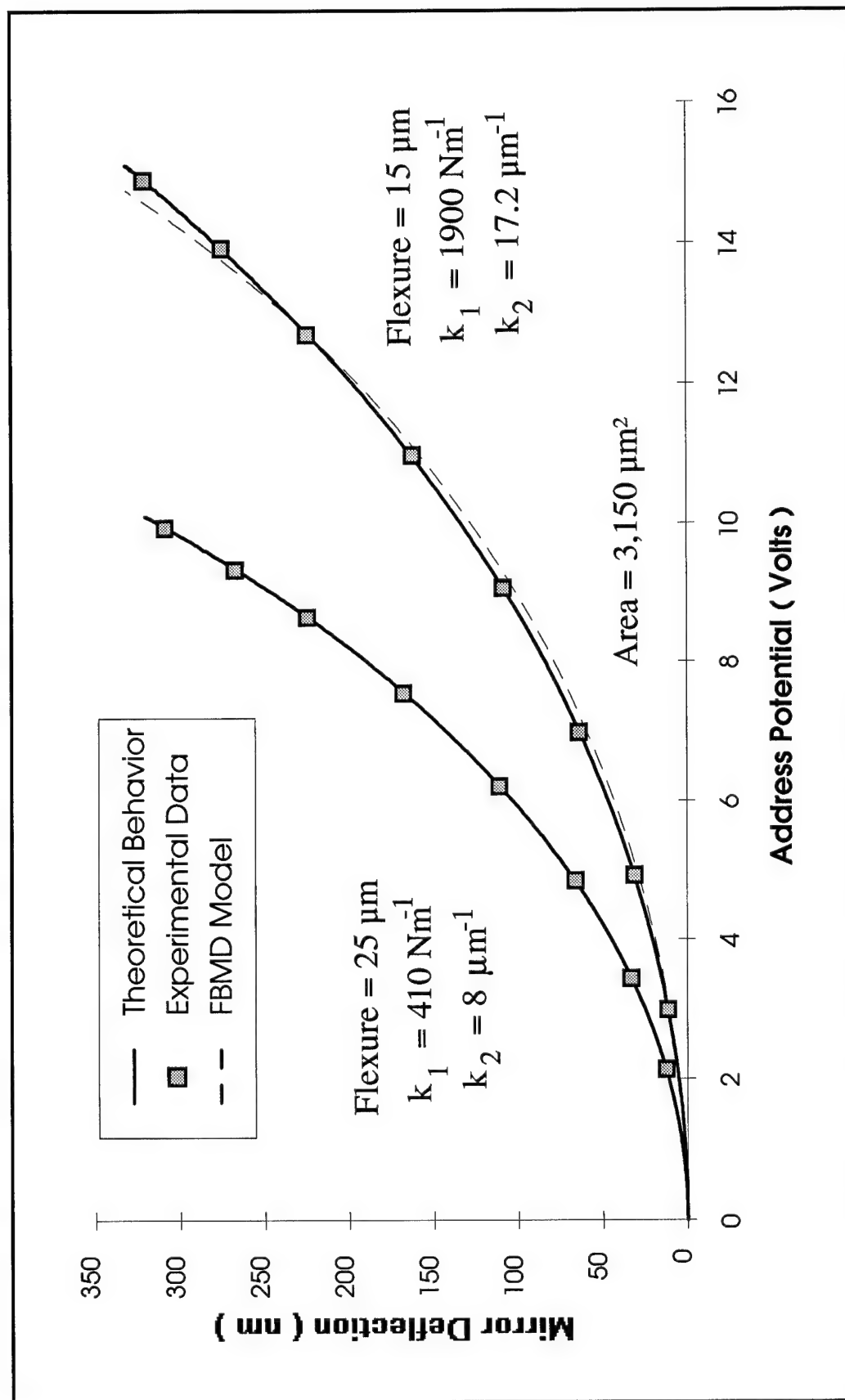
**Figure 5-9**
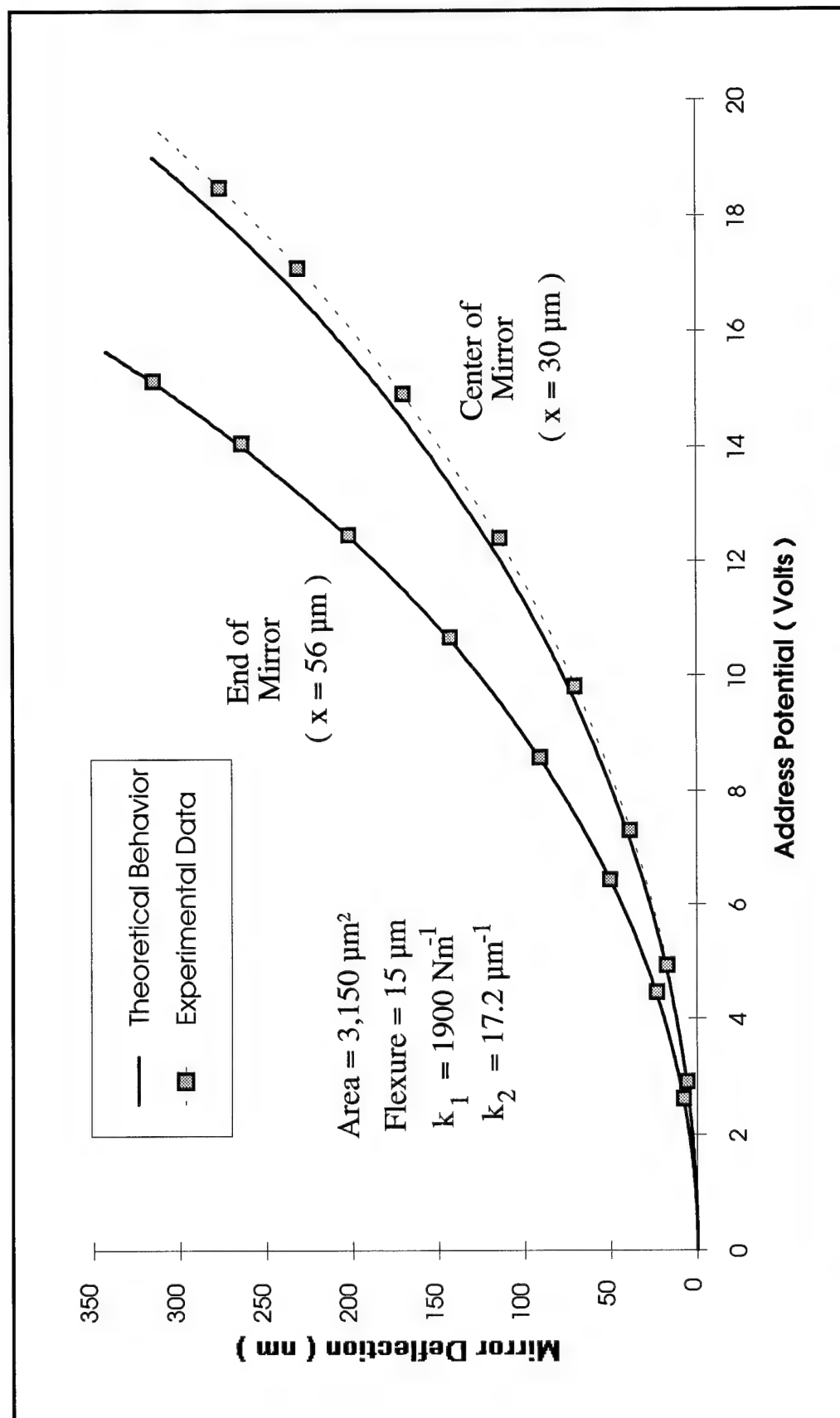
**Figure 5-10**
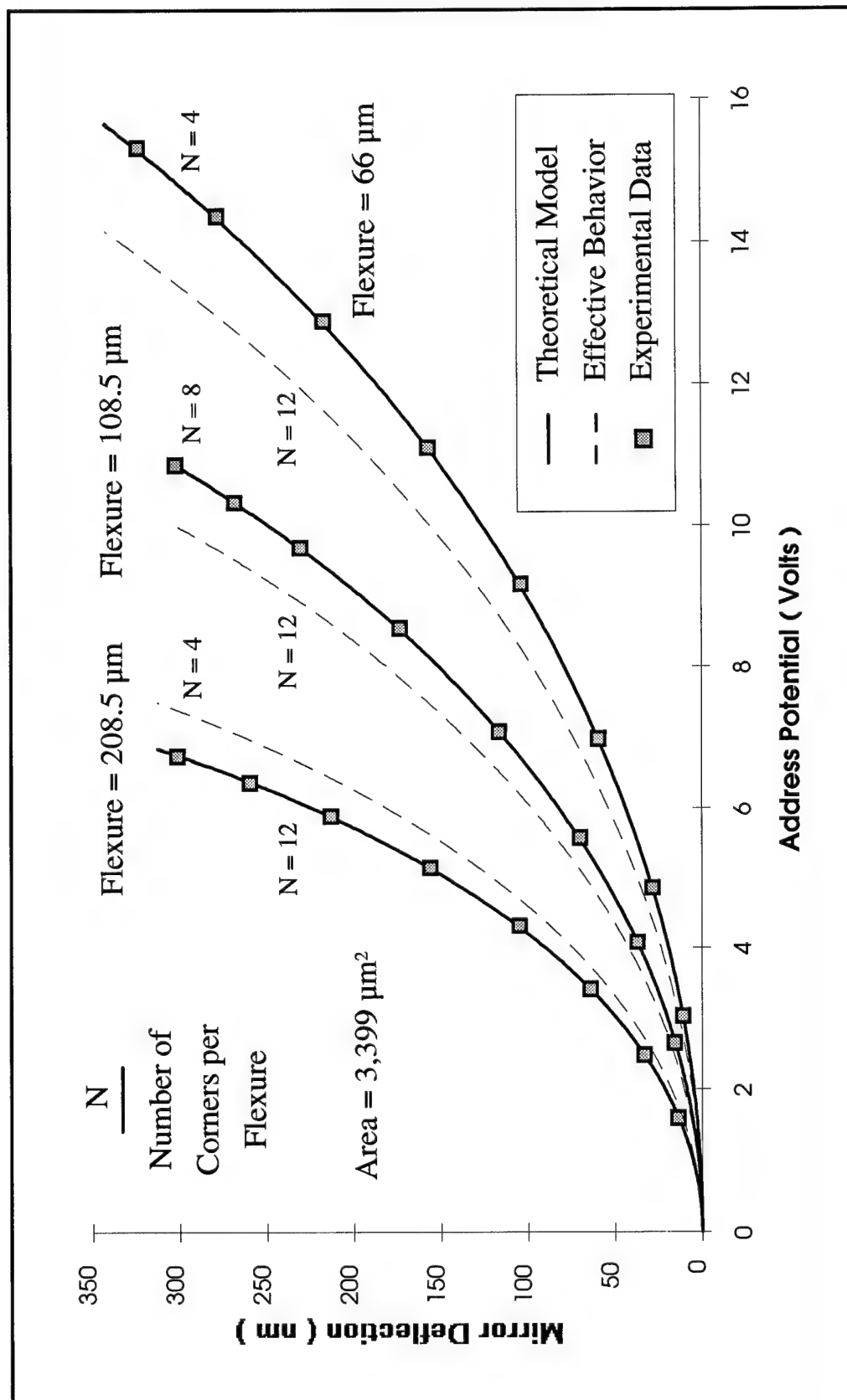
**Figure 5-11**

Figure 5-12

**Figure 5-13**

Legend:
- Mirror Center (dashed)
- Four Corners (solid)

Area = 3,716 µm²
Flexure = 132 µm

7 nm

X-axis: Address Potential ( Volts ), 0 to 18
Y-axis: Mirror Deflection ( nm ), 0 to 350

Figure 5-14

Figure 5-15

The figure shows a plot of Maximum Mirror Deflection (nm) versus Mirror Surface Area ($\mu m^2$). The vertical axis ranges from 0 to 6 nm, and the horizontal axis ranges from 0 to 10000 $\mu m^2$. Three curves are labeled $x_s = 10 \ \mu m$, $x_s = 15 \ \mu m$, and $x_s = 20 \ \mu m$.

Parameters shown in the box:
$$d_{2\pi} = 316.4 \ nm$$
$$z_o = 2.5 \ \mu m$$

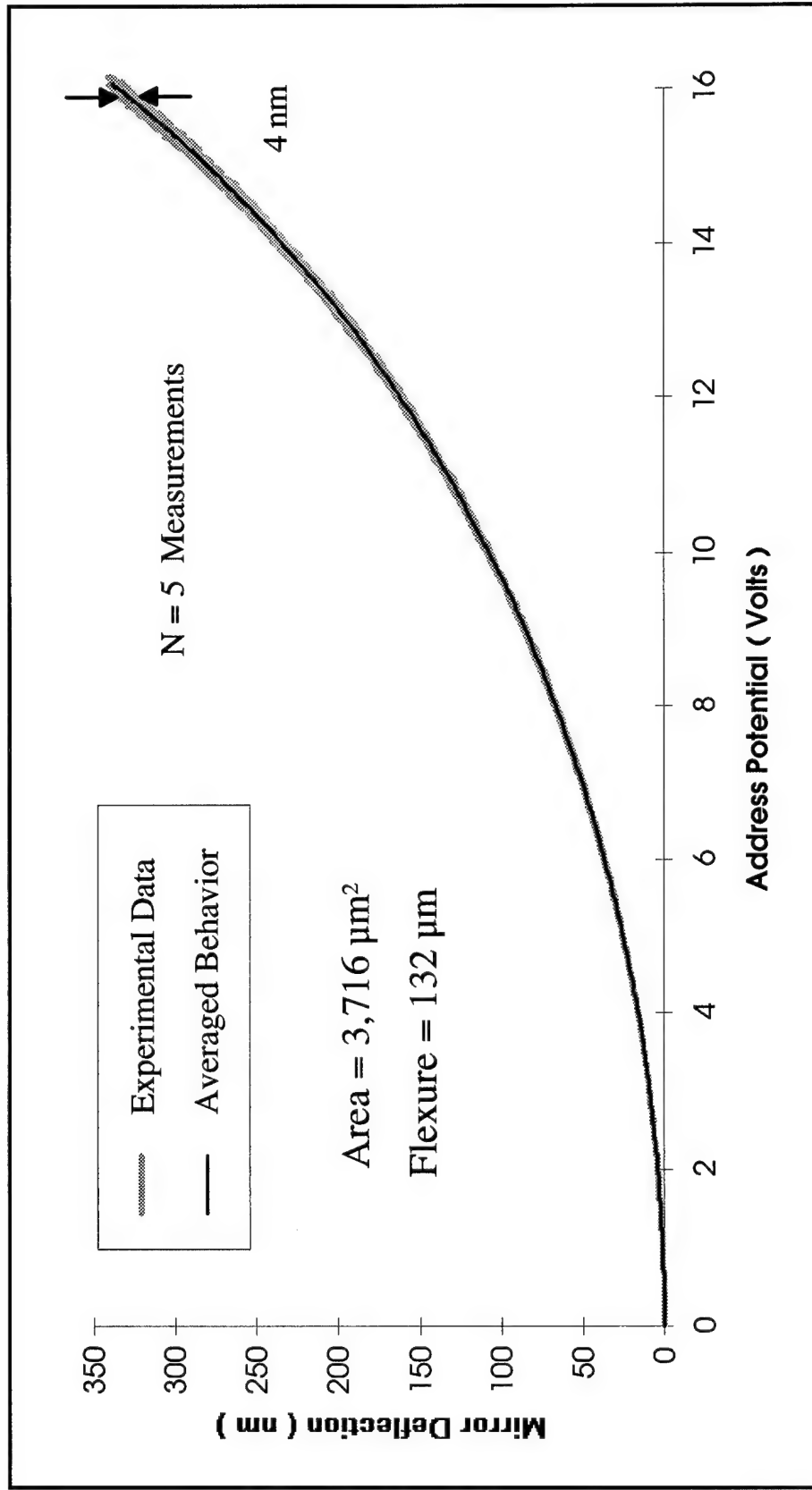Figure 5-16

**Figure 5-17**

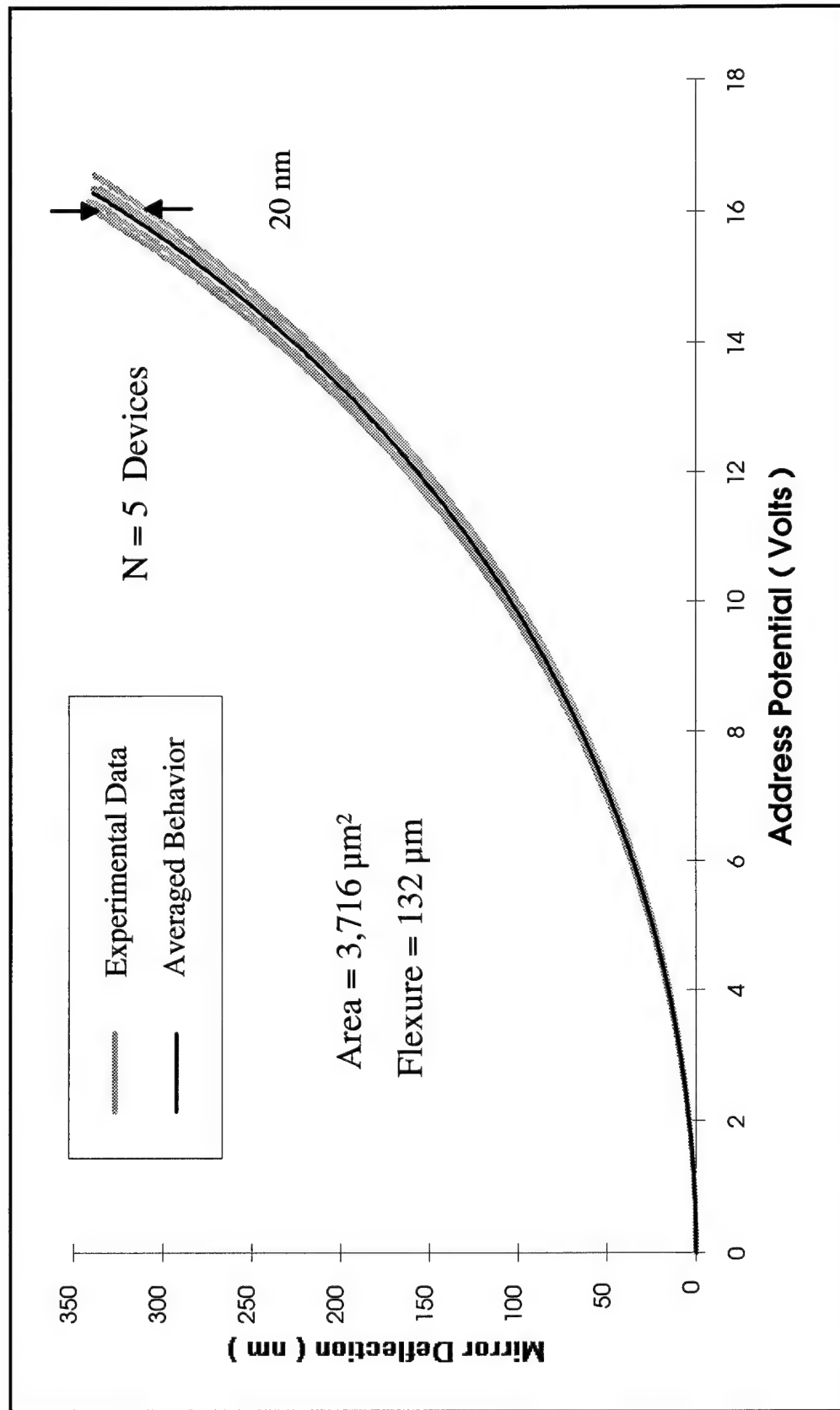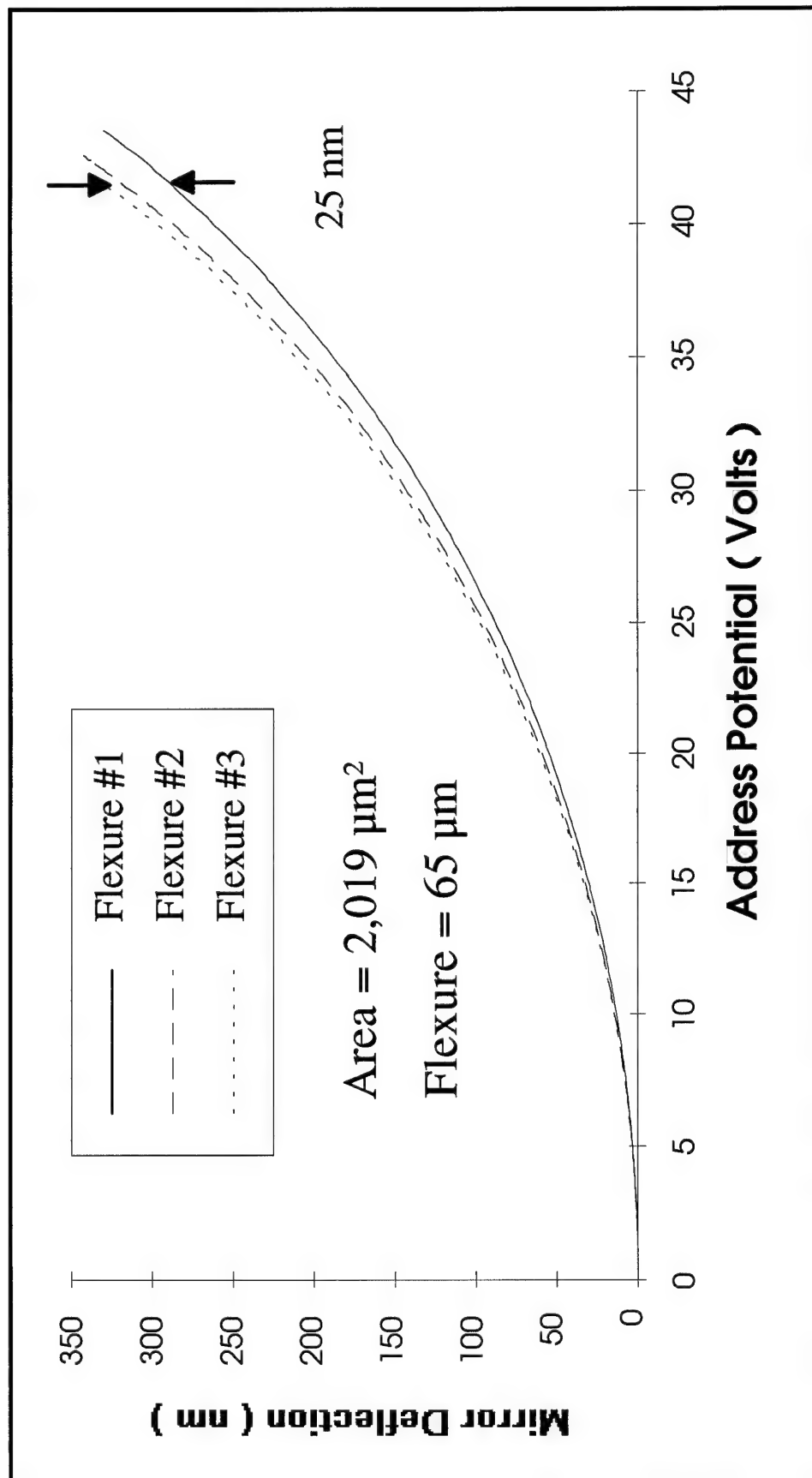**Figure 5-18**

Figure 5-19

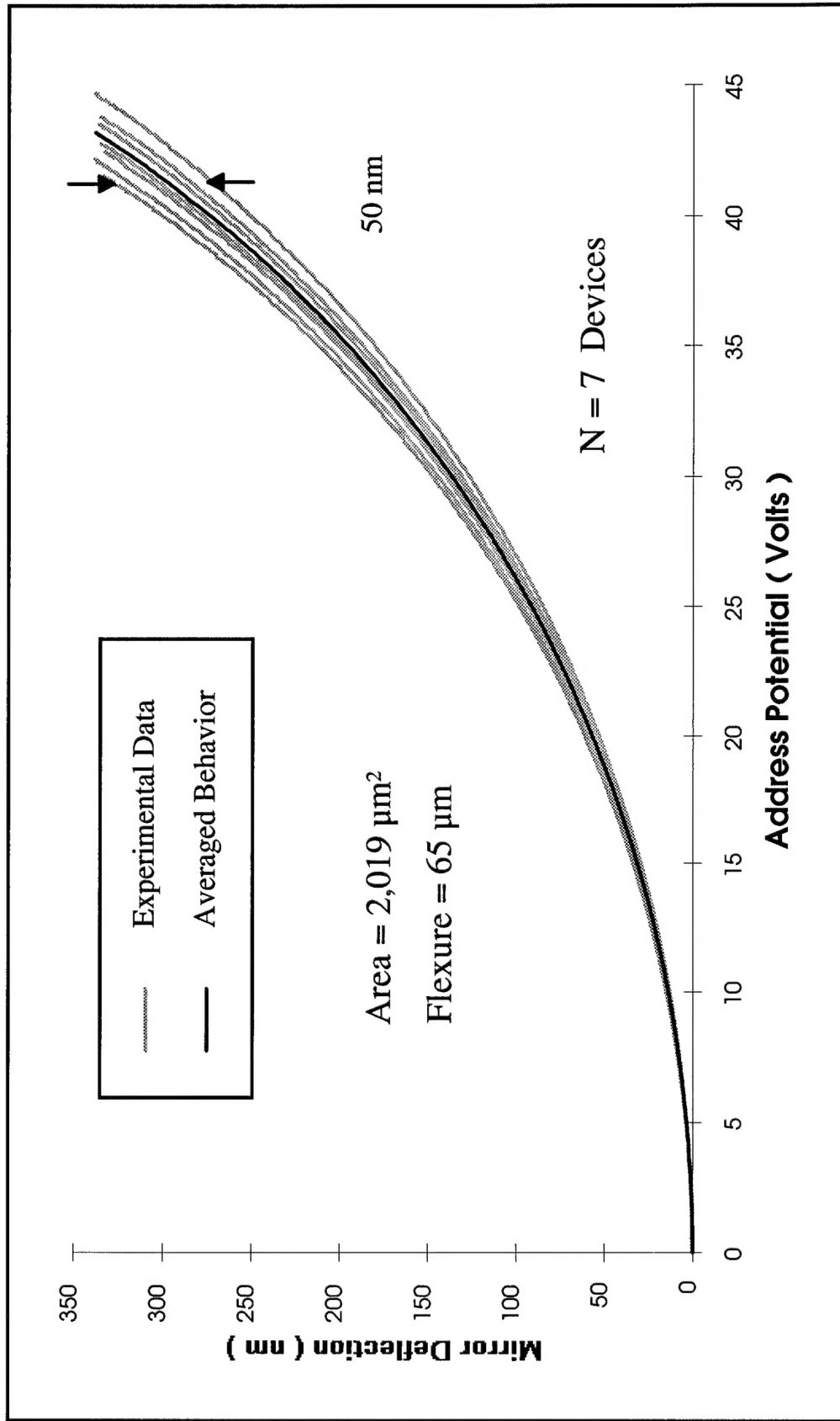**Figure 5-20**

Figure 5-21

Figure 5-22

# *VITA*

*NAME:*      M. Adrian Michalicek

   Mark Adrian Michalicek was born on July 16, 1970 in Cedar Rapids, Iowa. He
graduated from John F. Kennedy Senior High School on June 3, 1988 and later attended
Kirkwood Community College in Cedar Rapids, Iowa and Iowa State University in
Ames, Iowa. Cadet Michalicek joined the Cadet Wing at the United States Air Force
Academy in Colorado Springs, Colorado on June 28, 1989 and graduated as a member of
Cadet Squadron Eight (CS-08) on June 2, 1993 with a Bachelor of Science degree in
Space Physics. Second Lieutenant Michalicek's first assignment was to the Air Force
Institute of Technology at Wright-Patterson AFB, Ohio. While at AFIT, he married
Kimberly Anne Martin from Denver, Colorado on February 14, 1994 in Chicago, Illinois.
First Lieutenant Michalicek graduated from AFIT on June 13, 1995 with a Master of
Science degree in Electrical Engineering and was then assigned to Phillips Lab at
Kirtland AFB in Albuquerque, New Mexico.

# REPORT DOCUMENTATION PAGE

| 1. AGENCY USE ONLY (Leave blank) | 2. REPORT DATE | 3. REPORT TYPE AND DATES COVERED |
|---|---|---|
| | June 1995 | Master's Thesis |

**4. TITLE AND SUBTITLE**

DESIGN, FABRICATION, MODELING, AND TESTING OF SURFACE-MICROMACHINED MICROMIRROR DEVICES

**5. FUNDING NUMBERS**

**6. AUTHOR(S)**

M. Adrian Michalicek, 2nd Lieutenant, USAF

**7. PERFORMING ORGANIZATION NAME(S) AND ADDRESS(ES)**

Air Force Institute of Technology, WPAFB OH 45433-6583

**8. PERFORMING ORGANIZATION REPORT NUMBER**

AFIT/GE/ENG/95J-01

**9. SPONSORING / MONITORING AGENCY NAME(S) AND ADDRESS(ES)**

Captain Richard D. Shute, Wright Laboratory (WL/AAAI-2)
2241 Avionics Circle, WPAFB, OH 45433-7323

**10. SPONSORING / MONITORING AGENCY REPORT NUMBER**

**11. SUPPLEMENTARY NOTES**

**12a. DISTRIBUTION / AVAILABILITY STATEMENT**

Distribution Unlimited

**12b. DISTRIBUTION CODE**

**13. ABSTRACT (Maximum 200 words)**

The Flexure-Beam Micromirror Device (FBMD) is a phase-only piston style spatial light modulator demonstrating properties which can be used for phase adaptive-corrective optics. This thesis presents a complete study of new designs of FBMDs and other micromirror devices, from original design considerations through final device testing and verification of ideal and advanced models. The models relate the electrical and mechanical properties of the device by equating the electrostatic force of a parallel-plate capacitor with the counteracting spring force of the device's support flexures. For the advanced model of the Flexure-Beam micromirror device, the capacitor solution is derived via the Schwartz-Christoffel transformation such that the final solution accounts for non-ideal electric fields. This model describes the behavior of any Flexure-Beam device, given its geometry and material properties. It includes operational factors such as drive frequency and temperature, as well as fringing effects, mirror surface deformations, and cross-talk from neighboring devices. Comparisons are made between the ideal and advanced Flexure-Beam models.

Several forms of micromirror devices studied in this thesis were commercially fabricated in a standard surface micromachining process. Design considerations for these and other devices are presented. These micromirror devices were tested using a microscope-based laser interferometer which generates a continuous stream of data for each selected position on the mirror surface. Plots of this data describe the localized surface deflection as a function of drive voltage.

**14. SUBJECT TERMS**

micromirror devices, micromachining, MEM, MEMS, MUMPs, optical switching, micromechanical, flexure-beam, cantilever, interferometer, electrostatic actuation, thin-film elastic modulus, laser communication.

**15. NUMBER OF PAGES**

225

**16. PRICE CODE**

| 17. SECURITY CLASSIFICATION OF REPORT | 18. SECURITY CLASSIFICATION OF THIS PAGE | 19. SECURITY CLASSIFICATION OF ABSTRACT | 20. LIMITATION OF ABSTRACT |
|---|---|---|---|
| UNCLASSIFIED | UNCLASSIFIED | UNCLASSIFIED | UL |

## GENERAL INSTRUCTIONS FOR COMPLETING SF 298

The Report Documentation Page (RDP) is used in announcing and cataloging reports. It is important that this information be consistent with the rest of the report, particularly the cover and title page. Instructions for filling in each block of the form follow. It is important to *stay within the lines* to meet *optical scanning requirements*.

**Block 1.** Agency Use Only *(Leave blank)*.

**Block 2.** Report Date. Full publication date including day, month, and year, if available (e.g. 1 Jan 88). Must cite at least the year.

**Block 3.** Type of Report and Dates Covered. State whether report is interim, final, etc. If applicable, enter inclusive report dates (e.g. 10 Jun 87 - 30 Jun 88).

**Block 4.** Title and Subtitle. A title is taken from the part of the report that provides the most meaningful and complete information. When a report is prepared in more than one volume, repeat the primary title, add volume number, and include subtitle for the specific volume. On classified documents enter the title classification in parentheses.

**Block 5.** Funding Numbers. To include contract and grant numbers; may include program element number(s), project number(s), task number(s), and work unit number(s). Use the following labels:

| | | | | |
|---|---|---|---|---|
| **C** | - | Contract | **PR** - | Project |
| **G** | - | Grant | **TA** - | Task |
| **PE** | - | Program Element | **WU** - | Work Unit Accession No. |

**Block 6.** Author(s). Name(s) of person(s) responsible for writing the report, performing the research, or credited with the content of the report. If editor or compiler, this should follow the name(s).

**Block 7.** Performing Organization Name(s) and Address(es). Self-explanatory.

**Block 8.** Performing Organization Report Number. Enter the unique alphanumeric report number(s) assigned by the organization performing the report.

**Block 9.** Sponsoring/Monitoring Agency Name(s) and Address(es). Self-explanatory.

**Block 10.** Sponsoring/Monitoring Agency Report Number. *(If known)*

**Block 11.** Supplementary Notes. Enter information not included elsewhere such as: Prepared in cooperation with...; Trans. of...; To be published in.... When a report is revised, include a statement whether the new report supersedes or supplements the older report.

**Block 12a.** Distribution/Availability Statement. Denotes public availability or limitations. Cite any availability to the public. Enter additional limitations or special markings in all capitals (e.g. NOFORN, REL, ITAR).

| | | |
|---|---|---|
| DOD | - | See DoDD 5230.24, "Distribution Statements on Technical Documents." |
| DOE | - | See authorities. |
| NASA | - | See Handbook NHB 2200.2. |
| NTIS | - | Leave blank. |

**Block 12b.** Distribution Code.

| | | |
|---|---|---|
| DOD | - | Leave blank. |
| DOE | - | Enter DOE distribution categories from the Standard Distribution for Unclassified Scientific and Technical Reports. |
| NASA | - | Leave blank. |
| NTIS | - | Leave blank. |

**Block 13.** Abstract. Include a brief *(Maximum 200 words)* factual summary of the most significant information contained in the report.

**Block 14.** Subject Terms. Keywords or phrases identifying major subjects in the report.

**Block 15.** Number of Pages. Enter the total number of pages.

**Block 16.** Price Code. Enter appropriate price code *(NTIS only)*.

**Blocks 17. - 19.** Security Classifications. Self-explanatory. Enter U.S. Security Classification in accordance with U.S. Security Regulations (i.e., UNCLASSIFIED). If form contains classified information, stamp classification on the top and bottom of the page.

**Block 20.** Limitation of Abstract. This block must be completed to assign a limitation to the abstract. Enter either UL (unlimited) or SAR (same as report). An entry in this block is necessary if the abstract is to be limited. If blank, the abstract is assumed to be unlimited.